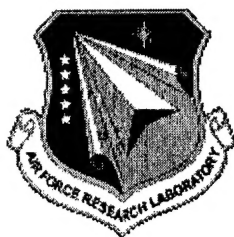


**PROCEEDINGS OF THE 2002 ANTENNA APPLICATIONS SYMPOSIUM -  
VOLUME I**

**Mr. Daniel Schaubert  
University of Massachusetts  
149 Aubinwood Road  
Amherst MA 01002**

**Final Technical Report: 18 September 2002 – 20 September 2002**

**APPROVED FOR PUBLIC RELEASE DISTRIBUTION UNLIMITED**



**AIR FORCE RESEARCH LABORATORY  
Sensors Directorate  
Electromagnetics Technology Division  
80 Scott Drive  
Hanscom AFB MA 01731-2909**

**TECHNICAL REPORT**

**TITLE: PROCEEDINGS OF THE 2002 ANTENNA APPLICATIONS  
SYMPOSIUM  
VOL I**

**APPROVED FOR PUBLIC RELEASE  
DISTRIBUTION UNLIMITED**

**NOTICE**

USING GOVERNMENT DRAWINGS, SPECIFICATIONS, OR OTHER DATA INCLUDED IN THIS DOCUMENT FOR ANY OTHER PURPOSE OTHER THAN GOVERNMENT PROCUREMENT DOES NOT IN ANY WAY OBLIGATE THE US GOVERNMENT. THE FACT THAT THE GOVERNMENT FORMULATED OR SUPPLIED THE DRAWINGS, SPECIFICATIONS, OR OTHER DATA DOES NOT LICENSE THE HOLDER OR ANY OTHER PERSON OR CORPORATION; OR CONVEY ANY RIGHTS OR PERMISSION TO MANUFACTURE, USE, OR SELL ANY PATENTED INVENTION THAT MAY RELATE TO THEM.

**THIS TECHNICAL REPORT HAS BEEN REVIEWED AND IS APPROVED FOR  
PUBLICATION.**

**\\SIGNED\\**

**HARVEY E. TOBIN  
Antenna Technology Branch  
Electromagnetics Technology Division**

**\\SIGNED\\**

**LIVIO D. POLES  
Chief, Antenna Technology Branch  
Electromagnetics Technology Division**

**\\SIGNED\\**

**ROBERT V. McGAHAN  
Technical Advisor  
Electromagnetics Technology Division**

**REPORT DOCUMENTATION PAGE**Form Approved  
OMB No. 0704-0188

Public reporting burden for this collection of information is estimated to average 1 hour per response, including the time for reviewing instructions, searching existing data sources, gathering and maintaining the data needed, and completing and reviewing this collection of information. Send comments regarding this burden estimate or any other aspect of this collection of information, including suggestions for reducing this burden to Department of Defense, Washington Headquarters Services, Directorate for Information Operations and Reports (0704-0188), 1215 Jefferson Davis Highway, Suite 1204, Arlington, VA 22202-4302. Respondents should be aware that notwithstanding any other provision of law, no person shall be subject to any penalty for failing to comply with a collection of information if it does not display a currently valid OMB control number. **PLEASE DO NOT RETURN YOUR FORM TO THE ABOVE ADDRESS.**

**1. REPORT DATE (DD-MM-YYYY)**

18-03-2003

**FINAL REPORT****18-20 September 2002****4. TITLE AND SUBTITLE**

Proceedings of the 2002 Antenna Applications Symposium – Volume I

**5a. CONTRACT NUMBER**

GSA#GS01K99BKM012

**5b. GRANT NUMBER****5c. PROGRAM ELEMENT NUMBER****6. AUTHOR(S)**

Daniel Schaubert, et al.

**5d. PROJECT NUMBER****5e. TASK NUMBER**

Task Order #R15701321

**5f. WORK UNIT NUMBER****7. PERFORMING ORGANIZATION NAME(S) AND ADDRESS(ES)**

Electromagnetics Technology Division

Sensors Directorate

Air Force Research Laboratory

80 Scott Drive

Hanscom AFB MA 01731-2909

**8. PERFORMING ORGANIZATION  
REPORT****9. SPONSORING / MONITORING AGENCY NAME(S) AND ADDRESS(ES)**

Electromagnetics Technology Division

Sensors Directorate

Air Force Research Laboratory

80 Scott Drive

Hanscom AFB MA 01731-2909

**10. SPONSOR/MONITOR'S  
ACRONYM(S)**

AFRL/SNHA

**11. SPONSOR/MONITOR'S REPORT  
NUMBER(S)****12. DISTRIBUTION / AVAILABILITY STATEMENT**

APPROVED FOR PUBLIC RELEASE. DISTRIBUTION UNLIMITED. OTHER REQUESTS FOR THIS DOCUMENT SHALL BE REFERRED TO DTIC-OMI, 8725 JOHN J. KINGMAN RD, FT BELVOIR, VA 22060-6218

**13. SUPPLEMENTARY NOTES**

Volume I contains pages 1 - 220

Volume II contains pages 221 - 456

**14. ABSTRACT**

The Proceedings of the 2002 Antenna Applications Symposium is a collection of state-of-the-art papers relating to antenna arrays, millimeter wave antennas, simulation and measurement of antennas, integrated antennas, and antenna bandwidth and radiation improvements.

**15. SUBJECT TERMS**

Antennas, Phased Arrays, Digital Beamforming, Millimeter Waves, Antenna Measurements

**16. SECURITY CLASSIFICATION OF:**

Unclassified

**a. REPORT**

Unclassified

**b. ABSTRACT**

Unclassified

**c. THIS PAGE**

Unclassified

**17. LIMITATION  
OF ABSTRACT**

SAR

**18. NUMBER  
OF PAGES**

228

**19a. NAME OF RESPONSIBLE  
PERSON** Harvey Tobin**19b. TELEPHONE NUMBER (include  
area code)**  
781-377-9473Standard Form 298 (Rev. 8-98)  
Prescribed by ANSI Std. Z39.18

## 2002 ANTENNA APPLICATIONS SYMPOSIUM

18 – 20 September 2002  
Monticello, Illinois

### Volume I

<b>Low Cost Transmit/Receive Module for Space Ground Link Subsystem</b>	<b>1</b>
Sarjit S. Bharj, Alex Merzhevsky, Narendra Patel, Paul Oleski, Shiang Liu, Boris Tomasic and John Turtle	
<b>Multi-Beam Phased Array Antennas</b>	<b>18</b>
R.Q. Lee, S. Romisch and Z. Popovic	
<b>Space Fed Subarrays using a Displaced Feed</b>	<b>28</b>
Robert J. Mailloux	
<b>Adaptive Processing using a Direct Data Domain Approach from Single Snapshot of Data in the Presence of Near Field Scatterers</b>	<b>47</b>
Kyungjung Kim, Tapan. K. Sarkar and Magdalena Salazar Palma	
<b>Digital Beamforming Algorithms for Obtaining Ultralow Sidelobe Array Antenna Patterns</b>	<b>76</b>
W.R. Pickles, W. K. Kahn, J.B.L. Rao, and D.P. Patel	
<b>Ku Band Active Phased Array Antenna for Mobile DBS Reception</b>	<b>106</b>
Cheol Sig Pyo, Jong Moon Lee, Young Keun Yoon, Won Kyu Choi, and Jae Ick Choi	
<b>Overview of the Multifunction RF Effort – An Army Architecture for an Electronically Scanned Antenna</b>	<b>119</b>
Steven Weiss, Robert Dahlstrom, Ozlem Kilic, Edward Viveiros, Steven Tidrow, Frank Crowne, Eric Adler	
<b>Dielectric Resonator Antennas and Their Potential for Millimeter Wave Applications</b>	<b>130</b>
Ahmed A. Kishk	



<b>Simulation of Vehicle Antennas by the Multilevel Fast Multipole Algorithm</b>	<b>140</b>
H.Y. Chao, K. Pirapaharan, V. Bodrov, T.J. Cui, H.P. Hsu, G. Huff, X.J. Zhang, J.S. Zhao, J. Bernhard and W.C. Chew	
<b>Design Study for Three-Frequency, Dual-Polarized FSS Subreflector</b>	<b>148</b>
Katherine E. Zink and Daniel H. Schaubert	
<b>CDMA Capacity Increases Measured Using Two-Antenna-Receiver Handsets</b>	<b>171</b>
Michael J. Wengler, Gregory A. Breit, Hussein Hachem, Yi-Cheng Lin, Randy Standke, and Ernest Ozaki	
<b>Measurement and Analysis of a Conformal Wing Array</b>	<b>192</b>
David Curtis, Boris Tomasic, Ryan Thomas, Scott Santarelli and Hans Steyskal	
<b>Volume II</b>	
<b>A Broadband Materials Measurements Technique Using the Full Frequency Extent of the Network Analyzer</b>	<b>221</b>
Tim Holzheimer	
<b>Bandwidth and Efficiency of Some Electrically Small Antennas</b>	<b>256</b>
Paul E. Mayes and Paul W. Klock	
<b>A Discussion on the Effective Volume and Radiation Properties of Small Non-Euclidean Wire Monopole Antennas</b>	<b>283</b>
Steven R. Best	
<b>Investigation of Polarization Purity and Port Isolation in Linearly and Circularly Polarized Microstrip Patch Antennas with Ground Plane Serrations</b>	<b>307</b>
G.H. Huff, G. Cung, and J.T. Bernhard	
<b>On the Performance Properties of a Multiband Conical Monopole Antenna</b>	<b>320</b>
Steven R. Best	

<b>Miniaturization of Microstrip Patch Antennas Using the Sierpinski Fractal Geometry</b>	<b>329</b>
Kiyun Han, Frances J. Harackiewicz and Seokchoo Han	
<b>Ultra Wide-Band Radiating Element for Cellular Wireless Applications</b>	<b>342</b>
Narian Izzat, Fred Hunt and Kevin Linehan	
<b>Improved Impedance Bandwidth Prediction of Stacked Reconfigurable Bowtie Antennas</b>	<b>353</b>
J. Hazen and J. T. Bernhard	
<b>Structure Integrated Patch Element for X-Band Application</b>	<b>363</b>
Robert Sekora	
<b>Infinite Arrays of Tapered Slot Antennas With and Without Dielectric Substrate</b>	<b>372</b>
S. Kasturi, A.O. Boryssenko and D.H. Schaubert	
<b>ARO Sponsored Programs in Antenna Research</b>	<b>391</b>
W.D. Palmer	
<b>A Rotman Lens Implementation for Multi-Function RF Antenna Applications</b>	<b>401</b>
R. Dahlstrom and A. Bayba	
<b>A Two-Dimensional Millimeter Wave Phase Scanned Lens Utilizing Analog Photonic Band Gap Waveguide Phase Shifters</b>	<b>413</b>
J.B. West, J.C. Mather, J.P. Doane, H. Xin, H. Kazemi and A. Higgins	
<b>Miniature Controlled Receive Pattern Antenna for GPS</b>	<b>434</b>
V. Sanchez, E. Caswell, A. Miller, D. DeCarlo and P. Rothenberg	

## Identifiers for Proceedings of Symposia

### The USAF Antenna Research and Development Program

Year	Symp. No.	Identifier
1951	First	
1952	Second	C054 520
1953	Third	AD63794
1954	Fourth	AD63139
1955	Fifth	AD90397
1956	Sixth	AD114702
1957	Seventh	AD138500
1958	Eighth	AD301151
1959	Ninth	AD314721
1960	Tenth	AD244388 (Vol. 1)
		AD319613 (Vol. 2)
1961	Eleventh	AD669109 (Vol. 1)
		AD326549 (Vol. 2)
1962	Twelfth	AD287185 (Vol. 1)
		AD334484 (Vol. 2)
1963	Thirteenth	AD421483
1964	Fourteenth	AD609104
1965	Fifteenth	AD474238L
1966	Sixteenth	AD800524L
1967	Seventeenth	AD822894L
1968	Eighteenth	AD846427L
1969	Nineteenth	AD860812L
1970	Twentieth	AD875973L
1971	Twenty-First	AD888641L
1972	Twenty-Second	AD904360L
1973	Twenty-Third	AD914238L

# Antenna Applications Symposium

		TR#	ADA#
1977	First	None	955413
1978	Second	None	955416
1979	Third	_____	077167
1980	Fourth	_____	205907
1981	Fifth	_____	205816
1982	Sixth	_____	129356
1983	Seventh	_____	142003; 142754
1984	Eighth	85-14	153257; 153258
1985	Ninth	85-242	166754; 165535
1986	Tenth	87-10	181537; 181536
1987	Eleventh	88-160	206705; 206704
1988	Twelfth	89-121	213815; 211396
1989	Thirteenth	90-42	226022; 226021
1990	Fourteenth	91-156	237056; 237057
1991	Fifteenth	92-42	253681; 253682
1992	Sixteenth	93-119	268167; 266916
1993	Seventeenth	94-20	277202; 277203
1994	Eighteenth	95-47	293258; 293259
1995	Nineteenth	96-100	309715; 309723
1996	Twentieth	97-189	341737
1997	Twenty First	1998-143	355120
1998	Twenty Second	1999-86	364798
1999	Twenty Third	2000-008 (I) (II)	386476; 386477
2000	Twenty Fourth	2002-001 Vol I & II	
2001	Twenty Fifty	2002-002 Vol I & II	

# **LOW COST TRANSMIT/RECEIVE MODULE FOR SPACE GROUND LINK SUBSYSTEM**

**Sarjit S Bharj**  
**Alex Merzhevsky**  
**Narendra Patel**

**Paul Oleski**  
**Shiang Liu**  
**Dr. Boris Tomasic**  
**John Turtle**

**AFRL, Rome.**  
**Aerospace Corporation**  
**AFRL, Hanscom**  
**AFRL, Hanscom**

## **ABSTRACT**

A low cost Transmit/Receive module for the Space Ground Link Subsystem, SGLS, has been designed and manufactured for the next generation of Phase Array Antenna for the Air force Satellite Control Network, AFSCN. Each Transmit/Receive module consists of four channels comprising of two receive channels and two transmit channels. The module consists of high selectivity ceramic bandpass filters, polarization selection, four 4-bit phase shifters, four 5 bit digital attenuators, dual low noise amplifiers, and dual power amplifiers, capable of transmitting a minimum 1-watt per output per channel. The RF portion of the module utilizes ground coplaner waveguide structure. The module is designed for Hot-condition replacement and has active bias network for the high efficiency GaAs power amplifiers. To meet the cost objectives, the RF connectors have been designed for insertion into beam forming structure using novel connection format and making DC and RF signals availability on the same side of the module. The control of the T/R module is connected via single Field Programmable Gate Array, FPGA, through a GPIB computer interface. The paper will present the unique aspects of the design, the cost analysis, challenges, and unique interboard connectivity.

## **INTRODUCTION**

Low cost component design and implementation issues are critical in developing a practical phased array antenna. Combined RF, Digital and monolithic circuits are important but not only the critical issue.

Affordable antenna arrays operating at microwave frequencies are envisioned to consist of active modules that employ microwave integrated circuits at each radiating element of the aperture. The antenna system consists of separate receiver and transmit aperture capable of rapid beam motion. The transmit antenna should be capable of high radiated power levels and the receive antennas must achieve a high G/T ratios. Beam agility and high-radiated power levels in association with the close spacing between the radiators drive the antenna design. The requirement for fast beam switching will requires digital processing circuits to calculate phase shift settings. A high RF radiated power level developed from closely spaced RF amplifiers generates very large heat densities. This forces the transmit antenna to increase in area to where beam pointing accuracy limits the array size. The great number of elements in the array emphasizes the need to develop a practical method of distributing control signals throughout the array. A Geo-Disic Spherical phase array antenna is considered for Air Force Satellite Communication network. Implicit in the system function array is the need to operate the array in full duplex operation. Additionally the array should be capable of controlling fundamental radiation characteristics such as beamwidth, beam size, sidelobe levels and radiated power, in order to realize different antenna characteristics required by the various

satellites. The array aperture consists of a large number of radiating elements that are spaced approximately half a wavelength at the upper end of the operational frequency band. The frequency response and excitation of each element in the aperture can be independently controlled. The aperture can be fully or partially utilized either to direct energy over a large volume or intentionally directed in a certain direction. Additionally, radar and communications require both transmission reception of energy where as ESM and ECM systems require only reception of energy. The capability of the array to provide transmit and receive functions simultaneous and to rapidly alter the set of configurations is possible due to active element control circuit. The active control circuits allow the Phase Array Radar to control their radiation characteristics. The aperture can be uniformly illuminated to achieve maximum gain or tapered illuminated to achieve low sidelobes or shaped beam. The combination of the variable attenuator and phase shifter permits the array Illumination to be modified and the antenna beam to be scanned in any direction. The filter specifies the portion of the aperture used by a particular system. The phase shifter, the variable attenuator and the amplifier are components that have been developed in MMIC, microwave monolithic integrated circuit technology, in the last decade.

The requirement of high degree of isolation between transmit and receive channels focused the effort to investigate the exact performance that can be achieved from the low-cost ceramic filters and traditional combline filters. In addition, low cost MMIC based power amplifiers for transmit channel have were also located. Other effort was directed towards the design of a low-cost phase shifters.

Other important factors that were considered in the development of the T/R module were:

- T/R modules interface with beamformer
- Hot condition Operation
- Polarization Diversity
- Dual Transmit and Receive Channels
- Low Cost with Justification
- High Isolation between Transmit and Receive Channels
- Digital Control on Board
- Rugged and Reliable

### **System Block Diagram**

The block diagram for the Transmit/ Receive module is detailed in Figure 1. The transmit section of the T/R module consist of two control circuits at the input, each compressing of a four BIT digital phase shifter and a 5-BIT digital attenuator, which are combined in a Wilkinson power combiner. The output of the combiner is amplified in a driver amplifier and fed into a 90-degree hybrid through a single pole double throw switch. The quadrature outputs of the hybrid are amplified via MMIC amplifiers to a power output of in excess of 30 dBm and transmit through high rejection bandpass ceramic filters. The specifications for the transmit and receive channels are detailed in Table I and II.

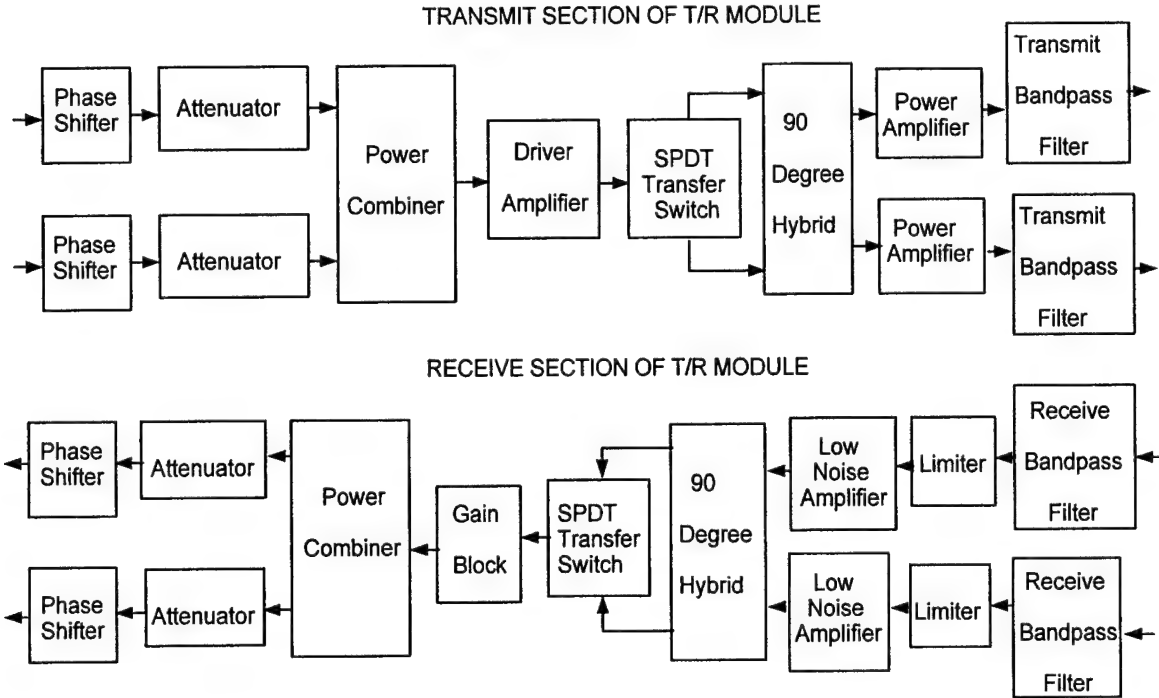


**Figure 1: The block diagram of Transmit/Receive module**

**Table I: Specification for Transmit Channel**

PARAMETER	SPECIFICATIONS
Frequency	1.764-1.842GHz
Gain	20dB
Power output per channel	30dB
Phase shift	360°
Control	Electronics
Retrofit	Change in Hot condition
Efficiency	> 40 %
Spurious Levels	<-85
Attenuation	3 to 10 dB

**Table II: Specification of Receive Channel**

PARAMETER	SPECIFICATIONS
Frequency	2.2-2.3 GHz
Gain	30dB
Noise Figure	1.2dB
Phase shift	360°
Attenuation	30dB min

The main components of the Transmit/Receive module are:

- Transmit Filter with 100dB rejection at receive frequency
- Receive filters with high rejection at transmit frequency
- Low noise MMIC amplifiers
- High Power MMIC driver and Power MMIC amplifiers
- Quadrature and in phase hybrids
- 5 Bit Transmit and Receive digital Phase Shifter
- 5 BIT digital control attenuators for transmit and receive channel
- Limiters for receiver channel
- SPDT switch for Polarization selection
- Xilinx digital controller

### TX and RX Filters

Two filters are required to maintain optimum performance. The transmit filter, inserted before the transmit antenna, prevents wideband noise from entering the receiver, and degrading performance. The receive filter, inserted after the receive antenna, prevents the coupled transmit signal from degrading the linearity of the receive Low Noise Amplifier (LNA). The transmit filter are made of high Q ceramic resonators. It consists of six resonators in a coaxial structure. The main goal was to have high rejection of at least 100dB at the receiver frequency. The receive channel filters are also made of ceramic resonators very similar to those of transmit filters. The receive filters were designed for low loss and a rejection of at least 50 dB at the transmit frequencies. The measured performance of the Transmit and receive filters is detailed in Figure 2 and 3. Table III and IV show the filter specifications.

**Table III:** Specification of Transmit Filter

PARAMETER	SPECIFICATIONS
Frequency	1.764-1.842 GHz
Insertion loss	1.0dB Max
Return loss	<-15dB
Rejection at 2.2 GHz	<-150

**TABLE IV:** Specification of Receive Filter

PARAMETER	SPECIFICATIONS
Frequency	1.22-2.3 GHz
Insertion loss	1.0dB Max
Return loss	<-15dB
Rejection at 2.2 GHz	<-100



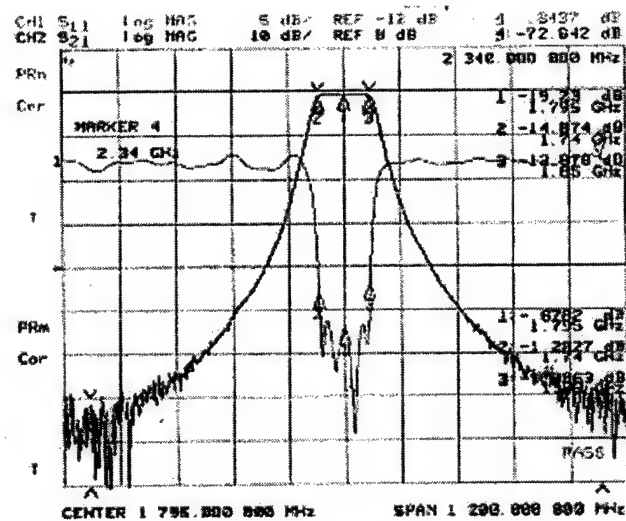


Figure 2: The measured performance of Transmit Filter

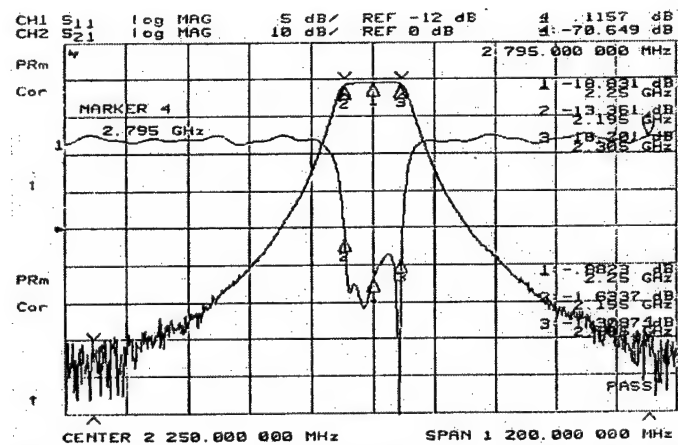


Figure 3: The measured performance of Receive Filter:

### Low Noise MMIC Amplifier

The Low noise amplifier can either be designed or use a MMIC amplifier. For a frequency of 2.2 to 2.3 GHz, Silicon Germanium devices such as BFP520, BFP620 and Silicon Germanium MMIC amplifier MZX 2641 were evaluated. Max2641 was selected due to its low cost and ease of use. The performances of the LNA candidates are compared in Table V.

TABLE V: The Performance of BFP 520 and MAX 2641

PARAMETER	BFP520	MAX2641
Frequency	2.2-2.3 GHz	2.2-2.3 GHz
Noise Figure	1.1dB	1.23dB
Gain	20dB	14dB
IP3	25dBm	10dBm
Package	Surface mount	Sot-23

### High Power MMIC Amplifier

For the power amplifier, multitudes of MMICs were available. One such MMIC was evaluated and used for Transmit channel, with power output capability of 32 dBm. The Amplifier provides a gain of 20dB with a power-added efficiency exceeding 40 percent over 1.7 to 1.9 GHz band. The data for AP 119 DCS MMIC is show in below table.

**TABLE VI: MMIC Power Amplifier**

PARAMETER	SPECIFICATIONS
Frequency	1700-1900 MHz
Gain	20dB
VSR	10:1
Operational Voltage	3.5 Max drain voltage 10V
Package	SSOP-16-enhanced surface mount
Gain Control	30dB
Control Voltage	-3 to -1 volts
Phase change with control	10° Maximum
Power output	32dBm

The measured performance is detailed in Figure 4 below.

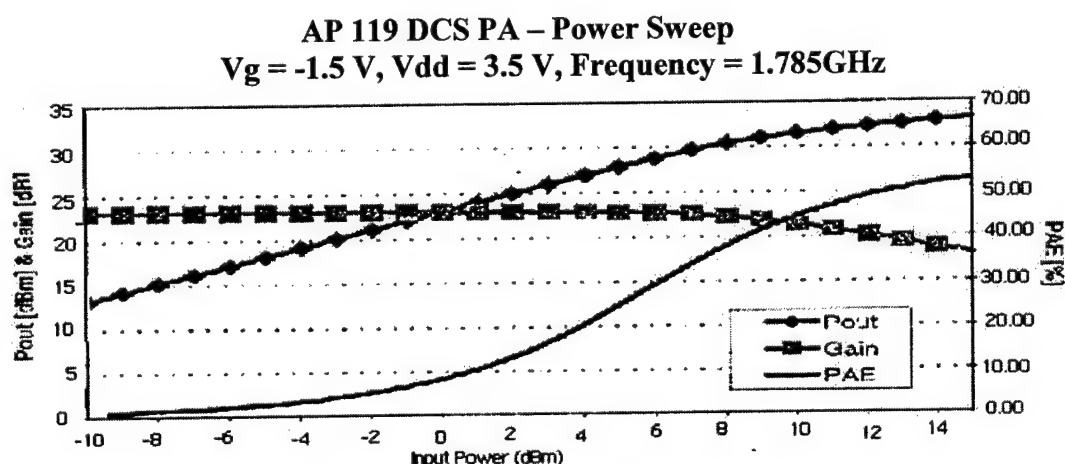


**Figure 4: Measured MMIC amplifier performance.**

### 5 Bit Transmit and Receive Phase Shifters

A phase shifter design based on the MMIC switch incorporating a single double pole double throw was procured from Marconi. This device essentially replaces two single pole double throw switches. The component count reduced from 10 devices per phase shifter, (Total 40 for T/R module) to 5 devices per phase shifter (20 per T/R module). The design of the Transmit and Receive channel phase shifters was detailed in Ref 1. The insertion loss of the phase shifter was measured at 8dB with a total change in insertion loss of 0.4dB in all phase states. The measured performance of the transmit and receive channel phase shifters are detailed in Figure 5 and Figure 6.

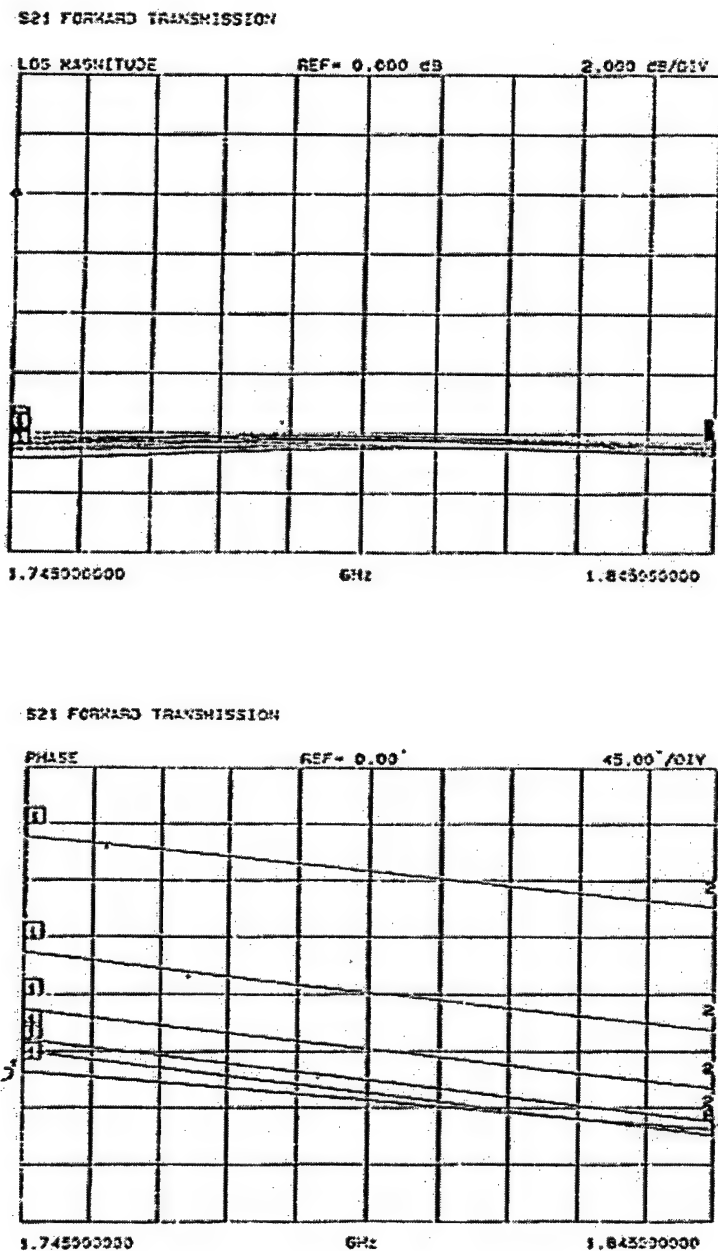


**Figure 5:** The measured performance of transmit channel phase shifter

#### **Limiters for Receive channel protection**

Surface mount limiters have been designed and performance measured. The active device in a narrow I region pin diodes with a DC return for current in the self-bias mode. The design of the T/R module is based on Coplanar Wave Guide with a ground. The diodes are therefore mounted directly across the 50 Ohms. The insertion loss is 0.2dB. The flat leakage is sufficient to protect the LNA.

# S21 FORWARD TRANSMISSION

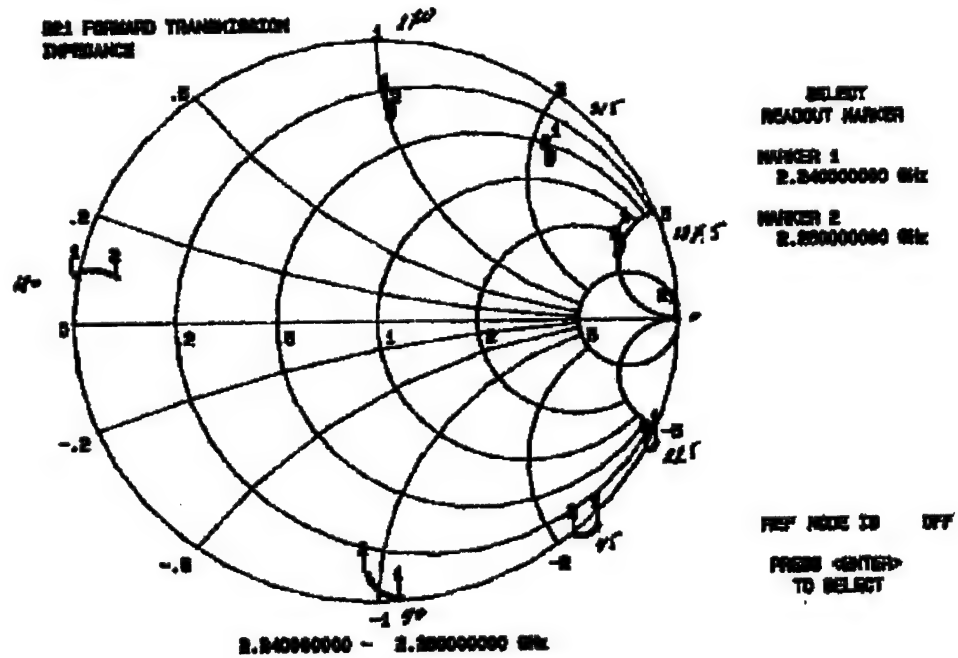
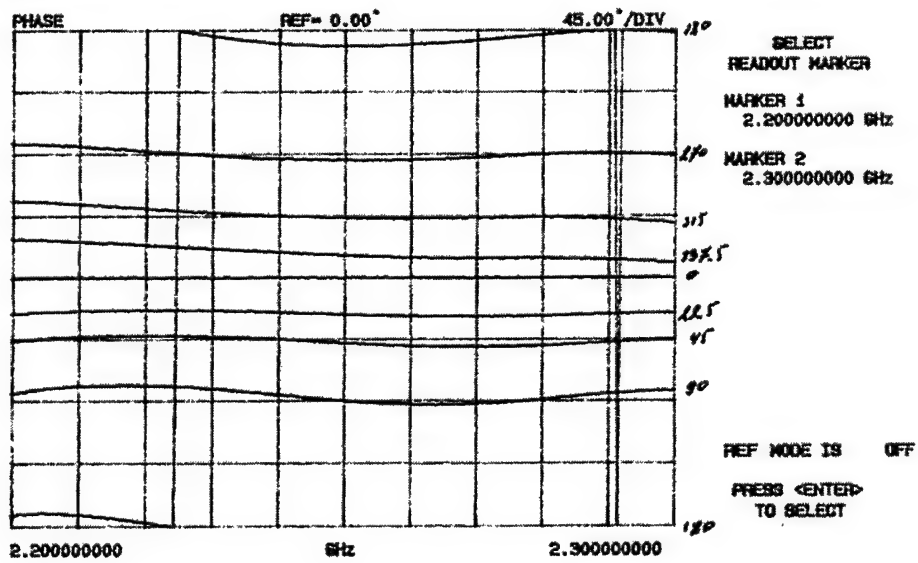
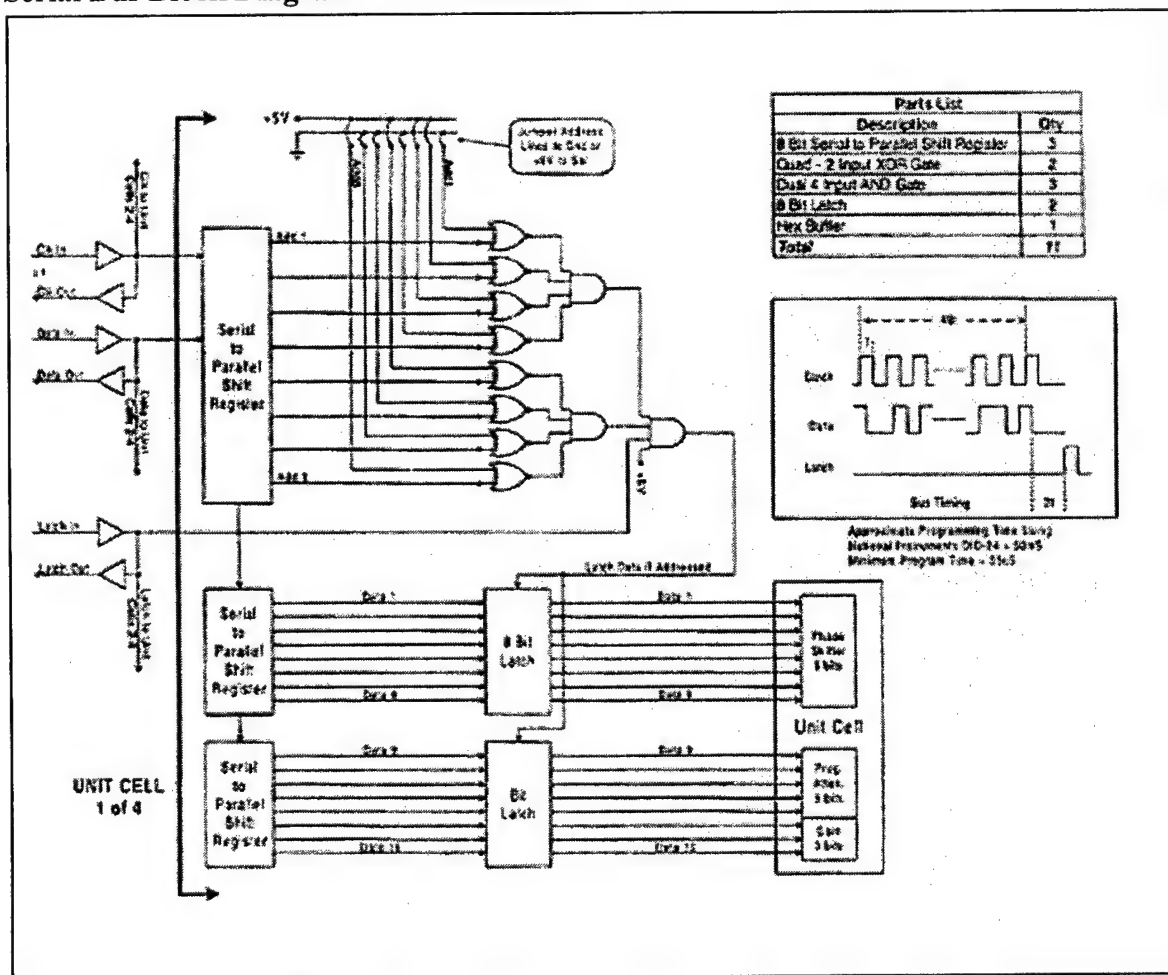


Figure 6: The measured performance of receive channel phase shifter

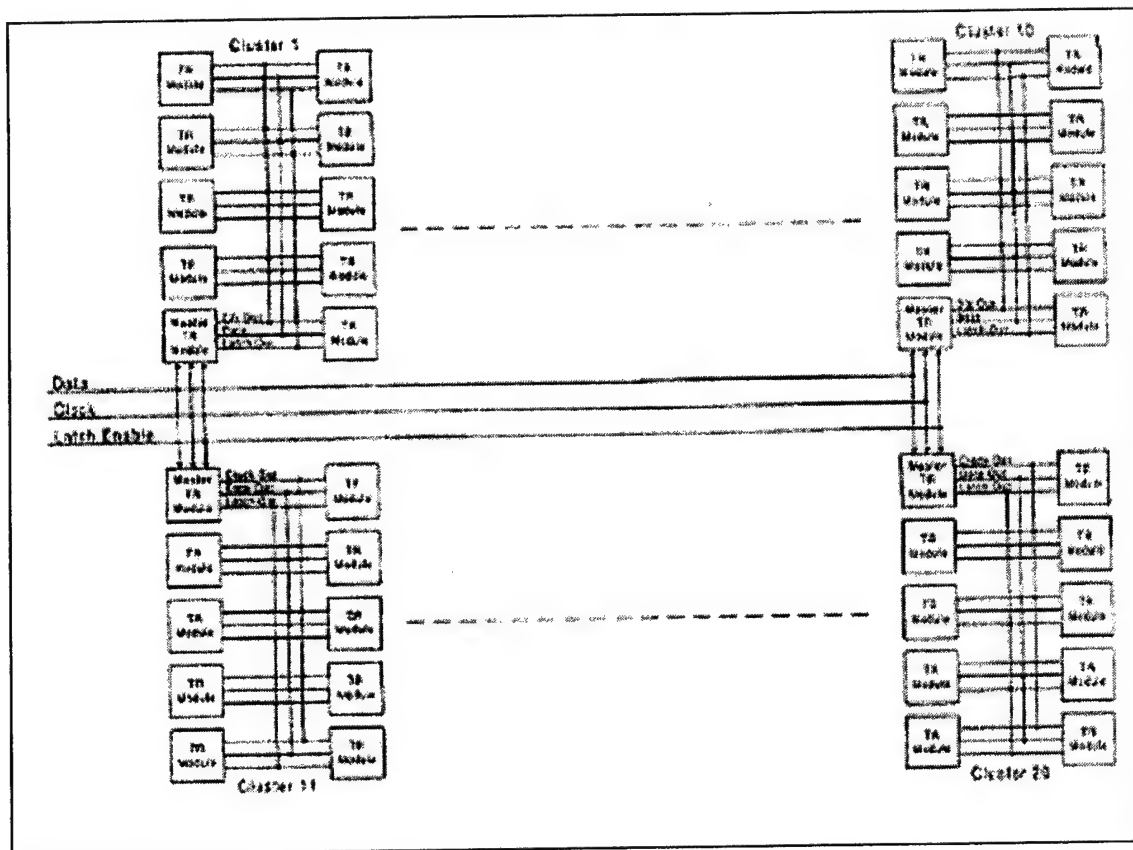
### Xilinx digital controller

The purpose of the serial to parallel bus arbitrator is to accept serial commands and unit address data and pass these commands to a parallel bus connected to a uniquely addressable unit. The input signals to this circuit are data, data clock and latches enable; the outputs are 16 parallel command lines connected to a Single programmable unit. Four addressable units are grouped into a single Transmit/Receive module. In order to avoid hardware redundancy, one unit can be addressed with a base address and the remaining three can be indirectly addressed. In addition, to compensate for data and clock line fanout for a large number of modules, a single module can act as a "master" module for several modules by buffering the clock, data and latch lines. 32 bits of serial data is clocked into a 32-bit wide shift register. Command data is stored in bits 0 to 15 and the desired unit's address is stored in bits 16 to 31 allowing for 65536 possible units. Once all 32 serial bits are stored in the shift register, a unit with a matching address is determined to exist, and the latch line is subsequently set high for a clock pulse, commands are latched out to the addressed 16 line parallel bus. Each unit is indirectly addressed 0-3 by subtracting the module's base address from the intended unit's address. The serial to parallel bus arbitrator circuit is now ready to receive the next serial stream of data.

### Serial Bus Block Diagram for T/R module



## Serial Bus Topology for 200 T/R modules maximum:



## T/R Module Layout

The original Transmit/Receive module layout was conducted in a manner where the inputs/outputs from the beam former was on the opposite end, to the antenna output/input respectively. Later, it was clear that the input/output from the beam former to the antenna output/input needs to be on the same side to allow module exchange in the hot condition. The width of T/R module was restricted to a maximum of 3 inch. The RF board was fabricated using grounded coplanar technology to reduce coupling and grounding effects. The control board was fabricated on Multilayered FR-4 substrate.

The Completely assembled Rf section of the T/R module is shown in Figure 7. The Receive and transmit filters are inserted via the back to ensure isolation. These are visible on the fully assembled controlled board shown in Figure 8.

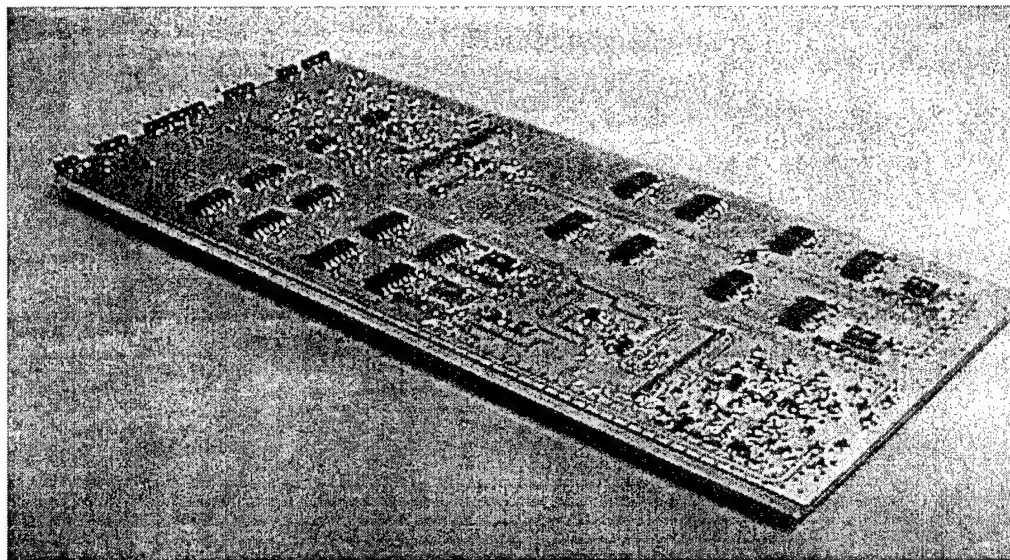


Figure 7: RF section of T/R Module

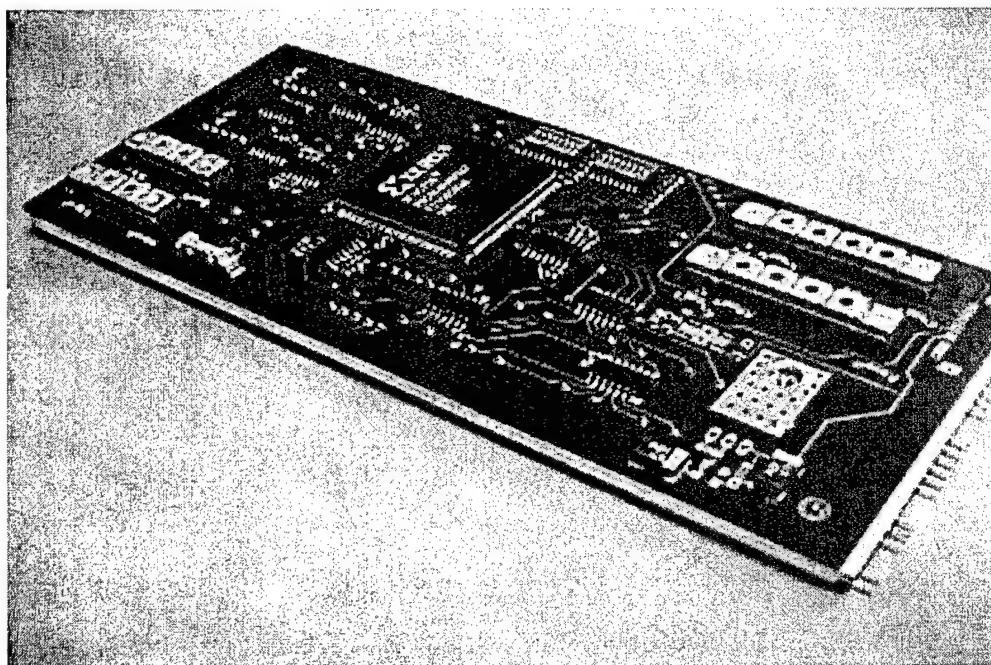


Figure 8: Control section of T/R Module



## Design To Cost

The design to cost of the T/R module has been conducted from project initiation. From onset, the cost associated with the components without any compromise in the performance has been the guiding rule. The availability of the active devices for the PCS market has really influenced the cost of amplifiers and phase shifters. Added with novel design and layout, the design to cost goal is near reality. The individual cost associated with the components is detailed below in tabular fashion..

**TABLE VII: Digital Control DTC**

Component	Per module	\$ 10	\$ 50	\$ 100	\$ 500	\$ 1000	\$ 5000	\$ 10K	\$ 50K	\$ 100K
Resistor	58	1.00	1.00	1.00	1.00	1.00	1.00	1.00	1.00	1.00
Capacitor	31	1.00	1.00	1.00	1.00	1.00	1.00	1.00	1.00	1.00
Transistors	4	0.02	0.02	0.02	0.02	0.02	0.02	0.02	0.02	0.02
Xilinx	1	20.00	20.00	20.00	20.00	20.00	20.00	20.00	20.00	20.00
ICs	10	1.60	1.60	1.60	1.60	1.60	1.60	1.60	1.60	1.60
Regulators	2	0.50	0.50	0.50	0.50	0.50	0.50	0.50	0.50	0.50
Connectors	3	0.90	0.90	0.90	0.90	0.90	0.90	0.90	0.90	0.90
Interconnects	58	0.50	0.50	0.50	0.50	0.50	0.50	0.50	0.50	0.50
Board	1	10.00	10.00	10.00	10.00	10.00	10.00	10.00	10.00	10.00
Assembly	1	50.00	50.00	50.00	50.00	50.00	50.00	50.00	50.00	50.00
Test	1	25.00	25.00	25.00	25.00	25.00	25.00	25.00	25.00	25.00

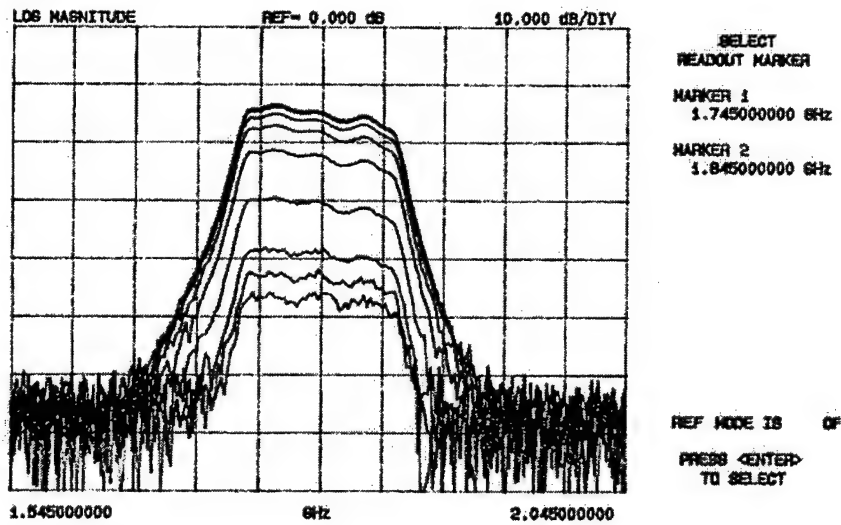
**TABLE VIII: RF SECTION DTC**

		\$ 10	\$ 50	\$ 100	\$ 500	\$ 1K	\$ 5K	\$ 10K	\$ 50K	\$ 100K
Resistors	23	1.00	1.00	1.00	1.00	1.00	1.00	1.00	1.00	1.00
Capacitors	46	1.00	1.00	1.00	1.00	1.00	1.00	1.00	1.00	1.00
Transistors	6	2.00	1.00	1.00	1.00	1.00	1.00	1.00	1.00	1.00
MMIC	2	5.00	5.00	4.00	4.00	3.00	3.00	2.50	2.50	2.00
RX Filter	2	120.00	78.00	56.00	40.00	32.00	28.00	26.00	14.00	10.00
TX Filter	2	180.00	116.00	84.00	50.00	48.00	42.00	40.00	20.00	16.00
Power Amplifier	2	40.00	40.00	40.00	12.34	11.32	10.00	9.80	8.00	8.00
Phase Shifter	16	48.00	48.00	48.00	48.00	45.00	32.00	32.00	31.20	30.40
Attenuator	4	48.00	48.00	48.00	44.00	25.40	27.00	22.40	20.00	18.00
LNA	4	5.00	5.00	4.00	4.00	4.00	3.00	2.50	2.00	2.00
Switches	4	12.00	10.70	10.70	10.70	10.00	8.00	6.80	2.80	2.00
Limiter	2	5.00	5.00	5.00	4.00	4.00	3.00	3.00	2.00	1.50
Counter	2	0.50	0.50	0.50	0.50	0.50	0.50	0.50	0.50	0.50
Connectors	24	1.40	1.40	1.40	1.40	1.40	1.40	1.40	1.40	1.40
Board	1	20.00	15.00	13.00	11.00	8.50	8.10	8.00	7.90	7.85
Heat Sink	1	68.00	68.00	64.00	35.00	5.00	5.00	5.00	5.00	5.00
Assembly	1	150.00	140.00	130.00	125.00	40.00	40.00	30.00	10.00	10.00
Test	1	200.00	190.00	180.00	155.00	99.00	55.00	25.00	15.00	15.00
<b>Total</b>		<b>904.90</b>	<b>765.60</b>	<b>581.60</b>	<b>557.94</b>	<b>339.12</b>	<b>269.00</b>	<b>217.90</b>	<b>145.30</b>	<b>133.65</b>



## MEASURED T/R DATA:

821 FORWARD TRANSMISSION

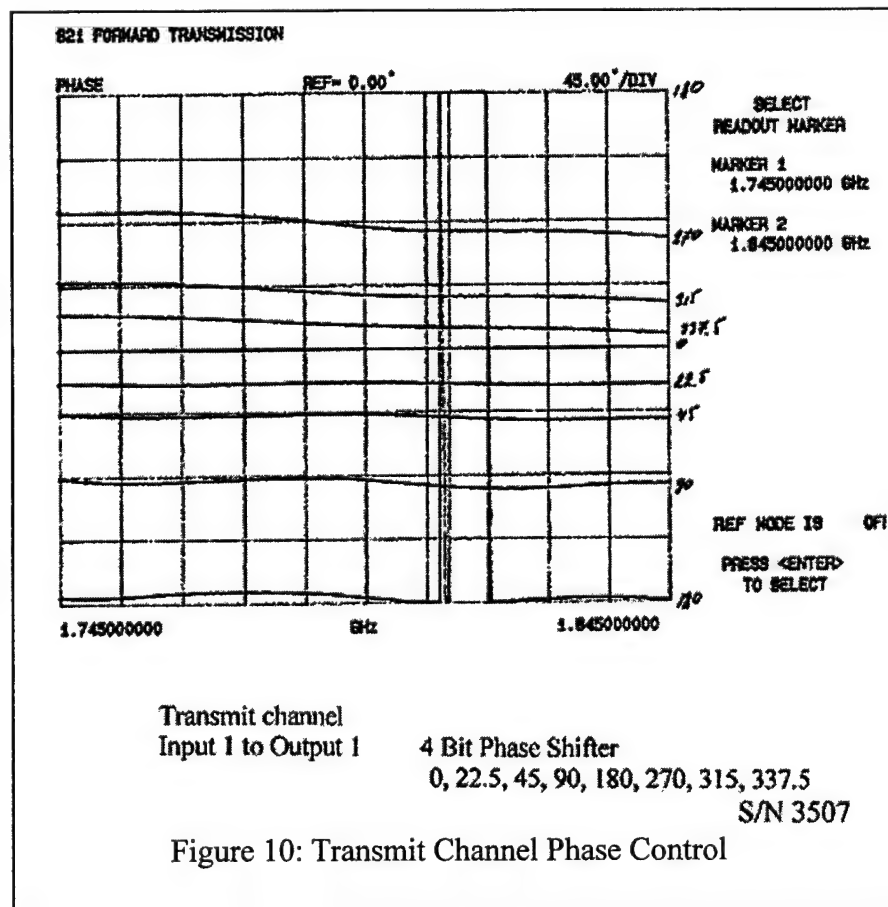


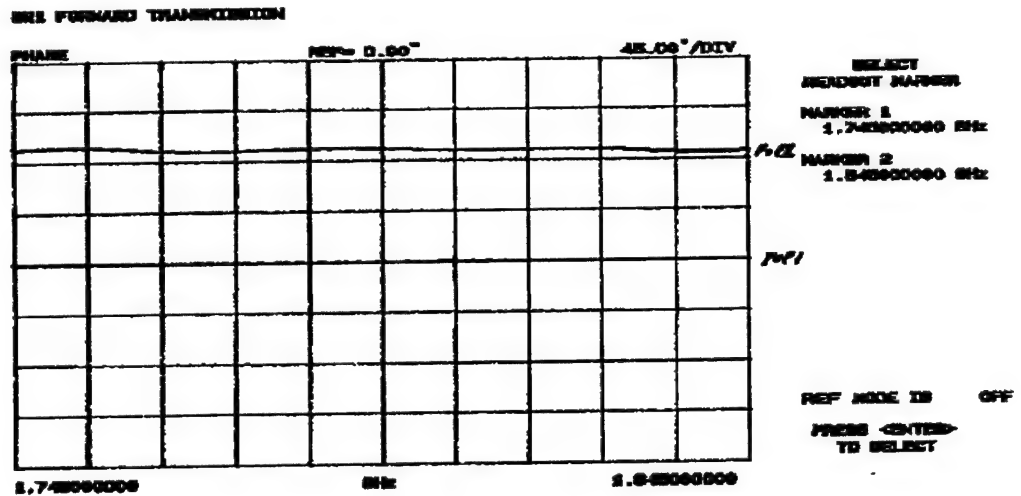
Transmit channel  
Input 1 to Output 1

In band step Attenuation  
0, 1, 2, 4, 8, 16, 24, 28, 31 (dB)

S/N 3507

Figure 9: Transmit Channel with Amplitude Control





Transmit channel  
Input 1 to Output 1

Switch Polarization  
0, 90

S/N 3507

Figure 11: Transmit Channel Polarization Switch

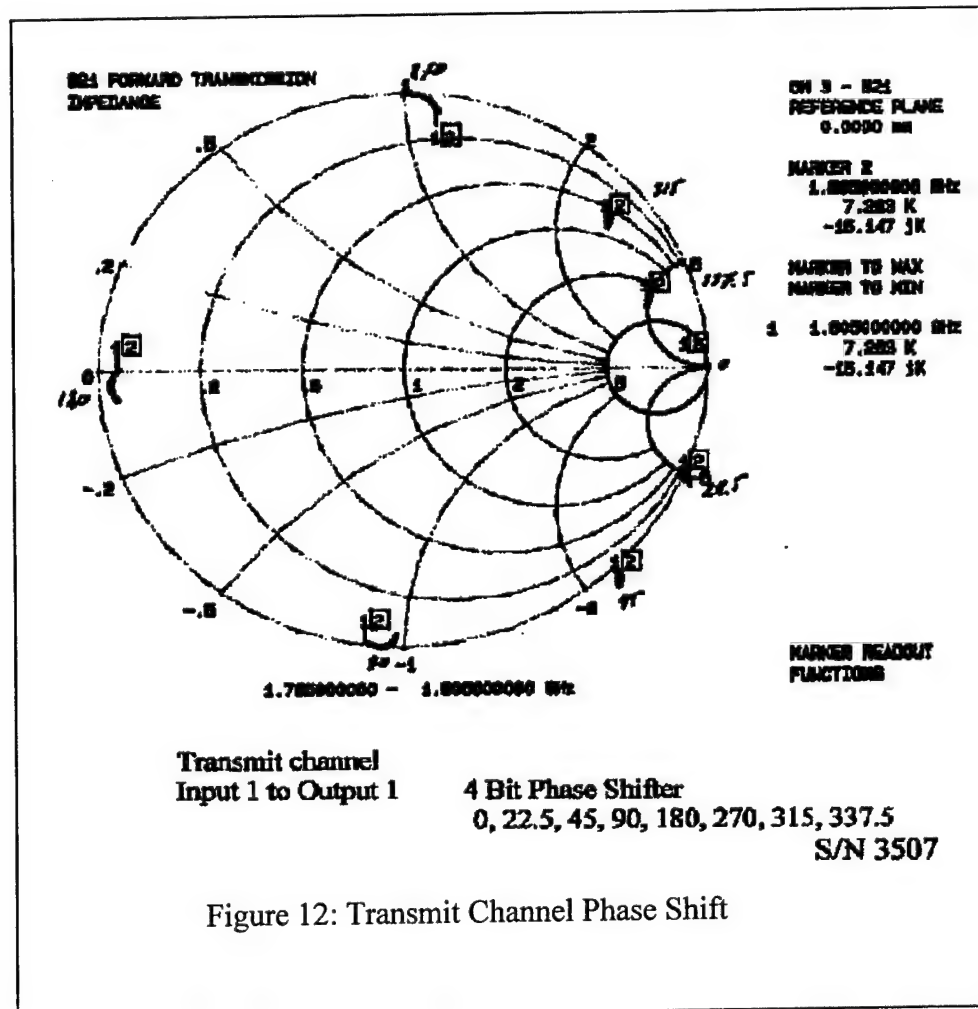
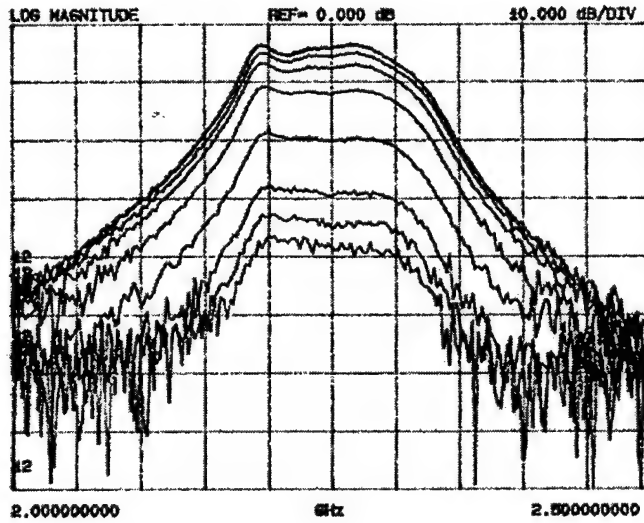


Figure 12: Transmit Channel Phase Shift

# S21 FORWARD TRANSMISSION



SELECT  
READOUT MARKER  
MARKER 1  
2.000000000 GHz  
MARKER 2  
2.000000000 GHz

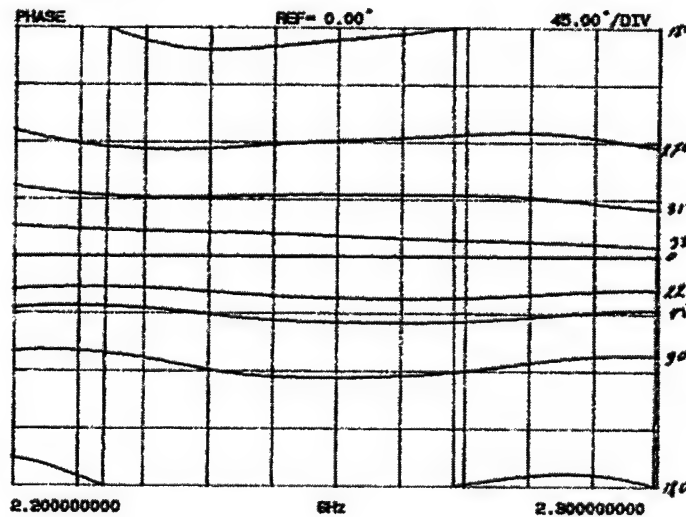
REF MODE IS OFF  
PRESS <ENTER>  
TO SELECT

Receive channel  
Input 1 to Output 1

In band step Attenuation  
0, 1, 2, 4, 8, 16, 24, 28, 31 (dB)  
S/N 3507

Figure 13: Receive Channel Amplitude Control

# S21 FORWARD TRANSMISSION



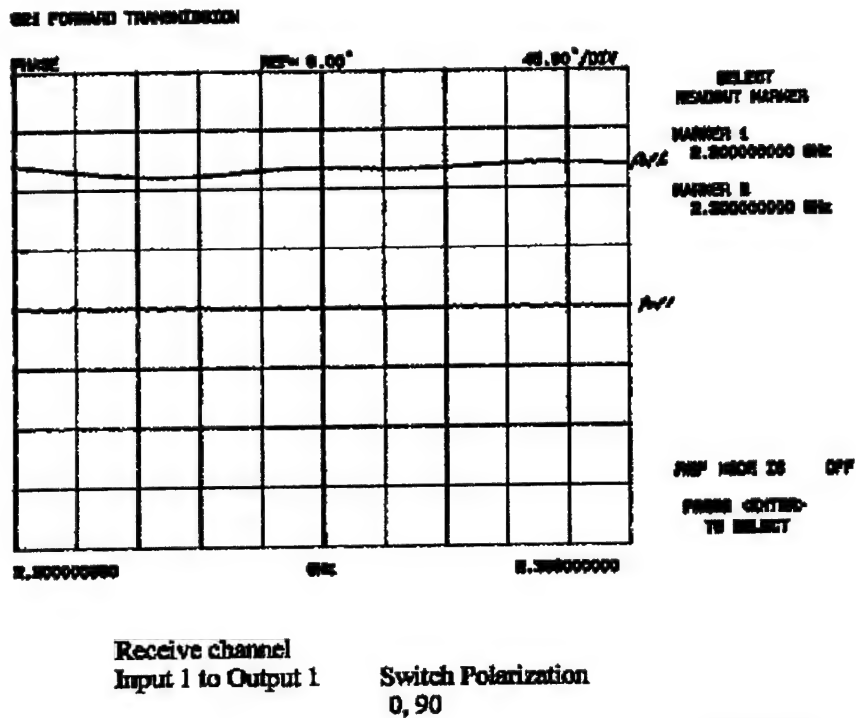
SELECT  
READOUT MARKER  
MARKER 1  
2.200000000 GHz  
MARKER 2  
2.300000000 GHz

REF MODE IS OFF  
PRESS <ENTER>  
TO SELECT

Receive channel  
Input 1 to Output 1

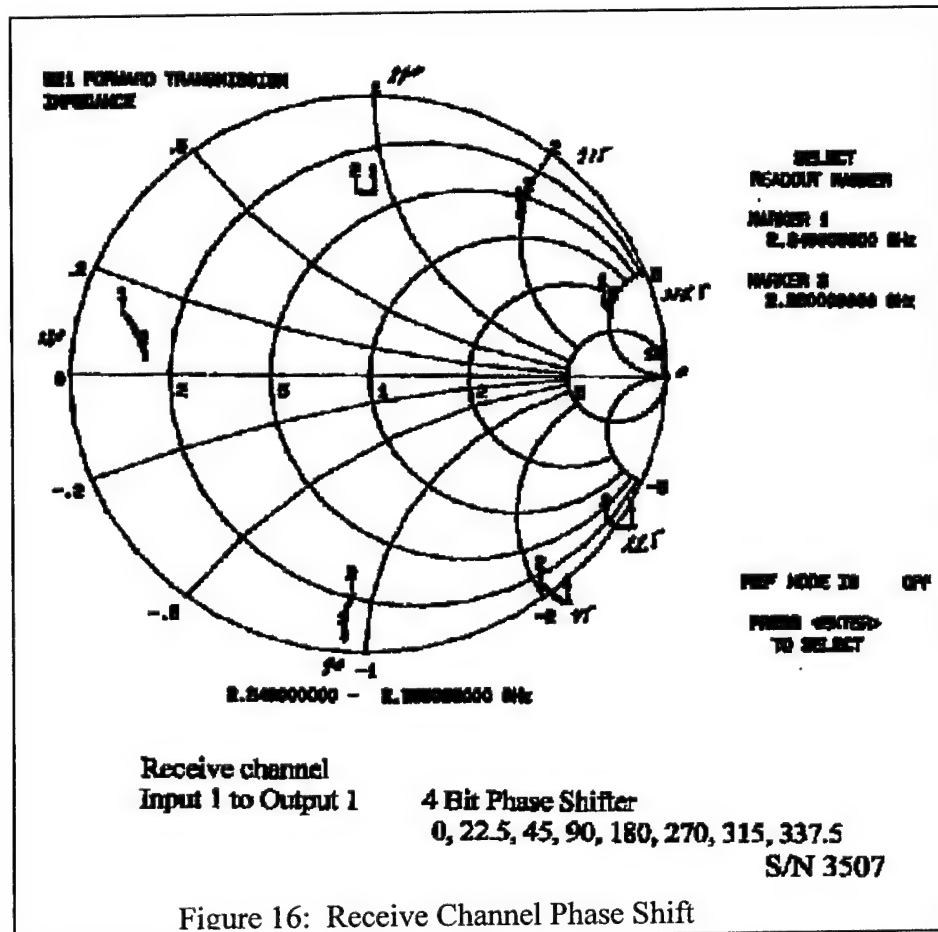
4 Bit Phase Shifter  
0, 22.5, 45, 90, 180, 270, 315, 337.5  
S/N 3507

Figure 14: Receive Channel Phase Shifter



S/N 3507

Figure 15: Receive Channel Switch Polarization



S/N 3507

Figure 16: Receive Channel Phase Shift

## CONCLUSIONS

A Transmit/Receive module has been developed for the SGLS band operation. Sixteen T/R modules were fabricated and tested. A design to cost exercise was conducted to ensure a low cost product. In the transmit section a power output of 30 dBm per channel, with a 4-BIT phase shifter and a 5-BIT attenuator, and polarization switching has been achieved. An overall gain of 30 dB was achieved. In the receive channel a noise figure of 2dB was measured with an overall gain of in excess of 20 dB. This channel also included 4-BIT phase shifter and 5-BIT attenuators. In its present form, the T/R module is reproducible. The next phase of development will focus on extending the T/R module for SGLS and USB frequencies.

## REFERENCES

- Ref [1] 'Affordable Antenna Array For Multiple Satellite Links  
2000 Antenna Applications Symposium. P 401  
Sarjit S Bharj, A. Merzhevskiy, P. Oleski, B. Tomasic, S. Liu

## **Multi-Beam Phased Array Antennas**

R.Q. Lee<sup>1</sup>, S. Romisch<sup>2</sup> and Z. Popovic<sup>2</sup>

<sup>1</sup>NASA Glenn Research Center, Cleveland, OH 44135

<sup>2</sup>University of Colorado, Boulder, CO 80309

### **Abstract**

**Many of NASA's future missions require multiple accesses to work together as a single system. To accomplish these missions, multi-beam phased array antennas are required to communicate between satellites flying in fixed formation. In this paper, a comparison of different multi-beam systems will be given followed by detailed discussions of the lens array architecture and test results.**

### **Introduction**

NASA has planned as many as 39 science missions over the next twenty years to study the origin of the universe, the Sun, the Earth, and other neighboring planets [1]. Many of these missions require multiple assets to work together as a single system. For example, Stellar Imager will require many satellites in a centralized formation flying, and the Mars mission will use multiple rovers, probes and satellites. To accomplish these missions, multiple, steerable beam antennas are required to collect diverse scientific mission data from formation-flying spacecrafts.

This paper concerns with the development of a multi-beam lens array antenna for crosslink communications between satellites in tight formation. The application considered requires several simultaneous beams at different angles with each capable of dual frequency and dual polarization. The angle of each beam can be fine-tuned of about 5 degree around the fixed positions by amplitude controls of the feed elements. This allows pointing correction with satellites slightly out of formation. For feasibility demonstration, a 56-element planar discrete lens array, space-fed with two small array feeds along the focal arc, has been built and tested through collaborative efforts with the University of Colorado. In the paper, a comparison of different multi-beam antenna systems will be given followed by detailed discussions of the lens array architecture and test results.

### **Comparison of Multi-Beam Antenna System**

Multi-beam antenna systems can generally be divided into three basic classes: reflector, phased array and lens. For multi-beam applications, the most serious

problem in a reflector antenna is the aperture blocking by a cluster of feeds, which contributes to large blockage losses. Further, reflector antenna suffers from coma and spherical aberrations, and therefore is not suitable for producing multiple beams [2]. The various aberrations greatly limit the scan range of the reflector to only a few beamwidths (typically about  $10^\circ$ ). Compensation of aberrations using step zoning and reactive surface loading is difficult and generally adds cost, weight and volume to the antenna system. Reflector antennas often achieve beam steering by mechanical means; thus have size, weight and life-cycle cost disadvantages particularly for space applications. In recent years, reflectarray, a planar version of the reflector, has been considered as substitute for the reflector antennas. Reflectarrays are fabricated using standard PCB technique, and thus have cost, size, and weight advantages over solid reflectors, especially for implementation in space. Another advantage is that the back is accessible for interfacing with the aperture and cooling. There are works currently going to insert phase shifters in the radiating elements of the reflector to achieve beam scan. For multi-beam applications, reflectarrays still face the same blockage and aberration problems as the reflector antennas.

Using active phased array to generate multiple beams has long been in the minds of many researchers. In addition to compact size, light-weight and lower life-cycle cost, active phased arrays can achieve beam agility, diversity, reconfigurability, and adaptivity to complex signal environments. Insertion of microwave monolithic integrated circuits (MMIC) technology into antenna systems using low power and low noise amplifiers in close proximity to the radiating elements also offers significant improvement in the array transmit efficiency, receive system noise figure, low sidelobe level and overall array reliability through graceful degradation. Based on hybrid approach, a Ka-band  $4 \times 4$  active subarray module of dimensions  $3.2 \text{ cm} \times 3.2 \text{ cm} \times .75 \text{ cm}$  has been demonstrated by NASA/Texas Instruments in 1994. The active array module delivers 75 watts effective isotropic radiated power (EIRP) with 1990 device technology, and using the state-of-the-art device and manufacturing technology, has the potential of delivering 750 watts EIRP [3]. Since then, progress in active phased array has been in stagnation due to high cost, and problems associated with high density device integration and heat removal. Besides high cost and complex array architecture, excess RF losses in the corporate (or Butler matrix) feed networks and phase shifters also contribute to very low antenna efficiency, making the active array unattractive for multi-beam applications. A schematic of an active phased array is shown in Fig. 1. To generate multi-beams, multiple beamforming networks on separate layers are required, increasing the already complex array architecture multifold.

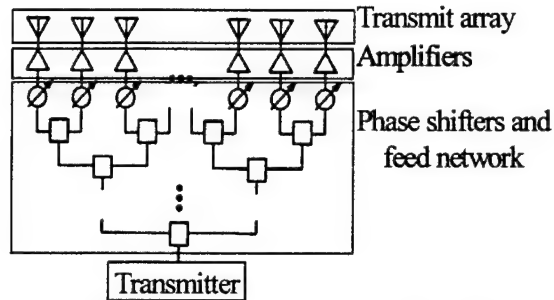
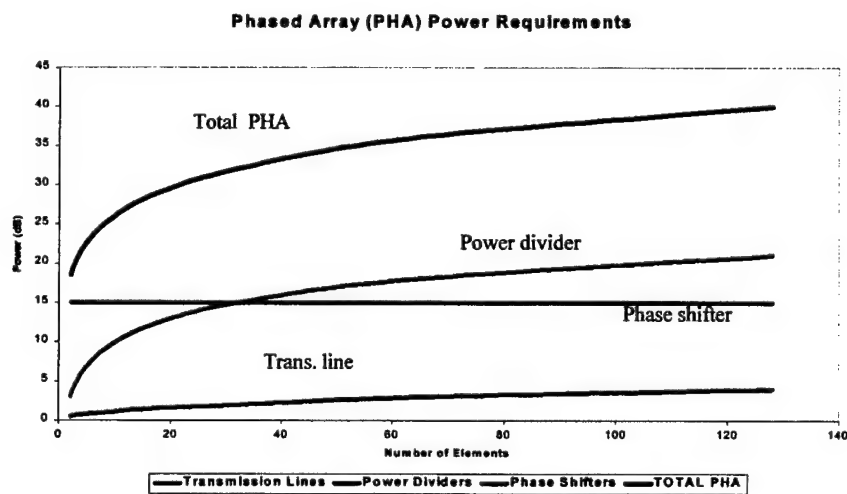
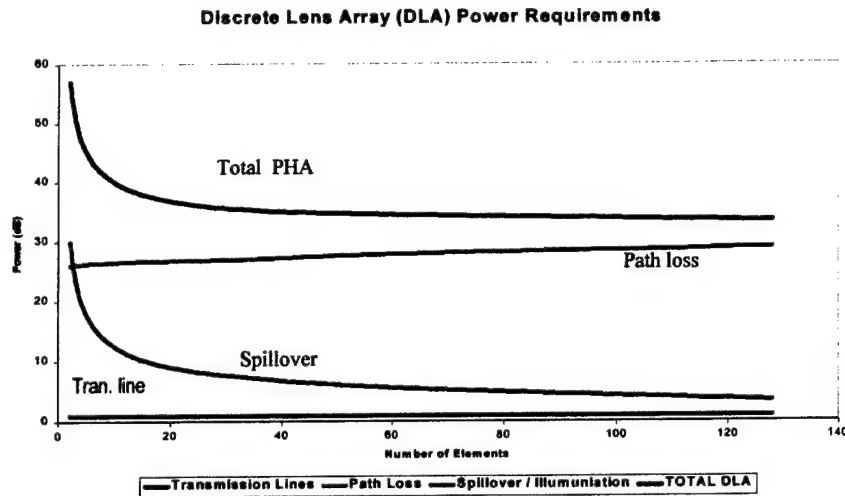


Fig. 1. Schematic of an active phased array

An important advantage of a discrete planar lens array is the simplicity in the feed network. The spatial feed allows a multi-beam configuration with only minor modifications in system design, avoiding the high complexity of a multi-layer corporate feed network as required by the PHA. Since the antenna is fed spatially, there is no RF losses associated with a corporate (or Butler matrix) feed network of a phased array. Consequently, higher efficiency can be achieved resulting in lower power requirement. Fig. 2 shows the input power requirement for a phased array with corporate feed network (PHA) and for a planar discrete lens array (DLA), assuming same EIRP from both arrays. Unlike phased arrays where feed loss increases with array size, feed loss in a lens array with more than 50 elements is nearly independent of the number of elements. The difference in losses is attributed to different loss mechanism in the two arrays. The main losses in the PHA are in the transmission line, power divider and phase shifters which depend







(b)

Fig. 2 Power requirement as function of number of elements for (a) phased array (PHA) and (b) discrete lens array (DLA)

on the number of elements, while the most significant source of loss in the DLA is the path loss in free space that increases only negligibly with the lens size. The spillover losses improve with the size of the DLA, and the transmission line loss is generally small because of short lengths. Moreover, unlike the lossy and heavy dielectric or metal-plate lenses, planar lens arrays are fabricated using standard PCB technology, making them lightweight, easy to manufacture, and easy to optimize for large scan angles [4]. The radiating elements on the feed-side and radiating-side of the lens can be easily designed for dual frequency and dual polarization operation, thus greatly extending the system capability. Compared to reflectarrays, the DLA does not have the feed blockage problem, and is less sensitive to phase errors introduced by element and feed position variations.

### Dual-Beam Discrete Lens Array Design

The basic multi-beam DLA architecture for transmission is shown in Fig. 3. The DLA consists of two arrays with transmission lines connecting corresponding radiating elements on both sides through coupling slots. The multiple beams are obtained with multiple spatial feeds placed along a focal surface on the feed side of the array with each feed position corresponding to a beam in a different direction. In general, four geometric degrees of freedom can be applied in lens

radiating-side surface, (3) relative position of the elements in the two surfaces, and (4) the length of the transmission line joining corresponding elements in the two surfaces. The planar discrete lens described in this paper uses two degrees of freedom, namely (3) and (4), to achieve good off-axis focusing with two perfect focal points lying on a focal arc or with a cone of best focus [5]. In the design, the transmission lines are of different electrical length for each element to provide proper phase delays for equal path length from the feed to each element on the radiating-side of the lens. The larger delay is at the center element to mimic an optical lens, i.e. thicker in the center and thinner in the periphery. The radiating side array is designed the same way as with traditional array where the

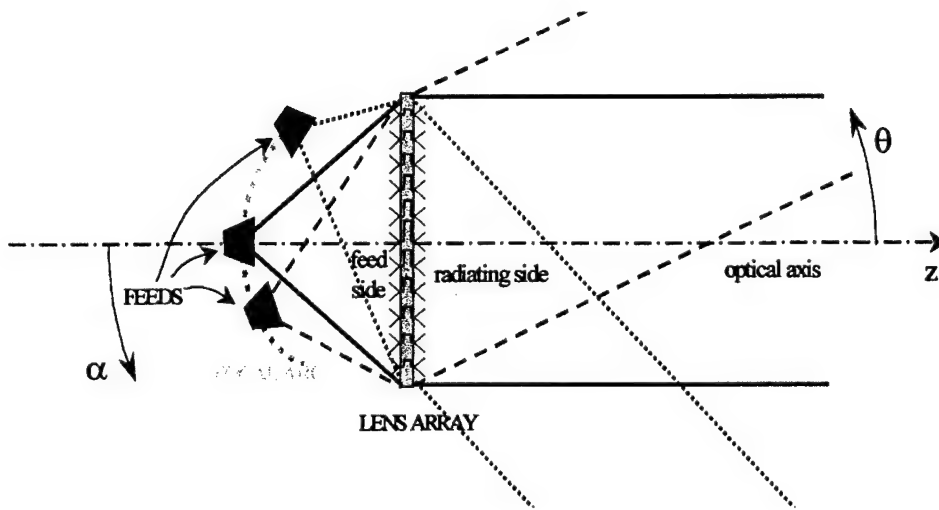


Fig. 3. Schematic of multi-beam transmit/receive lens array with 3 beams :  
 $\alpha$  - angle the feed made with respect to the optical axis,  $\theta$  - scan angle

spacing and type of element is chosen in accordance with performance specifications such as grating lobes, sidelobe levels and beamwidth.

Antenna element design : Fig. 4 (a) shows a dual-frequency patch antenna for the lens array. The antenna, fabricated on 15 mil thick substrate with  $\epsilon_r = 6.15$  (Rogers 6006<sup>TM</sup>), is designed to radiate two orthogonal linearly polarized waves at 25.4 and 27.4 GHz. Quarter-wave transformers are used to match the antenna to 50 $\Omega$  transmission lines, which are used to connect the feed-side patch with the

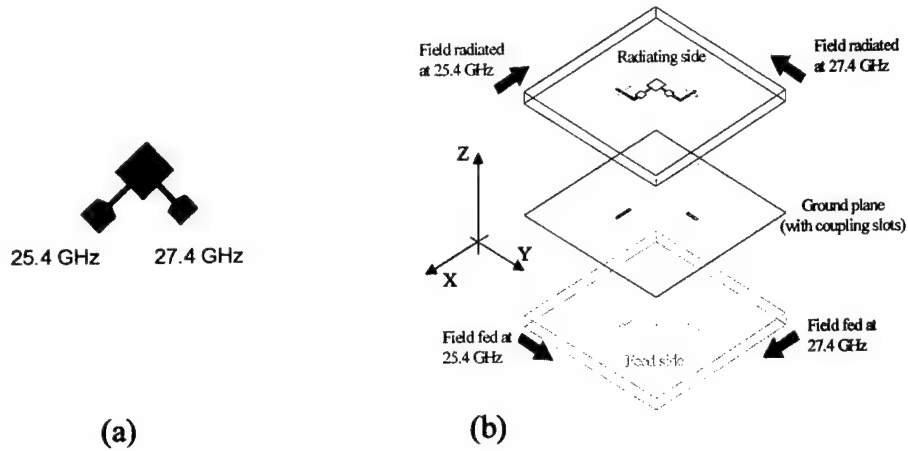


Fig. 4. Schematic of (a) a dual-frequency patch and (b) 3-D view of one element showing slot coupling and orthogonal polarization between the two arrays

corresponding radiating-side patch through coupling slots in the ground planes. As indicated in Fig. 4 (b), the polarization of the feed-side and the radiating-side patches are orthogonal to each other to improve polarization isolation between the two arrays. Fig.5 shows the measured and simulated results for the cross talk and matching of four different antenna elements (A1, A4, A5, A6) in the array.

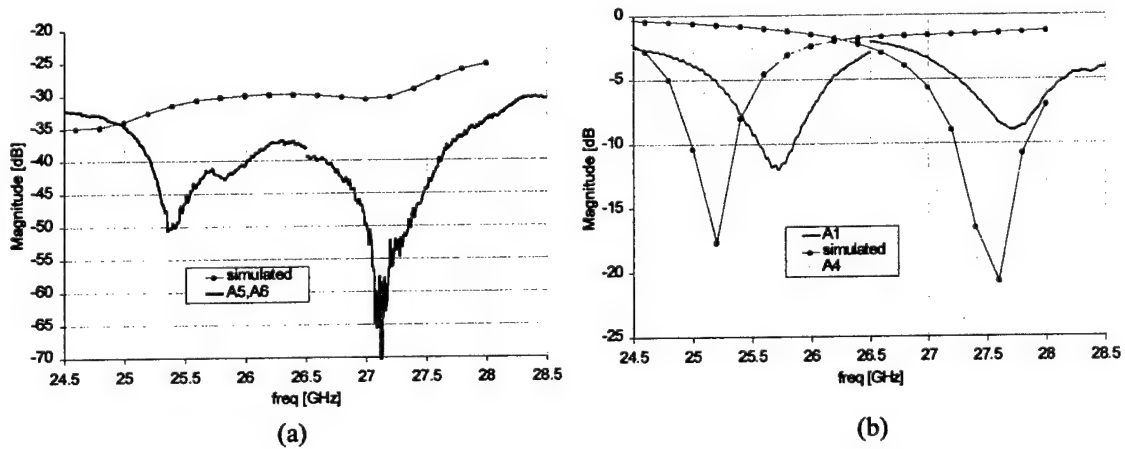


Fig. 5. Measured and simulated cross-talk (a) and matching (b) at the two feeds at the two feeds for different elements in the array

**Lens design :** The dual-beam discrete lens array was designed for cone of best focus at  $\theta = \pm 30^\circ$  with symmetry around the z-axis ( $\theta = 0^\circ$ ) [5]. Both the feed-side and the radiating-side arrays consist 56 elements, which are arranged in

triangular lattice with  $0.66\lambda_0$  horizontal spacing and  $\lambda_0$  vertical spacing. The spacing will provide enough space to fit the antenna module and still avoid grating lobes for feed placed at  $\theta = \pm 30^\circ$ . By imposing two degrees of freedom in the design creates displacements in the relative position of corresponding elements in the two arrays. As a result, a transmission line layer buried between the two arrays is required to connect the feed-side element with the radiating-side element through coupling slots. Fig. 6 shows the cross-sectional view of the final

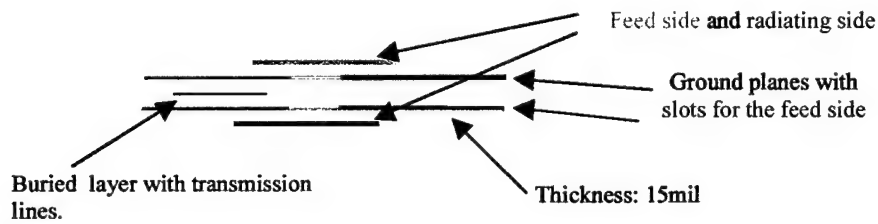


Fig. 6. Cross-sectional view of the multi-layer DLA structure

DLA structure which is made up of five metal layers and four dielectric layers.

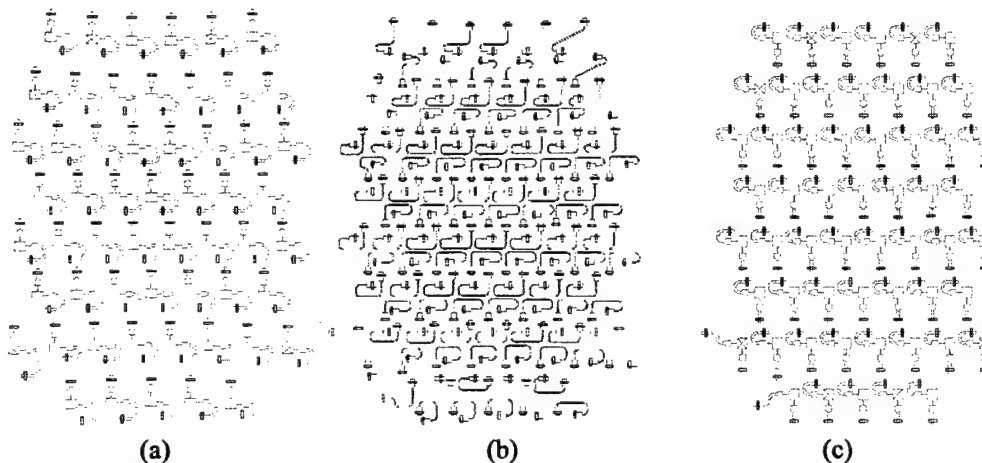


Fig. 7. Layout drawings of the metal layers: (a) feed-side with slots, (b) buried layer with transmission lines and slots, and (c) radiating-side with slots

Fig 7 displays the layout drawings of the three metal layers. The planes with slots are ground planes where only the slots are represented in the drawing for clarity.

**Fine beam steering using amplitude control:** Due to the fact that the lens array behaves like a discrete Fourier Transform, amplitude variation at the feed in the image plane correspond to phase steering of the radiated beam in the far field. This is in contrary to the conventional phased array approach where phase steering is used to achieve beam steering. Fine beam steering can be achieved with a single variable gain element of a 2-element array feed. Fig. 8 shows main-lobe steering of  $\pm 2.5^\circ$  with normalized amplitude variation from 1 to 0.1 on the feed.

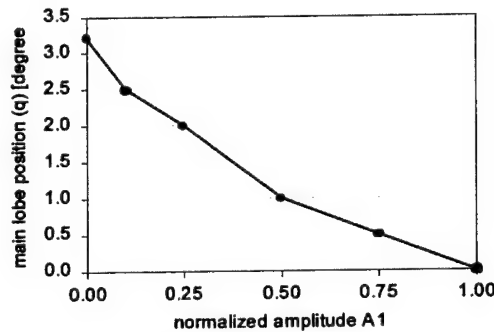


Fig. 8. Simulated main-beam position with amplitude variation for a 2-elment array feed

### Experimental Results

The 56-element prototype lens, fed spatially with two array feeds at  $\theta = \pm 30^\circ$ ,

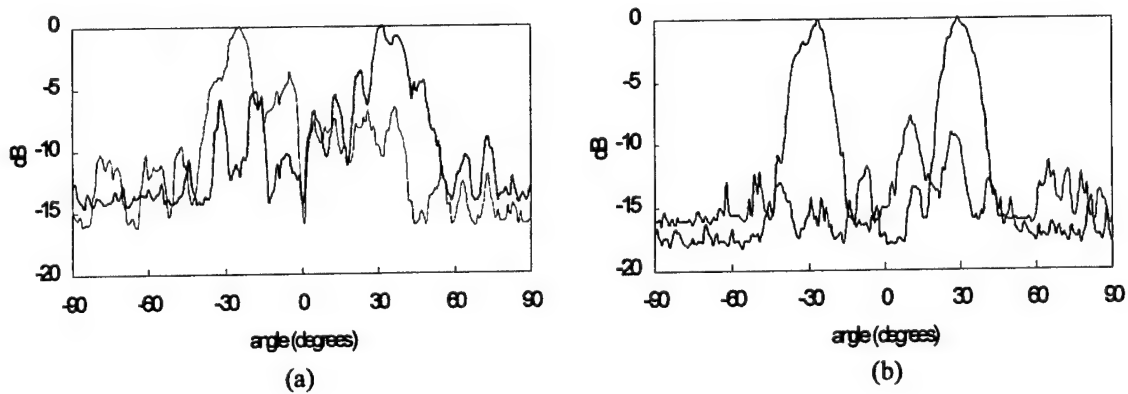


Fig. 9. Measured dual-beam radiation patterns at (a) 24.7GHz, and (b) 26.7 GHz

was fabricated and tested in a far field antenna range. Each array feed has two input ports for transmit or receive signals at the two design frequencies of 25.5 and 27.5 GHz. Fig.9 shows the measured radiation patterns at 24.7 and 26.7 GHz.

The patterns exhibit two distinct beams at the  $\pm 30^\circ$  scan angles. However, there is a shift of about 3% in the operating frequencies with respect to the design frequencies of 25.5 and 27.5 GHz due to fabrication tolerances. Also, it is noticed that the lower frequency patterns have unusually high sidelobes that are partly caused by reflection from the array fixture and from an array feed with poor matching and isolation characteristics. Covering all edges of the array housing with absorber did eliminate some reflections, and using an open end waveguide as feeds produced significant improvement in the sidelobe levels as shown in Fig. 10.

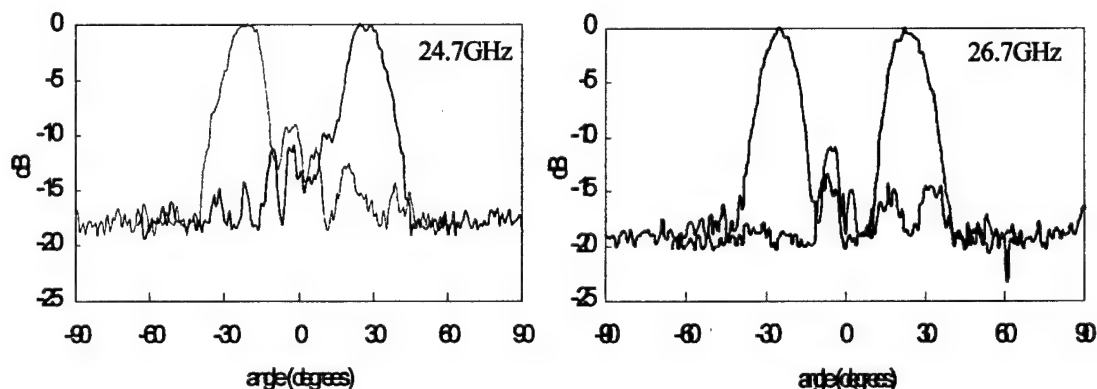


Fig. 10. Measured radiation patterns at the two frequencies for the lens with open waveguide feed.

### Summary

Planar discrete lens array features low cost, low loss, light-weight, and simple structure as compared to other types of multi-beam array systems. In the paper, design and measured results of a dual-beam, dual-frequency DLA have been presented. Further, small angle steering with amplitude variations of the feeds avoiding the use of phase shifter has been demonstrated.

### References

1. *Spectrum Requirements and Allocation Survey Report and Recommendations*, February 8, 2002, Goddard Space Flight Center.
2. Y. T. Lo and G. A. Deschamps, *Multiple Beam Antenna Study*, Electromagnetics Laboratory Report No. 77-6, March 1977.

3. S. Sanzgiri, D. Bostrom, W. Potenger and R.Q. Lee, "A hybrid tile approach for Ka band subarray modules," IEEE Trans. Antenna. and Propagation, Vol. 43, No. 9, pp. 953-959, Sept. 1995.
4. D. popovic, and Z. Popovic, "Multibeam antenna with polarization and angle diversity", to be published in IEEE Trans. Ant. And Prop., Special issue on Wireless Communications.
5. D.T. McGrath, "Planar three dimensional constrained lenses," IEEE Trans. on antenna and Propagation, Vol. AP-34, No. 1, pp. 46-50, 1986.

# Space Fed Subarrays using a Displaced Feed

Robert J. Mailloux  
Air Force Research Laboratory  
Sensors Directorate  
80 Scott Drive  
Hanscom AFB, Massachusetts, 01731-2909  
E-mail: robert.mailloux@hanscom.af.mil

**Abstract:** A multiple beam (transform) feed for a phase-scanned lens has the desirable property of forming subarrays for the insertion of time delays across the large aperture. However, at certain scan angles and particular frequencies the multiple beam feed can have a focus at its front face. This phenomenon can be unacceptable when transmit amplifiers are used at this location since it requires that all power be provided from a few or even a single feed port. This paper presents a procedure for defocusing the feed to avoid the large dynamic range problem and spread the required power among a larger fraction of feed elements.

## 1. Introduction

Space fed overlapped subarray systems are an appropriate array architecture for inserting time delay into very large phased array systems. For arrays scanned to wide scan angles (say  $60^\circ$ ), time delays become necessary when the required fractional bandwidth  $\Delta f/f_0$  is more than the array beamwidth (in radians). This paper addresses a recently uncovered difficulty with such systems, one that is of major consequence if transmit modules are used at the feed output ports.

Figures 1 through 5 illustrate the use of time delayed subarrays for large arrays with phase shifters at the array face. An array with phase shifters alone forms its beam at the angle  $\theta$  whose sine is

$$u = \sin \theta = (f_0 / f) \sin \theta_0 \quad (1)$$

Where  $\theta_0$  is the beam peak at center frequency  $f_0$ . If the array is large, and its beamwidth narrow, then there can be significant loss, called "squint loss", due to the beam moving off of the target direction at frequencies away from center frequency. Grouping elements into contiguous subarrays, as shown in Figure 1, can reduce this squint loss, but can incur the large quantization lobes shown in the



figure. Figures 2 and 3 suggest that synthesizing special pulse-like subarray patterns can suppress these quantization lobes while simultaneously reducing the squint loss. Figure 4 shows that a space fed array configuration can be used with a multiple beam (or transform) feed to produce the desired pulse shaped subarray patterns, and then superimposed to form low sidelobe radiated beams.

The geometry of Figure 4 is often called a dual transform network or overlapped subarray network. It's behavior is described in several texts<sup>1,2,3</sup> as well as in numerous journal articles<sup>4,5</sup>. In all of the cited references, it is assumed that the array is a passive network, or active devices are placed at the element level. The objective lens is an equal path length-structure with a cylindrical back face, and a single focal point. The lens has phase shifters at its front face, and these are used to produce a progressive phase front that scans the beam of the lens to any desired angle ( $\theta_0$ ) with direction cosine  $u_0 = \sin \theta_0$ . For this reason the objective lens is referred to as a "phase-shift" lens.

The objective lens is illuminated by a feed array that is in turn connected to a "transform" network, an  $M \times M$  multiple-beam network which might be a Butler Matrix, a focusing lens, or it could be a set of amplifiers and A/D converters followed by a digital beamformer that performs a DFT operation. Each of these produces a set of overlapping sinc-like illuminations, spaced a distance  $D_0$  apart across the main lens that constitute a set of overlapped subarrays. Each subarray radiates a pulse shaped pattern with phase center at the peak of a sinc-function. When all of the subarrays are driven by time-delayed signals, the array forms a beam that radiates in a fixed direction throughout a bandwidth that is roughly proportional to the subarray beamwidth. Typically the achievable instantaneous fractional bandwidth is about two-thirds of the theoretical maximum value  $(D_0/\lambda_0 \sin \theta_0)^{-1}$ .

Figure 5 shows several possible locations for transmit/receive (T/R) modules and poses a critical question that can impact the utility of these systems. Since they are most often proposed for large space arrays, there may be tens or even hundreds of thousands of elements at surfaces "A" and "B" ( in the two dimensional case). Despite obvious advantages of having one module per element, the cost of so many modules often precludes further consideration of this approach. Surface "D" is not an ideal location for T/R modules because of the loss in the multiple beam feed in addition to loss at the objective lens. Surface "C" appears to be an ideal compromise, being closer to the radiating lens than surface "D." However, the transform feed is usually placed with its output elements along a straight line through the focus of the objective lens, and this requires that the feed be a classic

multiple beam feed. At certain scan angles and frequencies this feed will have a focus at its front face. The large variation in current amplitudes makes the array output power vary significantly, with sometimes a single transmitter supplying all the power. This may be of little consequence if the whole network is fed by a single, high powered transmit source, but it causes significant difficulty when using modern solid state transmit modules. It is this feature, which could be described as a dynamic range issue, or also as an issue of net available power, that this work has sought to address.

## 2. The Dynamic Range Issue

As noted in the introduction, an obvious location for T/R modules is at the front of the feed array (Surface "C"), since this surface requires only a modest number of modules, and only suffers the added power loss due to signal passing through the objective lens/phase shifter combination. Unfortunately the signals at this surface undergo extreme levels of dynamic range. The most striking example is the transmit case, when all subarrays are excited with equal amplitude and off center frequency. One can show that on some  $i$ 'th feed element, the largest value of signal  $I_i$  occurs when

$$u_o = \frac{+i}{M \frac{D_o}{\lambda_o}} \left( \frac{K}{1-r} \right) \quad \text{for} \quad -\left( \frac{M-1}{2} \right) \leq i \leq \left( \frac{M-1}{2} \right) \quad (2)$$

for then  $I_i = M$ . The element indices  $i$  are taken as integers or half integers, according to equation 2, and centered about the array center. In the expression above,  $K=1$  for an orthogonal beamforming feed (Butler Matrix) and  $K=r$  for a time delay lens (Rotman). Figures 6A and 6B show the currents  $I_i$  at several of these critical angles for  $M = 16$  and  $D_o/\lambda_o = 16$  and  $r = f/f_o = 0.975$ . The critical angles are slightly different for the two beamformers as indicated on the figure and are in accordance with equation 2. The element index number  $i = 5.5$  is the only one with signal for the orthogonal beam feed case (6A), but for the time delayed lens (6B) that element has the strongest signal, but others have small residual signals. Figures 7A and 7B show the signals at some elements  $-6.5 \leq i \leq -0.5$  as a function of scan angle for and illustrate the repetitive nature of these peaks and zeros. The zeros are all coincident for the orthogonal feed case (Fig 7A) and occur at different values of  $u_o$  for the time delayed lens case. (Fig 7B).

Apart from this illustration of the severe dynamic range and power distribution problem, the figures also show that the region of peak amplitude moves across the face of the feed as the scan angle  $u_0$  is varied, with most intensity near the feed array center for small  $u_0$  and toward either array edge for larger  $|u_0|$ . Figure 7C shows the number of feed elements with significant power as a function of scan angle. This illustrates that for most angles only one of 16 feed elements carries significant power.

These three figures (5,6 and 7) have described the case of uniform illumination which is often the case for a transmitting radar. The receive case, often using a low sidelobe illumination, has a smaller dynamic range at the front face of the feed.

### 3. Analysis of the Geometry

Figure 8 shows the basic configuration and several relevant geometries that are proposed as solution. Assuming that the objective lens has a cylindrical back face, and the feed elements are located at  $(y,z)=(y_i,h)$ , with reference to Figure 8A, then the distance from each  $i$ 'th element to some point on the lens at some angle  $\phi$  is

$$\rho_i^2 = F^2 + h^2 + y_i^2 + 2Fh\cos\phi - 2Fy_i\sin\phi \quad (3)$$

Throughout this paper the above (near field) representation for distance will be used instead of any far field approximation, because of the short focal lengths considered. It will be assumed that the entire structure is enclosed in a parallel plane medium so the problem is reduced to two dimensions.

Assuming some excitation currents  $I_i$  at each  $i$ 'th feed element, the currents at the back face of the objective lens are:

$$A(n) = \sum_i I_i \frac{e^{-jk_0\rho_i}}{\sqrt{\rho_i}} \quad (4)$$

where the currents  $I_i$  are given by the sum over the  $M$  values of the input signals  $J_m$ . Each input signal  $J_m$ , applied to the input port of the multiple beam feed produces a series of currents  $I_i(m)$  at the feed's output ports, with  $i$  and  $m$  integers or half integers as given below. These currents are each weighted by the weights  $w_i(m)$  and summed to give the total

$$I_i = \sum_m w_i(m) I_i(m) \quad (5)$$

where 
$$I_i(m) = J_m e^{-jK 2\pi \left(\frac{m}{M}\right) i} \quad (6)$$

and  $K = 1$  for an orthogonal beam network (Butler Matrix)

and  $K = \frac{f}{f_o} = r$  for a time delay feed (Rotman Lens etc.)

for  $-\left(\frac{M-1}{2}\right) \leq i \leq \left(\frac{M-1}{2}\right)$  and  $-\left(\frac{M-1}{2}\right) \leq m \leq \left(\frac{M-1}{2}\right)$

For an  $N$ -element objective lens, the far field radiation is given:

$$f(u) = \sum_{n=-(N-1)/2}^{(N-1)/2} A(n) e^{\frac{j2\pi}{\lambda_0} (r \sin \theta - \sin \theta_0) n d_L} \quad (7)$$

where the  $\sin \theta_0$  term is due to the phase shift that has been added to scan the beam to  $\theta_0$ .

Equation 4 gives the aperture distribution  $A_n$  at the back face of the lens corresponding to the total current  $I_i$ . This expression is used for all calculations of radiated fields. However, for the purpose of determining the subarray signals  $J_m$ , it is convenient to assume a far field approximation. For the  $m$ 'th subarray, the aperture distribution on the objective lens back face is approximately

$$A(n) \approx \sum_{m=-(M-1)/2}^{(M-1)/2} w_i(m) I_i(m) e^{j \frac{2\pi i}{\lambda} d_y \sin \phi_n} \quad (8)$$

where we have defined the angle  $\phi_n$  such that the location of the  $n$ 'th element on the lens back face is

$$y_n = nd_L = F \sin \phi_n \quad (9)$$

$$\text{so } \sin \phi_n = \frac{nd_L}{F}$$

and the peaks of the  $A(n)$  illumination for any given " $m$ " are

$$\text{at } \frac{2\pi i}{\lambda} d_y \sin \phi_m = +2\pi K \left( \frac{m}{M} \right) i$$

$$\text{and } nd_L = K \left( \frac{m}{M} \right) \frac{F\lambda}{d_y} \quad (10)$$

The distance between any two such peaks is the distance between an  $m$ 'th subarray and an  $(m+1)$ 'st subarray peak, or:

$$D = KF \frac{\lambda}{d_y} \frac{1}{M} \quad (11)$$

At center frequency ( $f=f_0$ ) this spacing is:

$$D_o = \frac{F}{M} \frac{\lambda_o}{d_y} \quad (12)$$

so  $D = D_o$  for a time delay beamformer

and  $D = D_o/r$  for an orthogonal beamformer – (Butler Matrix).

The signals  $J_m$  are chosen to provide time delay for each  $m$ 'th subarray, but in addition they need to compensate for the phase shift already introduced across the array.

$$J_m = |J_m| e^{j \frac{2\pi}{\lambda_0} u_0 m D_0 (1-r)} \quad (13)$$

This set of subarray level input signals has constant phase at center frequency ( $r=1$ ) and at frequencies away from center frequency it introduces a time delay term while subtracting out the phases at locations  $mD_0$  in the main lens. While this compensates exactly for the time delayed beamformer (Rotman Lens) configuration, it introduces a small “squint” error for the orthogonal beam (Butler Matrix) feed, since those subarray centers are located at  $mD$  across the main lens and their location varies with frequency. This could be compensated for digitally, and replace  $D_0$  by  $D_0/r$  in the above, but throughout this discussion the equation 13 above is used directly, and is found to be a good approximation.

These currents  $I_i(m)$  radiate to form the desirable pulse-shaped subarray patterns for time delay insertion at the subarray level by time-delaying the signals  $J_m$ . The steep skirts of the subarray patterns serve to suppress any grating lobes due to the periodic quantization. Figure 2 shows a typical subarray pattern formed by this geometry, and the array pattern for a 256-element array with 8 tapered subarray weights.

#### 4. Results using a Displaced Feed

Figure 8 shows the basic configuration and several relevant geometries that are proposed as solution. The essence of the solution proposed here is to move the multi-beam feed either further from the lens than the focal point by the distance  $h$  ( $h>0$  for case of Figure 8B) or closer to the lens ( $h<0$  for case of Figure 8C). The logic then is to replace the multiple beam feed network by some synthesized network that, on transmit, produces either an appropriate converging field (Figure 8B) or a diverging field (Figure 8C). This new network is synthesized on the basis of having good subarraying properties, like the network and lens it replaces. The synthesis was conducted using an iterative alternating projection technique. Figure 9 outlines the procedure that is begun using the complex weights  $A_n$  in the aperture that were produced by the original focal plane beamformer. The far-field radiated pattern amplitude is computed and projected onto the space between two boundary upper and lower “masks”,  $M_U$  and  $M_L$ . The phase is initially constrained to have the same distribution as the phase of the focal plane feed, but left unconstrained for later iterations. The resulting far field distribution is then

inverse transformed back to the main lens, where it is truncated. Finally this solution is inverted using the LMS fit to the front face of the feed at its new location. This solution again is transformed using the near field transform (equation 4 ) and the procedure repeated until converged. The examples shown in this paper are for the geometry of Figure 8C.

The intention is to synthesize a network that can be implemented via digital beamformer, and in fact the advantage of digital beamforming is that a different set of weights can be selected for each subarray, in order to optimize performance.

Figure 10 compares two subarray pattern amplitudes for the subarray with index  $m=-5.5$ . The synthesis produces a pattern that is similar to that of the focal plane beamformer, but slightly narrower, indicating a reduced bandwidth. Since this synthesis is done digitally, it is convenient to synthesize a different set of weights  $w_i(m)$  for each subarray ( $m$ ).

Figure 11 compares the current on element number  $-5.5$  (fourth from the left edge of the feed) for the focal plane beamformer with that of the synthesized beamformer for a uniformly illuminated array. Both feeds show that the current on this element peaks at negative scan angle, but the focal plane feed has a much narrower dependence on scan angle, and plays a role for scan around  $-45^\circ$ .

Figure 12 shows the current on feed elements for an array with uniform illumination and scanned to broadside using a time delay feed. Figure 12A shows the current using the feed in the focal plane ( $h=0$ ), and though broadside is not one of the critical angles, still most of the power is constrained to two elements. Figures 12B and C show amplitude and phase for the array with the feed moved to a point closer to the lens by 4 wavelengths ( $h=-4\lambda$ ) than the focal point feed of 12A. This current is spread out among many more elements. 12C shows the phase controlling the diverging field on transmit.

Figure 13 is similar to 12, but for the uniformly illuminated array scanned to  $57^\circ$  ( $u_0=0.8379$ ), one of the critical angles. The figure compares the data of Figure 6B for the time delayed focal point feed, and again shows that more feed elements share the power.

Figure 14 illustrates that for most of these scan angles, at least 5 feed elements out of 16 carry significant power. This is a substantial improvement over the 1 or 2 elements with the focal plane feed.

Figure 15 shows a subset of element currents for the focal plane and displaced feeds, in this case for an input weighting that corresponds to a low sidelobe Taylor taper of  $-40$  dB. Again the focal plane feed has significant current on only two elements at a time, while there is far more overlap for the off axis synthesized beamformer.

Figure 16 shows the number of elements with significant power for the focal plane feed and the displaced feed with a synthesized beamformer. For the focal plane feed only one or two of the 16 feed elements are used, while the displaced feed uses four or five elements except at large scan angles. This advantage is not as large as for the transmit case, but still significant.

Figure 17 shows typical radiation patterns for the array of 256 elements grouped into 16 subarrays for insertion of time delay and amplitude weighting. A  $-40$  dB Taylor taper was chosen, and the network yielded near-sidelobes between  $-25$  dB and  $-30$  dB over the bandwidth. These sidelobe levels are essentially the same as for the focal plane feed (data not shown), so the only compromise is a small loss in bandwidth. The computed 5 % bandwidth corresponds to about a factor of 5 bandwidth increase relative to the array without time delays.

## **5. Summary and Conclusions:**

This paper has presented results of displacing the feed of a dual-transform wideband scanning systems in order to avoid the dynamic range problems associated with a focal plane feed. The focal plane feed is shown to never use more than two elements out of the 16 feed elements, while the synthesized feed illumination uses at least four or five of the feed elements while producing good subarray patterns and radiation patterns.

A future task is to examine the mutual coupling conditions for the feed elements operating in the converging or diverging field area.

## **6. Acknowledgement**

The author is grateful to the Air Force Office of Scientific Research for sponsoring this work, to Dr. Joseph Teti of Emergent Information Technologies



Inc., and Dr. Mark Mitchell of Georgia Tech. Research Institute who first introduced me to this problem and its consequences.

## 7. References

- [1] R. Tang, "Survey of Time-Delay Steering Techniques," Phased Array Antennas, pp. 254-260, Artech House, Dedham, MA, 1972
- [2] R. J. Mailloux, "Special Array Feeds for Limited Field-of-View and Wide-Band Arrays," Chapter 8 in Phased Array Antenna Handbook, pp 511-521, Artech House Inc, 1994
- [3] R. Tang and R.W. Burns, "Phased Arrays," Ch 20 in Antenna Engineering Handbook, pp. 20-51, R.C. Johnson, Editor, Third Edition 1993
- [4] R. L. Fante, "Systems Study of Overlapped Subarrayed Scanning Antennas", IEEE Trans. Vol. AP-28, No.5, pp. 668-679, Sept 1980
- [5] H. L. Southall, D.T. McGrath, "An Experimental Completely Overlapped Subarray Antenna", IEEE Trans. Vol. AP-34, No. 4, pp. 465-474, April 1986

**Figure 1: Subarrays for Large Wide-Band Arrays**  
Subarrays reduce the number of time delays

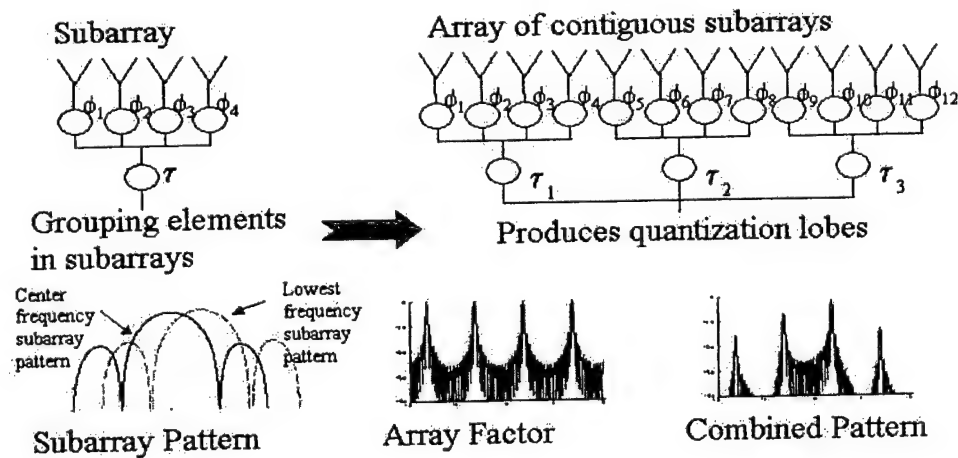


Figure 2: Pattern of 256 element array with 8 tapered subarray weights

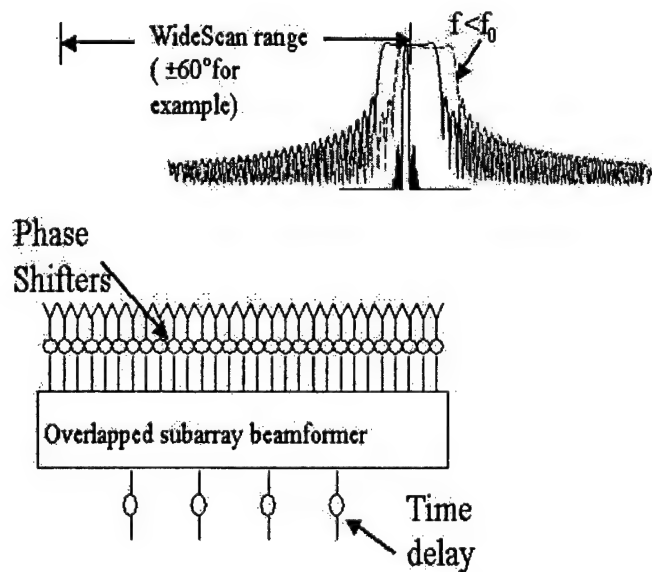
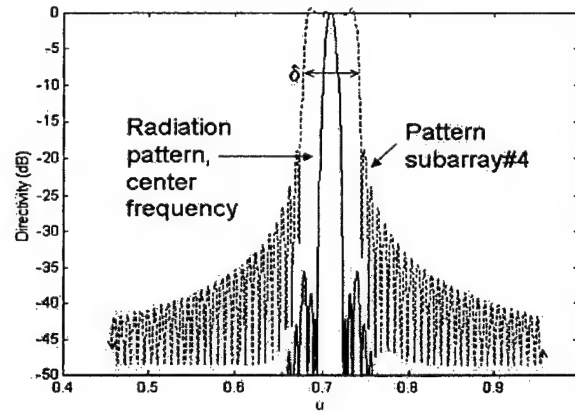
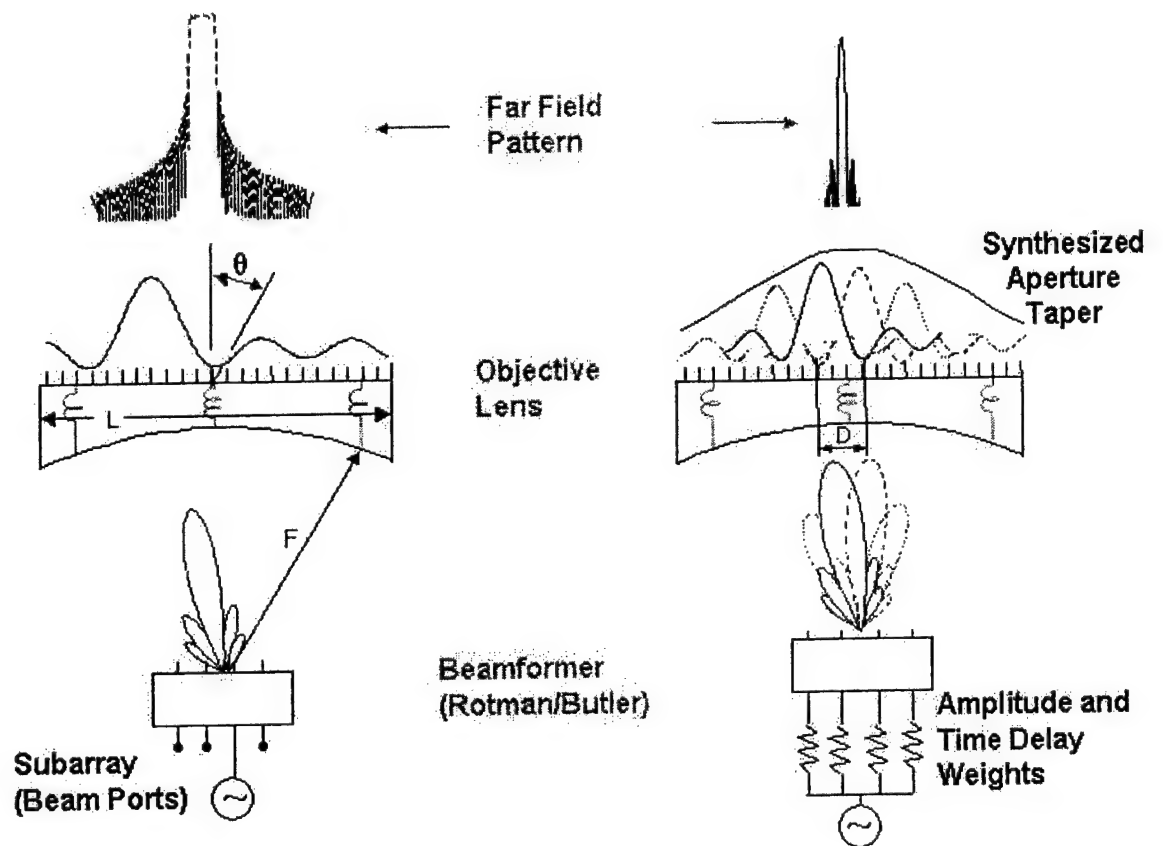
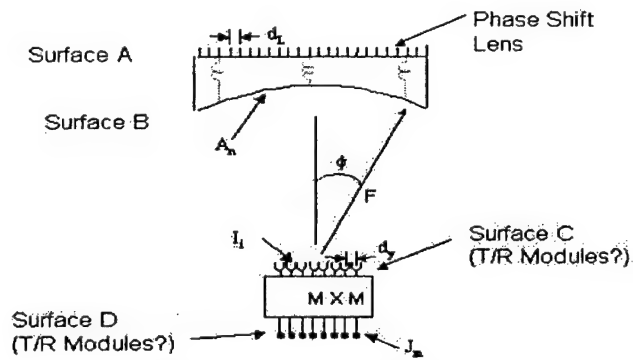


Figure 3: Overlapped subarrays to reduce the number of time delays in large arrays at wide scan angles



**Figure 4: Overlapped Subarrays for Wideband Scanning**

- High loss architecture, 6 dB or more.  
Where to put amplification ?



T/R modules (amplification) at surface C seems ideal ! Figure 5

## Normalized Current on Feed Elements

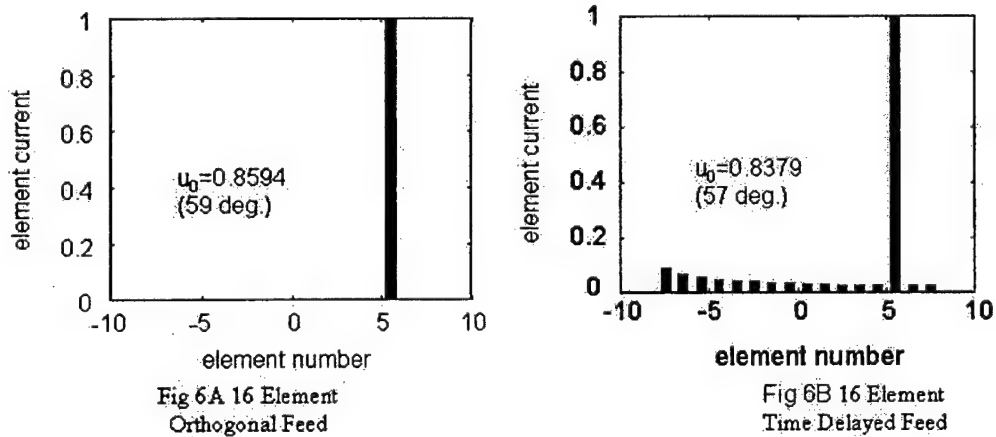


Figure 6: Normalized Current on Elements at Critical Angles with Focal Plane Beamformer ( $h_1 = 0$ ) for Uniformly Illuminated Array at  $f = 0.975 f_0$

## Current on Elements

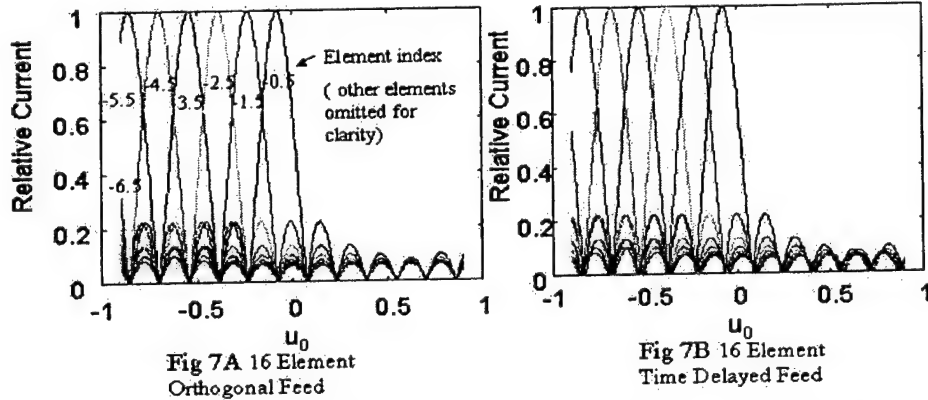


Figure 7: Normalized Current Amplitude on Elements at  $f = .975 f_0$  and with Focal Plane Beamformer ( $h = 0$ ) for Uniformly Illuminated Array

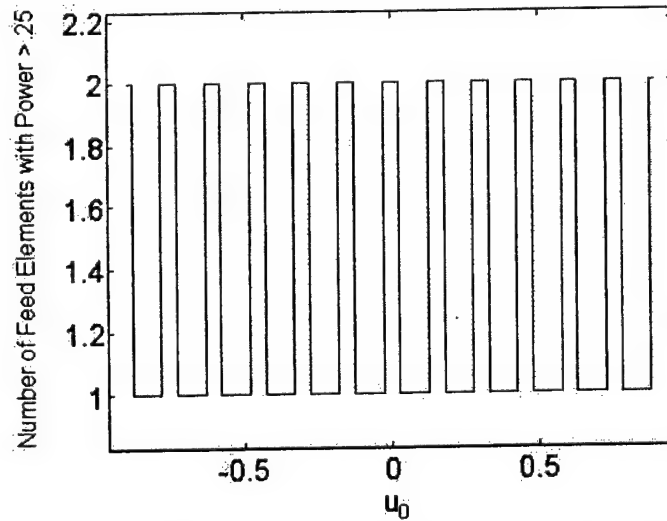


Figure 7C: Number of Elements with Normalized Power  $> 0.25$  of Maximum Element Power (time delayed feed at focal plane)

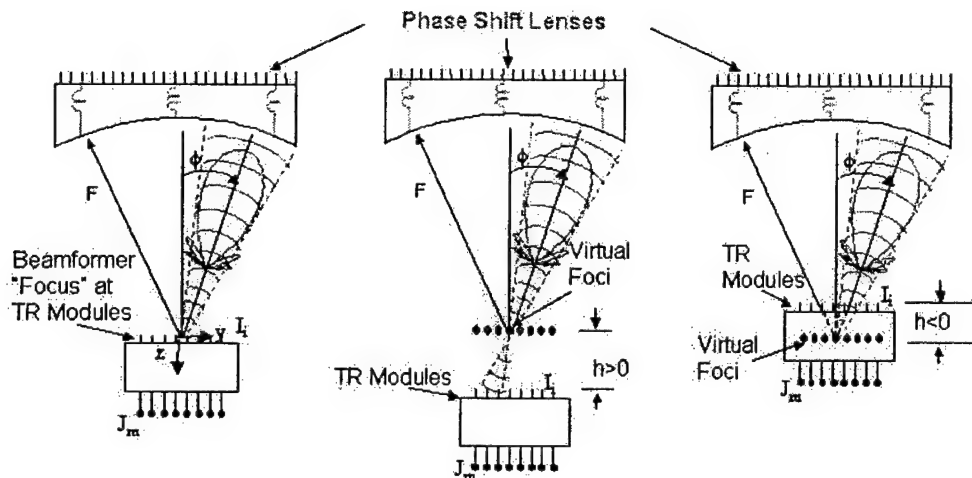
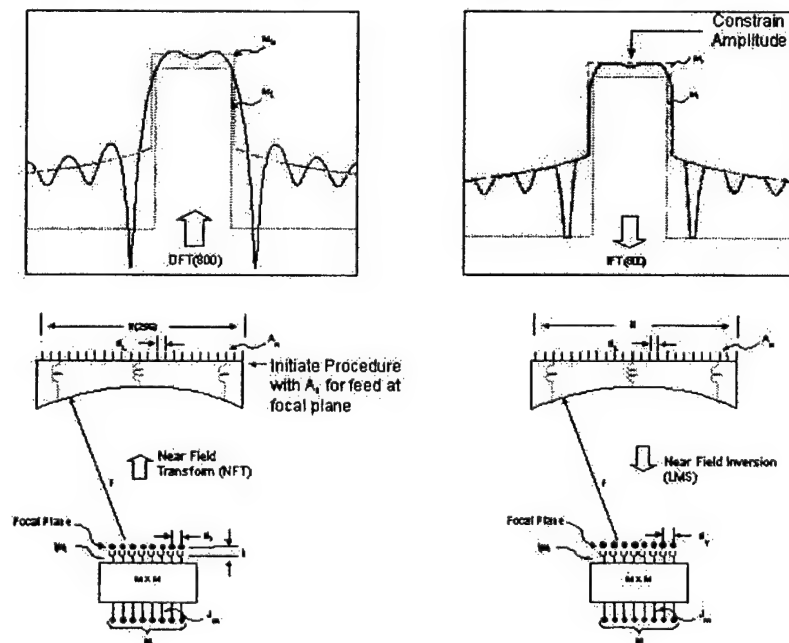


Figure 8: Alternative Subarray Beamformer Configurations

Figure 9: Alternating Projection Method Used to Optimize Subarray Patterns for Feed Beyond Focal Plane



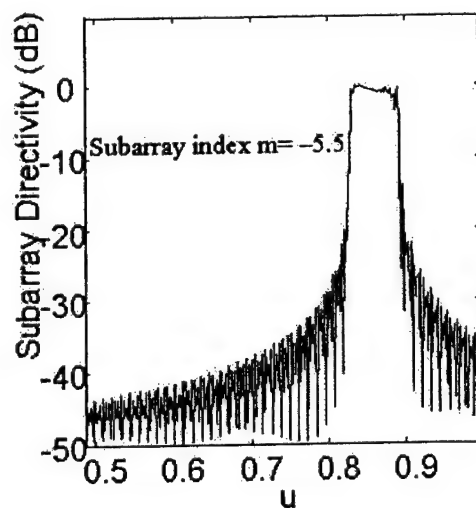


Figure 10A: focal plane beamformer

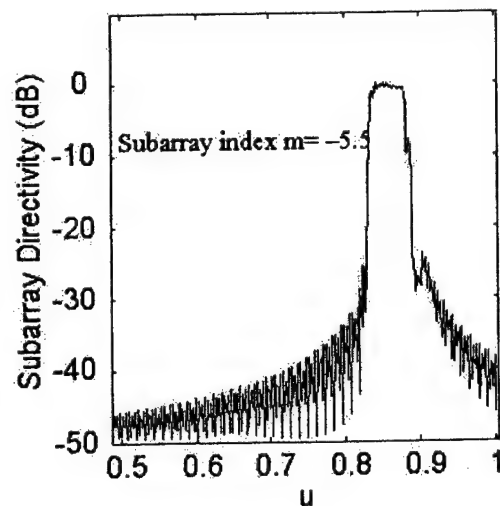


Figure 10B: synthesized beamformer

Figure 10: Subarray Patterns for  $u_0 = 0.8594$  Using Focal Plane and Synthesized Beamformer

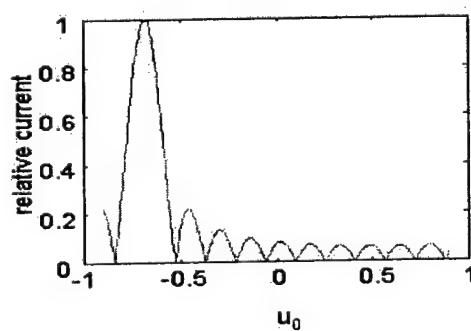


Fig11A: Focal Plane Beamformer ( $h=0$ )

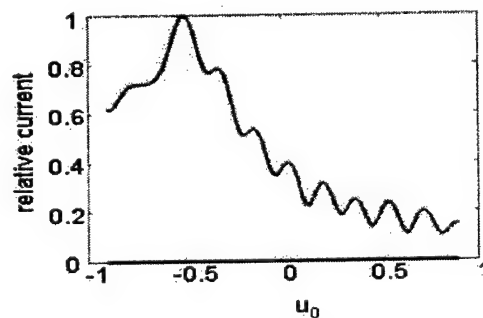


Fig11B: Synthesized Beamformer ( $h = -4$ )

Figure 11: Current on element number -5.5 for  $|u| < 0.9$  using time delayed feed

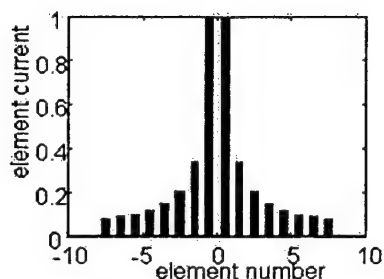


Fig12A: Focal Plane Beamformer

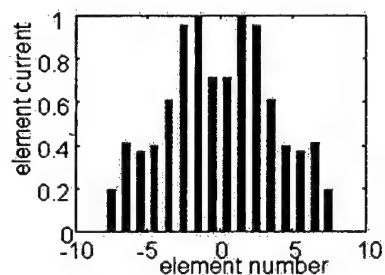


Fig12B: Synthesized Beamformer (h= -4)

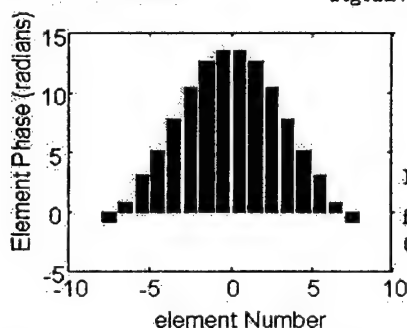


Fig12C: Phase of Current  
for Synthesized Beamformer  
(h= -4)

Figure 12: Normalized Amplitude and Phase of Current on Feed Elements of Uniformly Illuminated Array at Broadside

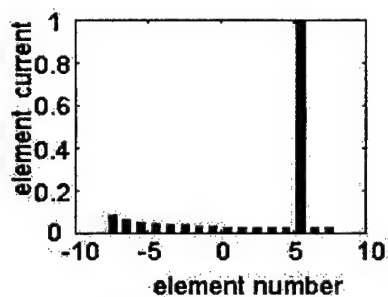


Fig13A: Focal Plane Beamformer

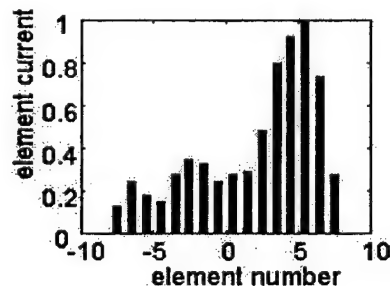


Fig13B: Synthesized Beamformer (h= -4)

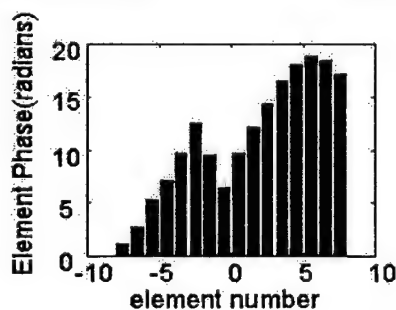


Fig13C: Phase of Current  
for Synthesized Beamformer (h= -4)

Figure 13: Normalized Amplitude and Phase of Current on Feed



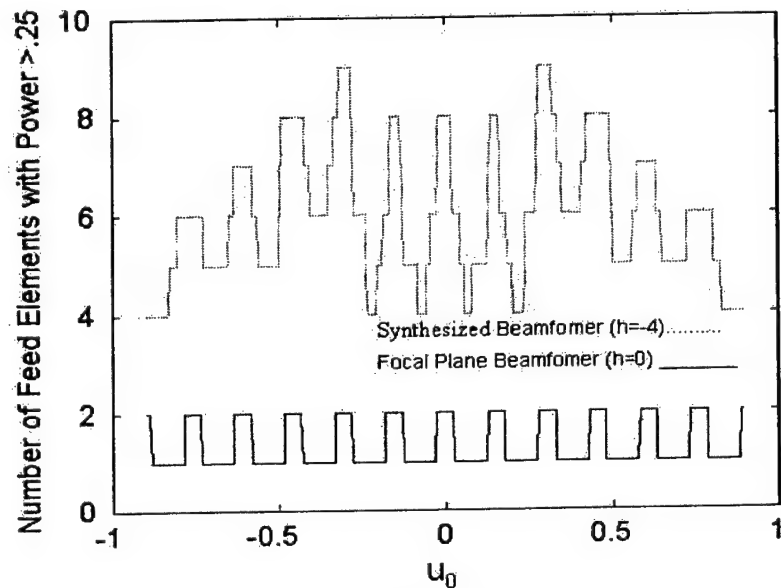


Figure 14: Number of Elements with Normalized Power  $> 0.25$  of Maximum Element Power for Array at Broadside and Uniform Illumination using a 16 element time delay beamformer

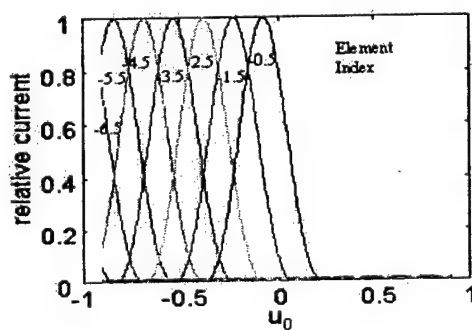


Fig 15A: Focal Plane Feed

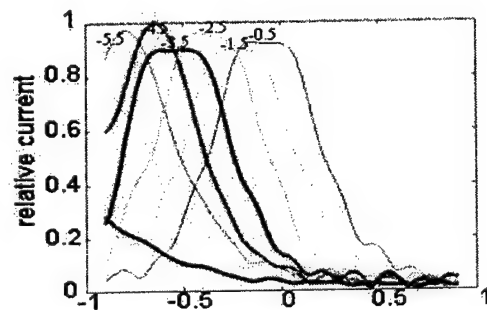


Fig 15B: Displaced Synthesized Feed

Figure 15: Current Amplitude on Elements with Focal Plane Feed ( $h = 0$ ) and Displaced Beamformer ( $h = -4$ )

(low sidelobe case)

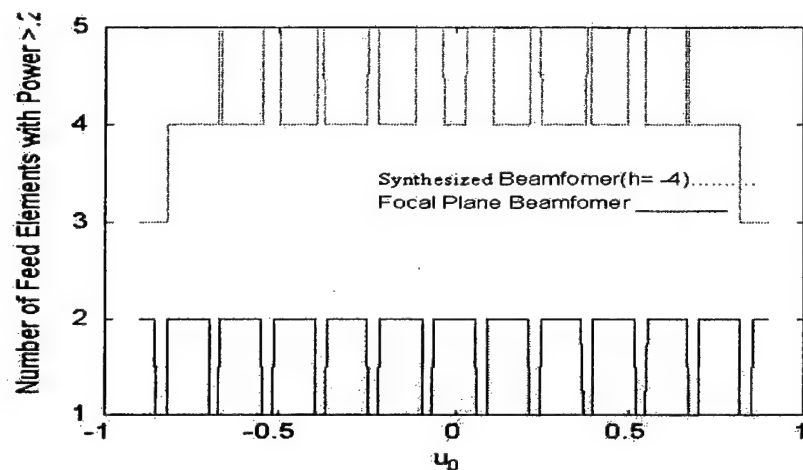


Figure 16: Number of Feed Elements with Normalized Power  $> 0.25$  of Maximum Element Power for Low Sidelobe Array

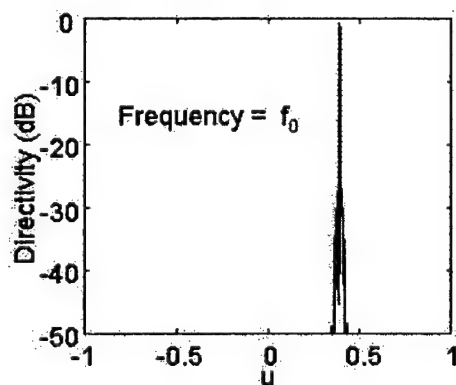


Fig17A

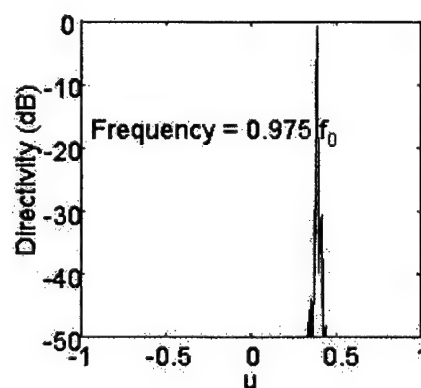


Fig17B

Figure 17: Radiated Patterns from Array using Displaced Feed with Synthesized Beamformer

# **ADAPTIVE PROCESSING USING A DIRECT DATA DOMAIN APPROACH FROM SINGLE SNAPSHOT OF DATA IN THE PRESENCE OF NEAR FIELD SCATTERERS**

***Kyungjung Kim and Tapan. K. Sarkar***

Department of Electrical Engineering and Computer Science  
121 Link Hall, Syracuse University  
Syracuse, New York 13244-1240 USA  
Tel: +1 (315) 443-3775; Fax: +1 (315) 443-4441  
Email: [kkim08@mailbox.syr.edu](mailto:kkim08@mailbox.syr.edu)  
[tk Sarkar@mailbox.syr.edu](mailto:tk Sarkar@mailbox.syr.edu)  
Home page: <http://web.syr.edu/~tk Sarkar>

***Magdalena Salazar Palma***

Grupo de Microondas y Radar, Dpto. Senales, Sistemas y Radiocomunicaciones  
ETSI Telecomunicacion, Universidad Politecnica de Madrid  
Ciudad Universitaria, 28040 Madrid, Spain.  
E-mail: [salazar@gmr.ssr.upm.es](mailto:salazar@gmr.ssr.upm.es)

**ABSTRACT:** Conventional adaptive techniques generally deal with antenna arrays that consist of omni directional isotropic radiating elements uniformly spaced. When the uniformity in the spacing is relaxed one then needs multiple snapshots in estimating the complex amplitude of the signal of interest (SOI) arriving from a known direction in the presence of multipaths, clutter and thermal noise. Usually a statistical methodology is used for the adaptive process which makes it difficult to incorporate the various electromagnetic effects like mutual coupling between the elements, presence of near field scatterers and so on and obtain a real time solution in a dynamic environment where the interference scenario may change from snap shot to snap shot.

The object of this article is to present an adaptive methodology that can not only deal with realistic antenna elements operating in a real environment but can also handle the effects of mutual coupling between the antenna elements. In addition, one can incorporate in this methodology the effects of near field scatterers and use of dissimilar antenna elements in the

array. The analysis is carried out by using a dynamic electromagnetic analysis tool. In addition, an array transformation technique is used to mitigate the various complex electromagnetic effects in a non-uniformly spaced non-planar array in the presence of the mutual coupling and transform the problem to that of a virtual linear array of uniformly spaced omni directional isotropic point radiators operating in free space. The preprocessed data from the interpolated virtual array is analyzed using a direct data domain least squares approach utilizing a single snapshot of data to estimate the strength of the signal of interest arriving from a known direction in the presence of coherent strong jammers, clutter and thermal noise. In addition, this methodology is quite amenable to real time processing.

Thus this adaptive methodology is split into two parts. First one uses an electromagnetic analysis tool in conjunction with an interpolation algorithm to transform the induced voltages in the real antenna elements due to the presence of mutual coupling and near field scatterers to that of a virtual array containing isotropic omni directional point radiators. Then a direct data domain least square method is applied to the pre processed data to obtain the desired signal strength in the presence of strong interferers, clutter and thermal noise. Numerical results are represented to illustrate the efficiency and accuracy of this method. No attempt has been made to cite the earlier references; the bibliography provides a list where supplemental information may be available.

## I. INTRODUCTION

Adaptive array signal processing has been used in many applications in such fields as radar, sonar, wireless mobile communication and so on. One principle advantage of an adaptive array is the ability to recover the desired signal while also automatically placing deep pattern nulls along the direction of the interference.

In conventional adaptive algorithms, the statistical approach based on forming an estimate of the covariance matrix of the received antenna voltages (measured voltages at the antenna terminals) without the signal is frequently used. However, these statistical algorithms suffer from two major drawbacks. First, they require independent identically distributed secondary data to estimate the covariance matrix of the interference. The formation of the covariance matrix is quite time consuming and so is the evaluation of its inverse. Unfortunately, the statistics of the interference may fluctuate rapidly over a short distance limiting the availability of homogeneous secondary data. The resulting errors in the

covariance matrix reduce the ability to suppress interference. The second drawback is that the estimation of the covariance matrix requires the storage and processing of the secondary data. This simply cannot be accomplished in real time for most applications.

Recently, a direct data domain algorithm has been proposed to overcome these drawbacks of a statistical technique [1]-[7]. In that approach one adaptively minimizes the interference power while maintaining the gain of the antenna array along the direction of the signal. Not having to estimate a covariance matrix leads to an enormous savings in memory and computer processor time and makes it possible to carry out an adaptive process in real time. The novelty of the proposed approach is that we analyze the antenna systems as spatial filters instead of treating them as temporal channels.

The use of real antenna elements and not omni directional point sources in an actual antenna array will also require an investigation into the capabilities of the direct data domain algorithms to perform adaptivity in non-ideal situations such as in the presence of mutual coupling between the elements of the array, near-field scatterers and obstacles located close to the array. This could also involve the various platform effects on which the antenna array is mounted.

Most adaptive algorithms assume that the elements of the receiving array are independent isotropic omni-directional point sensors that do not reradiate the incident electromagnetic energy. It is further assumed that the array is isolated from its surroundings. However, in a practical case, array elements have a finite physical size and reradiate the incident fields. The reradiated fields interact with the other elements causing the antennas to be mutually coupled. In [7], Adve and Sarkar observed that the degradation in the capabilities of direct data domain algorithms and suggested ways to improve it under some circumstances.

In [8], [9], the authors compensate for the effects of mutual coupling by relating the open circuit voltages (voltages at the ports of the array as if all were open circuited) with the voltages measured at the ports in an adaptive antenna array used for direction of arrival (DOA) estimation. In [7], Adve and Sarkar used the Method of Moments (MOM) to analyze the antenna array in which the entries of the MOM impedance matrix measure the interaction between the basis functions, i.e., they quantize the mutual coupling. In these works the compensation matrix is in general considered to be independent of the angle of arrival of the signals. However, in a more practical environment the presence of near field scatterers (i.e. building, the structure on which the array is mounted) will have effects on the array elements. The effects of these near field elements are similar to the effects of mutual coupling between the elements of the array. These environmental scatterers necessitate the development of a compensation matrix, which depends on the direction of arrival of signals including the undesired ones. In this paper, we shall use the measured steering vector in an

interpolation technique, which is contaminated by the presence of near field scatters as well as by the mutual coupling between the elements of the real array, to obtain the compensation matrix for a more accurate numerical analysis.

This presentation is divided into two distinct parts. In the first part we use the electromagnetic analysis along with an interpolation algorithm to transform the voltages that are measured/computed in a real array containing realistic antenna elements receiving signals in the presence of near field scatterers to a uniform linear virtual array (ULVA) consisting of isotropic omni directional point radiators. In this way we not only take into account the effects of mutual coupling and the near field scattering effects of the antenna array produced by the signal of interest but also due to the strong coherent interferers whose directions of arrival are unknown. The first stage preprocesses the voltages induced in the real elements and transforms them to a set of voltages that would be induced in an ULVA of isotropic omni directional point radiators radiating in free space.

During the second phase of the processing, these transformed voltages induced in the ULVA are processed by a direct data domain least squares method. In this phase, the goal is to estimate the complex signal amplitude given the direction of arrival in a least squares fashion when the signal of interest (SOI) is contaminated by strong interferers which may come through the main lobe of the array, clutter and thermal noise. The advantage of this methodology is that no statistical description of the environment is necessary and since we are processing the data on a snapshot-by-snapshot basis this new technique can be applied to a highly dynamic environment.

The article is organized as follows. In section II we formulate the problem. In section III we present the transformation technique incorporating mutual coupling effects between the array elements and near field scatterers. Section IV describes the direct data domain least squares approach. In section V we present simulation results illustrating the performance of the proposed method in a real environment. Finally, in section VI we present the conclusion.

## II. PROBLEM FORMULATION

Consider an array composed of  $N$  sensors separated by a distance  $d$  as shown in Figure 1. We assume that narrowband signals consisting of the desired signal plus possibly coherent multipaths and jammers with center frequency  $f_0$  are impinging on the array from various angles  $\theta$ , with the constraint  $0 \leq \theta \leq 180^\circ$ . For sake of simplicity we assume that the incident fields are coplanar and that they are located in the far field of the array. However, this methodology can easily be extended to the non-coplanar case without any problem including the added polarization diversity.

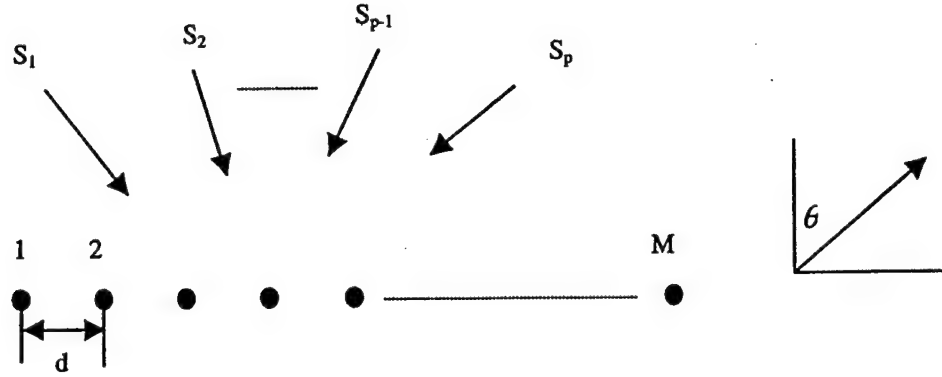


**Figure 1: A Linear Uniform Array.**

Using the complex envelope representation, the  $N \times 1$  complex vectors of phasor voltages  $[\underline{x}(t)]$  received by the antenna elements at a single time instance  $t$  can be expressed by

$$[\underline{x}(t)] = \begin{bmatrix} x_1(t) \\ x_2(t) \\ \vdots \\ x_N(t) \end{bmatrix} = \sum_{k=1}^m [\underline{a}(\theta_k)] s_k(t) + n(t) \quad (1)$$

where  $s_k(t)$  denotes the incident signal from the  $k^{\text{th}}$  source directed towards the array at the instance  $t$ .  $[\underline{a}(\theta)]$  denotes the steering vector of the array toward direction  $\theta$  and  $[n(t)]$  denotes the noise vector at each of the antenna elements. It is important to note that the array elements can be dissimilar and they can be non coplanar and may even be non-uniformly spaced. Here, the angle  $\theta$  is measured from the broadside direction as shown in Figure 1. We now analyze the data using a single snapshot of voltages measured at the antenna terminals.

Using a matrix notation, (1) becomes

$$[\underline{x}(t)] = [A(\theta)] [s(t)] + [n(t)] \quad (2)$$

where  $[A(\theta)]$  is the  $N \times m$  matrix of the steering vectors, referred to as the array manifold

$$[A(\theta)] = [a(\theta_1) \ a(\theta_2) \ \dots \ a(\theta_m)] \quad (3)$$

In a typical calibration methodology, a far field source  $s_k(t)$  is placed along the directions  $\theta_k$  and then  $[\underline{x}(t)]$  is the voltage measured at the feed point of the antenna elements in the array. Here  $[s(t)]$  is a  $m \times 1$  vector representing the various signals incident on the array at time instance  $t$ . In practice, this array manifold for a real array is contaminated by both effects of non-uniformity in the

individual elements and the inter element spacing may also be non-uniform to achieve greater aperture efficiency. Furthermore, there are mutual couplings between the antenna elements in the array, which undermine the performance of any conventional adaptive signal processing algorithm.

Hence, our problem can be stated as follows: Given the sampled data vector snapshot  $[\underline{x}(t)]$  at a specific instance of time, how do we recover the desired signal arriving from a given look direction while simultaneously rejecting all other interferences which may be coherent. Most signal processing techniques are based on the fact that a far-field source presents a linear phase front at the elements of the antenna array. However, as we shall demonstrate that the non-uniformity of a real array and the presence of mutual coupling between the elements of the real array and scatterers located close to the array undermines the ability of any adaptive algorithm to maintain the gain of the array along the direction of the signal while simultaneously rejecting the interferences. To compensate for the lack of non-uniformity of the real array and mutual coupling effects, we propose an interpolation technique based on the method of least squares which incorporates all the electromagnetic coupling effects as outlined in section III. With appropriate preprocessing using Maxwell's equations, any adaptive technique can be applied to real antenna arrays located in any arbitrary environment. However, the use of a direct data domain least squares procedure makes it possible to implement the algorithm in hardware and the solution can be obtained in almost real time.

### **III. AN ARRAY TRANSFORMATION TECHNIQUE USING LEAST SQUARES WHICH ACCOUNTS FOR ALL THE ELECTROMAGNETIC EFFECTS LIKE MUTUAL COUPLING AND PRESENCE OF NEAR FIELD SCATTERERS.**

For the first step of this adaptive method we transform the voltages that are induced in the actual antenna elements operating in any environment to a set of equivalent voltages that would be induced in a ULVA consisting of omnidirectional point radiators located in free space. The presence of mutual coupling between the antenna elements and existence of near field scatterers also disturb the capability of any algorithm to maintain the gain of the array along the direction of the signal while simultaneously rejecting the strong time varying coherent interferences. Hence, we need to preprocess the data to account for these undesired electromagnetic effects.



The preprocessing is to compensate for the lack of non-uniformity in a real array contaminated by the mutual coupling effects between the various elements. The methodology is similar to the one described in [10-12]. The procedure is based on transforming the non-uniformly spaced array into a uniform linear virtual array (ULVA) consisting of isotropic omnidirectional point radiators operating in vacuum through the use of a transformation matrix. Our basic assumption is that electrical characteristics of the array corresponding to the ULVA can be obtained through an interpolation of the real array, which is disturbed by various undesired electromagnetic couplings. The goal is to select the best-fit transformation,  $[T]$ , between the real array manifold,  $[A(\theta)]$ , and the array manifold corresponding to a uniform linear virtual array (ULVA) consisting of isotropic omnidirectional point radiators,  $[\bar{A}(\theta)]$ , such that  $[T][A(\theta)] = [\bar{A}(\theta)]$  for all possible angles  $\theta$  within a predefined sector. In this way we not only compensate for the various electromagnetic effects associated with the SOI but also correct for the interactions associated with coherent strong interferers whose direction of arrival we don't know. Since such a transformation matrix is defined within a predefined sector, the various undesired electromagnetic effects such as non-uniformity in spacing and mutual coupling between the elements and presence of near field obstacles for an array is made independent of the angular dependence.

The following is a step-by-step description of what needs to be done to obtain the transformation matrix  $[T]$  that will transform the real array manifold which is disturbed by various undesired electromagnetic effects such as mutual coupling and various near field effects to that of a ULVA.

(1) The first step in designing the ULVA is to divide the field of view of the array into  $Q$  sectors. If the field of view is  $180^\circ$ , it can be divided into 6 sectors of  $30^\circ$  each. Then, one of the  $q$  sectors is defined by the interval  $[\theta_q, \theta_{q+1}]$ , for  $q = 1, 2, \dots, Q$ . Or equivalently, only one sector of  $180^\circ$  extent can also be used. In that case  $Q = 1$ .

(2) Next we define a set of uniformly defined angles to cover each sector:

$$[\Theta_q] = [\theta_q, \theta_q + \Delta, \theta_q + 2\Delta, \dots, \theta_{q+1}] \quad (4)$$

where  $\Delta$  is the angular step size.

(3) We measure/compute the steering vectors associated with the set  $[\Theta_q]$  for the real array. This is done by placing a signal in the far field for each angle of arrival  $\theta_q, \theta_q + \Delta, \theta_q + 2\Delta, \dots, \theta_{q+1}$ . The measured/computed vector is different from the ideal steering vector, which is devoid of any undesired electromagnetic effects like the presence of the mutual coupling between the non-uniformly spaced elements and other near field coupling effects. Then, we obtain either

through measurement or using an electromagnetic analysis tool like WIPLD [13], to obtain the measured voltages at the antenna elements from:

$$[A_q(\Theta_q)] = [a(\theta_q), a(\theta_q + \Delta) \dots a(\theta_{q+1})] \quad (5)$$

This can either be actually measured or simulated and includes all the undesired electromagnetic coupling effects. Hence, each column of  $[A_q(\Theta_q)]$  represents the relative signal strength received at each of the antenna elements for an incident signal arriving from the angular direction  $\theta_q$ . The elements of the matrix are a function of only the incident angle of an incoming plane wave within that predefined sector.

(4) Next we fix the virtual elements of the interpolated array. We always assume that the ULVA consists of omni-directional isotropic sources radiating in free space. We denote by the section of the array manifold of the virtual array obtained for the set of angles  $\Theta_q$ :

$$[\bar{A}_q(\Theta_q)] = [\bar{a}(\theta_q), \bar{a}(\theta_q + \Delta), \dots \bar{a}(\theta_{q+1})] \quad (6)$$

where  $\bar{a}(\theta)$  is a set of theoretical steering vectors corresponding to the uniformly spaced linear array.

(5) Now we evaluate the transformation matrix  $[T_q]$  for the sector  $Q$  such that  $[T_q][A(\Theta_q)] = [\bar{A}(\Theta_q)]$  using the least squares method. This is achieved by minimizing the functional

$$\min_{T_q} \left\| [\bar{A}_q] - [T_q][A_q] \right\|. \quad (7)$$

In order to have a unique solution for (7), the number of direction vectors in a given sector must be greater than or equal to the number of the elements of array. The least square solution to (7) is given by [14]

$$[T] = [\bar{A}(\Theta_q)][A(\Theta_q)]^H \{[A(\Theta_q)][A(\Theta_q)]^H\}^{-1}. \quad (8)$$

where the superscript  $H$  represents the conjugate transpose of a complex matrix. Computationally it is more efficient and accurate to carry out the solution of (7) through the use of the Total Least Squares implemented through the Singular Value Decomposition [15].

The transformation matrix needs to be computed only once a-priori for each sector and the computation can be done off-line. Hence, once  $[T]$  is known we can compensate for the various undesired electromagnetic effects such as mutual coupling between the antenna elements, including the effects of near field scatterers, as well as non-uniformity in the spacing of the elements in the real array simultaneously. The transformation matrix  $[T]$  is thus characterized within the predefined angle. However, if there is only one sector, i.e,  $Q = 1$ , then there will be only one transformation matrix  $[T]$ .

(6) Finally, using (8), one can obtain the corrected input voltages in which all the undesired electromagnetic effects are accounted for and the measured snapshot of the voltages are transformed to that which will be obtained for a ULVA. Let that set be denoted by  $[x_c(t)]$ . Its value can be obtained through

$$[x_c(t)] = [T][x(t)] \quad (9)$$

Once (9) is obtained, we can apply the direct data domain algorithms to the preprocessed corrected voltages  $[x_c(t)]$  without any significant loss of accuracy.

Next a direct data domain least squares algorithm is now applied to the processed voltage sets  $[x_c(t)]$  to obtain the complex amplitude corresponding to the signal of interest in a least squares fashion.

#### IV. THE DIRECT DATA DOMAIN LEAST SQUARES PROCEDURE

Let us assume that the signal of interest (SOI) is coming from the angular direction  $\theta_d$  and our objective is to estimate its complex amplitude while simultaneously rejecting all other interferences. The signal arrives at each antenna at different times dependent on the direction of arrival of the SOI and the geometry of the array. We make the narrowband assumption for all the signals including the interferers. At each of the  $M$  antenna elements, the received signal given by (9) is a sum of the SOI, interference, and thermal noise. The interference may consist of coherent multipaths of SOI along with clutter and thermal noise. Here we model clutter as a bunch of electromagnetic waves coming through an angular sector. Hence, this model of clutter does not require any statistical characterization of the environment [1-7]. Therefore, we can reformulate (9) as

$$[\underline{x}(t)] = [\underline{s}_d] + \sum_{p=1}^{P-1} s_p a(\theta_p) + [n(t)] \quad (10)$$

where  $s_p$  and  $\theta_p$  are the amplitude and direction of arrival of the  $p^{\text{th}}$  interference, respectively and  $s_d$  is the SOI. If  $\theta_d$  is the assumed DOA of the SOI, then we can represent the received voltage solely due to the desired signal at the  $k^{\text{th}}$  sensor element as

$$s_d = s_d(t)e^{j\psi(\theta_d)} \quad (11)$$

The strength of the SOI,  $s_d(t)$ , is the desired unknown parameter which will be estimated for the given snapshot at the time instance  $t$ .  $\psi(\theta_d)$  does not provide a linear phase regression along the elements of the real array, when the elements

deviate from isotropic omni directional point sensors. This deviation from phase linearity undermines the capabilities of the various signal-processing algorithms. For a conventional adaptive array system we can now estimate the SOI by a weighted sum given by

$$y(t) = \sum_{k=1}^K w_k x_k(t) \quad (12)$$

or in a compact matrix form as

$$[y(t)] = [W]^T [X] = [X]^T [W], \quad (13)$$

where T denotes the transpose of a matrix. The two vectors [W] and [X] are given by

$$[W]^T = [w_1 \ w_2 \ \dots \ w_K], \quad (14)$$

$$[X]^T = [x_1 \ x_2 \ \dots \ x_K]. \quad (15)$$

Let [V] be a matrix, whose elements comprise of the complex voltages measured at a single time instance t at all the M elements of the array simultaneously. The received signals may also be contaminated by thermal noise. Let us define another matrix [S] whose elements comprise of the complex voltages received at the antenna elements of the ULVA due to a signal of unity amplitude coming from the desired direction  $\theta_d$ . However, the actual complex amplitude of the signal is  $\alpha$  which is to be determined. Then if we form the matrix pencil using these two matrices, we have

$$[V] - \alpha [S] \quad (16)$$

where

$$[V] = \begin{bmatrix} x_1 & x_2 & \dots & x_K \\ x_2 & x_3 & \dots & x_{K+1} \\ \vdots & & & \\ x_K & x_{K+1} & \dots & x_M \end{bmatrix}_{K \times K} \quad (17)$$

$$[S] = \begin{bmatrix} s_{d1} & s_{d2} & \dots & s_{dK} \\ s_{d2} & s_{d3} & \dots & s_{dK+1} \\ \vdots & & & \\ s_{dK} & s_{dK+1} & \dots & s_{dM} \end{bmatrix}_{K \times K} \quad (18)$$

represent only the undesired signal components. The difference between each of the elements of  $\{[V] - \alpha [S]\}$  represents the contribution of all the undesired signals due to coherent mutipaths, interferences, clutter and thermal noise (i.e., all undesired components except the signal). It is assumed that there are K equivalent

interferers and so the number of degrees of freedom is  $K = (M-1)/2$ . One could form the undesired noise power from (16) and estimate a value of  $\alpha$  by using a set of weights  $[W]$ , which minimizes the noise power. This results in [1-7]

$$([V] - \alpha[S])[W] = [0] \quad (19)$$

Alternately, one can view the left-hand side of (19) as the total noise signal at the output of the adaptive processor due to interferences and thermal noise:

$$[N_{out}] = [R][W] = \{[V] - \alpha[S]\}[W] \quad (20)$$

Hence, the total undesired power would be given by

$$[P_{undesired}] = [W]^H \{[V] - \alpha[S]\}^H \{[V] - \alpha[S]\}[W] \quad (21)$$

where the superscript  $H$  denotes the conjugate transpose of a matrix. Our objective is to set the undesired power to a minimum by selecting  $[W]$  for a fixed signal strength  $\alpha$ . This yields the generalized eigenvalue equation given by (19). Therefore,

$$[V][W] = \alpha[S][W] \quad (22)$$

where  $\alpha$ , the strength of the signal is given by the generalized eigenvalue and the weights  $[W]$  are given by the generalized eigenvector. Even though (22) represents a  $K \times K$  matrix, the matrix  $[S]$  is only of rank one. Hence, (22) has only one eigenvalue and that generalized eigenvalue is the solution for the SOI.

For real-time applications, it may be computationally difficult to solve the reduced rank generalized eigenvalue problem in an efficient way, particularly if the dimension  $K$  - the number of weights is large. For this reason we convert the solution of a nonlinear eigenvalue problem in (22) to the solution of a linear matrix equation.

We observe that the first and the second elements of the matrix  $[R]$  in (20) is given by

$$R(1) = x_1 - \alpha s_{d1} \quad (23)$$

$$R(2) = x_2 - \alpha s_{d2} \quad (24)$$

where  $x_1$  and  $x_2$  are the voltages received at the antenna elements 1 and 2 due to the signal, interferences and thermal noise, whereas  $s_{d1}$  and  $s_{d2}$  are the values of the signals only at the same elements due to an assumed incident signal of unit strength.

Define

$$Z = \exp \left[ j2\pi \frac{d}{\lambda} \sin \theta_d \right] \quad (25)$$

where  $\theta_d$  is the angle of arrival corresponding to the desired signals. Then  $R(1) - Z^{-1}R(2)$  contains no components of the signal as

$$s_{d1} = \exp\left[j2\pi \frac{id}{\lambda} \sin\theta_d\right] \quad \text{with } i = 1 \quad (26)$$

$$s_{d2} = \exp\left[j2\pi \frac{2d}{\lambda} \sin\theta_d\right] \quad \text{with } i = 2 \quad (27)$$

Therefore one can form a reduced rank matrix  $[U]_{(K-1) \times K}$  generated from  $[R]$  such that

$$[U] = \begin{bmatrix} X_1 - Z^{-1}X_2 & X_2 - Z^{-1}X_3 & \cdots & X_K - Z^{-1}X_{K+1} \\ \vdots & \vdots & & \vdots \\ X_{K-1} - Z^{-1}X_K & X_K - Z^{-1}X_{K+1} & \cdots & X_{N-1} - Z^{-1}X_N \end{bmatrix}_{(K-1) \times K} = [0] \quad (28)$$

In order to make the matrix full rank, we fix the gain of the subarray by forming a weighted sum of the voltages  $\sum_{i=1}^K W_i X_i$  along the direction of arrival of the SOI. Let us say the gain of the subarray is  $C$  in the direction of  $\theta_d$ . This provides an additional equation resulting in

$$\begin{bmatrix} 1 & \cdots & Z^{K-1} \\ X_1 - Z^{-1}X_2 & \cdots & X_K - Z^{-1}X_{K+1} \\ \vdots & \vdots & \vdots \\ X_{K-1} - Z^{-1}X_K & \cdots & X_{M-1} - Z^{-1}X_M \end{bmatrix}_{K \times K} \begin{bmatrix} W_1 \\ W_2 \\ \vdots \\ W_K \end{bmatrix}_{K \times 1} = \begin{bmatrix} C \\ 0 \\ \vdots \\ 0 \end{bmatrix}_{K \times 1} \quad (29)$$

or, equivalently,

$$[F][W] = [Y]. \quad (30)$$

Once the weights are solved by using (30), the signal component  $\alpha$  may be estimated from

$$\alpha = \frac{1}{C} \sum_{i=1}^M W_i X_i \quad (31)$$

The proof of (29)-(31) is available in [1]. As noted in [1], (29) can be solved very efficiently by applying the FFT and the conjugate gradient method, which may be implemented to operate in real time utilizing, for example, a DSP32C signal processing chip [16].

So for the solution of  $[F][W] = [Y]$  in (30), the conjugate gradient method starts with an initial guess  $[W]_0$  for the solution and lets [16]

$$[P]_0 = -b_{-1}[F]^H[R]_0 = -b_{-1}[F]^H\{[F][W]_0 - [Y]\}, \quad (32)$$

At the  $n^{\text{th}}$  iteration the conjugate gradient method develops

$$t_n = \frac{1}{\| [F][P]_n \|^2} \quad (33)$$

$$[W]_{n+1} = [W]_n + t_n [P]_n \quad (34)$$

$$[R]_{n+1} = [R]_n + t_n [Z][P]_n \quad (35)$$

$$b_n = \frac{1}{\| [F]^H [R]_{n+1} \|^2} \quad (36)$$

$$[P]_{n+1} = [P]_n - b_n [F]^H [R]_{n+1} \quad (37)$$

The norm is defined by

$$\| [F][P]_n \|^2 = [P]_n^H [F]^H [F] [P]_n \quad (38)$$

The above iterative procedures continue until the error criterion is satisfied. In our case, the error criterion is defined by

$$\frac{\| [F][W]_n - [Y] \|}{\| Y \|} \leq \sigma. \quad (39)$$

where  $\sigma$  denotes the number of effective bits of data associated with the measured voltages. Hence, the iteration is stopped when the normalized residuals are of the same order as the error in the data. The computational bottleneck in the application of the conjugate gradient method is to carry out the various matrix vector products. That is where the FFT comes in as the equations involved has a Hankel structure and therefore use of the FFT reduces the computational complexity by an order of magnitude without sacrificing accuracy [17].

The advantage of using the conjugate gradient method is that the iterative solution procedure will converge even if the matrix  $[F]$  is exactly singular. Hence, it can be used for real time implementations. Secondly, the number of iterations taken by the conjugate gradient method to converge to the solution is dictated by the number of independent eigenvalues of the matrix  $[F]$ . This often translates into the number of dominant signal components in the data. So, the conjugate gradient method has the advantage of a direct method as it is guaranteed to converge after a finite number of steps and that of an iterative method as the round off and the truncation errors in the computations are limited only to the last stage of iteration.

Next we illustrate how to increase the degrees of freedom associated with (30). It is well known in the parametric spectral estimation literature that a sampled sequence can be estimated by observing it either in the forward direction or in the reverse direction [1-7]. This we term as the backward model as opposed to the forward model just outlined. If we now conjugate the data and form the

reverse sequence, then we get an equation similar to (29) for the solution of weights  $W_m$ :

$$\begin{bmatrix} 1 & Z & \dots & Z^{K-1} \\ X_M^* - Z^{-1}X_{M-1}^* & X_{M-1}^* - Z^{-1}X_{M-2}^* & \dots & X_K^* - Z^{-1}X_{K+1}^* \\ \vdots & \vdots & & \\ X_{K+1}^* - X_K^* & X_K^* - X_{K-1}^* & \dots & X_2^* - Z^{-1}X_1^* \end{bmatrix}_{K \times K} \begin{bmatrix} W_1 \\ W_2 \\ \vdots \\ W_K \end{bmatrix}_{K \times 1} = \begin{bmatrix} C \\ 0 \\ \vdots \\ 0 \end{bmatrix}_{K \times 1} \quad (40)$$

where \* denotes the complex conjugate, or equivalently

$$[B][W] = [Y] \quad (41)$$

The signal strength  $\alpha$  can again be determined by (31), once (40) is solved for the weights.  $C$  is the gain of the antenna array along the direction of the arrival of the signal.

Note that in both cases of equations (30) and (41)  $[F]$  and  $[B]$ ,  $K = (M + 1)/2$ , where  $M$  is the total number of antenna elements. So we now increase the number of weights significantly by combining the forward-backward model. In this way we double the amount of data by not only considering the data in the forward direction but also conjugating it and reversing the increment direction of the independent variable. This type of processing can be done as long as the series to be approximated can be fit by exponential functions of purely imaginary argument. This is always true for the adaptive array case. There is an additional benefit. For both the forward and the backward method, the maximum number of weights we can consider is given by  $(M - 1)/2$ , where  $M$  is the number of antenna elements. Hence, even though all the antenna elements are being utilized in the processing, the number of degrees of freedom available is essentially half as that of the number of antenna elements. For the forward-backward method, the number of degrees of freedom can be significantly increased without increasing the number of antenna elements. This is accomplished by considering the forward and backward version of the array data. For this case, the number of degrees of freedom  $N$  can reach  $(M + 0.5)/1.5$ . This is approximately equal to 50% more weights or numbers of degrees of freedom than the two previous cases. The equation that needs to be solved for the weights in the combined forward-backward model is obtained by combining (29) and (40) into



$$\begin{bmatrix}
1 & Z & \dots & Z^{N-1} \\
X_1 - Z^{-1}X_2 & X_2 - Z^{-1}X_3 & \dots & X_N - Z^{-1}X_{N+1} \\
\vdots & \vdots & & \vdots \\
X_{N-1} - Z^{-1}X_N & X_N - Z^{-1}X_{N+1} & \dots & X_{M-1} - Z^{-1}X_M \\
X_M^* - Z^{-1}X_{M-1}^* & X_{M-1}^* - Z^{-1}X_{M-2}^* & \dots & X_N^* - Z^{-1}X_{N+1}^* \\
\vdots & \vdots & & \vdots \\
X_{N+1}^* - X_N^* & X_N^* - X_{N-1}^* & \dots & X_2^* - Z^{-1}X_1^*
\end{bmatrix}_{N \times N} \begin{bmatrix} W_1 \\ W_2 \\ \vdots \\ W_N \end{bmatrix}_{N \times 1} = \begin{bmatrix} C \\ 0 \\ \vdots \\ 0 \end{bmatrix}_{N \times 1} \quad (42)$$

or, equivalently,

$$[U][W] = [Y] \quad (43)$$

Once the increased degrees of freedom are used to compute the weights the complex amplitude for the signal of interest is determined from equation (31) where in the summation  $K$  is replaced by the new degrees of freedom  $N$ . Also as before the matrix  $[U]$  now has a block Hankel structure.

This illustrates how the direct data domain least squares approach can be implemented in real time by using single snapshots of data.

## V. NUMERICAL EXAMPLES

In this section we illustrate the above principles through some numerical simulations.

**1. Application in the absence of the mutual coupling:** As a first example consider a signal of unit amplitude arriving from  $\theta_s = 0^\circ$ . We consider a 17-element array of element spacing of  $\lambda/2$  as shown in Figure 1. The magnitude of the incident signal is varied from 1 V/m to 10.0 V/m in steps of 0.1 V/m while maintaining the jammer intensities constant, which are arriving from  $-50^\circ$ ,  $-30^\circ$ ,  $30^\circ$ . The signal-to-thermal noise ratio at each antenna element is set at 20 dB. All signal intensities and directions of arrival are summarized in Table I. Here, we assume that we know the direction of arrival of the signal but need to estimate its complex amplitude.

If the jammers have been nulled correctly and the signal recovered properly, it is expected that the recovered signal have a linear relationship with respect to the intensity of the incident signal. Figure 2 plots the results of using the direct data domain approach presented in Section-III. The magnitude and the phase are shown. As can be seen, this magnitude displays the expected linear relationship and this phase has been varied within very small value. The beam

pattern associated with this example is shown in Figure 3. Here, we set the magnitude of the desired signal to be 1 V/m and the other parameters are as given Table I. The nulls are deep and occur along the correct directions.

**Table I**  
Parameters of the Incident Signals

	Magnitude	Phase	DOA
Signal	1.0 - 10.0 V/m	0.0	0°
Jammer #1	1.0 V/m	0.0	-50°
Jammer #2	1.0 V/m	0.0	-30°
Jammer #3	1.0 V/m	0.0	20°

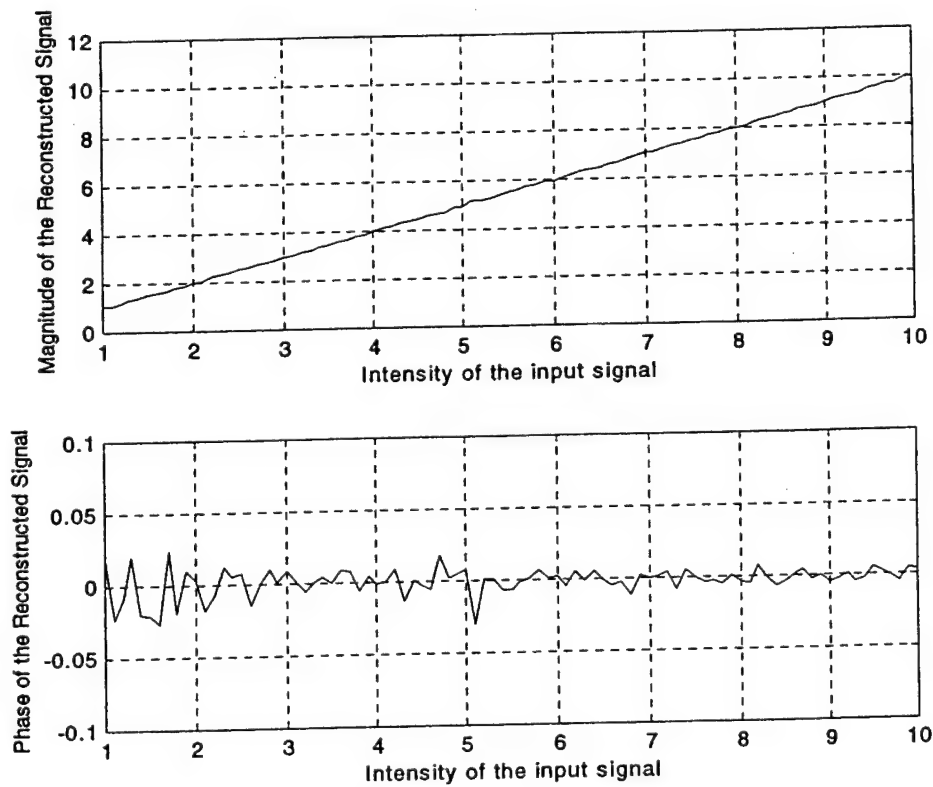


**Figure 2:** Estimation of the Signal of Interest (SOI) in the presence of jammers and thermal noise.

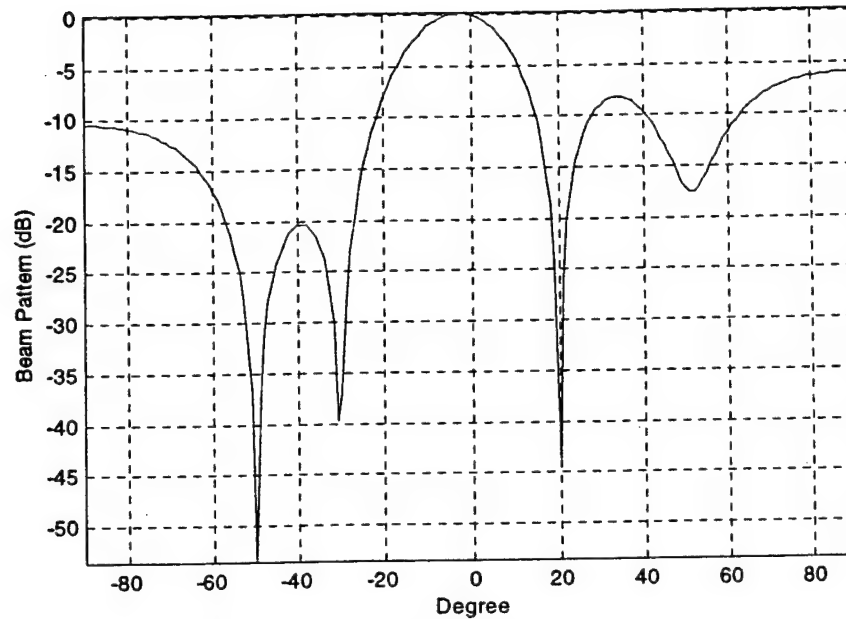


**Figure 3:** Adapted Beam Pattern in the presence of the jammers and thermal noise.

For the second example, the intensity of the jammer signal is varied from 1 V/m to 1000 V/m in steps of 10 V/m while the intensity of the desired signal is fixed at 1V/m. All signals intensities and directions of arrival are summarized in Table II. The signal-to-thermal noise ratio at each antenna element is set at 20 dB.

**Table II**  
Parameters for the SOI and Interference

	Magnitude	Phase	DOA
Signal	1.0 V/m	0.0	0°
Jammer #1	1 V/m	0.0	-50°
Jammer #2	1 V/m	0.0	-30°
Jammer #3	1-1000 V/m	0.0	20°

Figure 4 shows the results of using the direct data domain approach. The fluctuations of the magnitude and phase of the estimated signal are very small even when there is a very strong interference.

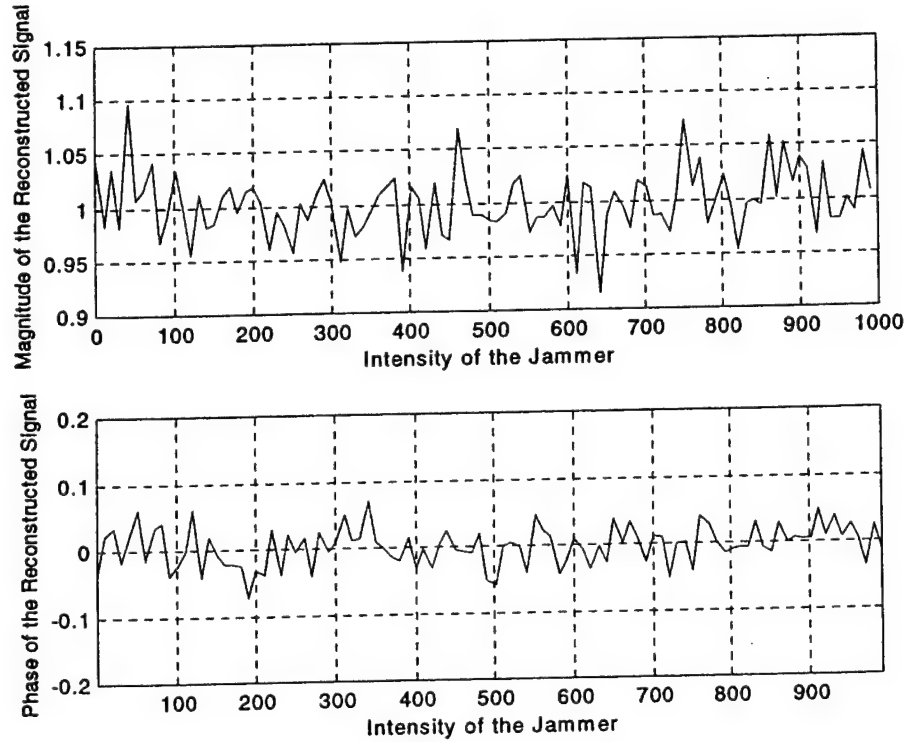


**Figure 4:** Estimation of the reconstructed signal in the presence of the strong jammer.

The beam pattern associated with this adaptive system when the field strength of the strong jammer is 500 V/m is shown in Figure 5. This demonstrates that the strong jammer has been suppressed enough so as to recover the proper amplitude of the signal.

**2. Application in the presence of the mutual coupling:** Next we consider a semi circular array consisting of half wave dipoles as shown in Figure 6. It consists of 24 half-wave thin-wire dipole antenna elements. Each element is identically loaded at the center by  $50\Omega$ . The radius of the semicircular array is 3.82 wavelength. The dipoles are z-directed, of length  $L = \frac{\lambda}{2}$  and radius  $r = \frac{\lambda}{200}$ , where  $\lambda$  is the wavelength of operation. The details of the semi circular are presented in Table III.

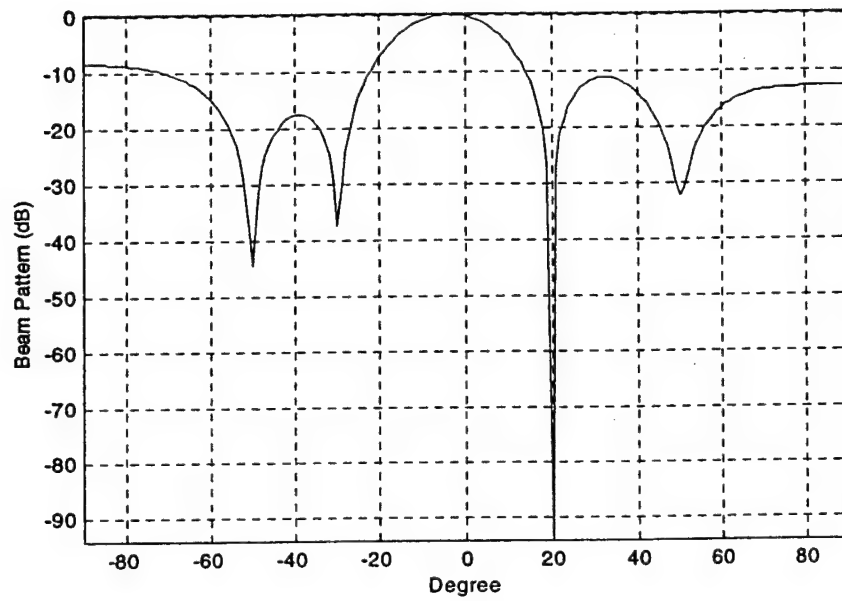


**Figure 5:** Adapted Beam pattern in the presence of the jammers.

Semicircular array (SCA)

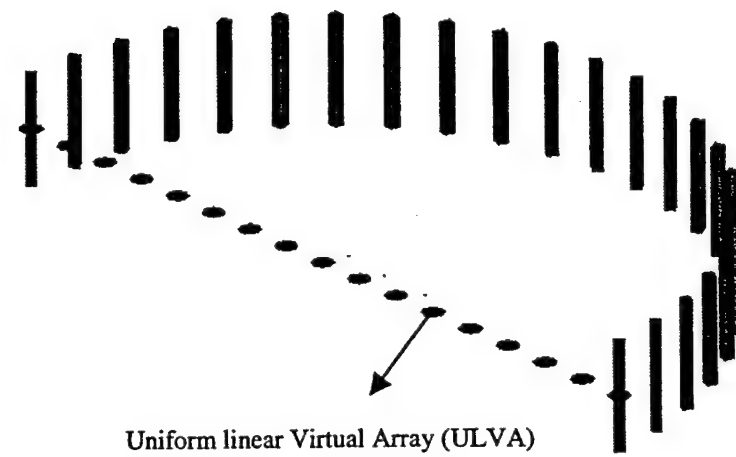


**Figure 6:** A Semicircular Array.

**Table III**  
Physical sizes of the elements for the semicircular array.

Number of elements in semicircular array	24
Length of z-directed wires	$\lambda/2$
Radius of wires	$\lambda/200$
Loading at the center	$50\Omega$

Then, as described in section IV, the real array is interpolated into a ULVA consisting of  $M = 17$  isotropic omni-directional point sources separated by a distance  $d/\lambda$ . Typically  $d$  is chosen to be close to  $\lambda/2$ . By choosing the reference point of the ULVA at the center of the real array, the steering vectors associated with the virtual array are given by

$$\bar{\mathbf{a}}(\theta) = \begin{bmatrix} e^{-\frac{j2\pi kd}{\lambda} \sin \theta} & \dots & e^{-\frac{j2\pi 2d}{\lambda} \sin \theta} & e^{-\frac{j2\pi d}{\lambda} \sin \theta} & 1 & \dots & e^{\frac{j2\pi d}{\lambda} \sin \theta} & e^{\frac{j2\pi 2d}{\lambda} \sin \theta} & e^{\frac{j2\pi kd}{\lambda} \sin \theta} \end{bmatrix}^T, \quad (44)$$

$N \times 1$

The distance  $d$  between the elements of the ULVA was chosen to be  $0.4775 \lambda$ . The incremental size  $\Delta$  in the interpolation region,  $\Theta = [-\theta_q, \theta_{q+1}] = [-60^\circ, 60^\circ]$ , is chosen to be  $1^\circ$ . In this case  $Q = 1$ . The sector chosen here, for example, is of  $120^\circ$  symmetrically located. Then, a set of real steering vectors are computed for the sources located at each of the angles  $\theta_q, \theta_q + \Delta, \theta_q + 2\Delta, \dots, \theta_{q+1}$ . The computed vector  $[\bar{\mathbf{a}}(\theta)]$  is then distorted from the ideal steering vector due to the presence of mutual coupling between the elements of the real array. The actual steering vectors having all the undesired electromagnetic effects are computed using WIPL-D [13]. Then, using (8) we obtain the transformation matrix to compensate for the effects of non-uniformity in spacing and the presence of mutual coupling between the elements of the real array. Finally, using (43), we can obtain the corrected input voltage in which the non-uniformity in spacing and mutual coupling effects are eliminated from the actual voltage.

Next, the magnitude of the incident SOI is varied from 1 V/m to 10.0 V/m in steps of 0.01 V/m while maintaining the jammer intensities constant, which are arriving from  $-20^\circ, 10^\circ, 40^\circ, 50^\circ$ . The signal-to-thermal noise ratio at each antenna element is set at 20 dB. All signals intensities and directions of arrival are summarized in Table IV and are given by

**Table IV**  
Parameters of the Signals

	Magnitude	Phase	DOA
Signal	1.0 - 10.0 V/m	0.0	10°
Jammer #1	1.0 V/m	0.0	-20°
Jammer #2	1.0 V/m	0.0	40°
Jammer #3	1.0 V/m	0.0	50°

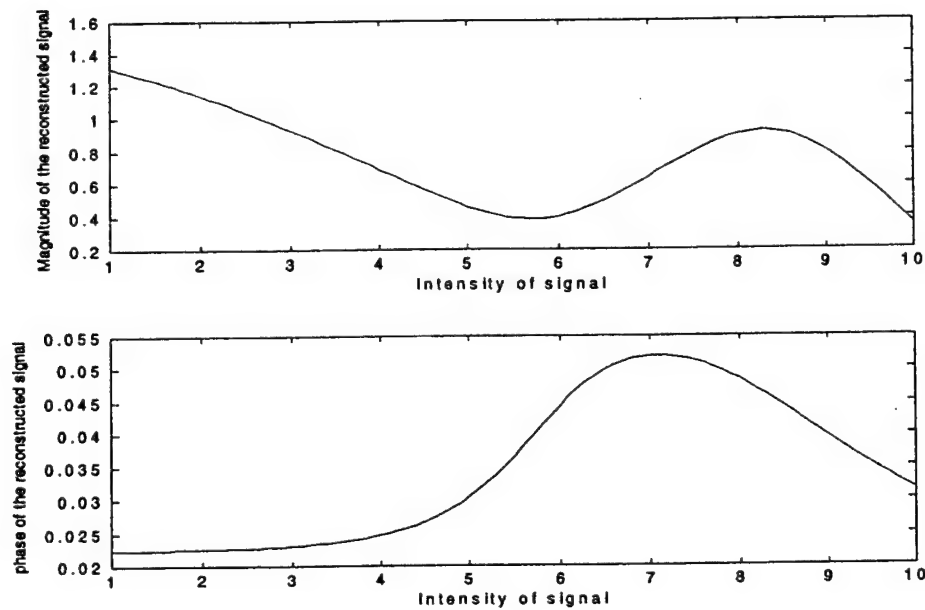


**Figure 7-(a):** Estimation of the SOI without compensating for mutual coupling.

If the jammers have been nulled correctly and the SOI recovered properly, it is expected that the recovered signal will have a linear relationship with respect to the intensity of the incident signal, implying that the various electromagnetic effects have been properly accounted for. The estimate for the SOI in Figure 7-(a) shows that the mutual coupling between the elements of the real array undermines the performance of the direct data domain approach if the various electromagnetic effects are not accounted for. Figure 7-(b) illustrates the superiority of the results when the direct data domain least squares approach is used after preprocessing the data to take into account the various mutual coupling effects. The estimated

amplitude and the phase for the SOI are shown in Figure 7(b). Here, the amplitude displays the expected linear relationship and the phase changes very little from zero degrees.

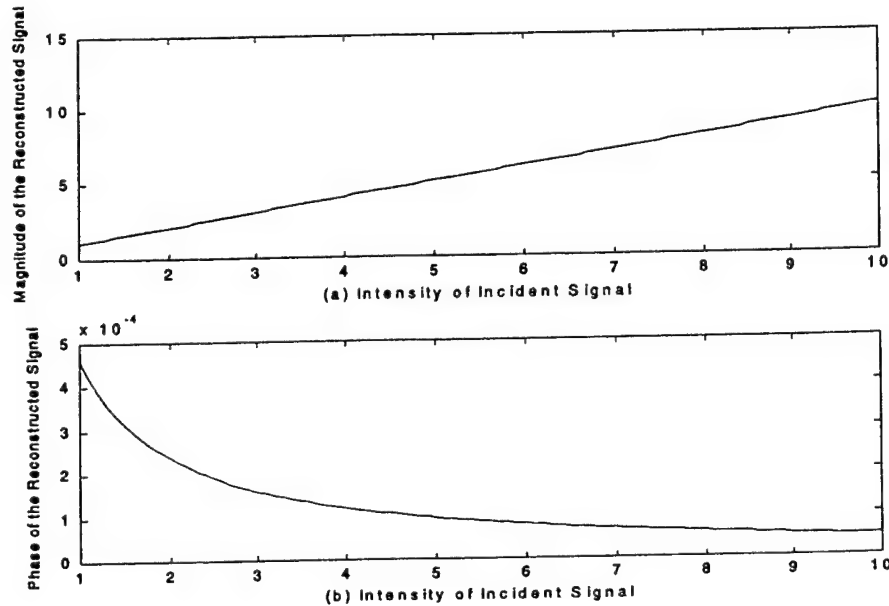


**Figure 7-(b):** Estimation of SOI after compensating for the mutual coupling.

The beam patterns associated with this example are shown in Figure 8-(a), (b). Here, we set the amplitude of the SOI to be 1 V/m and the other parameters are as given Table IV. Figure 8-(b) illustrates that the nulls are deep and are located along the correct directions. This indicates that the two step procedure illustrated in this article have properly modeled the real environment nulling the relevant interferers. However, we see that in Figure 8-(a) the nulls in the beam pattern are shallow and are displaced from their desired locations, as the undesired electromagnetic effects have not been properly taken into account. Hence, in this case the SOI cannot be recovered.

For the final example we consider the effects of large near field scatterers located close to the semicircular array. As shown in Figure 9, there is a large structure located within a distance, which is 5 times the radius of the semicircular array and is oriented along the direction of  $-20^\circ$ . The width of the structure is 7.26 wavelengths and its height is 15.28 wavelengths. Hence, the semicircular array and the scatterer have strong electromagnetic coupling in addition to the presence of mutual coupling between the elements. We again



consider the case of four incoming signals from  $-20, 10, 40, 50^\circ$ . The parameters for the desired signal and the jammers are summarized in Table IV.

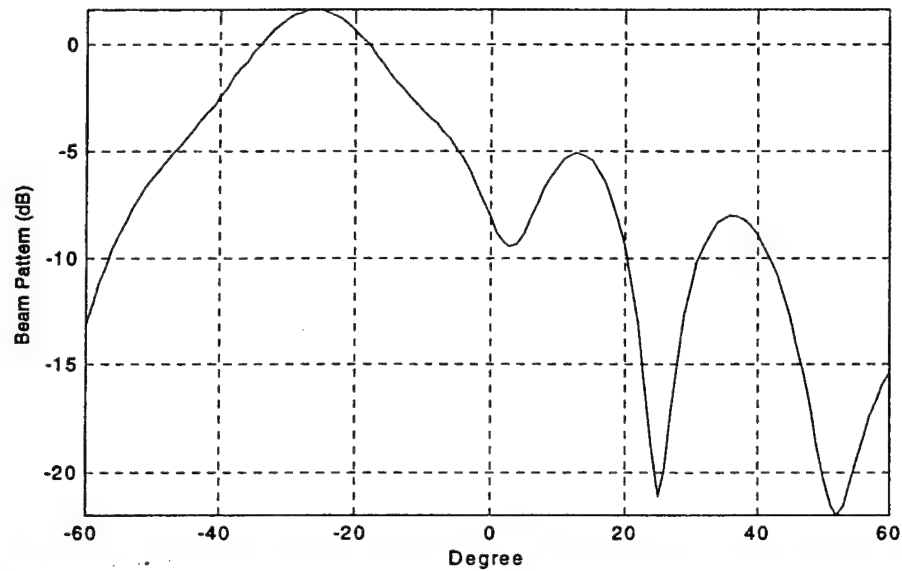


**Figure 8-(a):** Adapted Beam pattern without correcting for the mutual coupling.

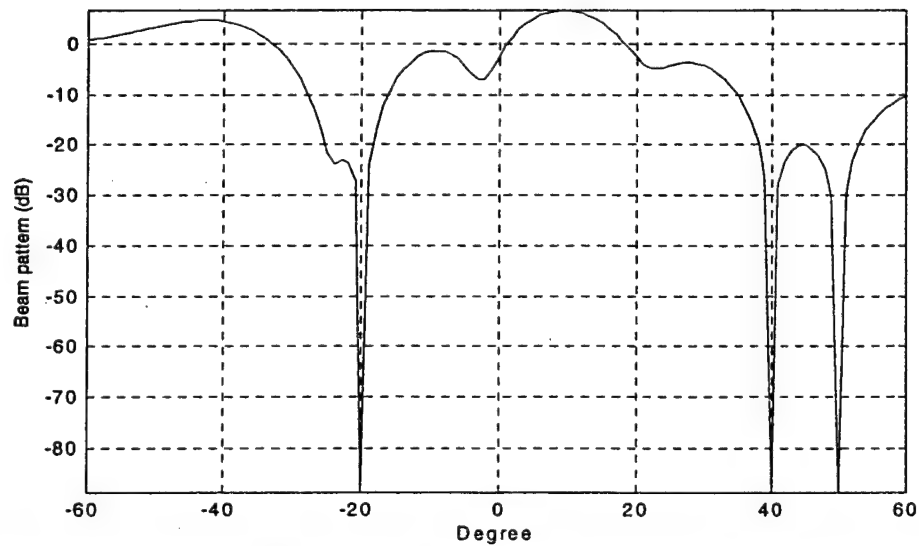


**Figure 8-(b):** Adapted Beam pattern after compensating for the mutual coupling.

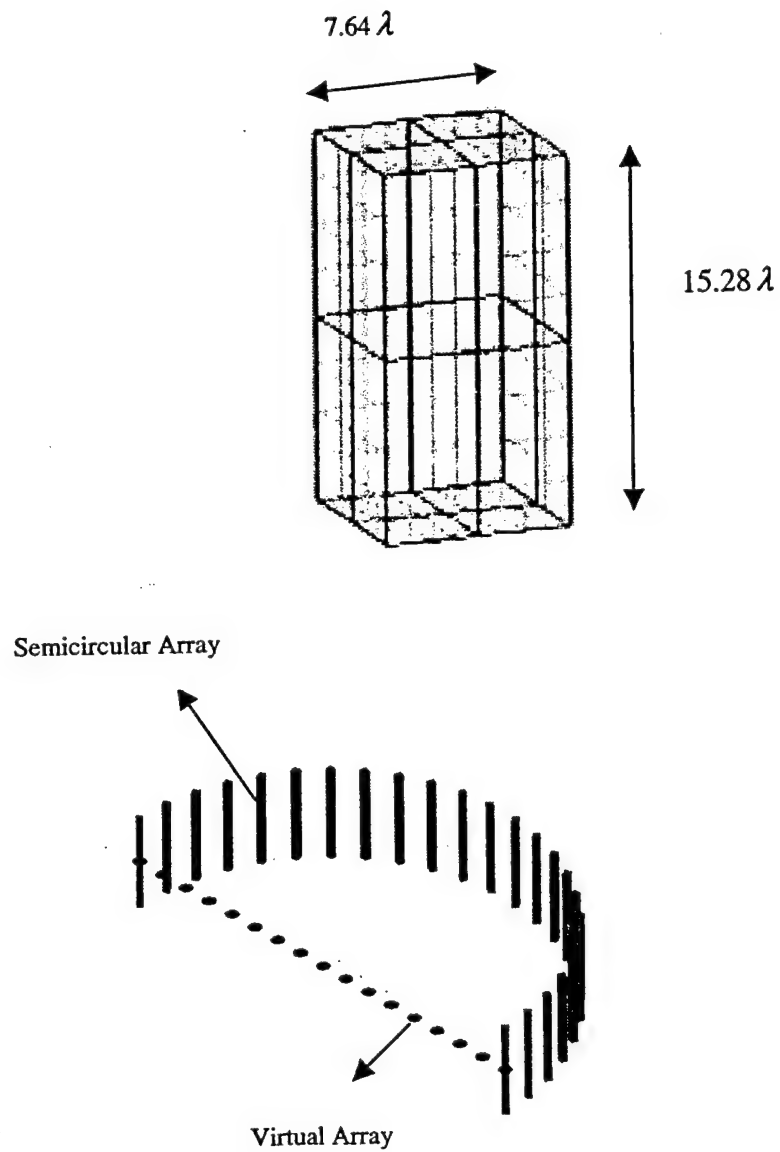


**Figure 9:** A Semicircular Array operating in the presence of a big obstacle.

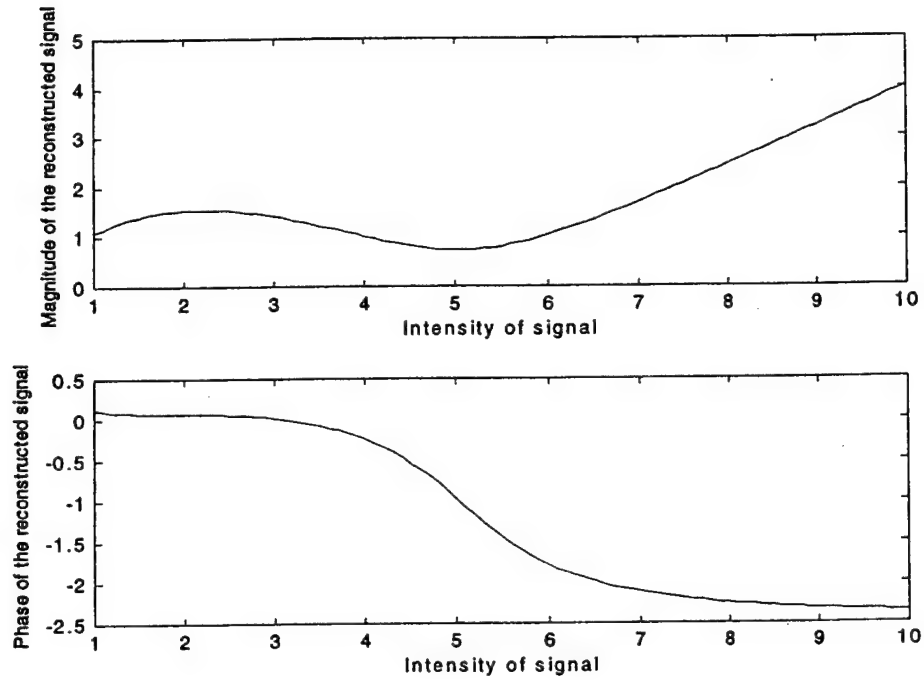


**Figure 10-(a):** Estimation for the SOI without compensating for the mutual coupling and the near field scatterer.

After we compensate for the various electromagnetic couplings and project the data to that due to a ULVA, we solve for the weights  $[W]$  using (43). Then, we estimate the amplitude of the desired signal through (31). Figure 10-(a) and (b) plots the amplitude and the phase for the SOI both in the presence and in the absence of mutual coupling between the elements of the array and the scatterer located close to the array. As can be seen, after compensation of the undesired electromagnetic effects, the expected linear relationship is clearly seen, implying that the jammers have been nulled and the SOI estimated with a good accuracy.

The adapted beam patterns associated with this example are shown in Figure 11 -(a) and (b) for the two cases considered above. When the mutual coupling is neglected the beam pattern in Figure 11-(a) clearly indicates that the interferers have not been nulled in a correct fashion. However, when the electromagnetic effects have been appropriately accounted, for the beam points correctly along the direction of SOI while simultaneously placing deep nulls along the direction of the interferers. By comparing the adapted beam patterns in Figures 8(b) and 11(b) it is seen that the presence of a large near field scatterer has indeed produced a wide null along that direction due to the diffraction effects of the interferer.

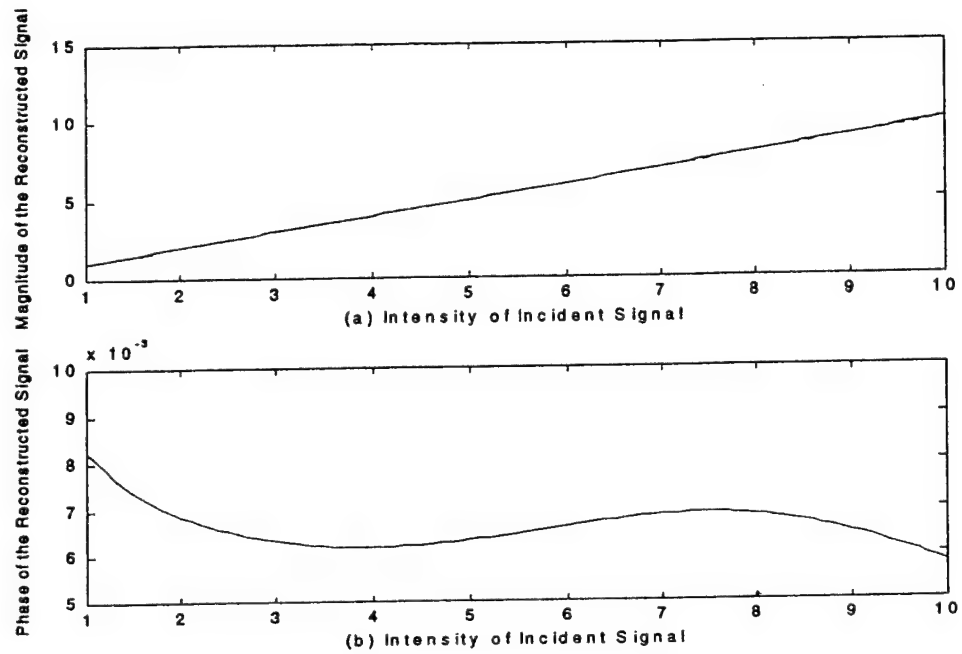


**Figure 10-(b):** Estimation of the SOI after compensating for the mutual coupling and effect of the near field scatterer.

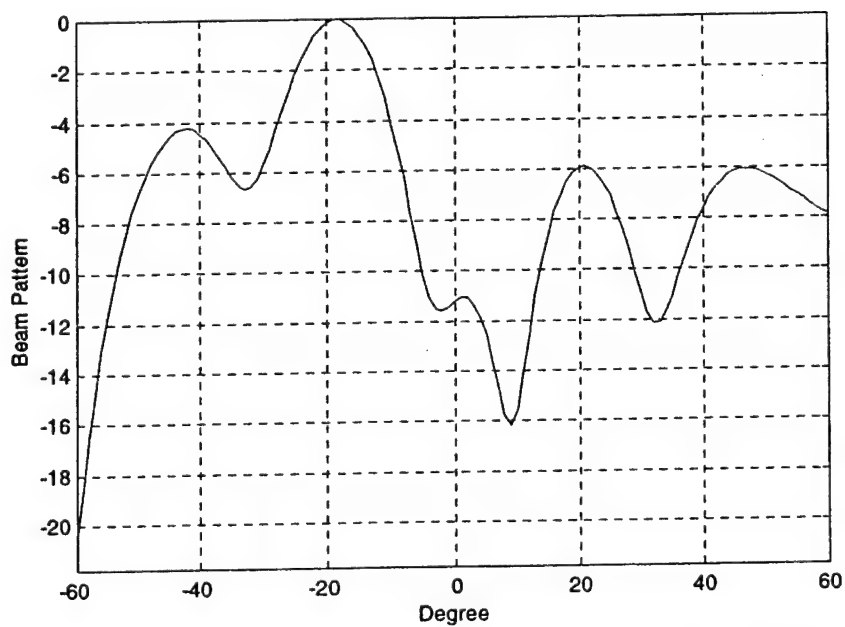


**Figure 11-(a):** Adapted Beam pattern without compensating for the mutual coupling and near field scatterer.

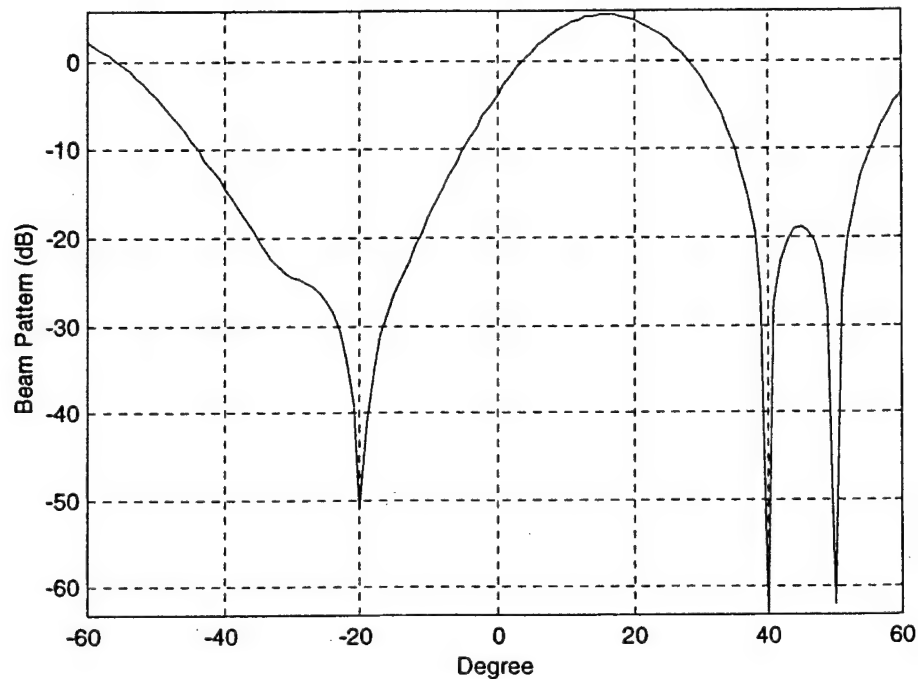


**Figure 11-(b):** Adapted Beam pattern after compensating for the mutual coupling and the near field scatterer.

## VI. CONCLUSION

The objective of this article has been to present a two-step process for using Adaptive Antenna Arrays operating in a real environment. At the first step a transformation matrix is determined which transforms the voltages induced at the feed points of the antenna elements operating in the presence of near field scatterers and the presence of mutual coupling between the antenna elements to that of the voltages induced in a uniform linear virtual array consisting of isotropic omni directional point radiators operating in free space. Such a transformation takes into account all the electromagnetic interactions between the antenna elements and its environment. The next step in the solution procedure involves applying a direct data domain least squares approach which estimates the complex amplitude of the signal of interest given its direction of arrival. The signal of interest may be accompanied by coherent multipaths and interferers, which may be located in angle quite close to the direction of arrival of the signal. In addition there may be clutter and thermal noise at each of the antenna elements.

In this approach since no statistical methodology is employed, there is no need to compute a covariance matrix. Therefore, this procedure can be implemented on a general-purpose digital signal processor for real time implementations.

## VII REFERENCE

- [1] T. K. Sarkar, J. Koh, R. Adve, R. Schneible, M. Wicks, S. Choi and M. Salazar-Palma, "A Pragmatic Approach to Adaptive Antennas", *IEEE Antennas and Propagation Magazine*, Vol. 42, No. 2, April 2000, pp. 39-55.
- [2] T. K. Sarkar, S. Park, J. Koh and R. A. Schneible, "A Deterministic Least Squares Approach to Adaptive Antennas", *Digital Signal Processing - A Review Journal*, Vol. 6, 185-194 (1996).
- [3] S. Park, Tapan K. Sarkar, "Prevention of Signal Cancellation in an Adaptive Nulling Problem," *Digital Signal Processing - A Review Journal*, Vol. 8, 95-102, 1998.
- [4] T. K. Sarkar, S. Nagaraja and M. C. Wicks, "A Deterministic Direct Data Domain Approach to Signal Estimation Utilizing Nonuniform and Uniform 2-D Arrays", *Digital Signal Processing - A review Journal*, Vol. 8, 114-125 (1998).
- [5] T. K. Sarkar, H. Wang, S. Park, J. Koh, R. Adve, K. Kim, Y. Zhang, M. C. Wicks and R. D. Brown, "A Deterministic Least squares Approach to Space Time Adaptive Processing (STAP)", *IEEE Trans. Antennas and Propagation*, Vol. 49, January 2001, pp. 91 - 103.
- [6] T. K. Sarkar and R. Adve, "Space Time Adaptive Processing Using Circular Arrays", *IEEE Antennas and Propagation Magazine*, Vol. 43, Feb 2001, pp. 138 -143.
- [7] Raviraj S. Adve and Tapan K. Sarkar, "Compensation for the Effects of Mutual Coupling on Direct Data Domain Adaptive Algorithms", *IEEE Trans. on Antennas and Propagation*, Vol. 48, No. 1, Jan. 2000.
- [8] I. J. Gupta and A. A. Ksienski, "Effects of mutual coupling on the performance of adaptive arrays," *IEEE Trans on Antennas and Propagation*, vol. 31, pp785-791, Sept. 1983.
- [9] K. M. Pasala and E. M. Friel, "Mutual coupling effects and their reduction in wideband direction of arrival estimation," *IEEE Trans. Aerospace and Electronics System*, vol. 30, pp. 1116-1122, Apr. 1994.
- [10] Benjamin Friedlander, "The root-MUSIC algorithm for direction finding with interpolated arrays," *Signal Processing*, Vol. 30, 1993, pp. 15-29.

- [11] Ta-Sung Lee, Tsui-Tsai Lin, "Adaptive beamforming with interpolation arrays for multiple coherent interferes," *Signal Processing*, Vol. 57, 197, pp. 177-194.
- [12] Mati Wax, Jacob Sheinvald, "Direction Finding of Coherent Signals via Spatial Smoothing for uniform Circular Arrays," *IEEE Trans. On Antennas and Propagation*, vol. 42, no 5, May 1994.
- [13] B.M. Kolundzija, J.S. Ognjanovic, T.K. Sarkar, "*WIPL-D: Electromagnetic Modeling of Composite Metallic and Dielectric Structures*", Artech House, Norwood, Mass., 2000.
- [14] G. H. Golub and C. F. Van Loan, "*Matrix Computations*", The Johns Hopkins Press, Baltimore, Md, 1989.
- [15] S. Van Huffel, "*Analysis of the total least squares problem and its use in parameter estimations*", Ph.D. Thesis, Dept. of Electrical Engg, Katholieke Universiteit Leuven, 1990.
- [16] R. Brown and T. K. Sarkar, "Real time deconvolution utilizing the fast Fourier Transform and the Conjugate Gradient method", presented at the 5<sup>th</sup> ASSP Workshop on Spectral Estimation and Modeling, Rochester, N.Y., 1980.
- [17] T. K. Sarkar, "*Application of the Conjugate Gradient Method to Electromagnetics and Signal Analysis*", Progress in Electromagnetics Research, Vol. 5, Elsevier, Mass. 1991.

# **DIGITAL BEAMFORMING ALGORITHMS FOR OBTAINING ULTRALOW SIDELOBE ARRAY ANTENNA PATTERNS**

W. R. Pickles<sup>1</sup>, W. K. Kahn<sup>2</sup>, J. B. L. Rao<sup>1</sup>, and D. P. Patel<sup>1</sup>

<sup>1</sup> Naval Research Laboratory, Radar Division, Washington, DC

<sup>2</sup> NRL Consultant, Department of Electrical and Computer Engineering,  
The George Washington University, Washington, DC

**ABSTRACT** Two methods for obtaining ultralow sidelobe patterns will be presented. The methods are applicable to antenna arrays in which the signals received from each element can be digitized. In the first technique, the measured or calculated mutual coupling coefficients between the elements are used to generate a matrix of correction factors. The second technique uses the measured or calculated far field patterns of each element in a terminated array environment to generate a matrix of correction factors. Results obtained by applying both methods to experimentally measured and numerically calculated array data will be presented. The similarities of the correction matrices calculated by each technique will be discussed. The advantages and disadvantages of each technique will be addressed.



## 1.0 Introduction

The very act of building an antenna implies the need for high directivity and low sidelobes. Any radiation that goes in unintended directions is at least wasted and possibly detrimental. Unfortunately physics and economics prevent the antenna designer from having exactly the antenna he desires. When economics is less of a factor than physics the antenna designer can hope to achieve sidelobes that are about 20 dB below isotropic through meticulous electrical and mechanical design of the array.

To first order the sidelobe level is inherent in the selected distribution of excitation among the array elements. At some angle, for example broadside, all the elements of the array may come into focus and the main lobe is generated. At other angles the elements of the array come partially back into focus and secondary lobes are generated. The secondary lobes are controlled by tapering the excitation in the aperture so that it is strong at the center and weak at the edges. Increasing the taper further reduces the sidelobe level until the sidelobe level caused by second order sources is reached.

Real antennas may have both electrical and mechanical errors which introduce amplitude and phase errors across the aperture. Conventional techniques of obtaining low sidelobes focus on controlling antenna excitation to achieve low sidelobes. An array comprised of many similar elementary antennas appears to offer obvious means for controlling the total excitation. The approach described here starts with an effort to eliminate the mechanical sources which increase sidelobes. It continues by developing an analytical model for the electrical sources which increase sidelobes and compensating for them through digital processing.

The secondary sources of sidelobes are scattering from the mechanical structure of the antenna and scattering from other elements. The elements of an array are usually electrically small antennas so they have broad beamwidths. Some of the energy radiated by the elements is intercepted by the structure and scattered, causing sidelobes. This source of sidelobes is controlled by using smooth surfaces, rolled edges, and absorbers. Some of the energy that reaches other elements is scattered; some is absorbed and may be partially re-radiated. Some

methods of controlling this source of sidelobes are non-systematic and excruciating. They require some degree of customization of each element in the array or the beam forming network feeding the array. Several design and construction iterations may be required. For antennas operating at microwave frequencies the controlling dimensional differences can be small and the corresponding tolerances can be very tight.

The method described here seeks to simplify and improve array control by using a number of identical elements constructed to close tolerances. Traditional methods would develop an analytical model of coupling to change the design of each element or output of the beamforming network. The method described here for receive array antennas uses an analytical model of coupling to implement a compensation algorithm in a digital processor. If the digital method of coupling compensation did not perform better than traditional methods it might not be worth the effort. However it appears that significantly better performance, approaching sidelobe levels 40 dB below isotropic, can be obtained using the methods described in this paper.

Our work follows earlier investigations of ultralow sidelobe techniques, notably that by Pettersson[1]. Pettersson used dipoles in his array while we are using slots. The advantages of using slots will be noted later. He used a small anechoic chamber to make his measurements and had to correct for the curvature of source fields in his calculations. We have a considerably larger compact range with an eight foot quiet zone. As this is being written we have a cylindrical near field scanner coming into operation. We hope to improve and/or increase confidence in the performance we have achieved.

## **2.0 Interelement Coupling**

Array antenna elements are designed to generate a particular radiation pattern when driven by specified currents at their input ports. However, if energy impinges from a neighboring element it may in general excite a different current distribution than when the given element is fed at its input port. As shown in Fig. 1, this will generate a scattering pattern which is different than the element's design radiation pattern. When this scattering is added into the radiated fields a

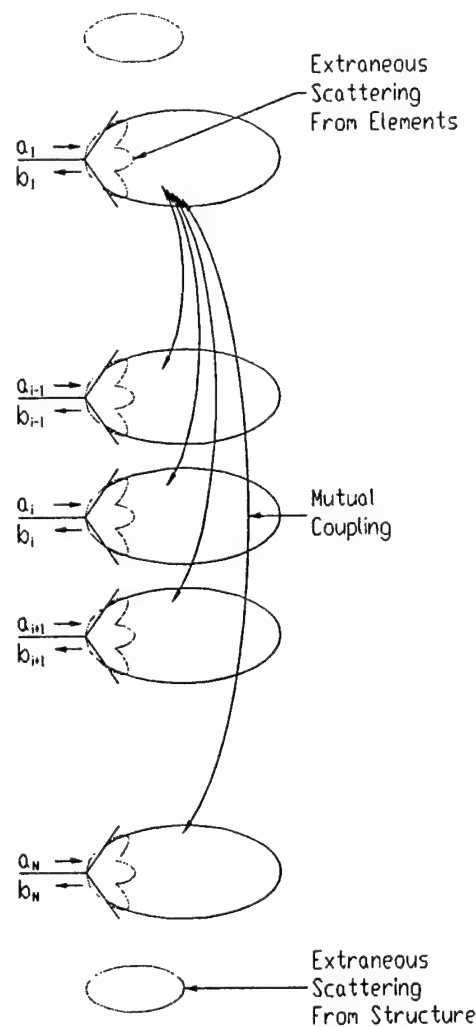


**Figure 1 - Sources of error in generating an array pattern**

distorted radiation pattern will be produced. On the other hand, if the scattering pattern is a scaled version of the radiation pattern, the sum of the scattering pattern and radiation patterns is another scaled version of the radiation pattern. Radiation patterns distorted by scattering patterns which are not scaled versions of the radiation patterns subvert the compensation technique described here. Therefore it is necessary to choose array elements which scatter with the same pattern as they radiate. With this condition met, excitation of any port of an N

element array will produce a total pattern which is the sum of a known radiation pattern and  $N-1$  known scattering patterns, the complex amplitudes of each yet to be determined.

A small dipole is an example of an element with radiation patterns and scattering patterns that are very nearly the same -- isotropic in the plane perpendicular to the dipole. A narrow slot is another candidate element. It is the magnetic current dual of a dipole and has dual pattern properties -- isotropic in the plane perpendicular to the long dimension of the slot.

### **3.0 Element Requirements**

The elements just described can be made "to disappear" by open circuiting the element at appropriate input ports. A small dipole will not effect its neighbors if the two arms are severed from each other. This is because the two arms have high reactance. The same effect occurs if an open circuit is placed in the feeding transmission line an integer number of half wavelengths away from the dipole. Similarly a slot can be made to disappear by placing a piece of copper tape across its middle or by placing an open circuit in the feeding transmission line an odd number of quarter wavelengths away. In practice there may a cavity behind the slot to couple energy from the transmission line to the slot, in which case the required position of the open circuit must be determined by experiment or analysis.

We chose a cavity-coupled, stripline-fed slot as the radiating element for our array. We made this choice because of the relative simplicity of etching identical slots as compared to constructing and positioning the dipoles identically. We also found it is easier to disable a slot with a piece of copper tape than to disable a dipole.

### **4.0 Array Antennas: Radiation and Reception**

For our application we need to compute the received voltage and current at each element in the array for an arbitrary incident plane wave field from given characteristics of the constituent elements and structure of the array antenna.

The correction of excitation of an array antenna by voltage sources with finite internal impedance which takes account of mutual coupling among the elementary antennas comprising the array in order to achieve a prescribed current

distribution is well known[2]. In particular, we will require:

- i) the location of the  $n$ th antenna element,  $\mathbf{r}(n)$ ,
- ii) the complex vector radiation pattern per unit input current to the  $n$ th antenna element in the open-circuited array environment,  $\mathbf{f}(n; \theta, \phi)$ . The vector direction of this (transmit) radiation pattern is taken parallel to the radiated electric far-field and dimensioned so that the magnitude-square is radiated power (watts/steradian/unit current),
- iii) mutual coupling among the array elements specified by the open-circuit impedance matrix,  $\mathbf{Z}$ , scattering matrix,  $\mathbf{S}$  or equivalent with respect to defined terminals at each antenna element, and
- iv) the termination or load at the terminals of each element.

For our purposes it will suffice to assume that the array antenna is comprised of identical elementary antenna elements with radiation pattern  $\mathbf{f}(\theta, \phi)$  of the "single mode"[3] or "canonical minimum scattering"[4] type. Such elements become invisible, i.e., do not scatter when an effective open-circuit is placed at appropriate terminal planes. For such elements the radiation pattern in the open-circuited array environment is the same as that of the isolated element. It follows from reciprocity arguments that an incident plane wave with electric vector equal to  $\mathbf{E}_{\text{INC}}$  at the origin of coordinates (located near or at one array element) produces the open circuit voltage,  $E(n)$  at the defined terminals of the  $n$ th array element

$$E(n) = j^4 \sqrt{\frac{\epsilon}{\mu}} 2\lambda \mathbf{f}(n; \theta, \phi) \cdot \mathbf{E}_{\text{INC}} \quad (1)$$

where

$$\mathbf{f}(n; \theta, \phi) = \mathbf{f}(\theta, \phi) \cdot \exp\{j\mathbf{k}(\theta, \phi) \cdot \mathbf{r}(n)\}. \quad (2)$$

The wave vector directed towards the source of the incident plane wave is

$$\mathbf{k}(\theta, \phi) = k[\mathbf{x} \sin \theta \cos \phi + \mathbf{y} \sin \theta \sin \phi + \mathbf{z} \cos \theta], \quad (3)$$

the position vector locating the  $n$ th array element is

$$\mathbf{r}(n) = \mathbf{x}\mathbf{x}(n) + \mathbf{y}\mathbf{y}(n) + \mathbf{z}\mathbf{z}(n), \quad (4)$$

and  $k=2\pi/\lambda$ .

The open-circuit voltages  $E(n)$  equal the respective generator voltages at the  $n$ th terminals of the Thevenin equivalent circuit for the array antenna in reception[5] shown in Fig. 2. Introducing matrix notation, we have

$$\mathbf{V} = \mathbf{E} + \mathbf{Z}\mathbf{I} \quad (5)$$

where  $\mathbf{V}$ ,  $\mathbf{E}$ , and  $\mathbf{I}$  are  $N$ -dimensional column matrices with elements  $V(n)$ ,  $E(n)$ , and  $I(n)$ , respectively.  $N$  is the number of elementary antennas in the array. When each array element is terminated in its own receiver module, the input impedance

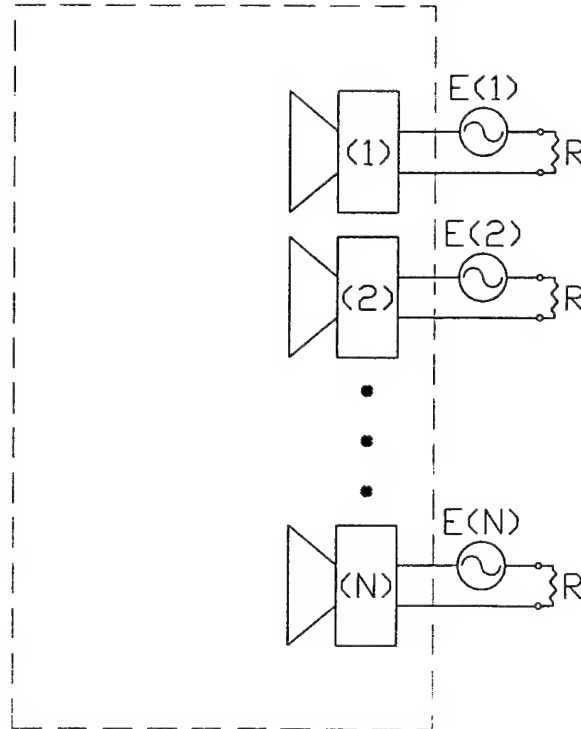


Figure 2 - Thevenin equivalent circuit for the array antenna in reception.

of which may be modeled as the resistance  $R$ , it is convenient to introduce incident (onto the array network) and reflected wave quantities  $a(n)$  and  $b(n)$

$$2\sqrt{R}a(n) = V(n) + RI(n) \quad (6)$$

$$2\sqrt{R}b(n) = V(n) - RI(n) \quad (7)$$

which are dimensioned so that the magnitude squares  $|a(n)|^2$  and  $|b(n)|^2$  are, respectively, the incident and reflected average powers. Like the voltages and currents, these are combined into column matrices  $\mathbf{a}$  and  $\mathbf{b}$  related by the normalized scattering matrix  $\mathbf{S}$ ,

$$\mathbf{b} = \mathbf{S}\mathbf{a} . \quad (8)$$

Substituting the expression for  $\mathbf{Z}$  in terms of  $\mathbf{S}$  into Eq. (5), we obtain

$$\mathbf{V} = \mathbf{E} + \mathbf{R}(\mathbf{I} - \mathbf{S})^{-1}(\mathbf{I} + \mathbf{S})\mathbf{I} . \quad (9)$$

We eliminate  $\mathbf{V}$  and  $\mathbf{I}$  in favor of  $\mathbf{a}$  and  $\mathbf{b}$ , the incident and reflected wave quantities. Upon proper termination of each element by a module with input impedance  $R$ ,  $\mathbf{a} = 0$ , and Eq. (9) becomes

$$\mathbf{b} = (\mathbf{I} - \mathbf{S})\frac{\sqrt{R}}{2}\mathbf{E} . \quad (10)$$

Evidently Eq. (10) may be solved to yield a matrix expression for  $\mathbf{E}$  as a function of  $\mathbf{b}$ , i.e.,  $\mathbf{E}(n)$  as a combination of all the  $b(n)$ ,

$$\frac{\sqrt{R}}{2}\mathbf{E} = (\mathbf{I} - \mathbf{S})^{-1}\mathbf{b} . \quad (11)$$

This is the desired result. In contrast to the phases of the  $b(n)$  or  $V(n)$ , the phases of the  $E(n)$  are directly the phases  $\mathbf{k}(\theta, \phi) \cdot \mathbf{r}(n)$  from which the direction of the source of the incident wave is evident. The matrix on the right which converts the observable  $b(n)$  into the theoretical  $E(n)$ , the terminal voltages that would be observed with zero antenna currents (with an ideal voltmeter) undistorted by mutual coupling, is "the correction" matrix. In principle the scattering matrix could be measured and the correction matrix computed from that result. However, once the existence of a correction matrix has been established as above, a less direct procedure described in §5.0, utilizing an overcomplete (or redundant) set of measurements produces a best value for the correction matrix in the sense of least squares. The advantages of the latter technique will be pointed out below.

### 5.0 Calculating the Correction Matrix Using an Overcomplete set of Measurements

From §4.0 we know there exists a correction matrix  $\mathbf{C}$  which will transform a set of excitations of the radiation patterns in a terminated array environment to an equivalent set of excitations of radiation patterns in an open circuit environment.  $\mathbf{C}$  can be found from the mutual coupling matrix of the array by:

$$\mathbf{C} = (\mathbf{I} - \mathbf{S}')^{-1} \quad (12)$$

where  $\mathbf{S}'$  is the transformed mutual coupling matrix of the array. The transformation is from the measurement terminal plane to an open circuit terminal plane if they are different.

Alternatively  $\mathbf{C}$  can be found statistically from the element radiation patterns. The matrix  $\mathbf{C}$  which is found this way is the best mapping of element radiation patterns in a terminated array environment to element radiation patterns in an open circuit array environment in a least squares sense. The matrix manipulations to perform a least squares fit employ the pseudo-inverse[6]. The result is the coefficient matrix for the linear equations connecting a data set comprising many more corresponding values of the input and output variables than the rank of the coefficient matrix.

The pseudo-inverse method is based on measurements of the phasor radiation patterns of each of the elements in the terminated array environment.



Here it is assumed that the number of angular increments in the pattern measurements,  $M$ , is considerably larger than the number of elements in the array,  $N$ . The measured radiation patterns are collected into an  $N \times M$  matrix  $\mathbf{M}$  where each row of the matrix corresponds to an element and each column of the matrix corresponds to an angular position.

The next step is to construct an exactly corresponding  $N \times M$  matrix  $\mathcal{J}$  of phasor radiation patterns of elements in the open circuit array environment. The patterns in  $\mathcal{J}$  can be either measured or calculated. If the patterns in  $\mathcal{J}$  are measured by rotating the receiving antenna, care must be taken to insure that each element follows the same path around the center of rotation as it did when its pattern was measured in the array environment. If the patterns in  $\mathcal{J}$  are calculated, the variation in phase caused by the displacement between the element center and the center of rotation must be accounted for. We always calculated  $\mathcal{J}$ .

From the previous discussion of mutual coupling, we know that a correction matrix  $\mathbf{C}$  can be found such that

$$\mathcal{J} = \mathbf{C}\mathbf{M} \quad (13)$$

If  $\mathbf{M}$  and  $\mathcal{J}$  were square matrices it would be a straightforward exercise to post-multiply both sides of Eq. (13) by  $\mathbf{M}^{-1}$  and solve for  $\mathbf{C}$ . Instead we must use the pseudo-inverse of  $\mathbf{M}$ . The pseudo-inverse of  $\mathbf{M}$  is found by noting that

$$\mathbf{M}\mathbf{M}^\dagger(\mathbf{M}\mathbf{M}^\dagger)^{-1} = \mathbf{1}$$

where  $\mathbf{M}^\dagger$  is the complex transpose of  $\mathbf{M}$  and  $\mathbf{1}$  is the unit matrix. The pseudo-inverse of  $\mathbf{M}$  then is given by

$$\mathbf{M}^\dagger(\mathbf{M}\mathbf{M}^\dagger)^{-1}$$

Finally the correction matrix is found by multiplying both sides of Eq. (13) by the pseudo-inverse of  $\mathbf{M}$

$$\mathbf{C} = \mathcal{J}\mathbf{M}^\dagger(\mathbf{M}\mathbf{M}^\dagger)^{-1} \quad (14)$$

## 6.0 Simulated Single Element Results

We used a commercially available method of moments code[7] to design a stripline-fed cavity-coupled slot radiator for our experimental array. However it developed that the simulation of 16 such slot radiators was too large for the capacity of the computer available to us. In lieu of slot radiators we modeled a substantially similar 16 element coplanar waveguide dipole array. A coplanar waveguide dipole is similar to a slot radiator, but the gain is 3 dB less because it radiates both above and below the ground plane.

The method of moments code simulates an idealized environment. All ground planes and dielectric layers in the simulation extend to infinity so there is no reflection or diffraction from the edges of the antenna. The results of the simulation agreed well with our theoretical expectations and were used to establish limits of what we might expect to obtain experimentally.

A coplanar waveguide dipole is shown in Fig. 3a. The dipole is oriented parallel to the y axis. Its radiation pattern in the  $\phi=0$  plane is shown in Fig. 3b. Note that we have used simply  $(-\theta)$  in place of  $(\theta, \phi=180^\circ)$  and that the radiation pattern in the plane perpendicular to the dipole is not quite isotropic. Rather it is slightly distorted by the feed line. The impedance of a single coplanar waveguide dipole is shown in Fig. 3c on an expanded Smith chart.

Fig. 4a shows a diagram of a coplanar waveguide dipole in of a 16 element array. All the dipoles are oriented parallel to the y-axis. One dipole is driven while all other elements are terminated in matched loads. This is an example of what we refer to as the "terminated array environment". Fig. 4b shows its radiation pattern in the  $\phi=0$  plane. Fig. 4c shows the impedance of the single element in a terminated array environment. By design, it is matched at the resonant frequency.

Fig. 5a shows another 16 element array of coplanar waveguide dipoles, all parallel to the y axis. The eighth element is driven while all the others are reactively terminated. The terminations are implemented with short circuited quarter wavelength stubs. Fig. 5b shows the radiation pattern in the  $\phi=0$  plane and Fig. 5c shows the impedance. Both show that the driven element is strongly affected by its neighbors. This is a counter example of what we call the "open circuit array environment." An open circuit must be placed at prescribed points in the transmission line to disable the element, in this instance placing a virtual short circuit right at the element.

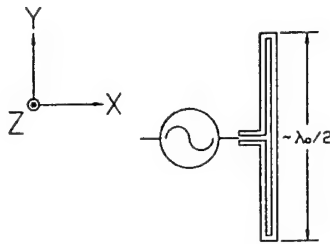


Figure 3a - Dimensions of Isolated Coplanar Waveguide Dipole.

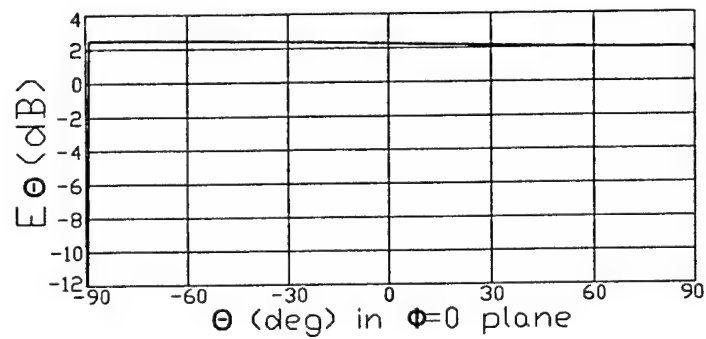


Figure 3b - Radiation Pattern of Isolated Coplanar Waveguide Dipole.

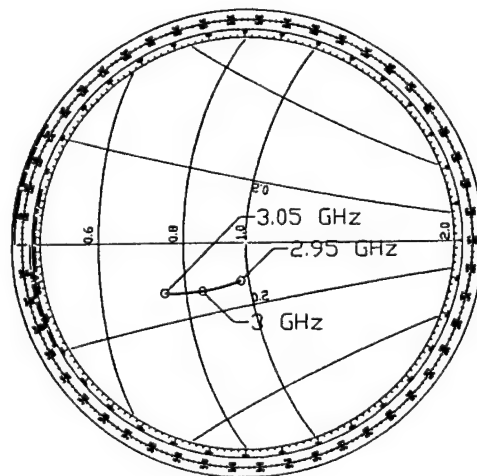


Figure 3c - Impedance Plot of Isolated Coplanar Waveguide Dipole.

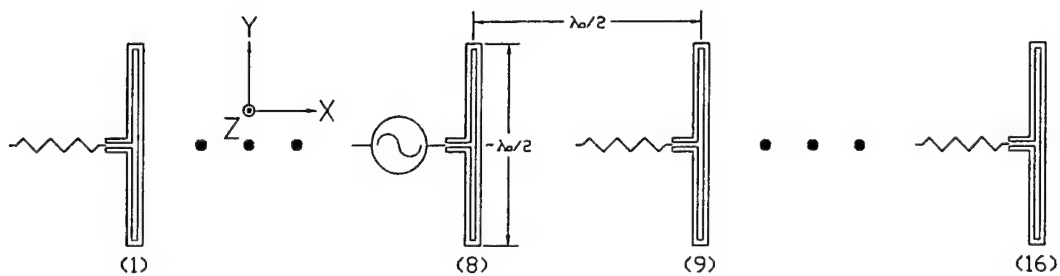


Figure 4a - Dimensions of coplanar waveguide dipole in terminated array environment.

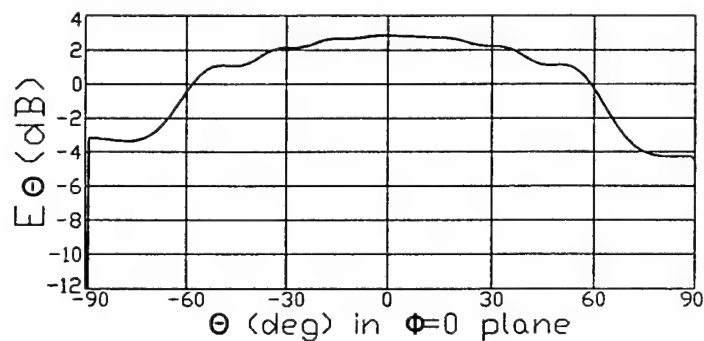


Figure 4b - Radiation pattern of coplanar waveguide dipole in terminated array environment.

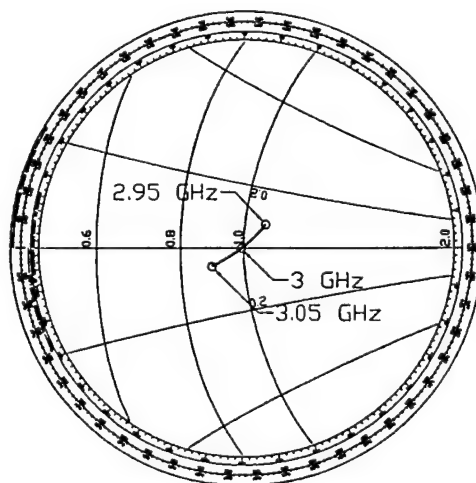


Figure 4c - Impedance plot of coplanar waveguide dipole in terminated array environment.

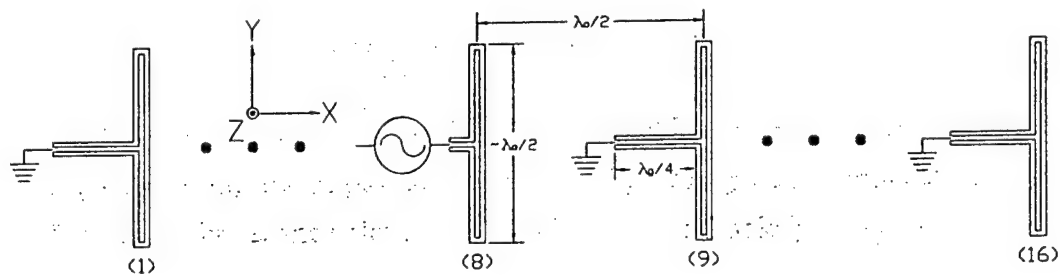


Figure 5a - Dimensions of coplanar waveguide dipole in open circuited array (counter example of open circuit array environment).

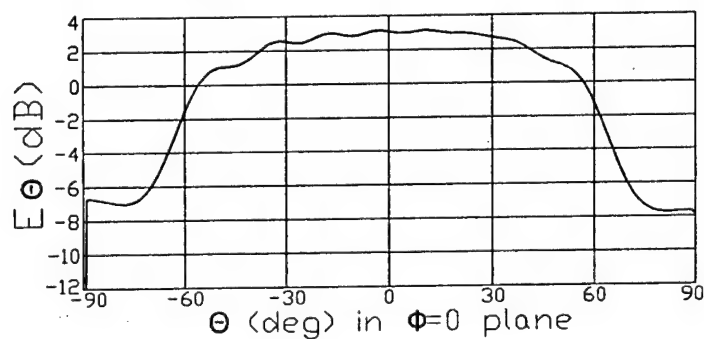


Figure 5b - Radiation pattern of coplanar waveguide dipole in open circuited array (counter example of open circuit array environment).

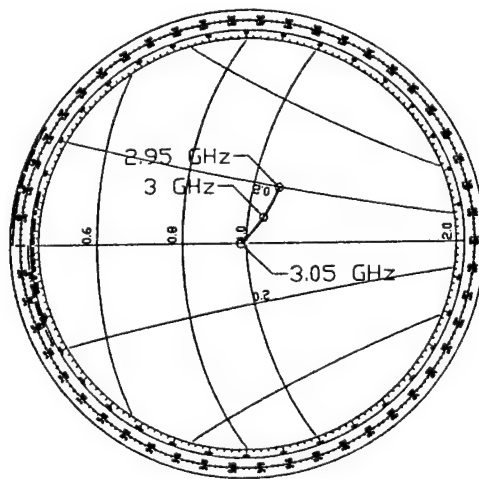


Figure 5c - Impedance plot of coplanar waveguide dipole in open circuited array (counter example of open circuit array environment).

Fig. 6a shows yet another excitation of the 16 element array of coplanar waveguide dipoles, all parallel to the y axis. The eighth element is driven while all the others are short circuited. The short circuits are virtual, having been implemented with open circuited quarter wavelength stubs. Fig. 6b shows the radiation pattern in the  $\phi=0$  plane and Fig. 6c shows the impedance. They are almost identical to the radiation pattern and impedance of the isolated element. This demonstrates the concept of disabling an array element with an appropriately placed open circuit as described in §3.0 and is an example of what we refer to as "open-circuited array environment." The effect is very good but not perfect. Of course a virtual short circuit is also frequency dependent. To make the neighboring elements completely disappear they must be covered (short-circuited) with copper tape.

## 7.0 Simulated Array Results

Another diagram of the simulated array of coplanar waveguide dipoles is shown in Fig. 7. It is similar to what was shown in Fig. 4a except that all elements are considered to be driven. A short circuited stub the same length as a dipole feed line is also shown in Fig. 7. It was simulated to determine its electrical length.

The 16 x 16 matrix of S-parameters for this array is shown on a polar chart in Fig. 8a for a frequency sweep from 2.95 GHz to 3.05 GHz is shown. The chart would be unreadable if every S-parameter was labeled. Instead families of S parameters are labeled. The elements on the main diagonal of the matrix are labeled " $m-n=0$ ", the elements on the first diagonal above or below the main diagonal are labeled " $m-n=\pm 1$ ", and the elements of the second diagonal above or below the main diagonal are labeled " $m-n=\pm 2$ ". Elements on higher order diagonals which tend towards zero are not labeled. For this array the coupling to neighboring elements is greater than the self reflection coefficient. The reflection coefficient of the short circuited stub is also shown on the chart. Its angle, which differs from the idealized value,  $\pi$ , was used to determine how far to transform reference planes of the S-parameter matrix to move to a terminal plane of an open-circuited array environment.

The S-parameter matrix transformed to a reference plane corresponding to an open circuited array environment is shown in Fig. 8b. The transformed S-parameter matrix subtracted from the unit matrix is shown in Fig. 8c. The correction matrix is shown in Fig. 8d. This was obtained by inverting the matrix shown in Fig. 8c.

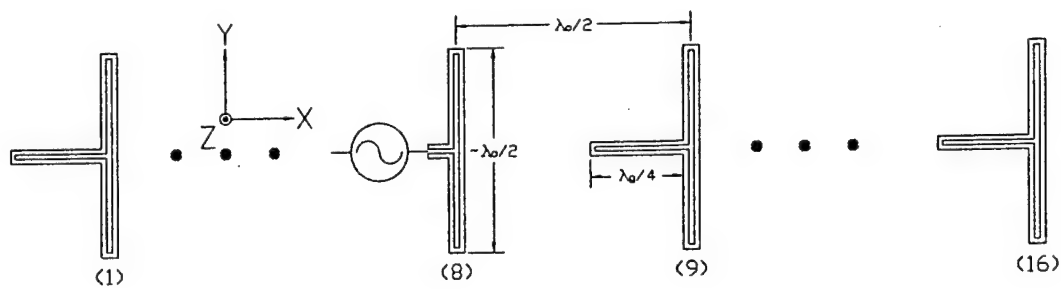


Figure 6a - Dimensions of coplanar waveguide dipole in open circuited array environment (short circuit at coplanar waveguide dipole).

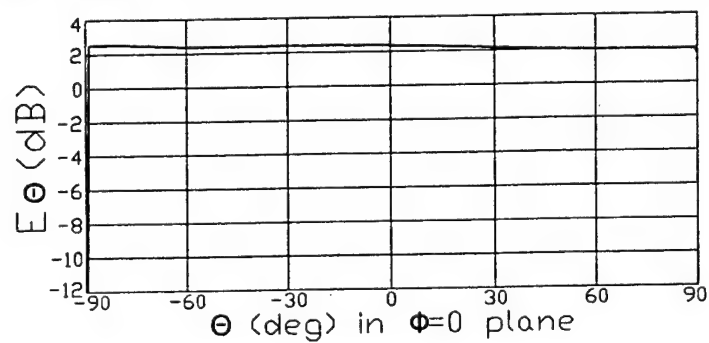


Figure 6b - Radiation pattern of coplanar waveguide dipole in open circuited array environment.

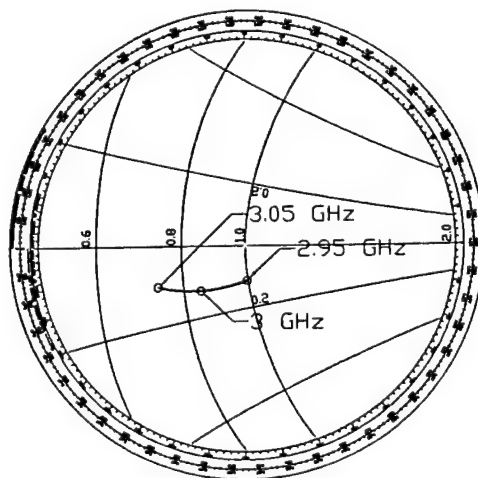


Figure 6c - Impedance plot of coplanar waveguide dipole in open circuited array environment.

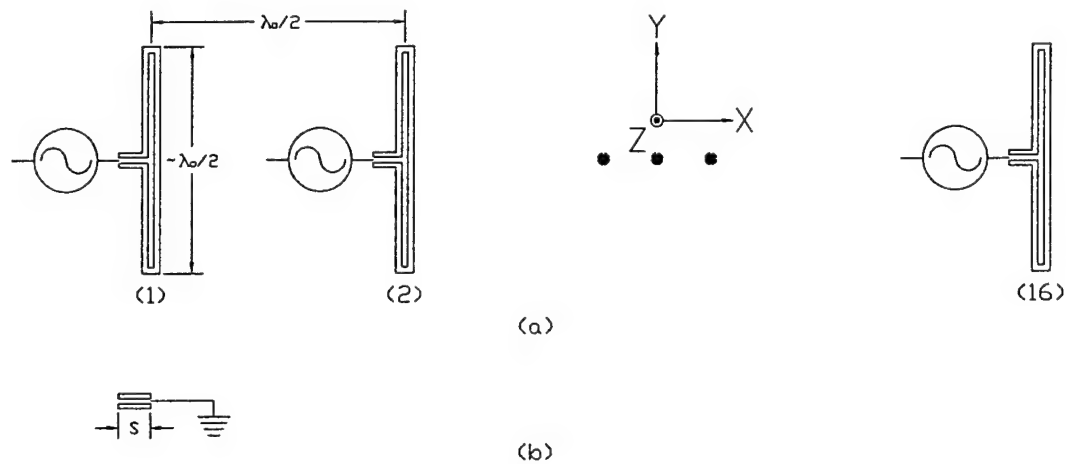


Figure 7 - (a) Configuration of full driven coplanar waveguide dipole array and (b) short circuited stub used to determine electrical length of feed line.

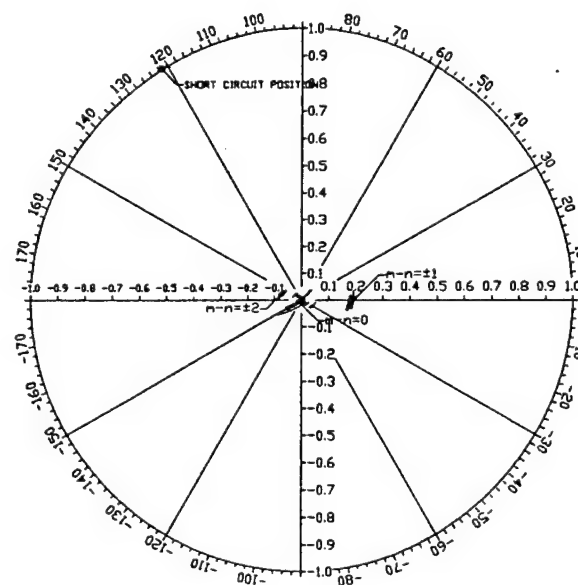


Figure 8a - Mutual coupling matrix of array shown in Fig. 7. Electrical length of feed line is also shown.



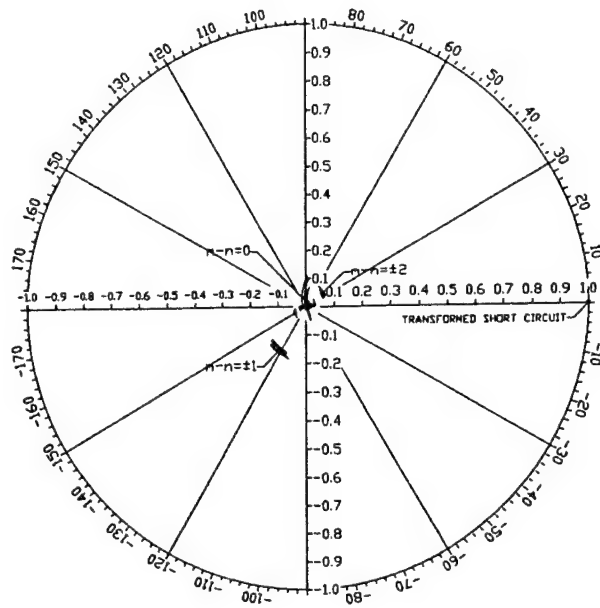


Figure 8b - Transformed mutual coupling matrix.

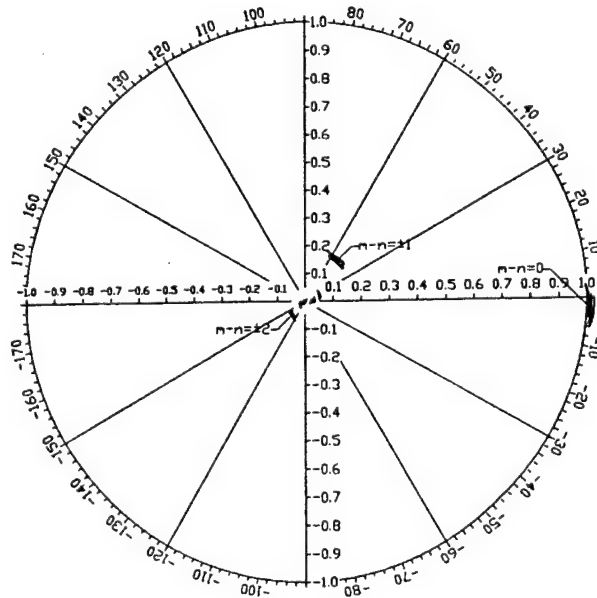


Figure 8c - Transformed mutual coupling matrix subtracted from unit matrix

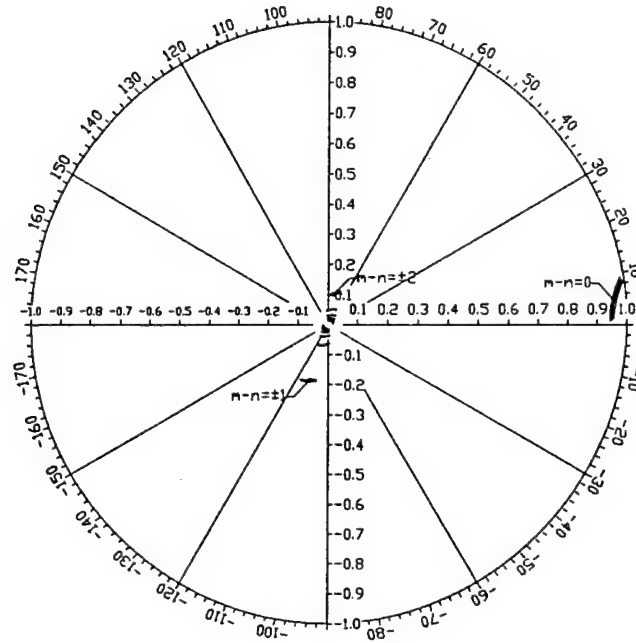


Figure 8d - Correction matrix, inverse of matrix in Fig. 8c.

Figs. 8a-8d show the matrix operations implied by Eq. (12). The diagonal elements are clustered near  $(1 + j0)$  while the off diagonal elements approach zero as they get further from the diagonal. This plot indicates what we would expect: if the elements are only moderately coupled, the correction to a desired input distribution is small.

## 8.0 Applying the Correction Matrix Calculated Using Mutual Coupling

The unnormalized scalar radiation pattern  $F$ , in the  $\phi=0$  plane, of an array with equally spaced elements, isotropic in  $\theta$ , is given by

$$F = \sum_n w_n \exp\{jnkd(\sin \theta - \sin \theta_0)\} \quad (15a)$$

where  $w_n$  is the amplitude of the  $n$ th source,  $k$  is the wavenumber,  $n$  is the element number, and  $d$  is the distance between elements.  $\theta$  is the pattern direction and  $\theta_0$  is the scan direction with reference to the normal of the array. This equation is commonly used without consideration of mutual coupling. In matrix form Eq.

(15) becomes

$$F = \sum_n w_n \mathcal{J}_{n,m} \exp(-jnkd \sin \theta_0) \quad (15b)$$

where  $\mathcal{J}$  is the matrix of element patterns measured in an open circuit array environment form §5.0.

In the course of improving our antenna and measurement technique we needed a standard to judge our interim results. We chose a 60 dB sidelobe Chebychev pattern as our benchmark because that has sidelobes about 10 dB better than our goal for a 16 element array of isotropic radiators. We plotted these broadside patterns; ideal, uncorrected for mutual coupling, and corrected respectively,

$$F_I(\Theta(m)) = \sum_n w_n \mathcal{J}_{n,m}, \quad (16a)$$

$$F_{UC}(\Theta(m)) = \sum_n w_n M_{n,m}, \text{ and} \quad (16b)$$

$$F_C(\Theta(m)) = \sum_k w_n \left( \sum_k C_{n,k} M_{k,m} \right). \quad (16c)$$

Eq. (16a) follows directly from Eq. (15b) with  $\theta_0=0$ . Eq. (16b) is obtained from Eq. (16a) simply by substituting  $\mathbf{M}$  for  $\mathcal{J}$  with the recognition that we would obtain imperfect patterns. We interpreted the sidelobe level obtained from Eq. (16b) as a measure of the effect of mutual coupling, and, in the case of measured data, how good our antenna was. Eq. (16c) was obtained from Eq. (16b) by substituting  $\mathbf{CM}$  for  $\mathbf{M}$ . The sidelobe levels obtained from Eq. (16c) were interpreted as a measure of the errors which remained after correction. Fig. 9a shows the data from our simulation of the 16 element coplanar waveguide dipole array plotted per Eqs. (16a-16c) using  $\mathbf{C}$  calculated from mutual coupling (Eq. 12). The data obtained from simulation indicates our antenna is very good to begin with, so the correction appears to have only a small effect.

The application of Eqs (15a-15b) to scanning depends on whether the array is used to transmit or receive. In transmission, the beam is scanned to some angle  $\theta_0$  and the pattern is calculated or measured as a function of  $\theta$ . In reception a plane wave arrives at the array from a distant source at some angle  $\theta$ , and the

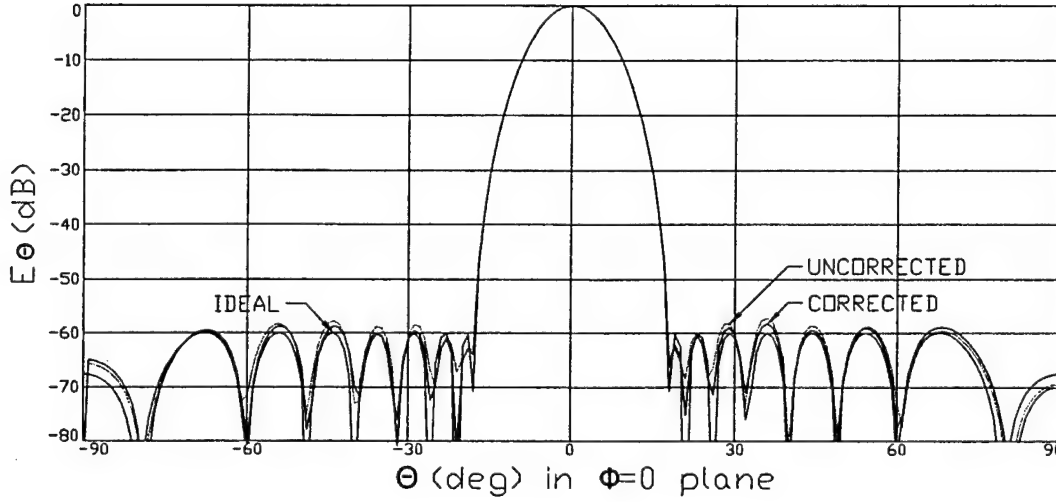


Figure 9a - Comparison of uncorrected and corrected radiation patterns with correction calculated using mutual coupling.

pattern is calculated or measured as a function of  $\theta_0$ . Our intended use for the array, and our development of the correction matrix  $\mathbf{C}$  here is for receive mode only. We calculated ideal, uncorrected, and corrected scan patterns for various angles of incidence  $\theta(m)$ , i.e. fixed  $m$ , using

$$F_I(\theta_0) = \sum_n w_n \mathcal{J}_{n,m} \exp(-jnk d \sin \theta_0), \quad (17a)$$

$$F_{UC}(\theta_0) = \sum_n w_n M_{n,m} \exp(-jnk d \sin \theta_0), \text{ and} \quad (17b)$$

$$F_C(\theta_0) = \sum_n w_n \left( \sum_k C_{n,k} M_{k,m} \right) \exp(-jnk d \sin \theta_0). \quad (17c)$$

Eq. (17a) follows directly from Eq. (15b) with the  $\theta_0$  functional dependence made explicit. Eq. (17b) was obtained from Eq. (17a) by substituting  $\mathbf{M}$  for  $\mathcal{J}$  and Eq. (17c) was obtained from Eq. (17b) by substituting  $\mathbf{CM}$  for  $\mathbf{M}$ . The data from our simulation of a coplanar waveguide dipole array, and with  $\mathbf{C}$  calculated from mutual coupling data are plotted per Eqs. (17a-17c) in Fig. 9b for  $\theta=30^\circ$

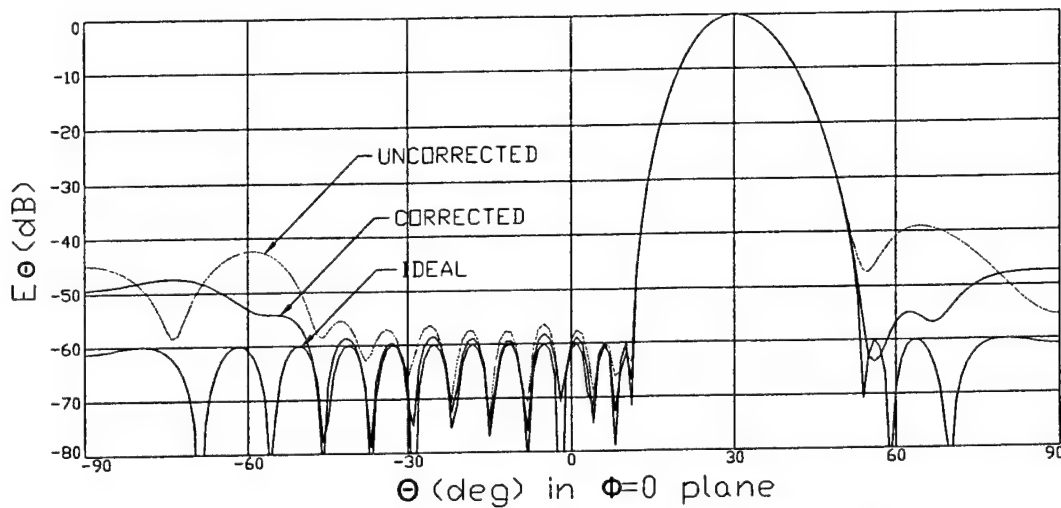


Figure 9b - Comparison of scanned radiation patterns for signal arriving at 30°. Correction calculated using mutual coupling.

Although it is not shown here, scan patterns for plane waves arriving at angles larger than 40° deteriorate quickly for large scan angles because of nearby grating lobes.

## 9.0 Applying the Correction Matrix Calculated Using the Pseudo-Inverse

Fig. 10 shows simulated data plotted per Eqs. (16b-16c) with  $C$  calculated from the pseudo-inverse and all other conditions the same as in Fig 9a. The patterns are nearly the same as those in Fig. 9a. Scanned patterns would be similar to those shown in Fig. 9b.

## 10.0 Comparison of Mutual Coupling and Pseudo-Inverse Methods

If the correction matrices calculated from mutual coupling,  $C_{MC}$  and the pseudo-inverse,  $C_{PI}$  were nearly identical it would be easy to compare them on an element by element basis, and the condition

$$C_{MC} C_{PI}^{-1} \cong 1$$

would hold. It would take a meticulous accounting for gain and phase in the pattern measurements to obtain the normalization to yield such good correspondence between  $C_{MC}$  and  $C_{PI}$ . However it would be reasonable to expect

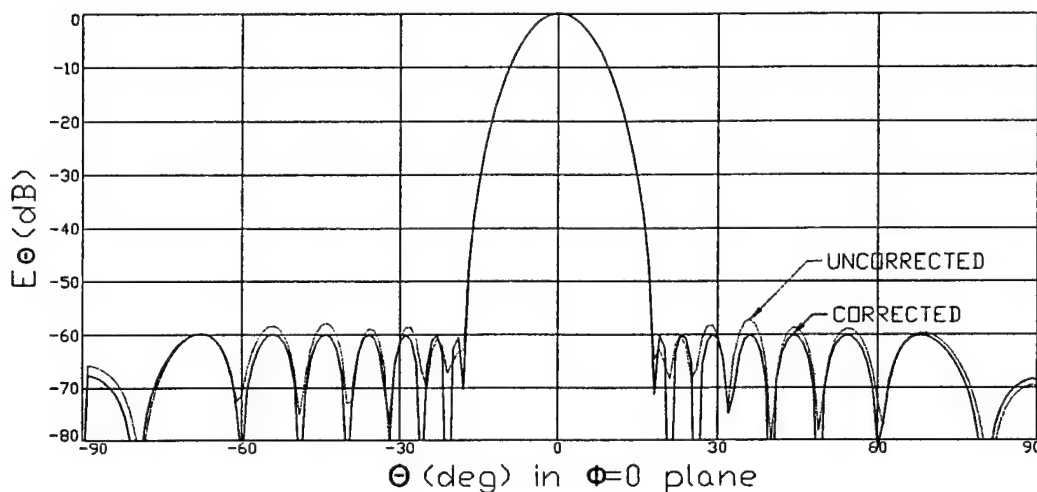


Figure 10 - Comparison of uncorrected and corrected radiation patterns. Correction calculated using pseudo-inverse.

that

$$\mathbf{C}_{MC} \mathbf{C}_{PI}^{-1} \cong \alpha \mathbf{1}$$

where  $\alpha$  is a complex constant. Fig. 11 shows a plot of  $\mathbf{C}_{MC} \mathbf{C}_{PI}^{-1}$  for our simulation. The diagonal elements are clustered around a point far from the origin which is what we expected. The off diagonal elements are clustered around zero. The degree that diagonal elements map to a non-zero point and the off diagonal elements map to zero is a measure of consistency between the two methods. There are a number of possible causes of inconsistency. The computational steps necessary to calculate and apply the correction matrix were numerically intensive which allows many chances for round off errors to creep in. Many calculations used large matrices, and some could have been ill conditioned. Isotropic radiation patterns were used to construct  $\mathcal{J}$ , but as shown in Fig. 3b, the isolated element pattern had about one half dB variation. There was some uncertainty in the length of the open circuit stub which disabled the coplanar waveguide dipole. For the model shown in Fig. 6a we initially chose the open circuit stub length to be one fourth wavelength from the geometric center of the dipole. There is a slight ripple

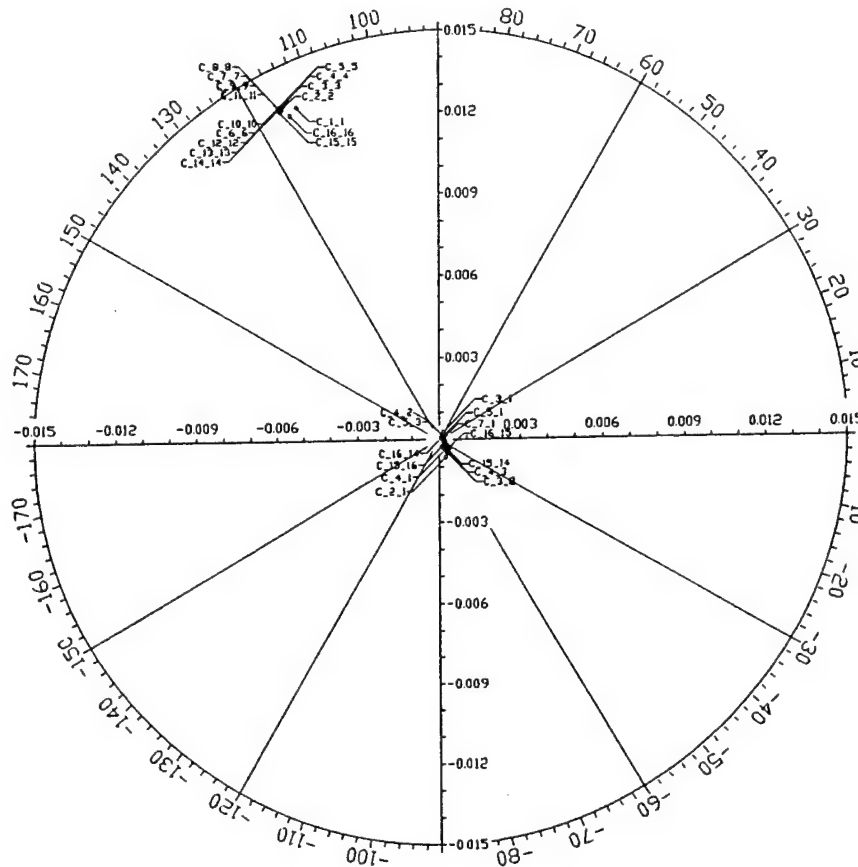


Figure 11 - Matrix product  $C_{MC}C_{PI}^{-1}$ .  $C_{MC}$  and  $C_{PI}$  calculated from simulation data.

in the element pattern shown in Fig. 6b. We found that increasing the open circuit stub length a fraction of a percent reduced but could not eliminate the ripple. The inability to eliminate the ripple can also be viewed as a departure from the "single mode" condition.

### 11.0 Experimental Antenna

The array antenna used in this investigation is drawn in Fig. 12. The array consisted of 16 columns and each column consisted of 4 slot elements arrayed in the H-plane. The column spacing was chosen to be exactly one half wavelength, while the element spacing within each column was 0.9 wavelengths. The vertical spacing was chosen to maximize gain, while the horizontal spacing was chosen to avoid grating lobes when scanning.

Fig. 13a shows a stripline-fed cavity-coupled slot antenna, designed by Clouston and Evans[8], which we tried to use for an element. Their antenna featured a cavity with feeds on opposite sides of the slot 180° out of phase. There is some adaptability in this design. If the width of the cavity is

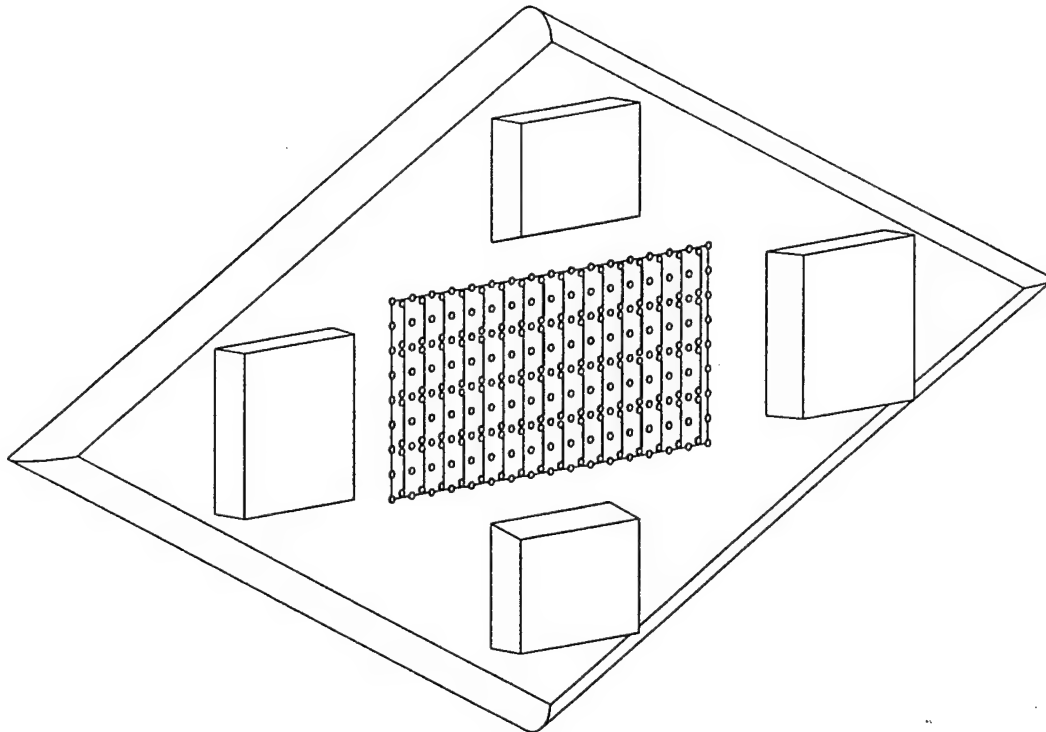


Figure 12 - NRL Ultra Low Sidelobe Array.

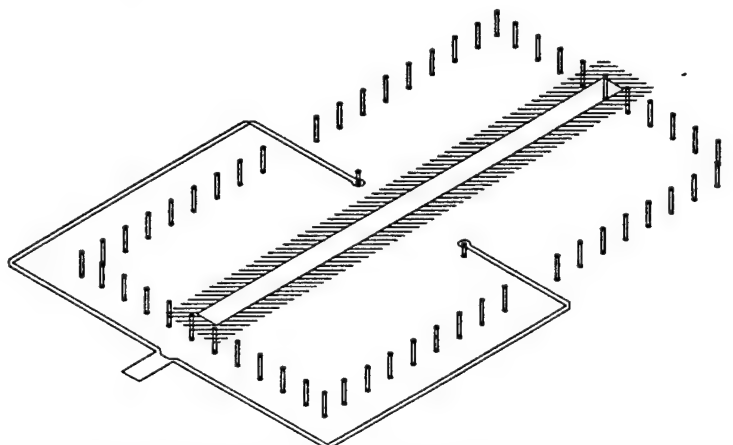


Figure 13a - Cavity coupled stripline feed slot antenna presented by Clouston and Evans



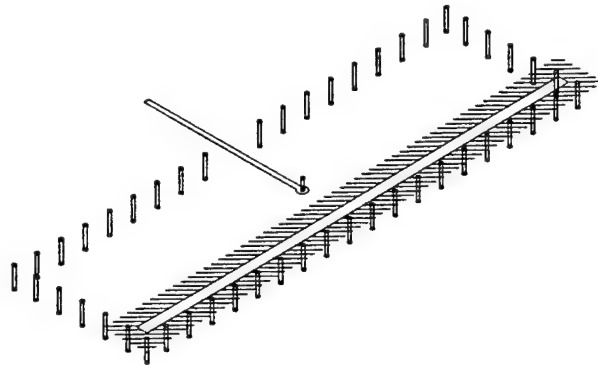


Figure 13b - Cavity coupled stripline feed slot antenna used in experimental array.

reduced, its length can be increased to maintain the resonant frequency. Even with this flexibility we could not fit it in the available space. However, we noted that there is a plane of anti-symmetry through the center of the slot so we split it in half along this plane to obtain the design shown in Fig. 13b. We were able to adjust the length and width of this design to resonate at the desired frequency while leaving room for a four way power divider in the space between columns.

The cavity is constructed with vias connecting the top and bottom grounds planes. The radiating slot is etched on one long side of the cavity and the stripline feed comes in from the middle of the opposite side. The feed line is shorted to the top ground plane only by a via, and the impedance is controlled by the position of the via with respect to the slot.

Referring back to Fig. 12, note the pattern of screw collars on the face of the array. They restrain but do not actually grasp the circuit boards. The screw collars were designed with narrow stems topped by wide flanges. The stems pass through holes in the circuit board and are about 0.002 inches longer than the thickness of the circuit board. This was done to keep from squeezing the dielectric, which might change the tuning of a cavity or alter the impedance of stripline. The pattern of screw collars is actually denser than needed to mechanically hold the circuit boards in place. Extra screw collars were added to insure that each radiator was surrounded by the same pattern of screw collars in its immediate neighborhood.

The diamond shaped ground plane shown in Fig. 12 was chosen to scatter

edge reflections away from the principal planes. Rolled edges were added to diffuse diffraction. We still detected interactions with the corners at high angles so we added patches of thick absorber between the slots and corners.

We measured the mutual coupling matrix for the antenna. The data from one such measurement is shown in Fig. 14. We quickly realized that even with a modern vector network analyzer it is difficult to measure mutual coefficients to the required level of accuracy. For this reason the pseudo-inverse method seems to be more practical.

With all the enhancements to pattern accuracy just described, the element radiation patterns of the NRL ultra-low sidelobe antenna were measured in a terminated array environment. The patterns were combined for uncorrected and corrected broadside patterns per Eqs. (16b-16c) with 60 dB Chebychev weighting. These patterns along with an ideal pattern calculated per Eq. (16a) are shown in Fig. 15a.

The correction matrix obtained in this way also "corrects" for residual errors in the compact range. It is therefore important to reduce any errors in the

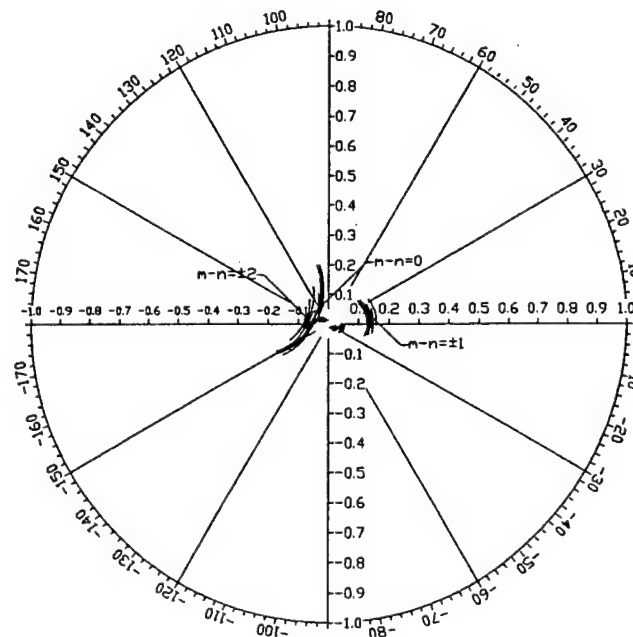


Figure 14 - Measured mutual coupling matrix for NRL ultra-low sidelobe antenna.

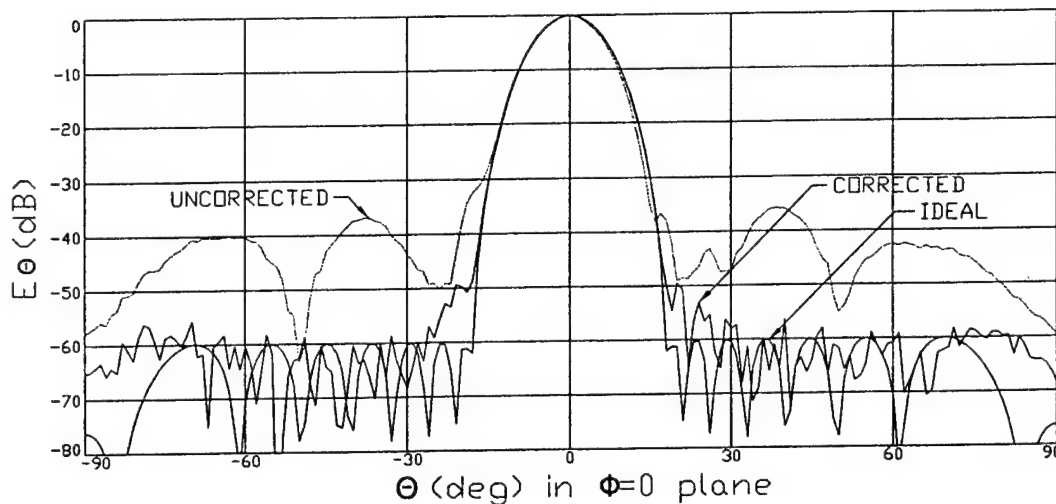


Figure 15a - NRL ultra-low sidelobe antenna measured patterns corrected using pseudo-inverse method.

compact range to an absolute minimum so that the correction matrix which is calculated will be applicable when the array is moved into other environments. To test the portability of our measurements we moved the antenna to a new position in the range one quarter wavelength closer to the source and repeated the measurements. Then we used the correction matrix calculated from the first set of measurements on the second set of measurements per Eqs. (16b-16b) with a 60 dB Chebychev weighting. The results are shown in Fig. 15b. We believe the increase in the sidelobe level is caused by residual reflections in the compact range.

The results presented so far were obtained using data measured sequentially from all sixteen columns. Sixteen digital receivers have been designed and built to measure the received signals of the columns simultaneously. A calibration technique has been developed to correct the amplitude and phase errors in the receivers. After all sixteen channels have been equalized, digital beamforming will be tested. When the digital receivers are incorporated into the array it will be possible to record many patterns quickly and improved calibration techniques may be developed.

## 12.0 Conclusion

We presented two different techniques to compensate for the effects of mutual coupling on the sidelobe level of an array. Both techniques require

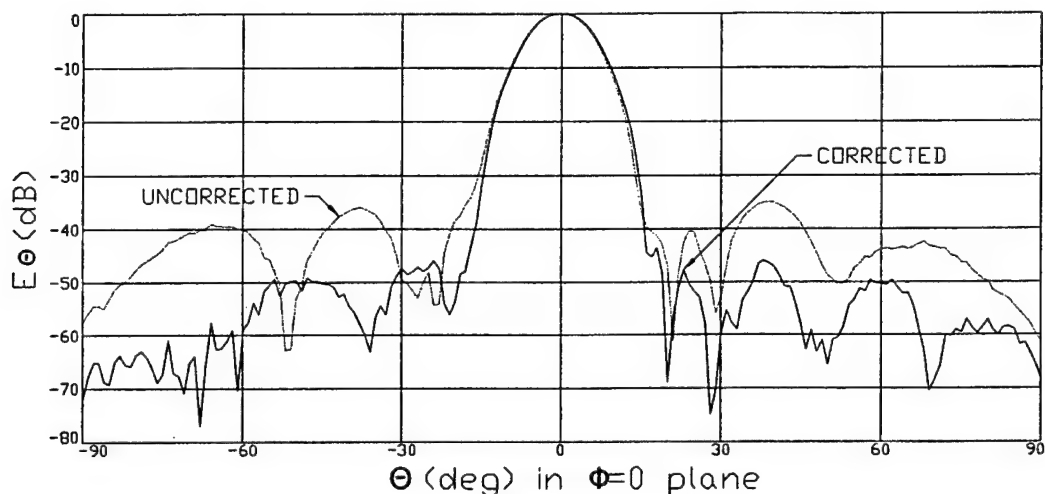


Figure 15b - NRL ultra-low sidelobe antenna moved one quarter wavelength from position of measurement shown in Fig. 14a. Correction matrix from first position applied to data from second position.

“single mode” type antenna elements. One technique uses electromagnetic calculation of the S-parameter matrix of the array while the other uses the measured far field element radiation patterns for calculating a correction matrix to compensate for mutual coupling. We applied both techniques to a simulated array and demonstrated that both work well in reducing the sidelobe levels. The two methods are linked. For “single mode” elements, information about mutual coupling is embedded in the element patterns measured in a terminated array environment. The technique that uses the element patterns seems to be more practical for use in a real array. Preliminary results, obtained using measured data, indicate that we can reduce the peak side level to better than 30 dB below isotropic, and the average sidelobe level to close to 40 dB below isotropic. These results do not include the effects of receiver errors.

### 13.0 Acknowledgments

Designing, building and testing the NRL ultra-low sidelobe antenna was truly a team effort that could not be accomplished without the help of many capable and dedicated individuals. John Valenzi, Mary Clare Herda, and Cliff Owen spent hours upon hours in the compact range taking patterns. They took patterns with copper tape, without copper tape, with loads and many variations.

They repeated the measurements in a tapered chamber. As this work is ongoing, data is now being taken with a cylindrical near field scanner.

Al Moffat painstakingly measured the mutual coupling matrix. He found all the type N loads in the Radar Division, and methodically tested every one to find the sixteen best for use in measuring the mutual coupling matrix.

This work was supported by the Office of Naval Research, Code ONR 31.

#### 14.0 References

- [1.] Pettersson, Lars, "An S-Band Digital Beamforming Antenna: Design, Procedures and Performance", FOA Defense Research Establishment, Linkoping, Sweden, Dec. 1999
- [2.] Kahn, W. K., "Impedance match and element pattern constraints for finite arrays," *IEEE Transactions on Antennas and Propagation*, vol. AP-25, pp. 747-755, November 1977.
- [3.] Borgiotti, G. V., "A novel expression for the mutual admittance for planar radiating elements," *IEEE Transactions on Antennas and Propagation*, vol. AP-16, pp. 329-333, May 1968.
- [4.] Kahn, W. K. and H. Kurss, "Minimum-scattering antennas," *IEEE Transactions on Antennas and Propagation*, vol. AP-13, pp 671-675, September 1965.
- [5.] Carlin, H. J. and A. B. Giordano, "Network Theory," Prentice-Hall, Inc., Englewood Cliffs, NJ.
- [6.] Sharf, L. L. "Statistical Signal Processing", Addison-Wesley Publishing Company, 1991
- [7.] Ensemble, Version 7, Ansoft Corporation, Four Station Square, Pittsburgh, PA
- [8.] E. N. Clouston and S. Evans, "A Triplate Stripline Slot Antenna Developed For Time-Domain Measurements on Phased Arrays", *IEEE Antennas and Propagation International Symposium Digest*, vol. 1, pp. 312-315, 1988.

# **KU BAND ACTIVE PHASED ARRAY ANTENNA FOR MOBILE DBS RECEPTION**

Cheol Sig Pyo, Jong Moon Lee, Young Keun Yoon, Won Kyu Choi, and Jae Ick Choi

Electronics and Telecommunications Research Institute (ETRI)  
161 Gajeong-dong, Yuseong-gu, Daejeon, 305-350, Korea  
[cspyo@etri.re.kr](mailto:cspyo@etri.re.kr)

**Abstract:** In this paper, a Ku-band active phased array antenna (APAA) using packaged monolithic microwave integrated circuit (MMIC) phase shifters was developed, which is used in vehicular antenna system for direct broadcasting satellite (DBS) reception at moving vehicles. Its design and performance were presented and described. It exhibits the antenna gain to noise temperature ratio (G/T) of 3 dB/K. The antenna beam is scanned electrically within  $46^{\circ} \pm 6^{\circ}$  in elevation.

## **1. Introduction**

A direct broadcasting satellite(DBS) service via Koreasat 3 is currently provided and there are many subscribers for a residential house. In addition, many people want to watch the DBS TV even at vehicles because it has advantages over terrestrial TV broadcasting with high quality, simultaneity, wide coverage, and so on. Several antenna systems for mobile DBS reception have been developed on the basis of various flat antennas mounted on vehicle's roofs[1,2,3]. The most attractive of these is an active phased array antenna technology. However, the conventional technology is very expensive, restricting its use in commercial products. To solve this, a modification in the phased array antenna is introduced using twelve active array elements for cost-effectiveness[4,5]. The system shows a high performance for receiving DBS, but is still expensive, large and tall to be

installed on a car due to low element gain, the connection loss between the radiator subarray and the active channel block (ACB), and the high cost phase shifter. Therefore, we have made a great effort to develop high efficiency radiator subarrays[6], to develop the low cost packaged monolithic microwave integrated circuit (MMIC) phase shifter, and have realized a small and low-profile active phased array antenna system mountable on a small car[7].

This paper describes the design of the active phased array antenna system and also presents experimental results. Section 2 describes the design of broadband circularly polarized patch array antenna with the corner-truncated square patch fed by a microstrip line and the stacked patch. Section 3 describes the design of the active phased array antenna using the low cost-packaged monolithic microwave integrated circuit (MMIC) phase shifter and presents the performance of the active phased array antenna, in which the antenna elements and the active circuitry are integrated on the same substrate. And then, introduces the integrated active phased array antenna system and presents its test results.

## 2. Broadband Circularly Polarized Patch Array Antenna

### 2.1 Design of the antenna element

Fig.1 shows the configuration proposed in order to obtain broadband circularly polarized single patch antenna[6]. The patch fed by a microstrip line and stacked patch are truncated to obtain circular polarization. This corner-truncated square patch has the two orthogonal modes of resonance, which respectively yield linear polarization along the directions of the two diagonal. To obtain good axial ratio, the feeding location is chosen to excite two modes in phase quadrature. As seen in the Fig. 1, lower patch and microstrip line are on the substrate with  $\epsilon_r=2.5$  and thickness=20mils, the stacked patch on the thin film is supported by lower foam, and this patch is covered by upper foam (thickness=2mm). Being very thin (0.04mm) with respect to wavelength, the film hardly affects radiation pattern. Based on the geometry shown in Fig. 1, the results of the simulation using ENSEMBLE 5.1 are shown in Fig. 2. A 10dB return loss bandwidth is 1.3GHz (11.2 – 12.5GHz[11%]), a 3dB axial ratio bandwidth is 0.7GHz (11.4 – 12.1GHz[6%]) and maximum gain is about 9.4dBic at 11.85GHz.

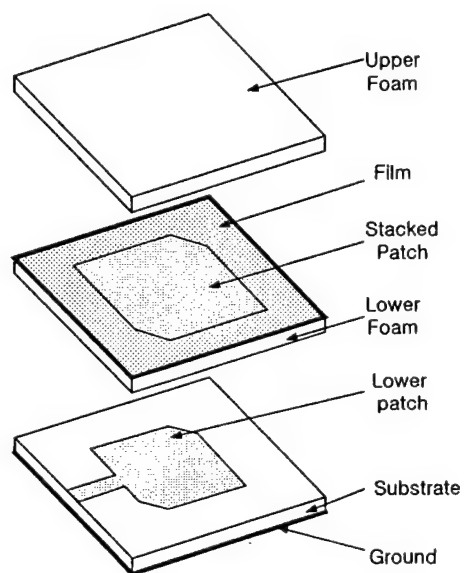


Fig. 1. Geometry of the single patch antenna

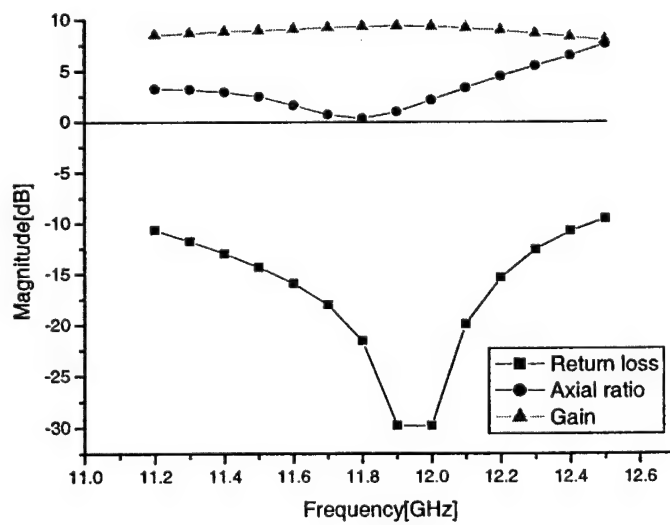


Fig. 2. Simulated results of the single patch



## 2.2 3x4 Radiator Subarray

The designed array structure is shown in Fig. 3. The distance between each patch is  $0.85\lambda_0$  and the array is designed using sequential rotation feed[6,7]. By using these sequential rotation feed, an antenna performance is better than that of single patch. The measured result compared with simulation is shown in Fig. 4. The maximum gain is 19.5 dBi and 3dB axial ratio bandwidth is 25% (9.8 GHz - 12.6 GHz). The simulated and experimental impedance bandwidths for VSWR < 2 are 15% (10.8 GHz - 12.55 GHz) and 15.2% (10.9 GHz - 12.7 GHz), respectively.

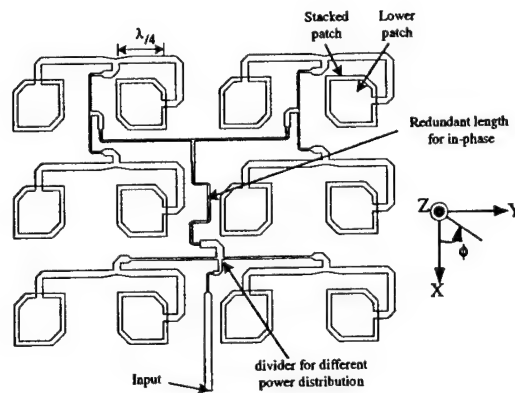


Fig. 3 Photograph of 3x4 subarray

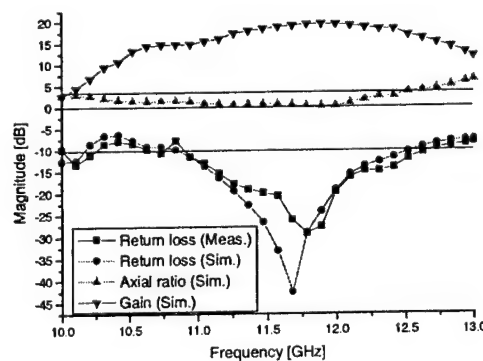


Fig. 4 Simulated and measured results of 3x4 subarray

The radiation pattern measured at 11.85GHz is shown in Fig. 5. The side lobe level is lower than -10dB and cross-pol level is lower than -25dB for broadside direction. The half power beamwidths (HPBW) are  $18.5^\circ$  in  $\phi=0$  plane and  $14.5^\circ$  in  $\phi=90$  plane, respectively.

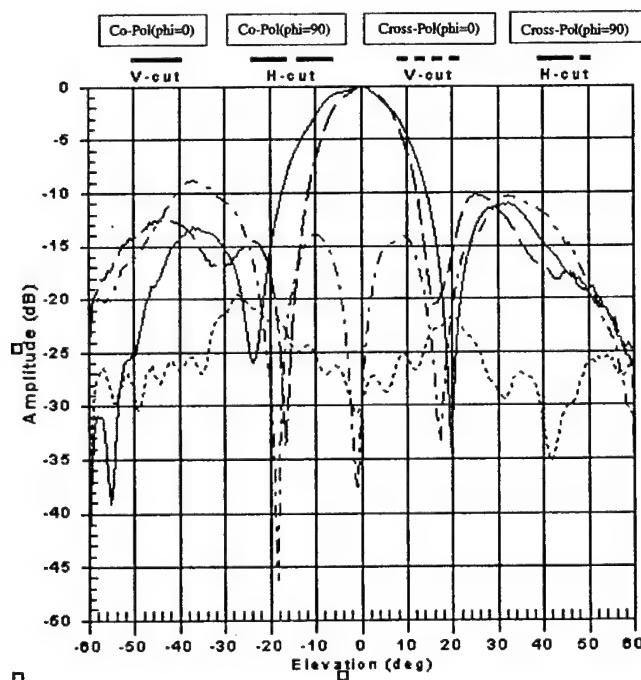


Fig. 5. Radiation pattern (meas.) of 3x4 subarray antenna (at 11.85 GHz)

### 3. Active Phased Array Antenna System

#### 3.1 Ku band MMIC phase shifter

A low cost, packaged 5-bit MMIC phase shifter shown in Fig. 5 has been successfully developed for Ku band mobile satellite communication applications. The MMIC chip with 5-bit digital control circuit shown in Fig. 6 was designed utilizing a 0.6 micron GaAs MESFET process technology and using via-hole technology to reduce inductance with ground, and packaged into ceramic package to prevent parasitic effects of the package.

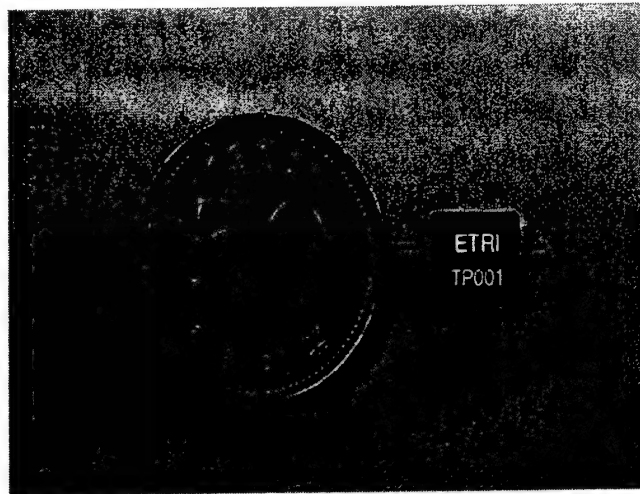


Figure 6. Photograph of a packaged MMIC phase shifter

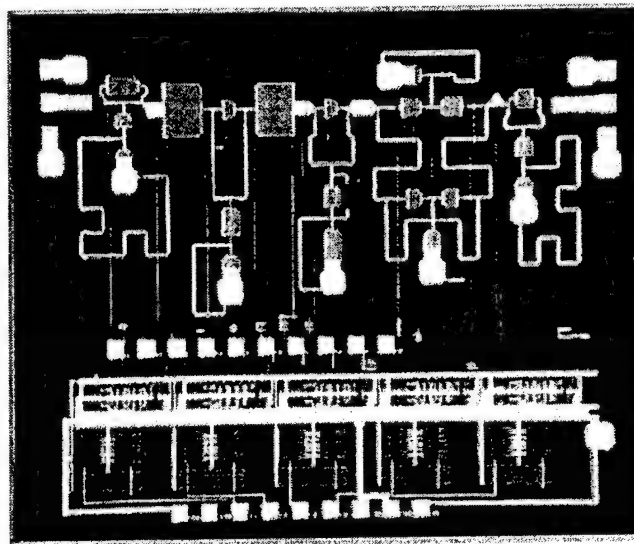
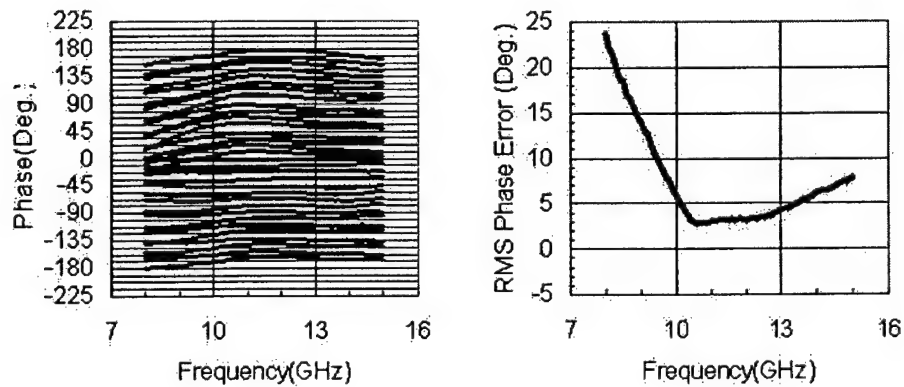


Figure 7. Photograph of the MMIC phase shifter chip layout

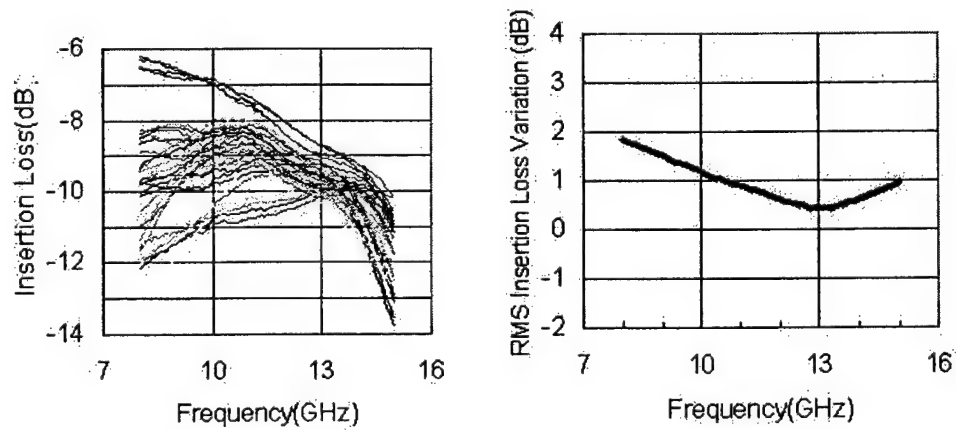
It exhibits low RMS phase error( $<5^\circ$ ) (Fig. 8), low insertion loss( $<10\text{dB}$ ) (Fig. 9), low RMS insertion loss variation( $<1\text{dB}$ ) (Fig. 9), and good return loss( $>9.5\text{dB}$ ) (Fig. 10) for all thirty-two phase states over the entire operational bandwidth in the  $10.7 \sim 12.75\text{ GHz}$  frequency range. It is easy to use because it has a user-friendly lead type of ceramic package and no external components is required. It will be commercialized soon and reduce the cost of implementing

phased array antennas for commercial use.



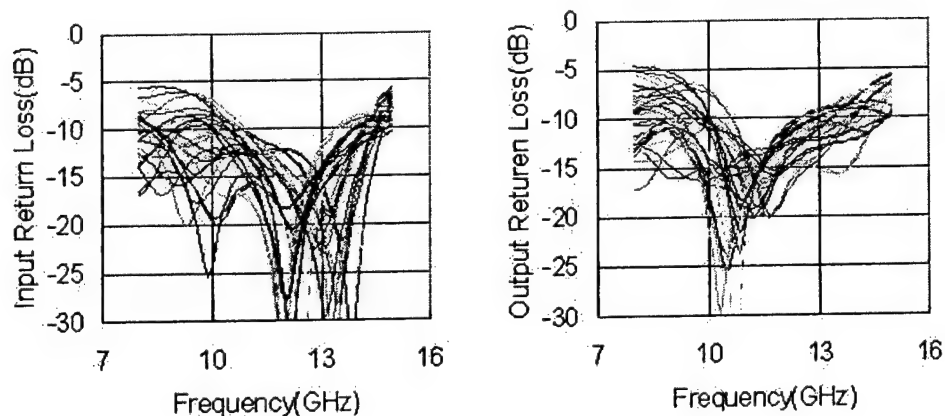
(a) Measured phase shift state (b) RMS phase error

Figure 8. Measured phase shift performance



(a) Measured insertion loss (b) RMS insertion loss variation

Figure 9. Measured insertion loss performance



(a) Input return loss

(b) Output return loss

Figure 10. Measured input/output return losses

### 3.2 Active Phased Array Antenna

The active phased array antenna consists of two active array modules arranged on the plane of the frame[7]. The active array module is composed of two active subarrays containing the microstrip patch subarray and the ACB, in which the devices such as low noise amplifiers(LNA) and MMIC phase shifters are integrated directly with the feeding network of radiating elements to improve the array performance on the same substrate (TLX-9, 20mil-thick,  $\epsilon_r=2.5$ ), and the subarrays are inclined at  $46^\circ$  to horizon. The developed active array module is shown in Fig. 11. The ACB performs the roles to amplify RF signal with low noise coming from the radiator and to form the beam for electronic beam scanning. The ACB is composed of the FETs, microstrip band pass filter (BPF), MMIC phase shifter, stabilized DC bias circuit, and the phase control interface part as shown in Fig. 12. By the design specification, the typical linear gain of the ACB is about 25 dB at initial phase state and its gain variation by phase control states is less than  $\pm 2$  dB, and the minimum phase control step is  $22.5^\circ$ . The phase response of the active channel block by each phase states was measured using a vector network analyzer and control program. The phase variation of it by phase control state was lower than  $\pm 5^\circ$  within operating band. Its typical noise figure is

0.8 dB.

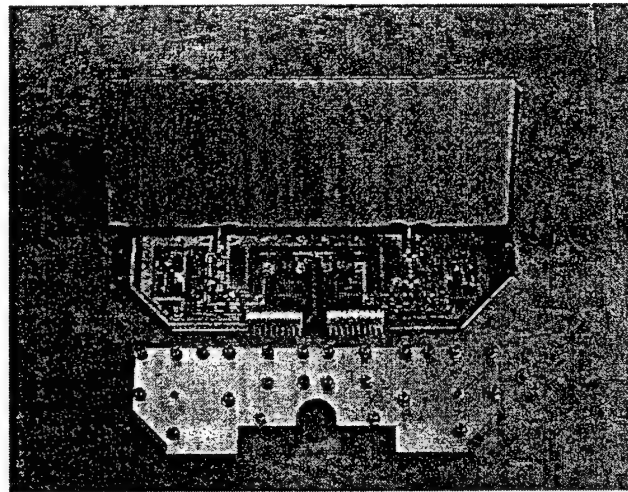


Fig. 11 Active array antenna module

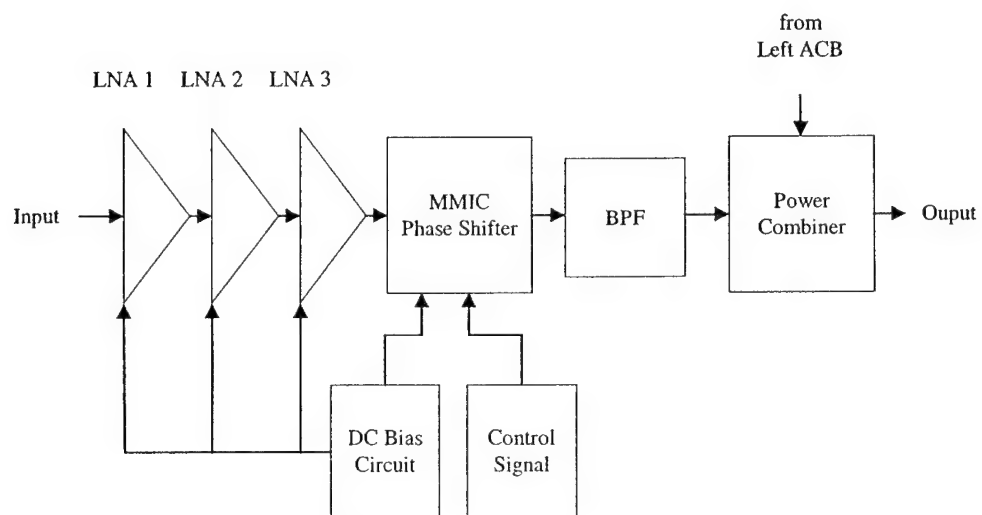


Fig. 12 Block diagram of ACB

### 3.3 Active Phased Array Antenna System

The integrated active phased array antenna system shown in Fig. 13 consists of two active array modules, a low noise block down converter, a beam steering controller, a tracking signal detector, a satellite tracking processor and a mechanical positioner[8]. Its size is 320(D) x 85(H) mm.

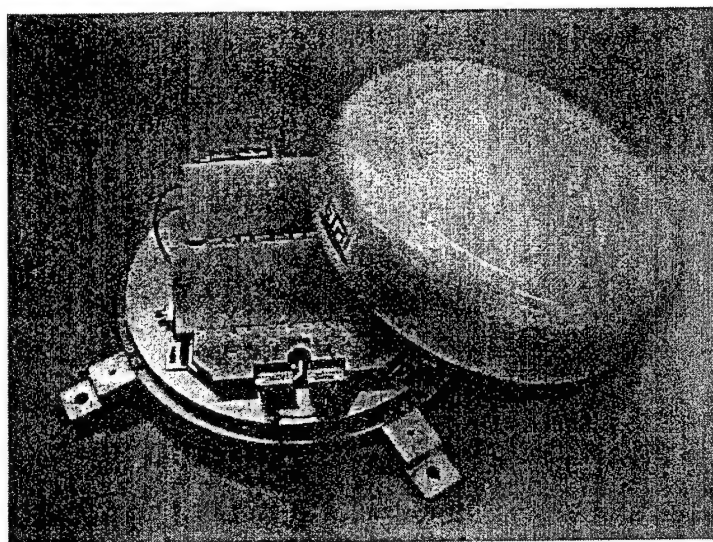
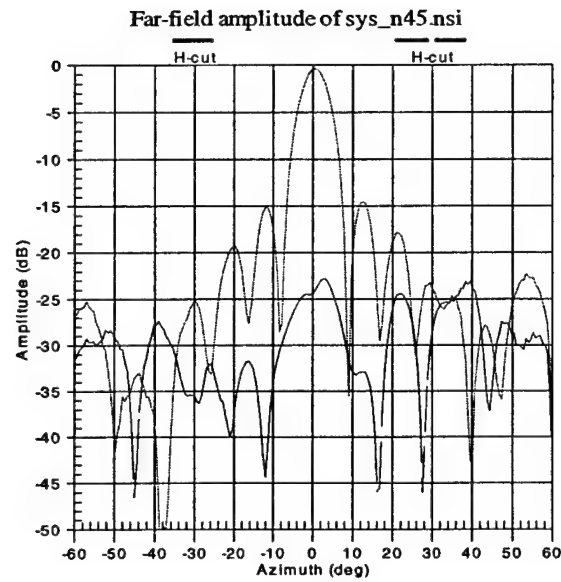
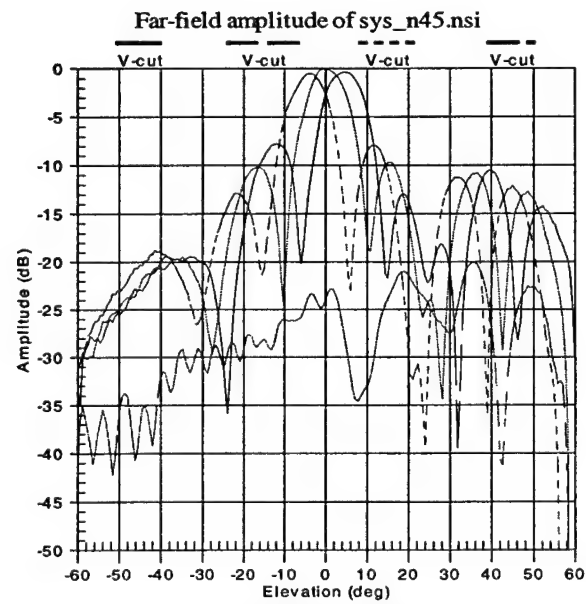


Fig. 13 Active phased array antenna system

The radiation patterns measured at 11.85 GHz are shown in Fig. 14. The side lobe level is lower than -10dB and cross-pol level is lower than -23dB for broadside direction. It provides  $46^{\circ} \pm 6^{\circ}$  electronic beam scanning in elevation. The carrier to noise power ratio (C/N) of the system was measured directly from DBS Koreasat 3 signal whose effective isotropic radiated power (EIRP) is 61 dBW at Daejeon and bandwidth is 21.3 MHz. It exhibits the C/N of about 13.8 dB as shown in Fig. 15. From the measured C/N, the system G/T can be calculated and it is about 3.0 dB/K when the free space loss is -205.4 dB and the atmospheric loss is -0.2 dB at clear sky.



(a) Azimuth plane



(b) Elevation plane

Fig. 14 Radiation patterns (meas.) of the antenna system (at 11.85 GHz)



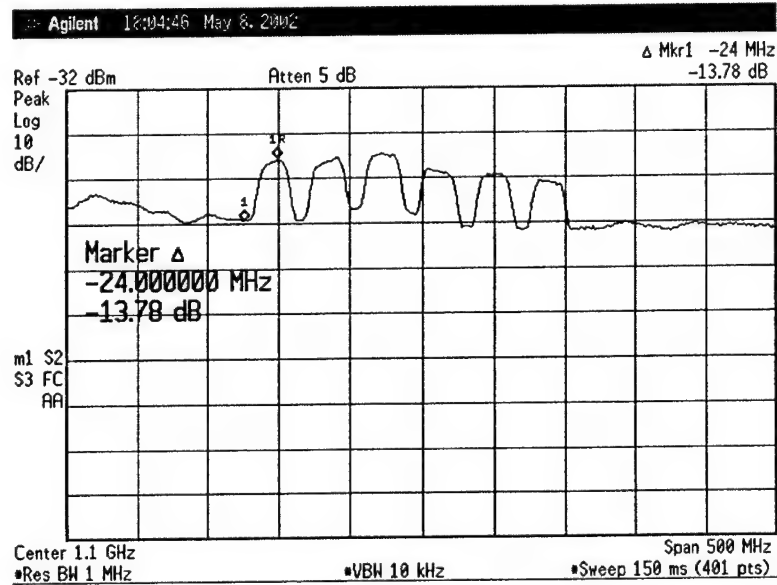


Fig. 15 Measured C/N of the system

#### 4. Conclusion

In this paper, the Ku-band APAA using the low cost-packaged MMIC phase shifters was developed, which is used in vehicular antenna system for DBS reception at moving vehicles. It exhibits the C/N of 13.8 dB from DBS Koreasat 3 whose effective isotropic radiated power (EIRP) is 61 dBW and bandwidth is 21.3 MHz. It provides the electronic beam scanning of  $46^\circ \pm 6^\circ$  in elevation. It is to be installed on a mechanical positioner which gives the mechanical beam steering of  $0^\circ \sim 360^\circ$  in azimuth. It will be combined with satellite tracking algorithm and verified by the moving vehicle test under various kinds of road conditions. The size and number of the active array module can be easily modified for various mobile multimedia service applications.

#### REFERENCES

- [1] K. Fujimoto, J.R. James, "Mobile Antenna Systems Handbook", Artech House, Inc., 1994.
- [2] Jiro Hirokawa, et al., "A Single-Layer Slotted Leaky Waveguide Array

Antenna for Mobile Reception of Direct Broadcast from Satellite," IEEE Trans. On Vehicular Technology, Vol.44, No.4, pp.749-754, Nov. 1995.

[3] S.I Jeon, et al., "Vehicular Active Antenna System with Combined Electronical and Mechanical Beam Steering for Reception from DBS in Ku-band", XXVII Moscow ICATT, Sept. 1998, pp. 72-77.

[4] S.I Jeon and D.G. Oh, "Active Phased Array Antenna for Mobile Multimedia Services via Satellite", 2000 Aerospace Conference, Vol.5, pp. 165-170, 2000.

[5] S.Y. Eom, Y.C. Moon, C.S. Pyo, C.G. Park, S.I. Jeon, D.C. Oh, "Design and Test of RACM in Ku-band Vehicular APAA System for DBS Reception", INTERNATIONAL CONFERENCE ON ELECTROMAGNETICS IN ADVANCED APPLICATIONS (ICEAA99), Torino, Italy, Sept. 1999, pp. 215-218.

[6] Wonkyu Choi, Cheolsig Pyo, and Jaeick Choi, "Broadband Circularly Polarized Corner-truncated Square Patch Array Antenna", 2002 AP-S International Symposium, San Antonio, June 2002, pp.220-223.

[7] J. M. Lee, W.K. Choi, C. S. Pyo, and J.I. Choi, "Ku-band Active Array Antenna Module for Mobile DBS Reception", to be published in the APMC 2002, November 19-22, 2002, Kyoto, Japan.

[8] C. S. Pyo, Y. G. Yoon, J. M. Lee, W.K. Choi, and J.I. Choi, "A LOW-PROFILE ACTIVE PHASED ARRAY ANTENNA SYSTEM FOR MOBILE DIRECT BROADCASTING SATELLITE RECEPTION", to be published in the 2002 Interim International Symposium on Antennas and Propagation, November 26-28, 2002, Yokosuka Reserach Park, Japan.

# **Overview of the Multifunction RF Effort – An Army Architecture for an Electronically Scanned Antenna**

**Steven Weiss, Robert Dahlstrom, Ozlem Kilic, Edward Viveiros, Steven Tidrow, Frank Crowne, Eric Adler**

***U.S. Army Research Laboratory***

**Sensors and Electron Devices Directorate (*SEDD*)**

***2800 Powder Mill Road, Adelphi, MD 20783***

***Tel. (301) 394-1987; Fax:(301) 394-5132: [sweiss@arl.army.mil](mailto:sweiss@arl.army.mil)***

**Abstract - A discussion of an Army's Architecture for an Electronically Scanned Antenna (ESA) array is presented. The antenna, suitable for integration into systems exploiting the Multifunction Radio Frequency (RF) concept, meets many of the needs for a Future Combat System (FCS) RF sensor. Many modular components of a first prototype for the ESA have been assembled and tested together and separately. Among the sub array components are a Rotman Lens (for azimuthal beamforming), ferroelectric true-time delay elements (for elevation beamforming), distributed MMIC (microwave and millimeter wave integrated circuits) amplifiers (for power and low-noise requirements), and separate aperture-fed patch antenna arrays (one for transmitting and one for receiving). The design was developed from a requirements standpoint such that a low profile ESA could evolve directly from the first prototype work. The final low profile version will keep the ESA amenable for non-obtrusive insertion on a variety of platforms. Various components of this antenna have been fabricated and tested and the results are presented.**

## **I. Introduction**

A multifunction sensor for an FCS sensor will need an ESA in order to rapidly and arbitrarily place the beam in a desired direction for the different radar and communication modes without moving parts [Figure 1]. A working ESA prototype [1] will demonstrate the feasibility of the multifunction RF concept. Using the initial (working) prototype as a baseline, subsequent versions can then have their architecture suitably modified to meet an objective ESA for FCS sensor requirements. These requirements include active and passive target acquisition, combat identification, active protection, command guidance, and secure point-to-point communications.

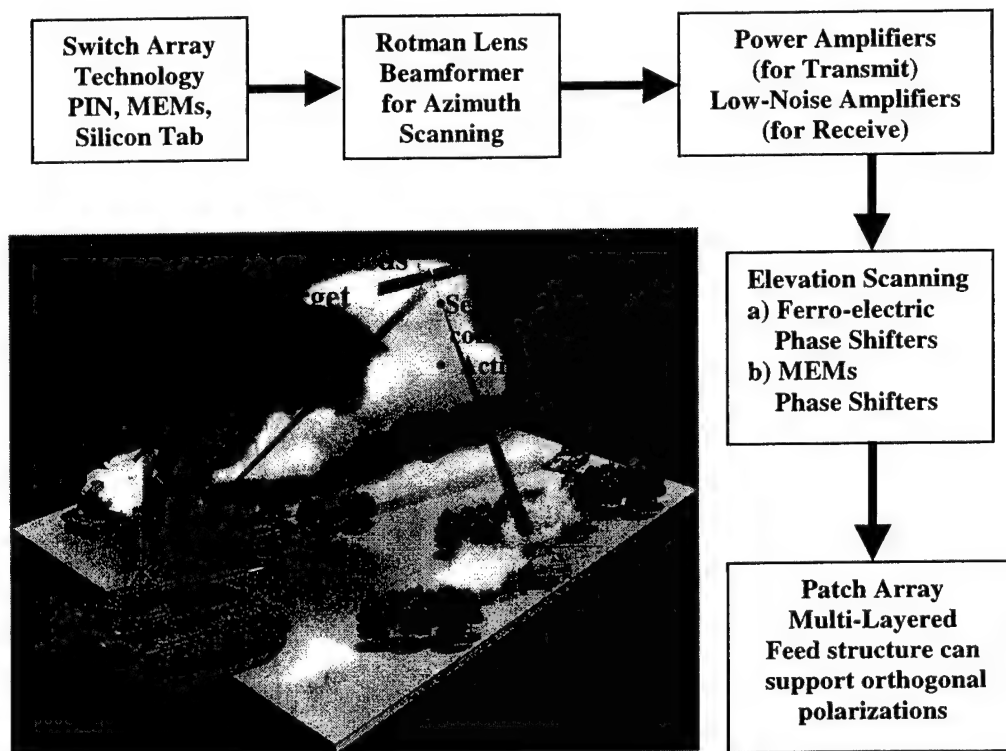


Figure 1 – Multifunction RF concept and block diagram of the ESA array.

## II. THE PATCH ARRAY

A scaled version of a dual aperture ESA has as its goal a  $3^\circ$  azimuth beam that can scan over a  $\pm 26^\circ$  field of view, while in elevation it has a  $10^\circ$  beam that can scan over a  $\pm 10^\circ$  field of view. The operational bandwidth is from 36.5 to 39.5 GHz, and an effective isotropic radiated power is specified as greater than 30 dBW. However, an objective ESA may require tighter beamwidths in azimuth and elevation, beam spoiling for broader beamwidth applications and ultimately higher power for long-range detection of low radar cross-section targets. Therefore, it was essential to select an ESA architecture that has the scalability potential.

The narrow-beam requirements of the multifunction RF sensor can be achieved with an array of low-profile broadband patch radiators. Such an array

was fabricated and its performance measured. This array is to be steered in the azimuth plane by appropriately shifting the phase front using a Rotman Lens beam former. The Rotman lens has multiple ports on its beam and array sides. The array ports connect directly to the antenna array, while an  $M \times N$  switching network selects the beam ports. Ultimately, the array will be steered in elevation by the addition of true-time delay transmission lines (ferroelectric based) that connect to each coupled fed radiating element. However, this version of the array utilized integrated frequency scanning to expedite the overall proof-of-concept.

A diagram of the frequency scanning feed used in each of the 32 columns of the array is presented in Figure 2. As real estate becomes a premium, at the operational frequencies required, a novel technique of feeding the apertures orthogonally has been utilized that maintains the progressive phase shift between elements (uniformly fed) while minimizing the amount of line length.

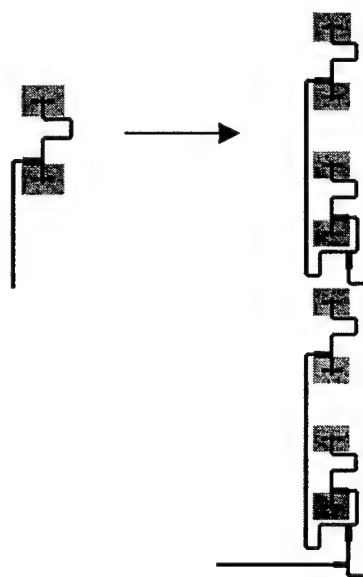


Figure 2 – Feed configuration for frequency scanning in elevation.

Figure 3 shows photographs of the front and back of a transmit/receive array. There are two (8 X 32) element arrays. The overall height (thickness) of this array is on the order of 1/10 inch. This photo shows each column fed by two corporate feeds. Measured patterns are presented in Figure 4.

In our final design, each individual patch in the columns will be fed off taps of a ferroelectric delay line. The ferroelectric material is low profile and

could be integrated into the substrate material from which the antenna arrays are fabricated. Note that the ferroelectric material would be positioned over the small slots (apertures) as will be explained subsequently.

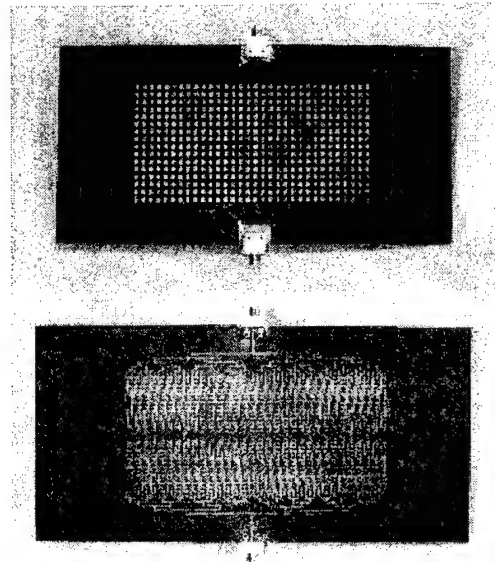


Figure 3 – Transmit and Receive arrays.

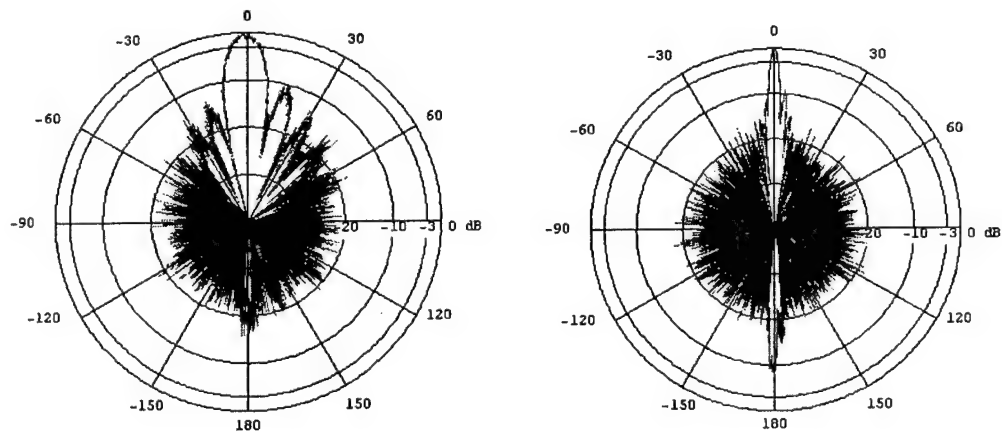


Figure 4 – Measured patterns for the frequency-scanned antenna array.

### III. FERRO-ELECTRIC PHASE SHIFTERS (ELEVATION SCANNING)

In traditional phased arrays, a phase shifter implement beam steering. There are many types of phase shifter technologies. It has long been known that ferroelectric materials can be used to make such components, since they can provide voltage-controlled phase shifts by virtue of their nonlinear dielectric response.

Our recent in-house phase shifter work has centered on a true-time-delay approach to generating the antenna phase shifts, in which a tapped delay line (usually some sort of microwave transmission line) is used to phase the antenna signals by sampling a nondispersive propagating wave at equal intervals along its path. An array phased in this way has a far-field pattern whose main lobe points at an angle  $\theta_{MB}$  is given by:

$$\theta_{MB} = \sin^{-1} \left( \frac{D\sqrt{\epsilon}}{d} \right), \quad (1)$$

where  $D$  is the spacing between taps,  $d$  is the distance between array radiators, and  $\epsilon$  is the dielectric constant of the delay line. Broadband signals can be transmitted without causing the beam to move, if  $\epsilon$  is frequency independent. This also means that angle  $\theta_{MB}$  is also frequency independent. If the transmission line is a microstrip line on a ferroelectric substrate, the field dependence of  $\epsilon$  makes it possible to steer the beam electrically with a single dc voltage between the strip and the ground plane.

However, there are problems with this implementation. In order to suppress coupling between array radiators, the spacing  $d$  between them is usually  $\lambda/2$ , where  $\lambda$  is the free-space wavelength of the carrier signal (typically, a few centimeters down to a millimeter for our applications). Because dielectric constants are extremely high in ferroelectrics (1000 to 4000), satisfying equation (1) with an  $\epsilon$  of 1000 requires values of  $D < d/30$ , and the delay line taps must be quite close together. This causes arcing and cross talk and makes the line difficult to manufacture.

Our approach to this problem is to replace the ferroelectric substrate with a guiding structure consisting of a thin slice of ferroelectric sandwiched between two "cladding" layers of low- $\epsilon$  material (Figure 5). We have found that there is a

frequency range within which a delay line based on this structure, which we call a *ferroelectric slab waveguide*, looks like a microstrip transmission line with an “average” dielectric constant much lower than that of the ferroelectric.

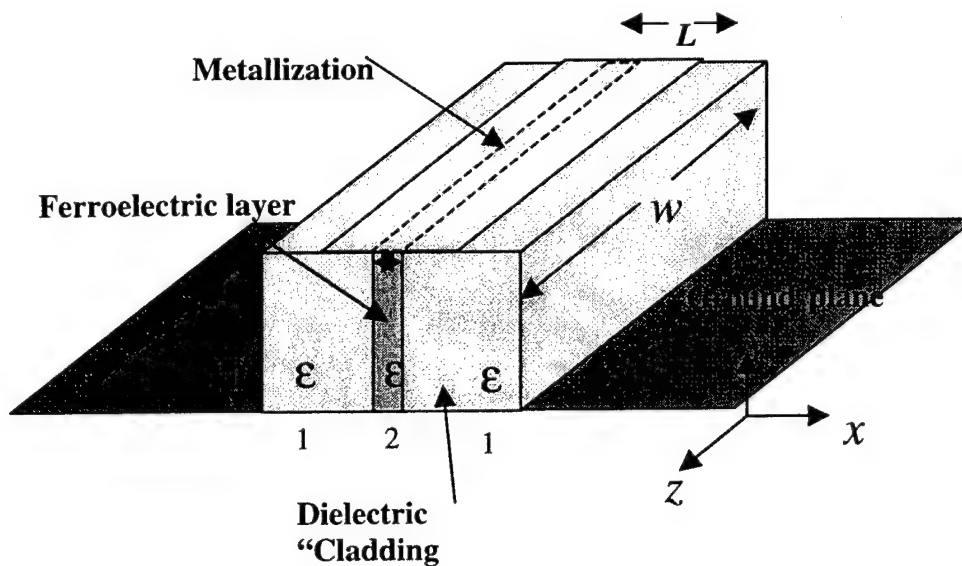


Figure 5 – Construction of the ferroelectric true-time delay line.

Figure 6 illustrates a technique for tapping off energy at progressive time delays along the ferroelectric line. The “taps” use apertures (just like aperture-

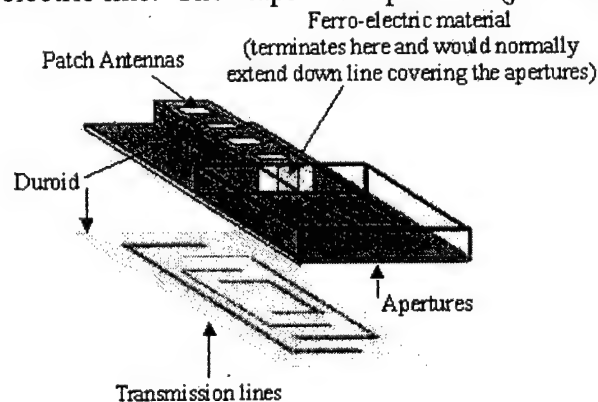


Figure 6 – Illustration of the “tapped” technique.

coupled patch antennas). The signal (with its time delay) is then coupled to an aperture fed patch antenna via a microstrip line.



#### IV. PACKAGING FOR LOW NOISE AND POWER AMPLIFIERS.

All amplifiers (either low-noise or power) will be housed in an octo-pac to streamline fabrication and maintenance (Figure 7). The left side of the module shown has a waveguide-to-microstrip transition to feed the vertical WR-22 waveguide ports of the Rotman lens. A Quasi-Yagi design developed by Itoh et al [2] was scaled to Ka-band and modeled using an electromagnetic (EM) simulator. The MMICs are assembled on carriers with two channels per carrier so that modules can easily be repaired in case of MMIC failure. The additional microstrip circuits shown are fabricated on low-loss fused silica substrates. The right side of the module has Corning Gilbert GPPO push-on connectors to interface with the patch antenna array. These connectors were selected to meet the 0.188-inch spacing of the array elements. Vertical glass bead feedthrus are used to bring the bias up through the base of the module. Bias sequence/protection circuits have been designed to properly bias and protect the GaAs HEMT (high electron mobility transistor) devices in the MMICs. A prototype of the eight-channel module has been fabricated and is shown in Figure 8. The carriers are shown in the module but have not been populated at this time.

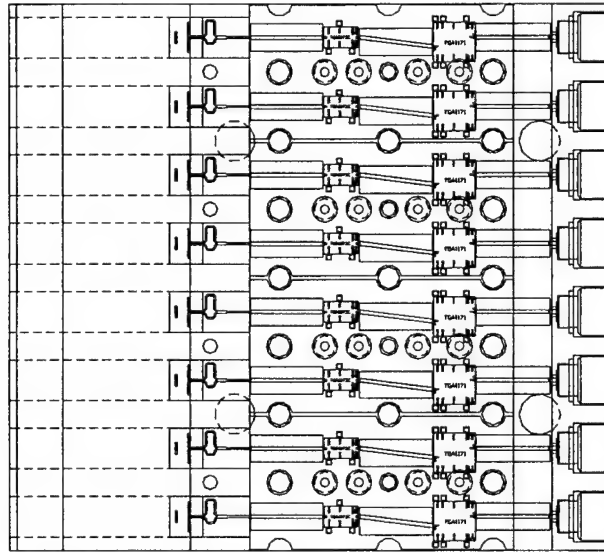


Figure 7 - A low-profile package suitable for power and low-noise amplifiers.

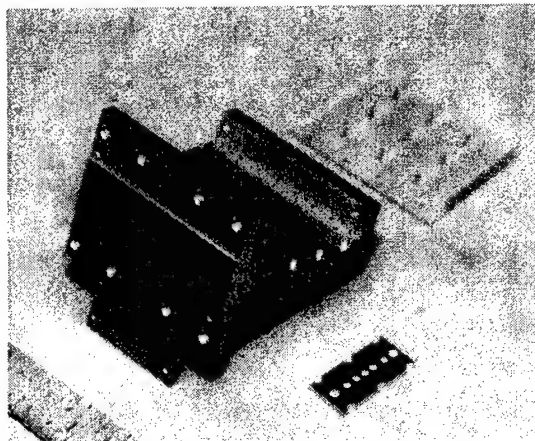


Figure 8 - Eight-channel module.

Several Ka-band MMICs [3] have been prototyped and tested to identify the best candidates for this application. One of the low-noise amplifiers (LNAs) tested is shown in Figure 9 and the test fixture for evaluating the MMICs is shown in Figure 10. The gain and return loss of the MMICs selected for the transmit and receive modules are shown in Figure 11. The LNA selected has a nominal noise figure of 2.1 dB, and the power amplifier has a saturated output power of 1 W.

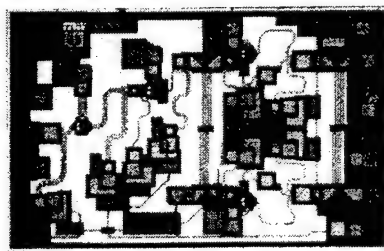


Figure 9 – Low-noise amplifier.

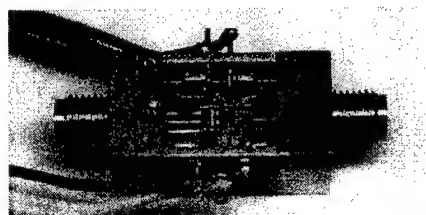


Figure 10 - Power amplifier in test fixture.

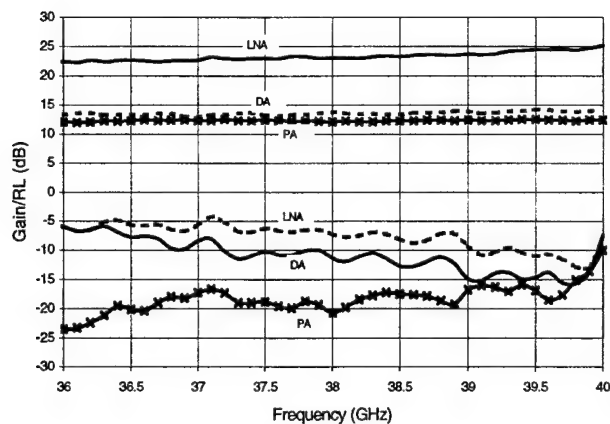


Figure 11 - Gain and return loss of MMICs selected for the transmit and receive modules.

## V. ROTMAN LENS

We have fabricated and tested a Rotman lens [3] that will serve as the azimuthal beamformer for our ESA (Figure 12). This lens is a simplified version of a Rotman Lens developed for ARL by the University of Georgia. Magic Tee junctions have been removed to simplify the manufacturing design with little loss in performance. Further improvements include an incorporated phase compensation network. To control beam-select ability, two concepts for MxN beam switching networks are being developed. One is a traditional pin diode approach capable of high-speed actuation while the other concept uses light-actuated silicon tabs that can handle high-power applications.



Figure 12 – Rotman lens beamformer.

## VI. INTEGRATED ESA ARRAY

A final vision of the architecture for the ESA is presented in Figure 13. Note two Rotman lenses (one for transmit and one for receive). The array side of the Rotman lens connects to the octo-pacs – with either low-noise or power amplifiers. The amplifiers are cascaded into the elevation phase shifters and, finally, to the patch antenna array.

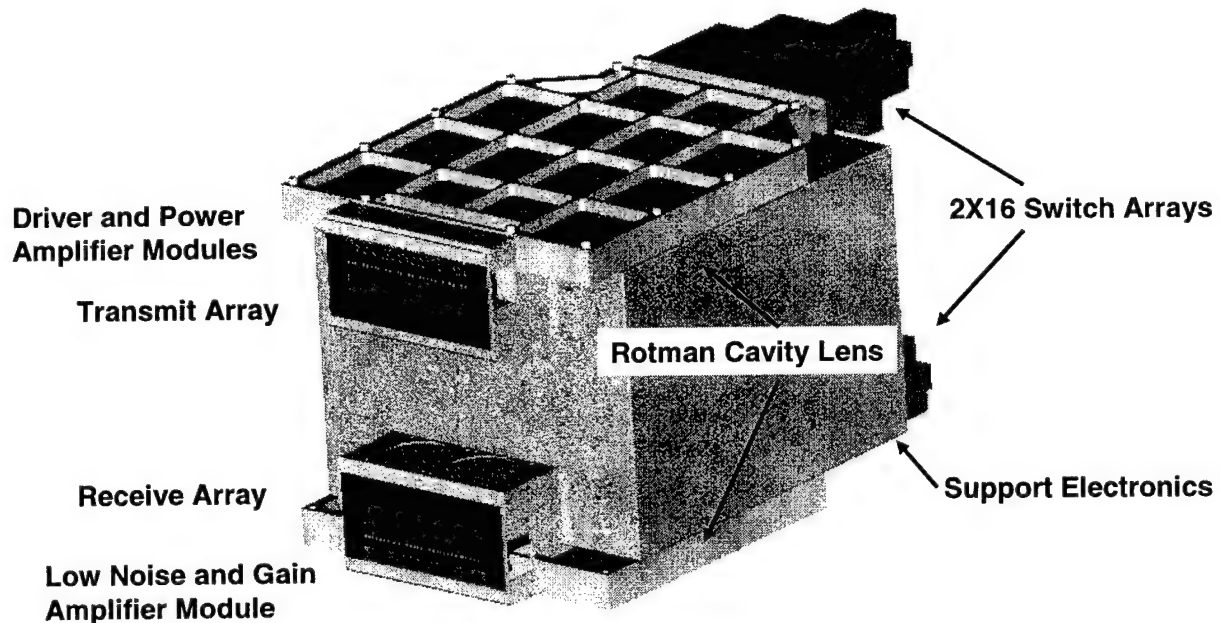


Figure 13 – Final architecture for the first prototype ESA array.

## VII. CONCLUSION

A viable ESA architecture for FCS multifunction RF sensor requirements has been developed. Component parts such as the antenna array, amplifiers, and the Rotman lens are performing as desired and are ready for insertion into a working prototype. The ferroelectric delay lines still requires a high level of engineering effort to ensure proper impedance matching and a uniform phase progression between the apertures. Multifunction field demonstrations of the ESA will occur early next year.

### References

1. S. Weiss, E. Adler, R. Dahlstrom, Edward Viveiros, Steven Tidrow, Frank Crowne, "A Low-Profile Architecture Implementation of an Electrically Scanned Antenna," GOMAC 2002 Conference, March 2002.
2. N. Kaneda, Y. Qian, T. Itoh, "A Broadband Microstrip-to-Waveguide Transition Using Quasi-Yagi Antenna," 1999 IEEE MTT-S International Microwave Symposium Digest, Anaheim, Ca, Vol.5 pp. 1431-1434, June 1999.
3. E. Viveiros, J. Speulstra, E. Adler, H. Hung, "Ka-Band MMIC Technology for an Electronic-Scan Antenna System," GOMAC, March 2001.
4. R. Dahlstrom, J. Clark, M. Conn, B. Scheiner, E. Adler, "A Wideband Rotman Lens Electronic Scanning Antenna Demonstration," Workshop on beamforming Technology and applications, July 2000.

# **DIELECTRIC RESONATOR ANTENNAS AND THEIR POTENTIAL FOR MILLIMETER WAVE APPLICATIONS**

**Ahmed A. Kishk**

Department of Electrical Engineering  
University of Mississippi, University, MS 38677  
ahmed@olemiss.edu

**ABSTRACT:** Dielectric resonator antennas made from low loss dielectric materials are proposed to be used at millimeter wave frequencies because of their high radiation efficiency and their wide bandwidth. The numerical analysis shows that the losses at the ka band are not significant. However, the designer should be aware of some problems that might exist, such as the air gap effect.

## **1. Introduction:**

One of the main problems for millimeter wave antennas is the material losses that deteriorate the antenna performance and reduce its efficiency. The other problem is related to the losses of the feeding network. It is required to have a highly accurate fabrication process with very low tolerance. Microstrip antennas are widely used in many frequency bands because of their ease of design and fabrications. However, at millimeter frequencies the efficiency of microstrip antenna arrays is less than 50%. Therefore, it is required to use materials with much lower losses than currently in use.

Dielectric resonators are made of high dielectric constant materials and have been used efficiently as microwave components in filter design because of their high quality factor. Many engineers have doubted their usefulness as radiators, thinking that they would not be efficient radiators and that they would have very small radiation bandwidths. It has been shown, however, that some modes have a small radiation Q-factor. This gives the indication that the bandwidth will be wide. Since, dielectric resonators are made of materials with much lower losses than the conducting microstrip patches, it is recommended to be used in place of the patches as radiators. Several techniques have been proposed to increase the bandwidth of the dielectric resonator antennas. Some of these techniques achieved a bandwidth of 25 to 50% [1-3]. The radiation

efficiency has also been predicted experimentally for some modes and found to be better than 98% [4]. Recently, interest in small efficient antennas has increased. One of the candidates is the dielectric resonator antenna (DRA), which is made of dielectric material with a high permittivity mounted on top of a ground plane or on a grounded dielectric substrate of lower permittivity [5]. This antenna promises to be more efficient than the microstrip antenna. The DRA elements are good candidates for array applications [6]. At millimeter frequencies, the feeding network causes most of the losses. DRA array can be fed with low loss feeding mechanism such as dielectric image waveguide [7].

An overview will be given for the development of the DRA and the possible problems that might exist in the construction of the antenna. Some results at different frequency bands will be presented to show the potential of using the DRA at the millimeter frequency bands.

## 2. DRA at millimeter frequencies:

**a) Probe Excitation:** A conical dielectric resonator is considered as shown in Fig. 1. The cone radii are  $a_U$  and  $a_L$  and height  $h$  is excited by a coaxial probe of length  $\ell_w$  and radius  $a_w$ . The probe is parallel to the  $z$ -axis and off the DRA center by a radial distance  $\rho_w$ . The probe excitation might not be suitable from the practical point of view at these frequencies. However, the coaxial probe is considered for ease of the analysis and to have some ideas about the proper dimensions of the DRA at millimeter frequencies. As a special case of the above geometry, a dielectric resonator disc above an infinite ground plane and a finite ground plane is considered. The  $HEM_{118}$  mode is excited for broadside radiation. The antenna parameters are  $a_U=a_L=a=1.1\text{mm}$ ,  $h=1\text{mm}$ ,  $\epsilon_r=12$ ,  $\ell_w=0.9\text{mm}$ ,  $a_w=0.1\text{mm}$  and  $\rho_w=0.9\text{mm}$ . The input impedance and the reflection coefficient are computed in Fig. 2 and 3, respectively, using the method of moments [8-9] for three cases, the lossless infinite ground plane, lossless square finite ground plane and lossy square finite ground plane of length 20mm made from copper. In the lossy case, the dielectric is considered with conductivity  $\sigma=0.002\text{ S/m}$ . It can be noticed that the resonant frequency is shifted up to a higher frequency in the case of finite ground plane. There is no significant difference between lossy and lossless cases. This is an indication that the analysis with no losses is acceptable and valid. This is also an indication of the high radiation efficiency of the DRA as reported before [4]. This antenna achieved about 6% bandwidth for better than -10dB reflection with  $50\Omega$  nominal reference impedance. As an indication that the  $HEM_{118}$  mode is excited, the radiation patterns for the above three cases are computed at 33.25GHz as shown

in Fig. 4. The lossy and lossless case of finite ground plane are identical. The radiation patterns are of broadside type.

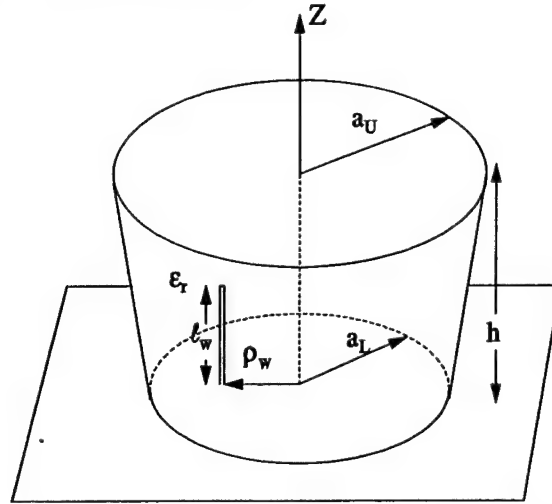


Fig. 1 Geometry of the DRA excited by a coaxial probe.

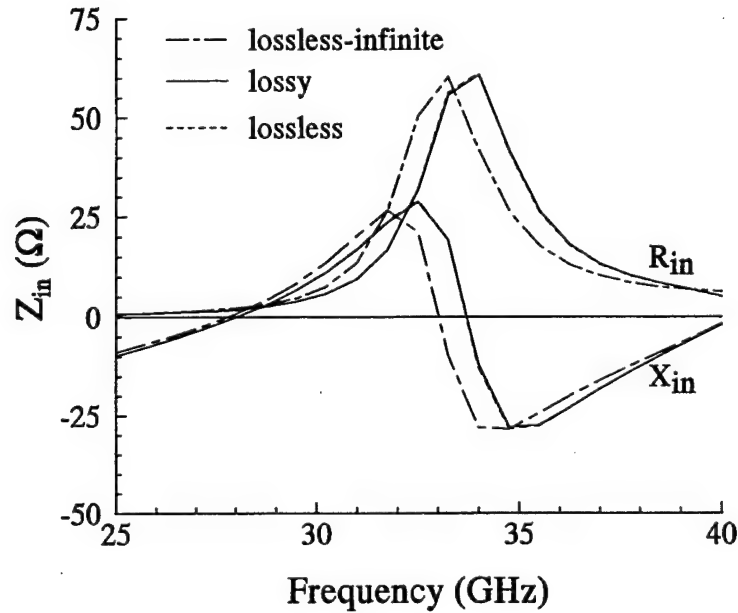


Fig. 2 Input impedance of a dielectric resonator disc excited by a coaxial plane with  $a_U=a_L=a=1.1\text{mm}$ ,  $h=1\text{mm}$ ,  $\epsilon_r=12$ ,  $\ell_w=0.9\text{mm}$ ,  $a_w=0.1\text{mm}$  and  $\rho_w=0.9\text{mm}$ . A copper conductor is used and lossy dielectric with  $\sigma=0.002\text{ S/m}$ .



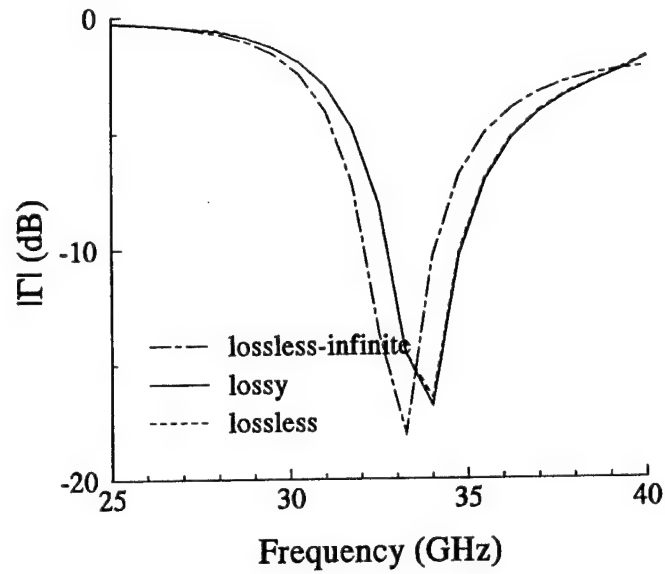


Fig. 3 Reflection coefficient of a dielectric resonator disc excited by a coaxial plane with  $a_U=a_L=a=1.1\text{mm}$ ,  $h=1\text{mm}$ ,  $\epsilon_r=12$ ,  $\ell_w=0.9\text{mm}$ ,  $a_w=0.1\text{mm}$  and  $\rho_w=0.9\text{mm}$ . A copper conductor is used and lossy dielectric with  $\sigma=0.002\text{ S/m}$ .

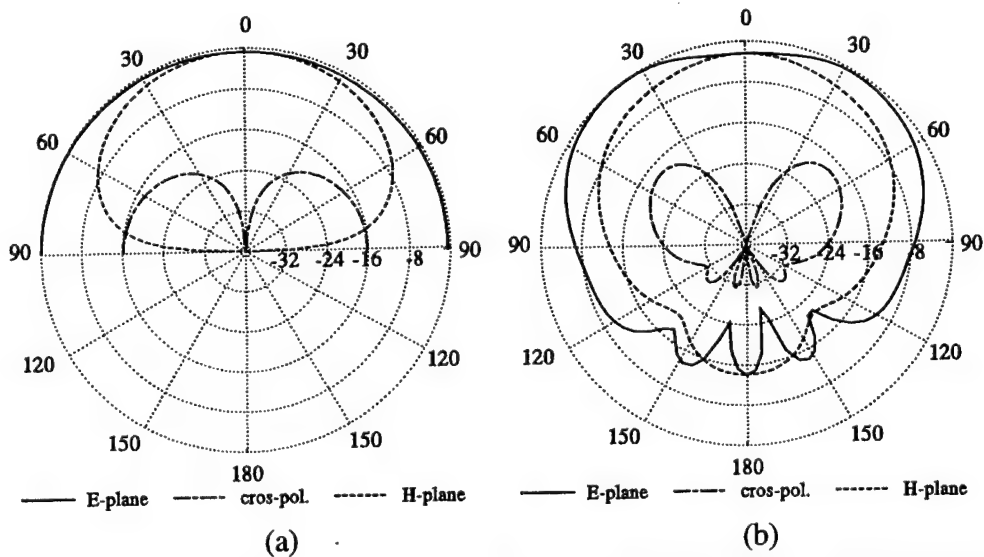


Fig. 4 Radiation patterns for the case in Fig. 2 at  $f=33.25\text{ GHz}$ . (a) infinite ground plane, (b) finite ground plane with length 20mm.

**b) Slot excitation:** The narrow slot excitation is also considered as shown in Fig. 5. The geometry of the DRA with narrow slot excitation is shown in Fig. 5a and the parameters of the slot coupled to the microstrip transmission line are shown in Fig. 5b. The input impedance and the return losses are computed using the method of moments [10]. Fig. 6 and 7 show the input impedance and the return losses, respectively, of a dielectric disc above an infinite ground plane excited by a narrow slot with  $a_U=a_L=a=1.1\text{mm}$ ,  $h=1\text{mm}$ ,  $\epsilon_r=12$ ,  $w_s=50\mu\text{m}$ ,  $L_s=1.4\text{mm}$ ,  $L_t=4.54\text{mm}$ ,  $y_s=0.0\text{mm}$ ,  $\epsilon_s=2.96$ , and  $d=63.5\mu\text{m}$ . The disc dimension is the same as that used above with the wire excitation, but the 10dB bandwidth is 4.5%. The bandwidth may be improved by a proper design for the coupling of the slot with the transmission line. It can also be noted that the minimum reflection coefficient occurs at a frequency different from the frequency of the input resistance peak. The matching band can be shifted to the input resistance peak position by shifting the microstrip transmission line off the center of the slot.

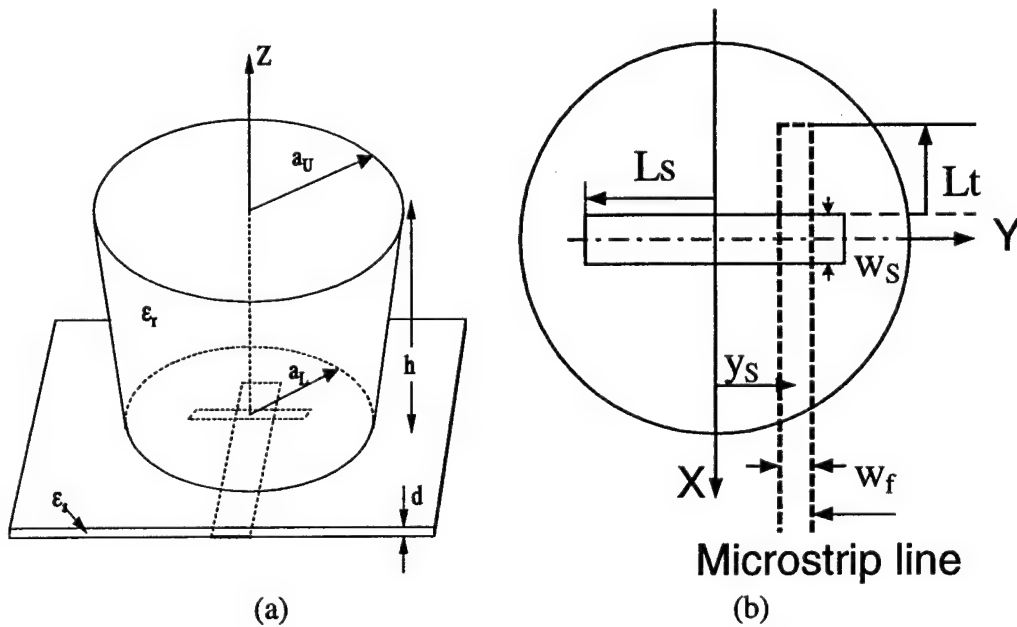


Fig. 6 (a) Antenna geometry, (b) Parameters of the slot and microstrip transmission line exciting a dielectric resonator with circular base. The circle is the dielectric surface intersecting the ground plane. The solid rectangle is the slot and the dashed line is the microstrip line under the ground plane and the slot.

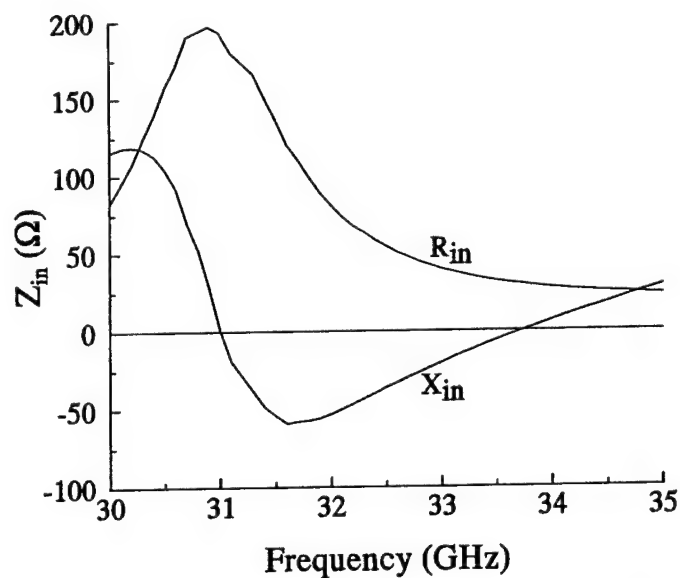
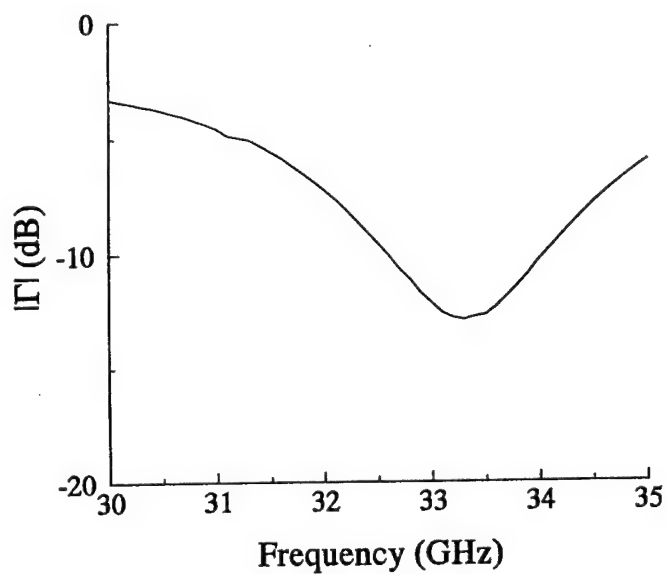


Fig. 6 Input impedance of a DR disc excited by a narrow slot with  $a_U=a_L=a=1.1$  mm,  $h=1$  mm,  $\epsilon_r=12$ ,  $w_s=50\mu\text{m}$ ,  $L_s=1.4$  mm,  $L_t=4.54$  mm,  $y_s=0.0$  mm,  $\epsilon_s=2.96$ , and  $d=63.5\mu\text{m}$ .



(b)  
Fig. 7 Reflection coefficients of a DR disc excited by a narrow slot with  $a_U=a_L=a=1.1$  mm,  $h=1$  mm,  $\epsilon_r=12$ ,  $w_s=50\mu\text{m}$ ,  $L_s=1.4$  mm,  $L_t=4.54$  mm,  $y_s=0.0$  mm,  $\epsilon_s=2.96$ , and  $d=63.5\mu\text{m}$ .

Another example of a bicone dielectric resonator is considered with  $a_U = 5\text{mm}$ ,  $a_L = 1.2\text{mm}$ ,  $h = 1.12\text{mm}$ ,  $\epsilon_r = 12$ ,  $w_S = 90\mu\text{m}$ ,  $L_S = 1.8\text{mm}$ ,  $L_t = 1.27\text{mm}$ ,  $y_S = 0.5\text{mm}$ ,  $\epsilon_S = 2.96$ , and  $d = 63.5\mu\text{m}$ . The input impedance is shown in Fig. 8 and the reflection coefficient is shown in Fig. 9. This antenna achieved approximately a 50% matching bandwidth with better than -10 dB reflections. Within the frequency band four modes are excited, each at different frequency. Unlike the off center probe excitation all these modes have field distributions in the form of  $\cos\phi$  variations because the narrow slot is centered with the symmetry axis of the DR. Therefore, the far field radiations will be of broadside type. Also, it should be mentioned that the symmetric slot excitation eliminates the cross-polarization in the H-plane.

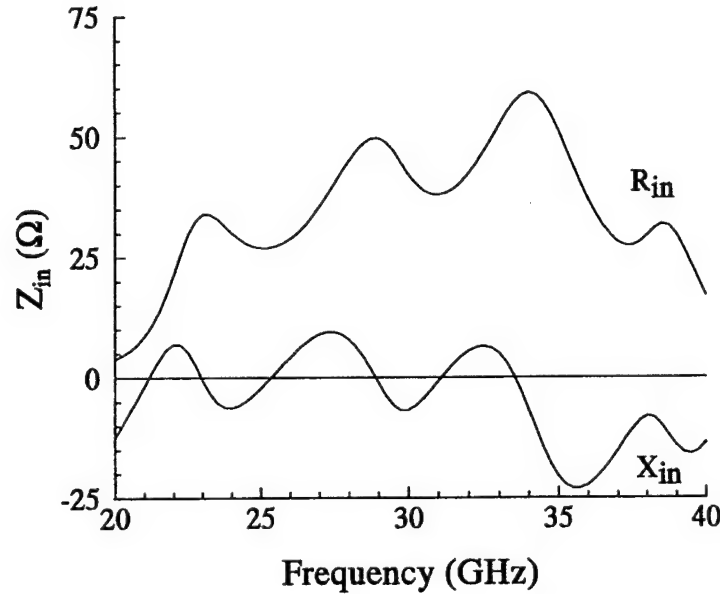


Fig. 8 Input impedance of a bicone DR excited by a narrow slot with  $a_U = 5\text{mm}$ ,  $a_L = 1.2\text{mm}$ ,  $h = 1.12\text{mm}$ ,  $\epsilon_r = 12$ ,  $w_S = 90\mu\text{m}$ ,  $L_S = 1.8\text{mm}$ ,  $L_t = 1.27\text{mm}$ ,  $y_S = 0.5\text{mm}$ ,  $\epsilon_S = 2.96$ , and  $d = 63.5\mu\text{m}$ .

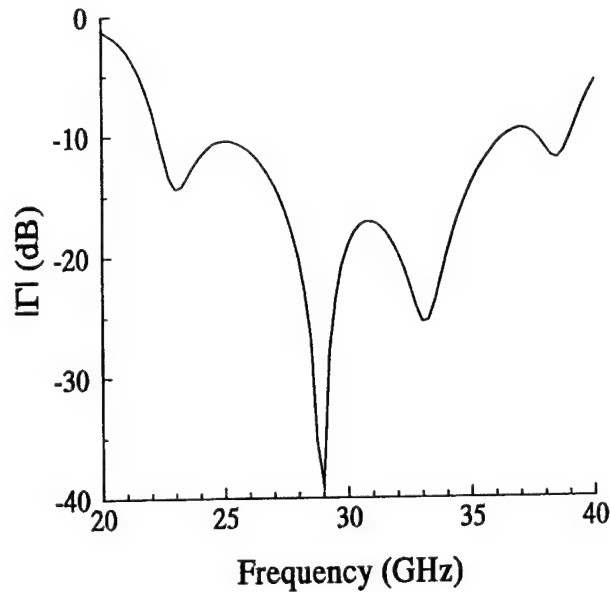


Fig. 9 Reflection coefficient of a bicone DR excited by a narrow slot with  $a_U = 5\text{mm}$ ,  $a_L = 1.2\text{mm}$ ,  $h = 1.12\text{mm}$ ,  $\epsilon_r = 12$ ,  $w_S = 90\mu\text{m}$ ,  $L_S = 1.8\text{mm}$ ,  $L_t = 1.27\text{mm}$ ,  $y_S = 0.5\text{mm}$ ,  $\epsilon_S = 2.96$ , and  $d = 63.5\mu\text{m}$ .

## 2. Air gap effect on the DR performance:

One of the problems related to the fabrication and assembly of the DRA above a conducting ground plane is the possibility of having an invisible air gap between the dielectric materials and the ground plane [11-12]. If the air gap is not controlled and is not considered during the design of the antenna, the obtained results from the antenna will be much different from what was predicted. This problem was investigated before at low frequencies. If we scale the antenna dimensions we can use the same results. The scaled antenna is a dielectric disc with radius  $a = 1.7\text{mm}$ , height,  $h = 1.6\text{mm}$ , and dielectric constant,  $\epsilon_r = 12$  above a ground plane and is excited by a coaxial probe with wire along the disc axis. In this case an omni-directional radiation patterns can be obtained because the  $\text{TM}_{118}$  mode is excited. The wire radius  $a_w = 2.35\mu\text{m}$ , and length  $\ell_w = 0.844\text{mm}$ . The measured input impedance of this antenna is shown in Fig. 10 with and without an air gap. It can be seen that the air gap has shifted the resonant frequency up. The shift increases as the dielectric constant increases or as the air gap width increases. More examples will be presented to show the effect of the dielectric constant on the input impedance and the resonant frequency. One of the

suggestions to eliminate this problem is to use a conductive adhesive to glow the DR with the ground plane.

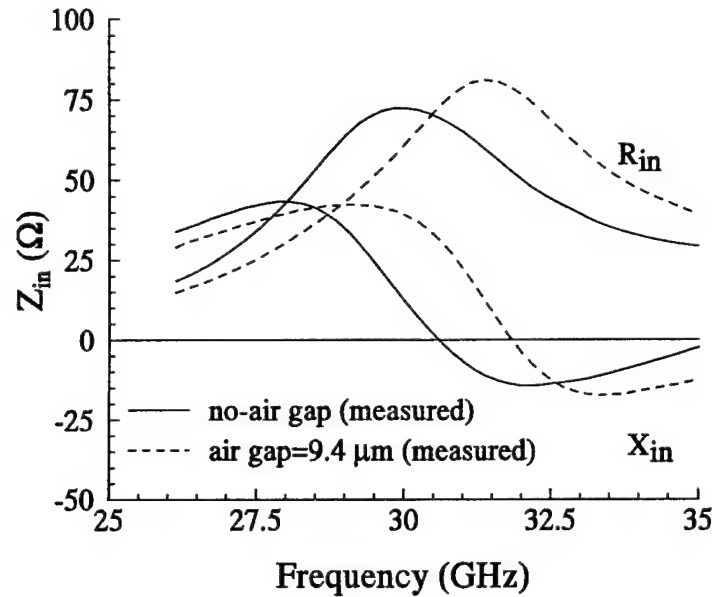


Fig. 10 Input impedance of a cylindrical dielectric resonator with  $a=1.7\text{mm}$ ,  $h=1.6\text{mm}$ ,  $a_w=23.5\mu\text{m}$ ,  $\ell_w=0.844\text{mm}$ , and  $\epsilon_r=12.0$ .

### 3. CONCLUSIONS

Numerical investigation is performed to study the possibility of using dielectric resonator antennas at millimeter frequencies. The analysis shows that this antenna could be a good candidate at these frequencies. Two different excitation mechanisms were investigated. The slot excitation shows a very promising method to be used because it does not require any machining to place the wire probe inside the DR. It was pointed out the possible problem that might exist due to presence of unpredicted air gap between the DR and the ground plane.

### Acknowledgment:

This work was partially supported by The Army Research Office under grant No. DAAD19-02-1-0074.

# REFERENCES:

- [1] A. A. Kishk, Yan Yin, and A. W. Glisson, "Conical Dielectric Resonator Antennas For Wideband Applications," *IEEE Transactions on Antennas and Propagation*, vol. 50, pp. 469-474, April 2002.
- [2] A. A. Kishk, "Tetrahedron and Triangular Dielectric Resonator Antenna with Wideband Performance," *2002 IEEE Antennas and Propagation Int. Symposium*, vol. 4, pp. 462-465, June 2002.
- [3] A. A. Kishk, A. W. Glisson and G.P. Junker, "Bandwidth enhancement for split cylindrical dielectric resonator antennas," *Journal of Progress in Electromagnetics Research*, vol. 33, pp. 97-118, 2001.
- [4] R.K. Mongia, A. Ittipiboon, and M. Cuhaci, "Measurement of radiation efficiency of dielectric resonator antennas," *IEEE Microwave and Guided Letters*, Vol. 4, No. 3, pp. 80-82, 1994.
- [5] A. A. Kishk, M. R. Zunoubi, and D. Kajfez, "A numerical study of a dielectric disk antenna above grounded dielectric substrate," *IEEE Trans. Antennas Propagat*, vol. 41, pp. 813-821, 1993.
- [6] A. Petosa, R. Larose, A. Ittipiboon, and A. Cuhaci, "Microstrip-fed array of multisegment dielectric resonator antennas," *IEE Proc.-Microwave Antennas Propag.*, Vol. 144, pp. 472-476, 1997.
- [7] A. Petosa, A. Ittipibon, Y. M. M. Antar, D. Roscoe and M. Cuhaci, "Recent advances in dielectric-resonator antenna technology," *IEEE Antennas Propag. Mag.*, vol. 40, no. 3, pp. 35-48, June 1998.
- [8] G. P. Junker, A. A. Kishk, and A. W. Glisson, "Input impedance of dielectric resonator antennas excited by a coaxial probe," *IEEE Trans. Antennas Propagat*, vol. 42, pp. 960-966, 1994.
- [9] B. M. Kolundzija, J. S. Ognjanovic, and T. K. Sarkar, "WIPL-D: Electromagnetic modeling of composite metallic and dielectric structures, Software and User's Manual," Artech House, Inc., 2000.
- [10] G. P. Junker, A. A. Kishk, and A. W. Glisson, "Input impedance of aperture coupled dielectric resonator antennas," *IEEE Trans. Antennas Propagation*, vol. AP-44, pp. 600-607, May 1996.
- [11] Junker, G.P., A. A. Kishk, A. W. Glisson, and D. Kajfez, "Effect of an air gap around the coaxial probe exciting a cylindrical dielectric resonator antenna," *Electronics Letters*, vol. 30, No. 3, pp. 177-178, 1994.
- [12] G. P. Junker, A. A. Kishk, A. W. Glisson, and D. Kajfez, "Effect of fabrication imperfections for ground-plane-backed dielectric resonator antennas," *IEEE Antennas and Propagation Magazine*, vol. 37, pp. 40-46, Feb. 1995.

# **Simulation of Vehicle Antennas by the Multilevel Fast Multipole Algorithm**

H. Y. Chao, K. Pirapaharan, V. Bodrov, T. J. Cui, H. P. Hsu, G. Huff, X. J. Zhang, J. S. Zhao, J. Bernhard, and W. C. Chew

Center for Computational Electromagnetics and Electromagnetics Laboratory  
Department of Electrical and Computer Engineering  
University of Illinois at Urbana-Champaign  
Urbana, IL 61801

## **Abstract**

As mobile communication, satellite navigation and broadcast services become prevalent, antenna systems are increasingly important for vehicle design. In order to maintain the shape of a vehicle, antennas are often placed in a complex environment, such as under a sunroof or on a non-ideal ground plane. Therefore, the radiation patterns highly depend on antenna location and surrounding scatterers. With numerical simulation, we can easily explore different design factors of prototype antennas. Although the multilevel fast multipole algorithm (MLFMA) has been applied to solve for radiation from vehicle antennas, available examples only involve simple monopoles. In this paper, we make MLFMA practical for solving complex antenna systems by enhancing it with the basis normalization (BN) and the self-interaction box inclusion (SBI) preconditioners. The above preconditioners significantly reduce the time for solving an ill-condition problem due to disparate mesh sizes and strong current interaction at the vicinity of antenna feeds. Simulation results are validated by measurements done in an anechoic chamber.

## **1. Introduction**

Simulation of vehicle antennas has long been an interest of electromagnetics society. Originally, only airborne and shipborne antennas were analyzed because of defense applications. Most of the simulations were done on supercomputers or high-end workstations. As personal computers become cheaper and more powerful in recent years, the simulation can be done on PCs for antennas on a full-sized vehicle with integral-equation based methods or hybrid methods. The emerging mobile communication also shifts the interests to simulation of personal communication devices on automobiles. For example, FM (98 MHz) and cellular-phone (860 MHz) antennas were simulated by the method of moments (MOM) for a Golf GL in [1,2]. However, the MOM is limited by its computational complexity and requires humongous resources for simulating a whole vehicle at PCS (1850-1990 MHz), GPS (1227 and 1575 MHz), and SDARS (2332-2345 MHz) bands.



A hybrid method, such as MOM plus physical optics (PO) or uniform theory of diffraction (UTD), is more practical for solving high-frequency radiation from antennas and vehicles simultaneously. The hybrid MOM/PO with an edge correction factors has been applied for solving radiation from vehicle antennas [3,4]. However, the hybrid method is based on many assumptions. First, the MOM region usually contains an electrically small antenna and the current radiates in presence of an electrically large, smooth ground plane, where the PO current is solved. Although the interaction between the MOM and PO regions is captured by a first-order approximation, the hybrid method works best when there is no backscattering into the MOM region. The hybrid method also assumes few unknowns in the MOM region. Therefore, a direct solver can be applied. The most important restriction is that the hybrid method is not developed for dielectric scatterers. Hence, the interaction between antennas and human beings cannot be simulated.

The antenna structures presented in this paper are mounted on a ground plane (antenna tray) that is neither electrically large nor smooth. One has to truncate the MOM region manually in the hybrid method, where the accuracy of results highly depends on the experience of an engineer. In addition, the antennas are adjacent to each other and the assumption of zero backscattering cannot be applied. When antennas are placed inside a car, there are backscattering from car body and the long-range interaction cannot be neglected. Moreover, the MOM region contains 4,000 to 10,000 unknowns, which requires large computational resources if a direct solver is used.

In this paper, we will present a fast algorithm that can solve complex antenna structures mounted on vehicles with an optimal computational complexity as  $O(N \log N)$ . The algorithm works for various dielectric scatterers, such as lossy inhomogeneous dielectric blocks, thin dielectric sheets, and dielectric coated metal surfaces. Since the main disadvantage of the MLFMA is the high iteration number for solving ill-conditioned radiation problem, we will introduce BN and SBI preconditioners as remedies.

## 2. Formulation

Antenna radiation and scattering problems involving conducting surfaces, wires, surface-wire junctions, and inhomogeneous dielectric materials can be solved the hybrid volume-surface integral equation (VSIE) [5]

$$\mathcal{L}_S(\mathbf{r}, \mathbf{r}') \mathbf{J}_S(\mathbf{r}') - \mathcal{K}_S(\mathbf{r}, \mathbf{r}') \mathbf{M}_S(\mathbf{r}') + \mathcal{L}_W(\mathbf{r}, \mathbf{r}') \mathbf{J}_W(\mathbf{r}') + \mathcal{L}_J(\mathbf{r}, \mathbf{r}') \mathbf{J}_J(\mathbf{r}') + \mathcal{L}_V(\mathbf{r}, \mathbf{r}') \mathbf{J}_V(\mathbf{r}') \Big|_{\text{tan}} = -\mathbf{E}^{inc}(\mathbf{r}) \Big|_{\text{tan}},$$

$$\mathbf{r} \in S, W, J,$$

$$\mathcal{L}_S(\mathbf{r}, \mathbf{r}') \mathbf{J}_S(\mathbf{r}') - \mathcal{K}_S(\mathbf{r}, \mathbf{r}') \mathbf{M}_S(\mathbf{r}') + \mathcal{L}_W(\mathbf{r}, \mathbf{r}') \mathbf{J}_W(\mathbf{r}') + \mathcal{L}_J(\mathbf{r}, \mathbf{r}') \mathbf{J}_J(\mathbf{r}') + \mathcal{L}_V(\mathbf{r}, \mathbf{r}') \mathbf{J}_V(\mathbf{r}') - \mathbf{E}(\mathbf{r}) = -\mathbf{E}^{inc}(\mathbf{r}),$$

$$\mathbf{r} \in V,$$

where  $\mathbf{J}_S$ ,  $\mathbf{J}_W$ ,  $\mathbf{J}_J$ , and  $\mathbf{J}_V$  are electric current densities on surfaces  $S$ , wires  $W$ , surface-wire junctions  $J$ , and in dielectric regions  $V$ , respectively.  $\mathbf{M}_S$  is the magnetic current density on imperfectly conducting surfaces  $S$ .  $\mathbf{E}^{inc}$  and  $\mathbf{E}$  are the incident and total fields, respectively. The electric field integral equation (EFIE) operators  $\mathcal{L}_\alpha$  and the magnetic field integral equation (MFIE) operator  $\mathcal{K}_S$  are

$$\mathcal{L}_\alpha \mathbf{J}_\alpha(\mathbf{r}) = i\omega\mu \int_\alpha d\mathbf{r}' \left( \bar{\mathbf{I}} + \frac{\nabla\nabla'}{k_0^2} \right) \cdot \mathbf{J}_\alpha(\mathbf{r}') g(\mathbf{r}, \mathbf{r}'), \quad \alpha = S, W, J, V,$$

and

$$\mathcal{K}_S \mathbf{M}_S(\mathbf{r}) = -\frac{1}{2} \hat{n} \times \mathbf{M}_S(\mathbf{r}) + \oint_S d\mathbf{r}' \mathbf{M}_S(\mathbf{r}') \times \nabla g(\mathbf{r}, \mathbf{r}'),$$

where  $g$  is the free space Green's function. For imperfect conducting surfaces, such as lossy conducting surfaces or conducting surfaces with thin dielectric coating, the impedance boundary condition (IBC) can be applied to reduce the number of unknowns on surface  $S$ . When the surfaces are resistive sheets (RS) or thin dielectric sheets (TDS), the VSIE has the following form

$$\mathcal{L}_S(\mathbf{r}, \mathbf{r}') \mathbf{J}_S(\mathbf{r}') - Z_S \mathbf{J}_S(\mathbf{r}') + \mathcal{L}_W(\mathbf{r}, \mathbf{r}') \mathbf{J}_W(\mathbf{r}') + \mathcal{L}_J(\mathbf{r}, \mathbf{r}') \mathbf{J}_J(\mathbf{r}') + \mathcal{L}_V(\mathbf{r}, \mathbf{r}') \mathbf{J}_V(\mathbf{r}') \Big|_{\tan} = -\mathbf{E}^{inc}(\mathbf{r}) \Big|_{\tan},$$

$$\mathbf{r} \in S, W, J,$$

$$\mathcal{L}_S(\mathbf{r}, \mathbf{r}') \mathbf{J}_S(\mathbf{r}') - Z_S \mathbf{J}_S(\mathbf{r}') + \mathcal{L}_W(\mathbf{r}, \mathbf{r}') \mathbf{J}_W(\mathbf{r}') + \mathcal{L}_J(\mathbf{r}, \mathbf{r}') \mathbf{J}_J(\mathbf{r}') + \mathcal{L}_V(\mathbf{r}, \mathbf{r}') \mathbf{J}_V(\mathbf{r}') - \mathbf{E}(\mathbf{r}) = -\mathbf{E}^{inc}(\mathbf{r}),$$

$$\mathbf{r} \in V,$$

where  $Z_S$  is the surface impedance. The TDS formulation is based on a limiting case of a volume integral equation [6].

The VSIE can be solved numerically by the method of moments (MOM). However, one can get the same solution with less memory requirement and CPU time by MLFMA [5,7]. Since MLFMA relies on iterative solvers, a high iteration number is the bottleneck for solving ill-conditioned radiation problems. The condition of impedance matrix is deteriorated by various factors, such as multiple reflection of waves, singular distribution of current, antennas operating at resonant frequencies, disparate mesh sizes, etc.

For antenna structures consist of electrically small features and a large ground plane (Fig. 1), an adaptive mesh is required for reducing the number of unknowns. Consequently, the self-interactions associated with small elements are much stronger than those of regularly sized elements. In order to equalize the magnitude of eigenvalues, the diagonal elements of an impedance matrix are normalized by a congruence transformation. Suppose the original matrix equation is  $\bar{\mathbf{A}}\mathbf{x} = \mathbf{b}$ , where  $\bar{\mathbf{A}}$  and  $\mathbf{b}$  represent the impedance matrix and excitation vector, respectively. The new matrix equation is  $(\bar{\mathbf{D}} \cdot \bar{\mathbf{A}} \cdot \bar{\mathbf{D}}) \cdot \bar{\mathbf{D}}^{-1} \cdot \mathbf{x} = \bar{\mathbf{D}} \cdot \mathbf{b}$ . The procedure is called basis normalization (BN).

The original MLFMA [7] is incorporated with a block-diagonal preconditioner (BDP) that is effective for scattering problems. A BDP uses the block-diagonal part of the impedance matrix as a preconditioner. Suppose the original matrix is  $(\bar{\mathbf{A}}_0 + \bar{\mathbf{A}}_1)\mathbf{x} + \bar{\mathbf{A}}_2\mathbf{x} = \mathbf{b}$ , where  $\bar{\mathbf{A}}_0$  is the block-diagonal part of the near interaction,  $\bar{\mathbf{A}}_1$  is the non-block-diagonal part of the near interaction, and  $\bar{\mathbf{A}}_2$  is the far interaction. Then, the new matrix equation is  $\mathbf{x} + \bar{\mathbf{A}}_0^{-1} \cdot (\bar{\mathbf{A}}_1 \cdot \mathbf{x} + \bar{\mathbf{A}}_2 \cdot \mathbf{x}) = \bar{\mathbf{A}}_0^{-1} \cdot \mathbf{b}$ . If the current near the feed of an antenna is initially solved by  $\bar{\mathbf{A}}_0^{-1}$  and the block is large enough to enclose the whole antenna, the load of the iterative solver is greatly alleviated. The procedure of shifting MLFMA blocks to include operating antennas is called self-interaction box inclusion (SBI).

The above algorithms have been validated for simple antenna structures with analytic solutions and different numerical implementations. In the following section, we will present simulation by MLFMA with BN and SBI preconditioners for PEC structures.

### 3. Examples

The first example demonstrates the effectiveness of BN and SBI preconditioners for a conjugate gradient (CG) solver. The antennas and the ground plane (Fig. 1) are first discretized into triangular patches and wire segments. Because the feed is located at the central antenna, it is enclosed in a SBI box. The current interaction within the box is solved by a direct solver. For the 10,944-unknown problem, MOM requires 938 MB of memory and 2.5 hours (9,009 sec.) of CPU time on a Dec Alpha 700MHz workstation. However, a three-level MLFMA only requires 365 MB of memory. The iteration numbers and total CPU time for different preconditioners are listed in Table I. Although the error bounds for all preconditioners are set at 0.001, the solutions, i.e. the input impedances, are different due to the change of impedance matrices and solution space.

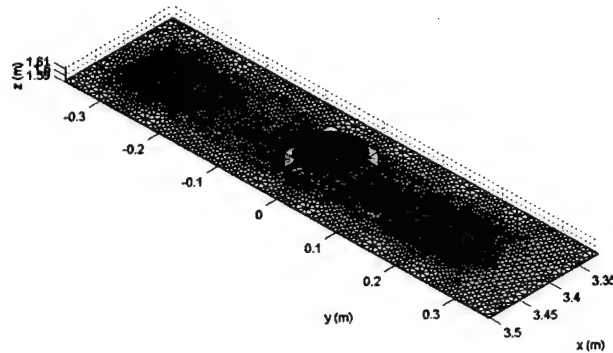


Figure 1. Disk monopole antennas mounted on a ground plane.

Table I. Performance of Different Preconditioners

Preconditioner	Iteration number	CPU time (sec)	Input impedance
BN	4,951	25,128	100.55+j298.07
BDP+BN	872	4,873	108.40+j316.97
BDP+BN+SBI	217	3,365	100.88+j312.29

Once the antenna radiation problems are solved efficiently, the next question is how well the solution agrees with measurement. The structure in Fig. 1 is further mounted on an antenna tray and its azimuth-plane radiation pattern is measured in an anechoic chamber. The measurement is compared with the simulation by a four-level MLFMA in Fig. 2.

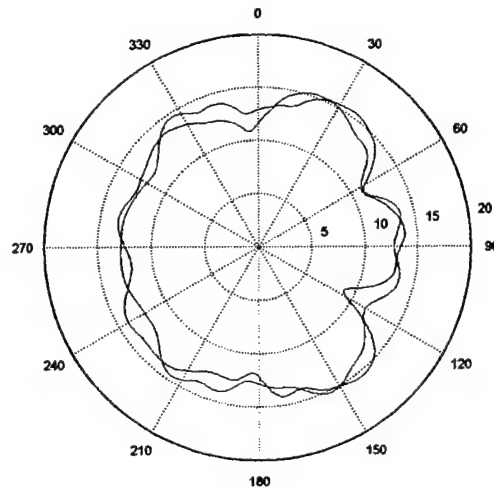


Figure 2. Measured (blue) and simulated (red) radiation patterns of a disk monopole antenna mounted on an antenna tray. Radiation patterns are normalized at 10 dB down.

Our ultimate goal is to develop an antenna simulation tool that can simulate arbitrary antenna structures mounted on a full-sized car. The limitation is mainly due to the size of DRAMs in a computer. When the structure consists of only resistive surface and wires, the symmetry of radiation and receiving patterns can be used. The memory requirement is reduced by 58% compared with that for structures with dielectric materials or impedance surfaces (Fig. 3).

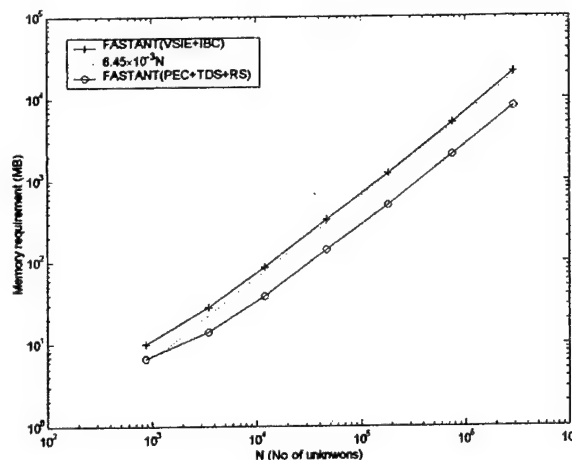


Figure 3. Memory requirement for simulating antennas mounted on a full-sized car.

To test the radiation patterns of antenna on different ground planes, the antenna used in the anechoic chamber measurement is mounted on a full-sized car in Fig. 4. Azimuth-plane radiation patterns for three settings are compared in Fig. 5: antennas with the rim of sunroof, antennas with the whole car roof, and antennas with the whole car. As the size of ground plane increases, more high frequency interference patterns appear in the radiation patterns. For the last setting, a seven-level MLFMA requires 931 MB of memory and 4 hours of CPU time to solve the 177,734-unknown problem.

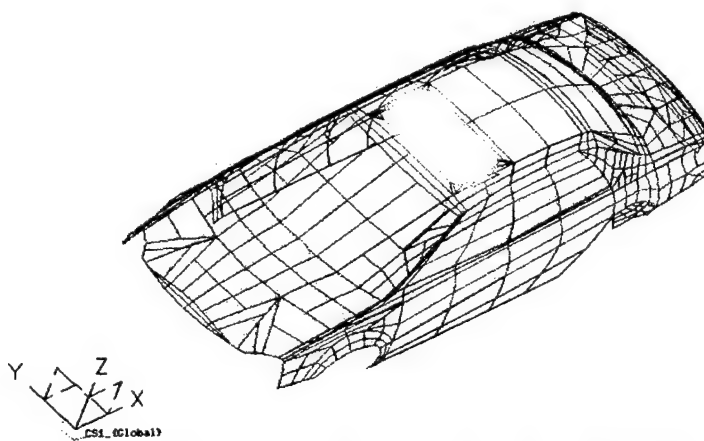


Figure 4. A full-sized car for mounting the antenna tray.

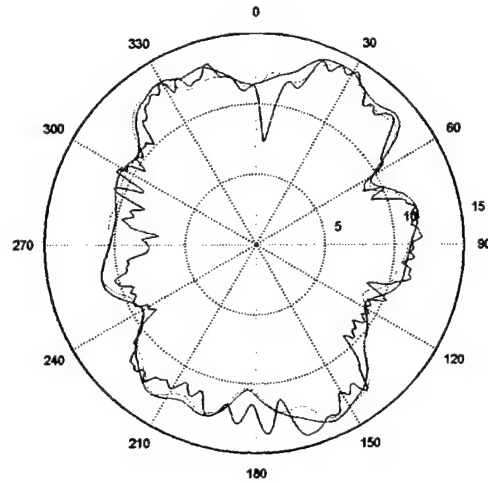


Figure 5. Radiation patterns of antennas on different ground planes. Antennas with the rim of sunroof (red), antennas with the whole car roof (green), and antennas with the whole car (blue).

It is impossible to simulate complex antenna structures mounted on a whole car without using SBI. Even if BN and BDP are applied, the convergence rate of the generalized minimal residual (GMRES) solver without SBI is still extremely slow (Fig. 6). Only SBI enables us reach an error bound of 0.01 within reasonable simulation time.

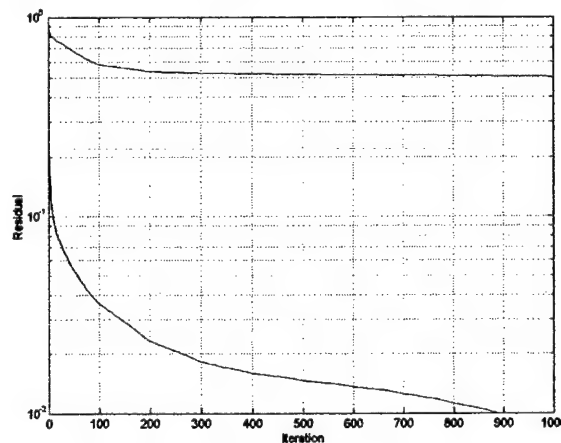


Figure 6. Residual for GMRES solvers with (blue) and without (green) a SBI preconditioner.

#### 4. Conclusion

A general VSIE-MLFMA algorithm is presented for solving antenna radiation and scattering in a complex environment. In order to reduce the iteration number for solving ill-conditioned radiation problems, the BN and SBI preconditioners are applied. The algorithm enables us to solve real-world antenna problems within a reasonable time on a workstation.

## 5. References

- [1] B. M. Notaros, M. L. Djordjevic, B. D. Popovic, and Z. Popovic, "Rigorous EM modeling of cars and airplanes," Proc. 1999 IEEE Radio and Wireless Conference, pp. 167-170, Denver, CO, Aug. 1-4, 1999.
- [2] M. L. Djordjevic and B. M. Notaros, "Highly efficient large-domain moment method analysis and CAD of radio frequency antennas mounted on or situated in vehicles," Proc. 2000 IEEE Vehicular Technology Conference, vol. 5, pp. 2373-2377, Boston, MA, Sep. 24-28, 2000.
- [3] U. Jakobus and F. J. C. Meyer, "A hybrid physical optics/method of moments numerical technique: theory, investigation and application," Proc. 4<sup>th</sup> IEEE AFRICON, vol. 1, pp. 282-287, Stellenbosch, South Africa, Sep. 24-27, 1996.
- [4] M. R. Daginnus, A. Stephan, and R. P. Kronberger, "Simulation and measurement results of complex integrated vehicle antenna systems for premium audio reception," SAE 2001 World Congress, Detroit, MI, Mar. 5-8, 2001.
- [5] H. Y. Chao, W. C. Chew, and C. C. Lu, "A fast volume-surface integral equation solver for radiation and scattering from wire antennas, IBC surfaces, and Inhomogeneous dielectric objects," 2002 IEEE AP-S International Symposium, San Antonio, Texas, June 16-21, 2002.
- [6] R. F. Harrington and J. R. Mautz, "An impedance sheet approximation for thin dielectric shells," IEEE Trans. Antennas Propagat., pp.531-534, July 1975.
- [7] J. M. Song, C. C. Lu, and W. C. Chew, "MLFMA for electromagnetic scattering by large complex objects," IEEE Trans. Antennas Propagat., vol. 45, pp. 1488-1493, Oct. 1997.

# Design Study for Three-Frequency, Dual-Polarized FSS Subreflector

Katherine E. Zink\*  
Orbital Sciences Corporation  
21700 Atlantic Blvd.  
Dulles, VA 20166  
zink.katherine@orbital.com

Daniel H. Schaubert  
Antenna Laboratory  
Electrical and Computer Engineering  
University of Massachusetts  
Amherst, MA 01003  
schaubert@ecs.umass.edu

\*Formerly at University of Massachusetts

**Abstract:** A three-frequency, dual-polarized FSS subreflector is needed to combine an existing 33- and 95-GHz feed with a new 13 GHz feed, creating the next generation of polarimetric cloud radars. The millimeter wave operating frequencies limit the choice of dielectric materials and fabrication techniques. This study considers means to achieve good, dual-polarization transmission at 13-GHz and good, dual-polarization reflection at 33 and 95 GHz. Crossed dipoles that are tightly coupled to linear dipoles provide an easily fabricated surface with control over both the reflection properties and the cross-polarization. The paper shows predicted performance of the FSS, which met the goals at 33 and 95 GHz. Means to improve the performance at 13 GHz are suggested.

## 1. Introduction

The University of Massachusetts operates a dual-frequency, dual-polarized radar system for cloud studies. The radar operates at 33 and 95 GHz in a dual-linear polarimetric mode. The primary aperture of the antenna system is a 1-m polystyrene lens with  $F/D = 1.8$ . A custom feed was designed to incorporate both frequencies and polarizations so that alignment of the beams would be insured so long as the feed remains in tact. A program of study was undertaken to design an upgrade to the radar system to (1) increase the aperture to 2 meters and (2) add a 13-GHz dual-polarized channel. A candidate design employing a 2-m offset reflector and the existing 33/95 GHz feed was proposed, Fig. 1. The critical component of this design is a three-frequency, dual-polarized FSS that separates the new 13 GHz signal from the 33/95 GHz signals. Prior to undertaking the design of a complete 2-m, offset antenna system, the properties of the FSS were studied to determine if performance goals could be met.



This paper describes some of the FSS configurations that were considered and some lessons learned during the study. A critical aspect of the FSS design is its performance at the millimeter wave frequencies, 33 and 95 GHz. The wide separation of these frequencies and the short wavelengths are likely to create problems for design and fabrication of the FSS. Our study focused on these two frequencies and emphasized printed elements on a readily available substrate (Duroid 5880) known to be useful up to 95 GHz. These restrictions eliminated some of the traditional FSS design parameters, but led to some interesting results that may be useful in other FSS applications. In particular, a combination of crossed dipoles and linear dipoles separated by a thin dielectric layer can separately control the reflection frequency and cross-polarization level of a dual-resonant FSS. The 13-GHz performance of the various FSS structures is included in the study, but further optimization for this frequency was not pursued.

At the conclusion of this study, a three-frequency FSS was obtained that met stringent reflection specifications at 33 and 95 GHz, and performs moderately well at the transmission frequency of 13 GHz. Improvement of the 13-GHz performance may be possible by methods discussed in the paper.

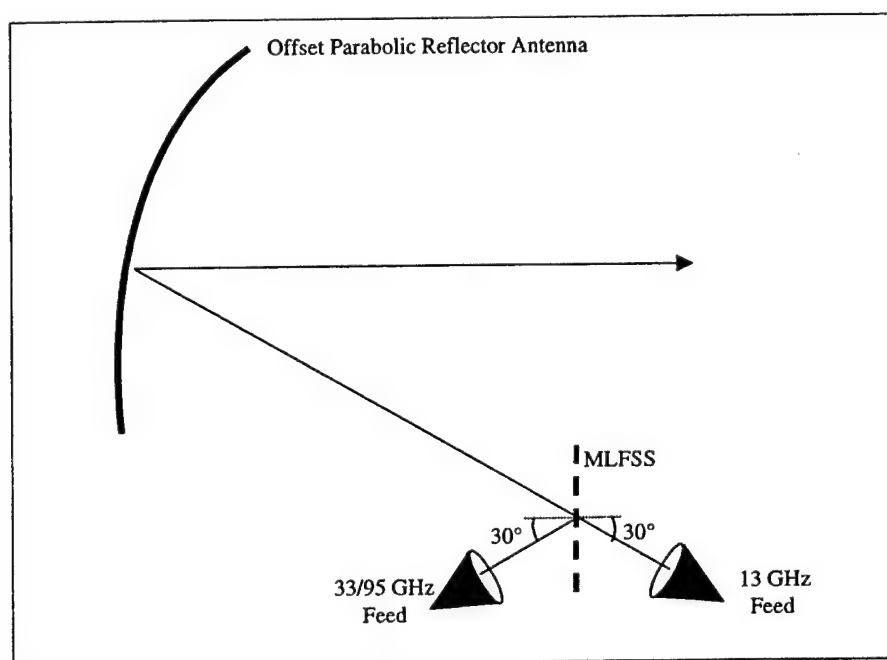


Figure 1. Proposed configuration for three-frequency, dual-polarized antenna system. A multi-layer FSS (MLFSS) is used to separate the beams into two channels.

## 2. Requirements

The requirements for the three-frequency antenna feed system are summarized in Table 1. The feed system should have equal beamwidths at all three frequencies in order to fully utilize the 2-m aperture at all frequencies.

Table 1. Antenna Feed Requirements

Frequencies	13, 33 and 95 GHz
Bandwidth	200 MHz at each frequency
Polarization	Dual-linear (H and V)
Beamwidth @ -10dB	$29^{\circ} \pm 3^{\circ}$
Integrated Cross-pol over -10 dB beamwidth	< -30 dB (two-way)
Reflection & Transmission Loss	< 0.5 dB for ideal materials
Phase Center Coincidence	< $45^{\circ}$

The integrated cross-polarization requirement is necessary to extract depolarization information about cloud particles within the illuminated volume. Because the feed has a -10 dB beamwidth of  $29^{\circ}$ , the planar FSS is required to operate over this range of incidence angles. Geometrical considerations of the antenna system suggested that the FSS be designed to operate for angles of incidence ranging from  $15^{\circ}$  to  $45^{\circ}$ .

For the purposes of the design study, the bandwidth of the FSS was defined as the range of frequencies over which reflected (transmitted) power is greater than -0.5 dB relative to the incident power and the reflection (transmission) coefficient phase varies by less than  $45^{\circ}$ . Additionally, the difference in the reflection coefficient phases for the 33 and 95 GHz reflection bands should be limited to  $45^{\circ}$ . These phase requirements insure that the reflector system can be properly focused at all three frequencies, but also dictate that the 33 and 95 GHz reflecting layers should be very close together to avoid strong angular variation of the phases at 33 and 95 GHz. Finally, to avoid the need to compute integrated cross-polarization of the FSS system, which depends on the details of the feed pattern, a peak limit of -30 dB is considered for cross-polarization. This is slightly more restrictive than the integrated cross-polarization specification in Table 1, but experience with the original dual-frequency antenna showed that the integrated cross-polarization is usually only 2-3 dB better than the peak value.

### 3. Design Study

#### *Background*

The proposed configuration in Fig.1 requires that the FSS transmit the lowest frequency, 13 GHz, and reflect both the 33 and 95 GHz. A complementary configuration would interchange the locations of the horn feeds and reverse the reflection and transmission properties of the FSS. After some preliminary analysis, the configuration in Fig. 1 was selected because it seems to fulfill the requirements better than a complementary screen. Because of the requirement to reflect two frequencies and transmit a third, a multi-layer FSS with multiple resonant frequencies was required. Past experience with multi-layer screens comprised of linear dipoles (single polarization) and with crossed dipoles led to the choice of crossed dipoles for this design study. A means to achieve two-frequency reflection is illustrated by the dual-resonant FSS comprised of separated layers of crossed dipoles, such as that in Fig. 2.

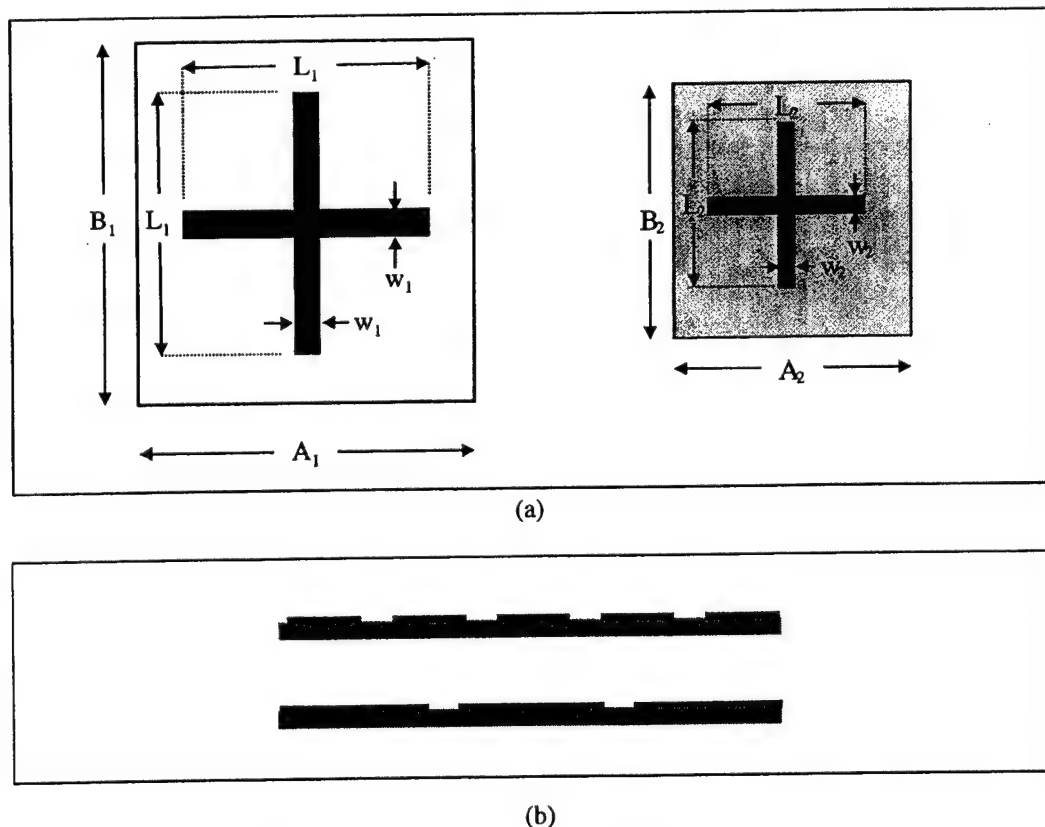


Figure 2. Dual-resonant crossed dipole FSS.

The plot in Fig. 3 depicts the reflection coefficient of a typical dual-resonant, multi-layer FSS. By adjusting various parameters of the multi-layer FSS, the frequencies and bandwidths of the reflection and transmission bands can be

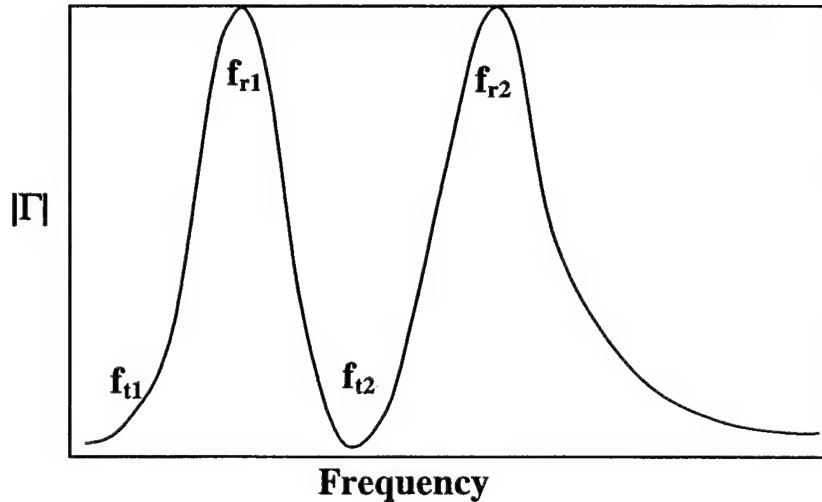


Figure 3. Sample reflection curve for dual-resonant, multi-layer FSS.

controlled. However, not all combinations of reflection and transmission frequencies are feasible. For the proposed antenna configuration in Fig. 1, the band spacings are

$$\begin{aligned} f_{r1} / f_{t1} &= 33 / 13 = 2.54 \\ f_{t2} / f_{r1} &= 95 / 33 = 2.88. \end{aligned}$$

These requirements are challenging because:

- 1) The low-frequency transmission band,  $f_{t1}$ , occurs because the dipoles become electrically small so that long wavelengths passing through the screen are only slightly affected. The lower frequency of 13 GHz is not sufficiently below the required resonance of the longer dipoles (33 GHz) for this to occur. This problem was not a major consideration in the present study. It is addressed briefly at the end of the paper.
- 2) The large ratio of the two reflection frequencies makes it difficult to obtain good reflection properties at both frequencies and avoid grating lobes at 95 GHz.
- 3) The optimum cross-polarization performance of the crossed dipole FSS does not occur at the frequencies where optimum reflection occurs.
- 4) Although the dielectric layers surrounding and supporting the printed elements significantly affect FSS performance, the availability of dielectric materials suitable for use at 95 and 33 GHz was considered to be a problem, so *this study*

*concentrated on ways to improve FSS performance by introduction of additional layers of dipoles printed on standard substrates.* Such a configuration is believed to be a viable means to fabricate a reliable FSS operating at millimeter wavelengths.

In the parameter study below, single-layer crossed dipole FSS are examined first to illustrate the dependence of cross-polarization on element dimensions and unit cell size. These examples are tuned near 33 GHz. Next, a second high-frequency FSS layer is added to obtain a dual-resonant FSS. This 95-GHz layer is separated from the 33-GHz layer by a thin (10 mil) Duroid substrate. Significant power is lost to grating lobes, degrading the high-frequency reflection band. Both rectangular and triangular grids are studied, but neither is satisfactory. The best design employs a 10-mil foam layer plus a 10-mil Duroid layer to separate the crossed dipole layers. This reduces the coupling between dipole layers and significantly reduces the power lost to grating lobes such that proper operation of the high frequency reflection band is obtained.

Two problems are common throughout the cases described above. First, the cross-polarization of the transmit band (13 GHz) is  $-20\text{dB}$  on average and the power transmitted does not consistently meet the  $-0.5\text{ dB}$  requirement. The second problem relates to the cross-polarization of the reflection bands. The optimum cross-polarization is obtained at a lower frequency than the optimum reflection. An additional 33-GHz FSS layer is added, consisting of linear dipoles printed on the opposite side of the 10-mil substrate and offset from the center of the crossed dipoles. These two layers are tightly coupled, producing dipoles with effective lengths that are greater than their physical lengths, and that may be greater than the unit cell size. The extra degrees of freedom obtained in this way allow the dipole length to be tuned so that the frequency of optimal cross-polarization and the resonant frequency coincide.

### ***Single Layer Crossed Dipole FSS***

Single layer crossed dipole FSS are examined to understand the effect of dipole dimensions and cells sizes on cross-polarization performance. The dimensions of the FSS are defined in the unit cell shown in Figure 4. Figure 5 shows the transmitted and reflected power, phase, and cross-polarization for  $A = 4.0\text{ mm}$  and  $L = 3.45, 3.55, 3.65, \text{ and } 3.75\text{ mm}$ . The dipole widths are equal to 10% of the dipole lengths and the elements are printed on a 10-mil substrate with  $\epsilon_r = 2.2$ . The frequency response is plotted for incident angles of  $\theta = 45^\circ$  and  $\phi = 45^\circ$ , where the worst-case cross-polarization performance occurs.

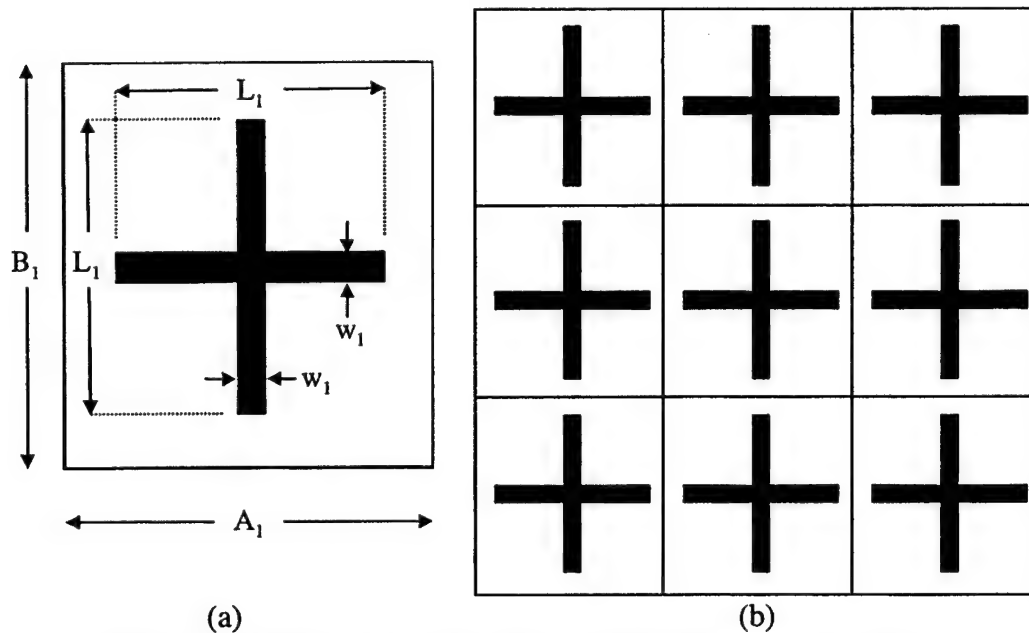


Figure 4. Dimensions of single-layer crossed dipole FSS for 33 GHz.

As expected, the resonant frequency decreases as  $L$  increases. For the single layer cases examined here,  $L = 0.40\lambda_r$ , where  $\lambda_r$  is the wavelength corresponding to the resonant frequency in each case. The reflected field in the reflection band is close to that of a perfect ground plane, where nearly all of the power is reflected and the phase is equal to  $180^\circ$  at the resonant frequency. The cross-polarization response in the reflection band has a distinct null for each FSS, leaving a narrow bandwidth over which the  $-30$  dB cross-polarization requirement is met. Unfortunately, the null of the cross-polarization occurs slightly below the resonant frequency of each FSS. For these single layer cases,  $L = 0.38\lambda_x$ , where  $\lambda_x$  is the wavelength corresponding to the frequency of the cross-polarization null.

The power transmitted at 13 GHz decreases as  $L$  increases due the downward shift in resonant frequency. Nonetheless the transmitted power fulfills the  $-0.5$  dB requirement. The phase of the transmitted wave varies slowly with frequency, which is desirable to minimize defocusing in the dual-reflector system. The cross-polarization at 13 GHz also increases as  $L$  increases, varying between  $-25.6$  and  $-22.8$  dB as  $L$  increases from 3.45 mm to 3.75 mm. This will be a limiting factor throughout the design study.

The size of the unit cell has a less pronounced effect on FSS performance. The dipole dimensions were fixed to  $L_1 = 3.65$  mm and  $w_1 = 0.365$  mm such that the reflected power is greater than  $-0.5$  dB at 33 GHz. The unit cell size is varied,

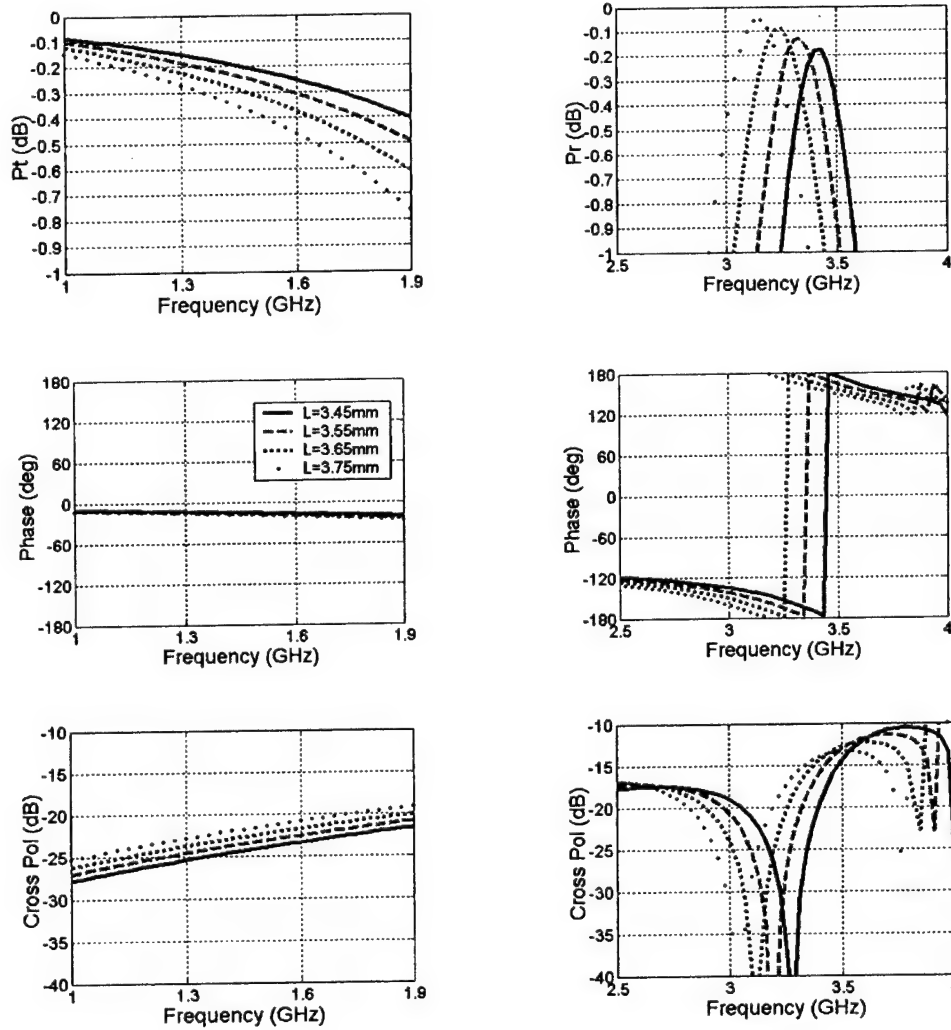


Figure 5. Single layer crossed dipole FSS. Reflected and transmitted power (top), phase (center), and cross-pol (bottom). Incident field polarized along x-directed dipole,  $\theta = 45^\circ$ ,  $\phi = 45^\circ$ .  $A_1 = 4.0$  mm,  $\epsilon_{r1} = 2.2$ ,  $t = 10$  mil,  $w_1 = 0.10 * L_1$ .

$A_1 = 3.75, 3.82, 3.90$ , and  $4.10$  mm. The analysis was carried out for x-polarized incidence with  $\theta = 45^\circ$  and  $\phi = 45^\circ$ . The results are plotted in Figure 6.

For a smaller cell size, the separation distance between the dipoles is smaller and mutual coupling makes the dipole lengths effectively larger, reducing the resonant frequency. Therefore, the resonant frequency increases slightly as  $A$  increases. Furthermore, the peak power in the reflection band decreases as  $A$  increases and the FSS becomes a less effective ground plane. Finally, Fig. 6 shows that the null

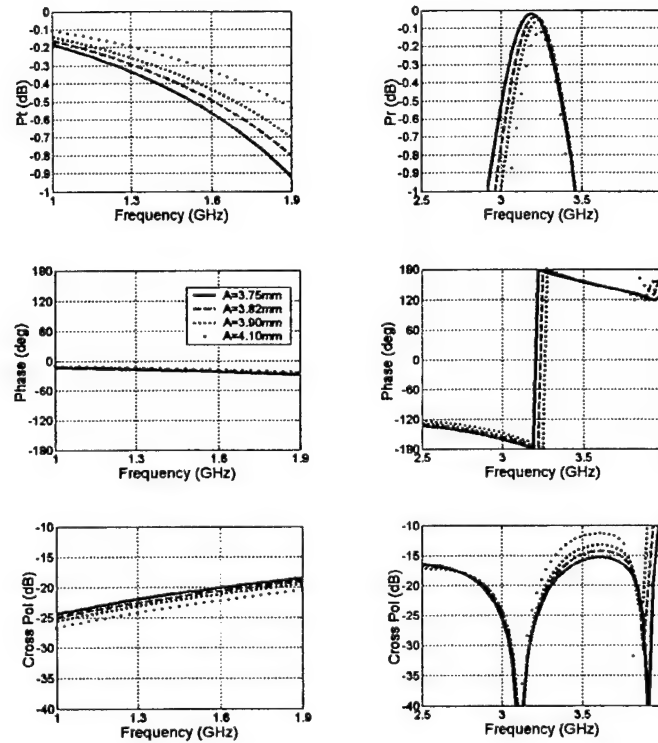


Figure 6. Single layer crossed dipole FSS. Reflected and transmitted power (top), phase (center), and cross-pol (bottom). Incident field parallel to one leg of dipole,  $\theta = 45^\circ$ ,  $\phi = 45^\circ$ .  $L_1 = 3.65$  mm,  $w_1 = 0.365$  mm,  $\epsilon_{r1} = 2.2$ ,  $t = 10$  mil.

in the cross-polarization is not dependent on the cell size for a single layer FSS.

The power transmitted at 13 GHz increases as  $A$  increases. This is due to the increased resonant frequency as  $A$  increases and also due to the decreased density of the dipole elements. The transmitted power fulfills the  $-0.5$  dB requirement and the phase of the transmitted wave varies slowly with frequency for all cases of unit cell size. The cross-polarization at 13 GHz also decreases as  $A$  increases, varying between  $-22.0$  and  $-24.3$  dB as  $A$  increases from 3.75 mm to 4.1 mm.

Two problems that arise are illustrated from the single layer studies described above. First, the location of the null in the cross-polarization field is highly dependent on the dipole length, as is the resonant frequency. For the single layer cases presented,  $L = 0.40\lambda_r = 0.38\lambda_x$ . The second problem is the poor cross-polarization performance in the transmit band. As noted in the Introduction, further optimization for 13 GHz is not pursued in this study.



### *Double-layer Crossed Dipole FSS*

A high-frequency FSS layer is added to the structure in this section. Single-layer studies showed that a crossed dipole FSS with  $L_2 = 1.2$  mm,  $w_2 = 0.12$  mm, and  $a_2 = b_2 = 1.28$  mm was suitable for operation at 95 GHz. The unit cells of each layer are shown in Figure 7a and a side view of the MFLSS is given in Figure 7b. The high-frequency layer is printed on the incident-field side of the substrate, the low-frequency layer is opposite. Hence, the FSS layers are separated by a 10-mil substrate. The resulting subarray, according to which the FSS is periodic, is illustrated in Figure 7c, along with a summary of structural parameters and of the major findings for this MLFSS configuration. Figure 8 shows the reflected and transmitted power, phase, and cross-polarization for the incident field parallel to a dipole leg and  $\theta = 45^\circ$ . The analysis was run for  $\phi = 0, 45$ , and  $90^\circ$  (E-, D-, and H-plane cuts). The low frequency layer dimensions are  $a_1 = b_1 = A = B = 3.82$  mm,  $L_1 = 3.65$  mm, and  $w_1 = 0.365$  mm, which were shown from the single-layer studies to result in a reflection band centered at 32 GHz.

For the closely spaced double-layer FSS, the high-frequency FSS layer significantly affects the lower reflection band. Specifically, coupling between the high- and low-frequency dipoles increases the effective length of the low-frequency dipoles, reducing the resonant frequency of the bottom layer to 27.5 GHz from the 32 GHz observed in the single-layer case. As in the single-layer cases described in the previous section, the null in the cross-polarization occurs at 26 GHz, below the resonant frequency of 27.5 GHz. Hence,  $L_1 = 0.33\lambda_{r1} = 0.32\lambda_{x1}$  for this closely spaced double-layer FSS.

The low-frequency transmitted power is decreased as a result of the shift in resonant frequency and no longer meets the  $-0.5$  dB requirement at 13 GHz. The addition of the high-frequency layer also most likely plays a role in the degradation of the transmitted power. As in the single-layer cases, the cross-polarization in the transmit band is high, with a worst case of  $-19$  dB in the diagonal plane.

The 95 GHz reflection band is severely degraded as compared to its single-layer case. The resonant frequency, as shown by the phase response, varies from 91 GHz in the H-plane to 98 GHz in the E-plane. The null in the cross-polarization for the high-frequency layer occurs at 90 GHz, which again is lower than the resonant frequency. For the high-frequency layer,  $L_2 = 0.37\lambda_{r2} = 0.36\lambda_{x2}$ . The degradation of performance is caused by the large amount of power coupled into grating lobes. Figure 9 shows that a large fraction of the power is lost to grating lobes between 85 and 100 GHz.

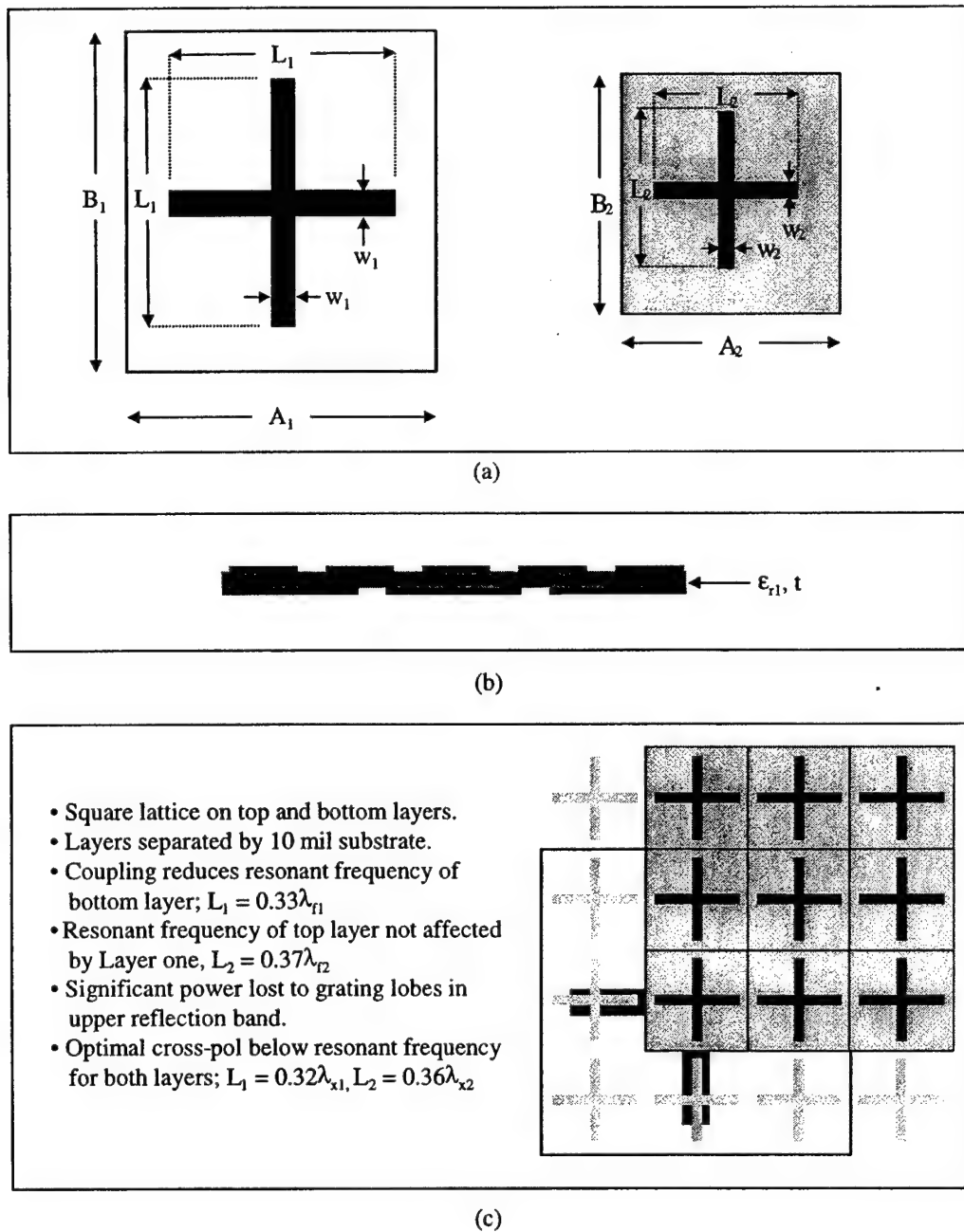


Figure 7. Double layer crossed dipole FSS. (a) Unit cells of layers one and two. (b) Side view of MLFSS. (c) Subarray of double-layer FSS and summary of results.

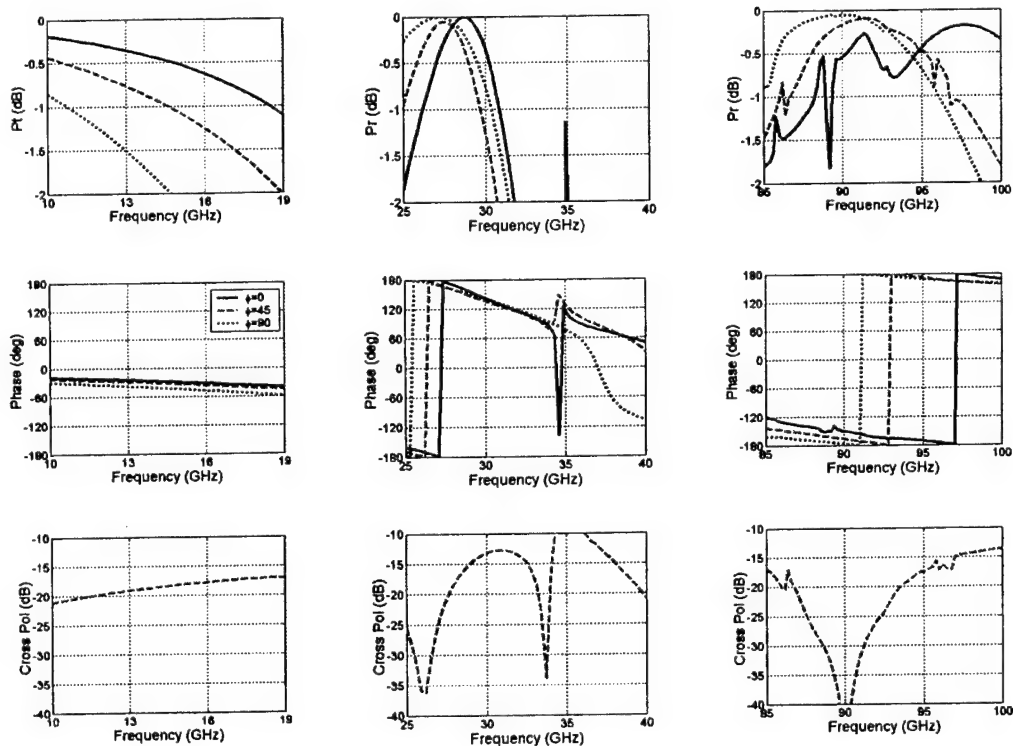


Figure 8. Double layer crossed dipole FSS. Reflected and transmitted power (top), phase (center), and cross-pol (bottom). Incident field parallel to a dipole leg,  $\theta = 45^\circ$ .  $L_1 = 3.65$  mm,  $w_1 = 0.365$  mm,  $L_2 = 1.2$  mm,  $w_2 = 0.12$  mm,  $A = B = a_1 = b_1 = 3.82$  mm,  $a_2 = b_2 = 1.28$  mm,  $\epsilon_{r1} = 2.2$ ,  $t = 10$  mil.

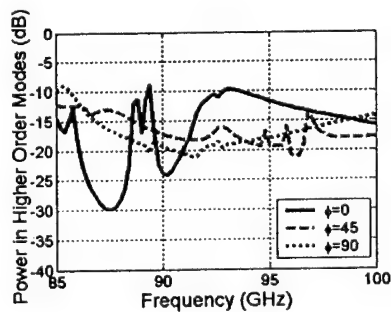


Figure 9. Double layer crossed dipole FSS. Power lost to grating lobes. Incident field parallel to dipole leg,  $\theta = 45^\circ$ .  $L_1 = 3.65$  mm,  $w_1 = 0.365$  mm,  $L_2 = 1.2$  mm,  $w_2 = 0.12$  mm,  $A = B = a_1 = b_1 = 3.82$  mm,  $a_2 = b_2 = 1.28$  mm,  $\epsilon_{r1} = 2.2$ ,  $t = 10$  mil

### ***Double-layer Crossed Dipole FSS with Modified Grid Configuration***

Two steps were taken in order to improve the reflection and transmission band properties of the double-layer FSS.

- 1) The element dimensions on the low-frequency layer were adjusted to  $L = 2.8$  mm and  $w = 0.28$  mm to increase the resonant frequency to 33 GHz. The cell size was set at  $A = B = 3.1$  mm, which is relatively large compared to the dipole length, in order to increase the transmitted power at 13 GHz.
- 2) A triangular lattice was incorporated on layer two in order to increase the density of dipoles per unit cell and improve the 95 GHz reflection band properties. This was achieved by setting the unit cell on layer two to  $A = B = 1.55$  mm, but defining the basis functions for two dipoles per unit cell. One dipole is centered in the unit cell and the second dipole is offset by  $A/2 = 0.775$  mm in the x- and y- directions. The dipole dimensions on layer two are  $L = 1.4$  mm and  $w = 0.10$  mm.

The unit cells, side view, and subarray for this case is illustrated in Figure 10a, 10b, and 10c, respectively. The conclusions drawn from this MLFSS are also summarized in Figure 10c.

Figure 11 shows the results of the double-layer FSS with the modified grid configuration. The common bandwidth in the reflection band is centered at 33 GHz as opposed to 27 GHz seen in the previous case. The frequencies where the phase of the reflected wave is  $180^\circ$  no longer corresponds to the frequencies of peak reflected power, however the phase difference between the 33 and 95 GHz reflection bands is less than  $45^\circ$ , as required. The null in the cross-polarization occurs at 30.5 GHz, which is below the operating frequency of the lower reflection band;  $L_1 = 0.32\lambda_{r1} = 0.29\lambda_{x1}$ . As a result, the cross-polarization is greater than -20 dB in the lower reflection band.

The 13 GHz transmission band has improved from the previous case, but not enough to meet the -0.5 dB requirement. The worst-case transmitted power is -0.95 dB in the H-plane, and the worst case cross-polarization is only -21 dB.

The upper reflection band is still degraded due to grating lobes, and the null in the cross-polarization is well below the resonant frequency of the upper layer, where  $L_2 = 0.44\lambda_{r2} = 0.40\lambda_{x2}$ .

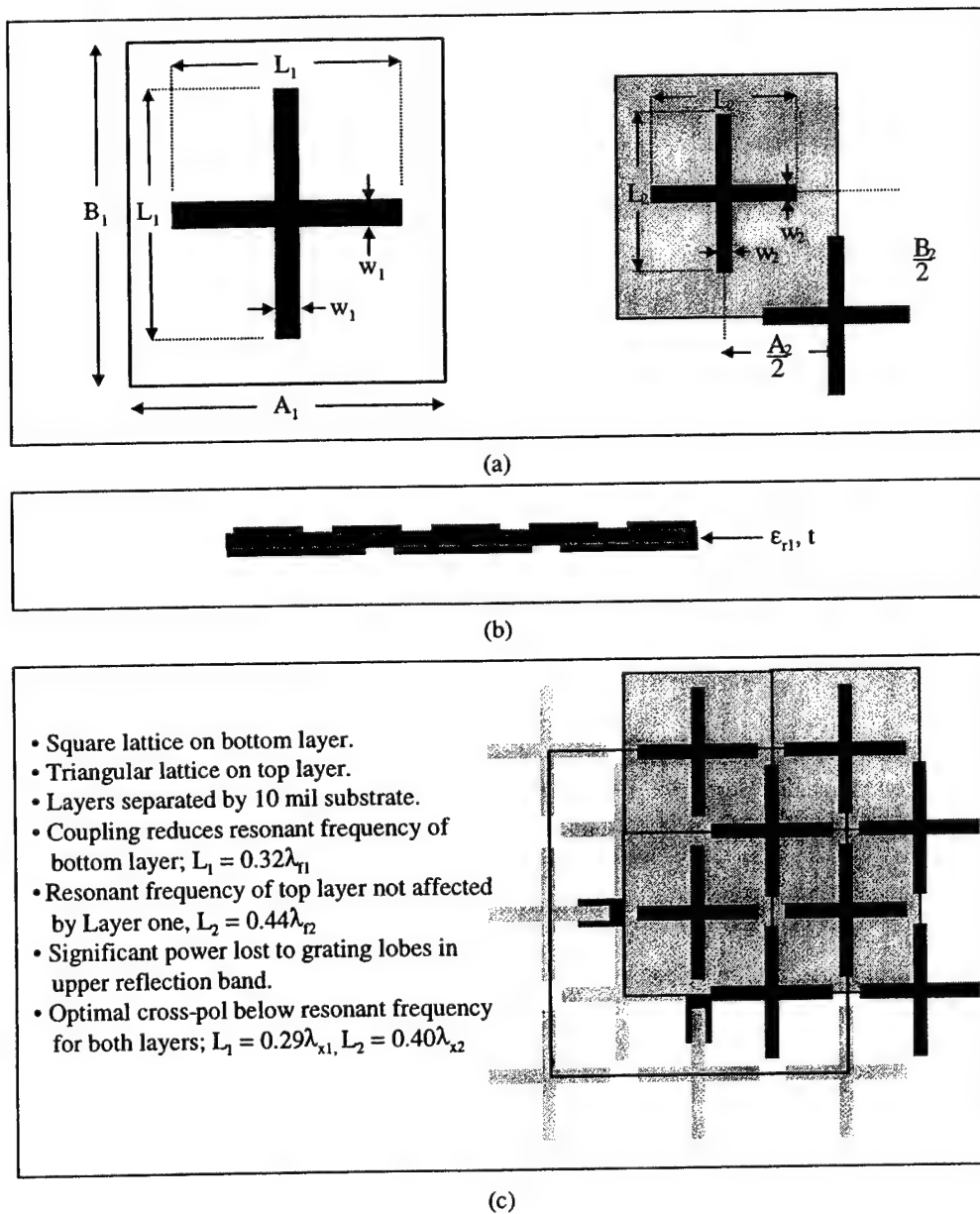


Figure 10. Double layer crossed dipole FSS with modified grid configuration. (a) Unit cells of layers one and two. (b) Side view of MLFSS. (c) Subarray of double-layer FSS and summary of results

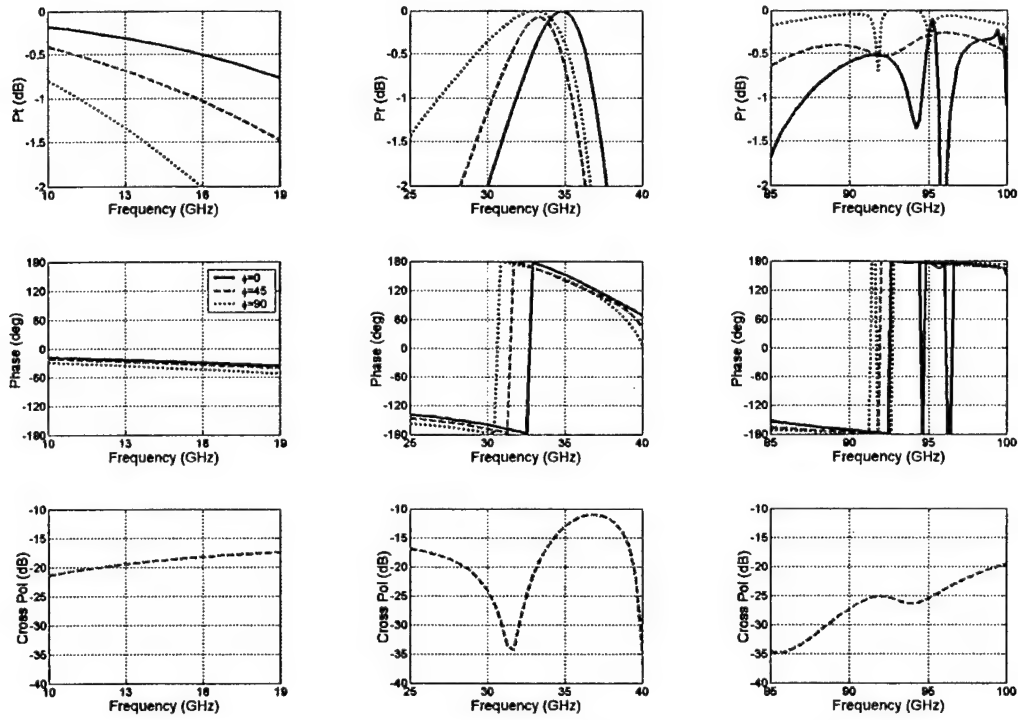


Figure 11. Double layer crossed dipole FSS with modified grid configuration. Reflected and transmitted power (top), phase (center), and cross-pol (bottom). X-polarized incident field,  $\theta = 45^\circ$ .  $L_1 = 2.80$  mm,  $w_1 = 0.28$  mm,  $L_2 = 1.4$  mm,  $w_2 = 0.10$  mm,  $A = B = a_1 = b_1 = 3.10$  mm,  $a_2 = 1.55$  mm,  $b_2 = \Delta_2 = 0.775$  mm,  $\epsilon_{r1} = 2.2$ ,  $t = 10$  mil.

### *Double-layer FSS with modified grid configuration and layer separation*

Previous studies of single-polarized FSS comprised of linear dipoles showed that layer-to-layer coupling of the low-frequency and high-frequency dipoles contributes to grating lobe problems at the high-frequency. To reduce the layer-to-layer coupling in the dual-polarized FSS, the high- and low-frequency layers are separated by a thin foam layer, as shown in the side view of Figure 12b.

One result of separating the FSS layers and reducing the coupling between elements on each layer is that the resonant frequency of the bottom layer approaches that of its corresponding single layer. Three cases of layer one unit cell size and dipole dimensions are plotted in Figure 13 for incident angles of  $\theta = 45^\circ$  and  $\phi = 45^\circ$  and for fixed layer two element dimensions of  $L_2 = 1.4$  mm and  $w_2 = 0.10$  mm. To maintain a commensurate subarray, the unit cell size on the

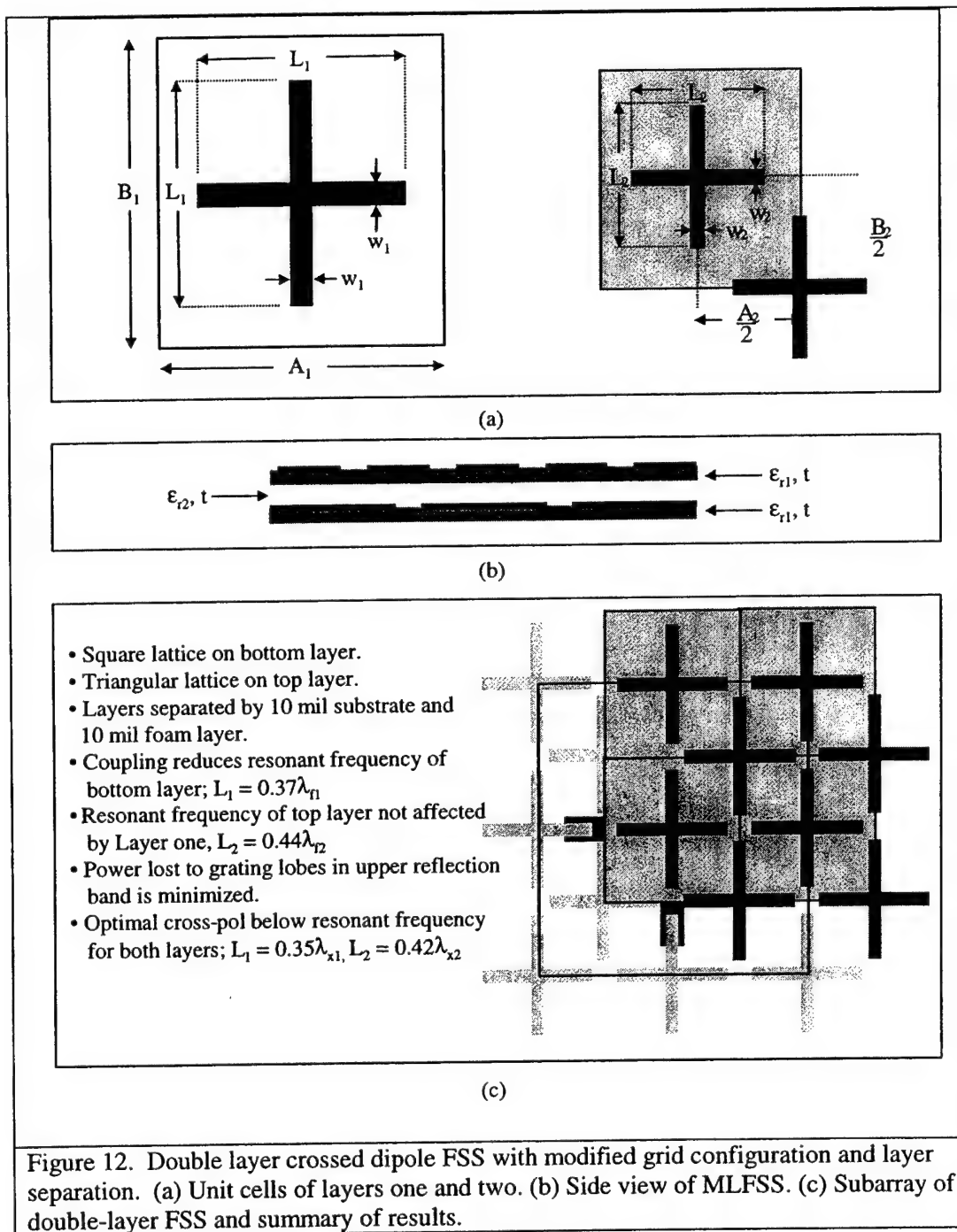


Figure 12. Double layer crossed dipole FSS with modified grid configuration and layer separation. (a) Unit cells of layers one and two. (b) Side view of MLFSS. (c) Subarray of double-layer FSS and summary of results.

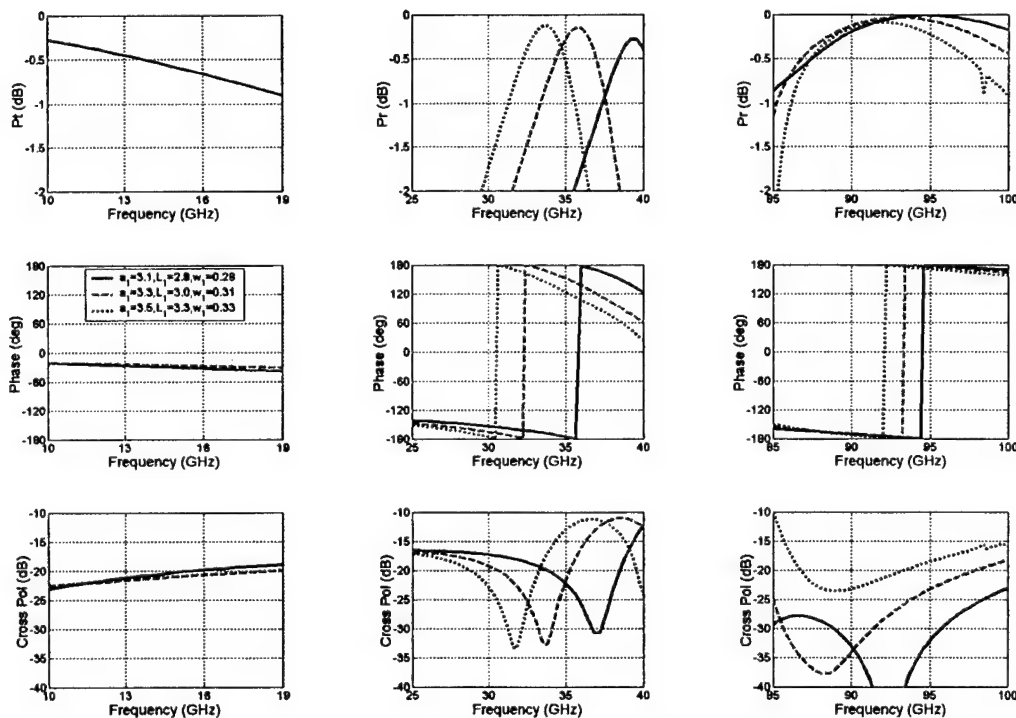


Figure 13. Double layer crossed dipole FSS with modified grid configuration and small layer separation. Reflected and transmitted power (top), phase (center), and cross-pol (bottom). X-polarized incident field,  $\theta = 45^\circ$ ,  $\phi = 45^\circ$ .  $L_2 = 1.4$  mm,  $w_2 = 0.10$  mm,  $\epsilon_{r1} = 2.2$ ,  $\epsilon_{r2} = 1.04$ ,  $t = 10$  mil,  $a_2 = a_1/2$ .

95-GHz layer is adjusted for each 33-GHz layer cell size, hence  $a_2 = b_2 = 1.55$  mm, 1.65 mm, and 1.75 mm, corresponding to  $a_1 = b_1 = 3.1$  mm, 3.3 mm and 3.5 mm.

The double-layer FSS with  $L_1 = 2.8$  mm,  $w_1 = 0.28$  mm,  $a_1 = 3.1$  mm is identical to the double-layer FSS discussed in the previous section with the exception of the 10-mil foam separation layer. Figure 13 shows that the resonant frequency of the bottom layer increases to 39.5 GHz from 33 GHz in the previous case, which is an indication of reduced coupling between the high- and low-frequency layers. Again the resonant frequency is proportional to the dipole length, where  $L_1 = 0.37\lambda_{r1}$  for each double layer case. This relationship is approaching that of a single layer FSS, where  $L = 0.40\lambda_r$ . The cross-polarization is dependent on the dipole length in the same manner as previously described,  $L_1 = 0.35\lambda_{x1}$ .

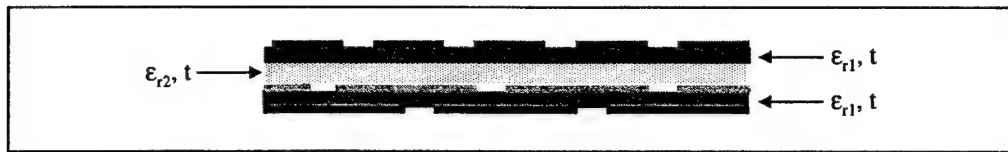


A significant improvement is observed in the high-frequency band. The power lost to grating lobes has decreased and a wide reflection bandwidth is obtained near 95 GHz. The resonant frequency decreases slightly as  $a_2$  increases due to reduced coupling between dipole elements on layer two. The phase of the reflected power is equal to  $180^\circ$  at the frequency where the maximum power is reflected. This phase response is unlike the phase response in the low frequency reflection band, where the phase sweeps through  $180^\circ$  at frequencies below the maximum power reflected. This results in an offset in the upper and lower reflection band phases, but the difference is less than  $45^\circ$ . As in the previous cases, the frequency of optimal cross polarization is below the resonant frequency of the upper layer for  $a_2 = 1.55$  cm. The cross-polarization response for the cases of  $a_2 = 1.65$  and  $a_2 = 1.75$  mm is broader, and a less distinct null is observed below the resonant frequency in each case. The overall cross-polarization level is higher in these cases as compared to  $a_2 = 1.55$  mm, and it increases significantly with increasing cell size of the 95-GHz layer.

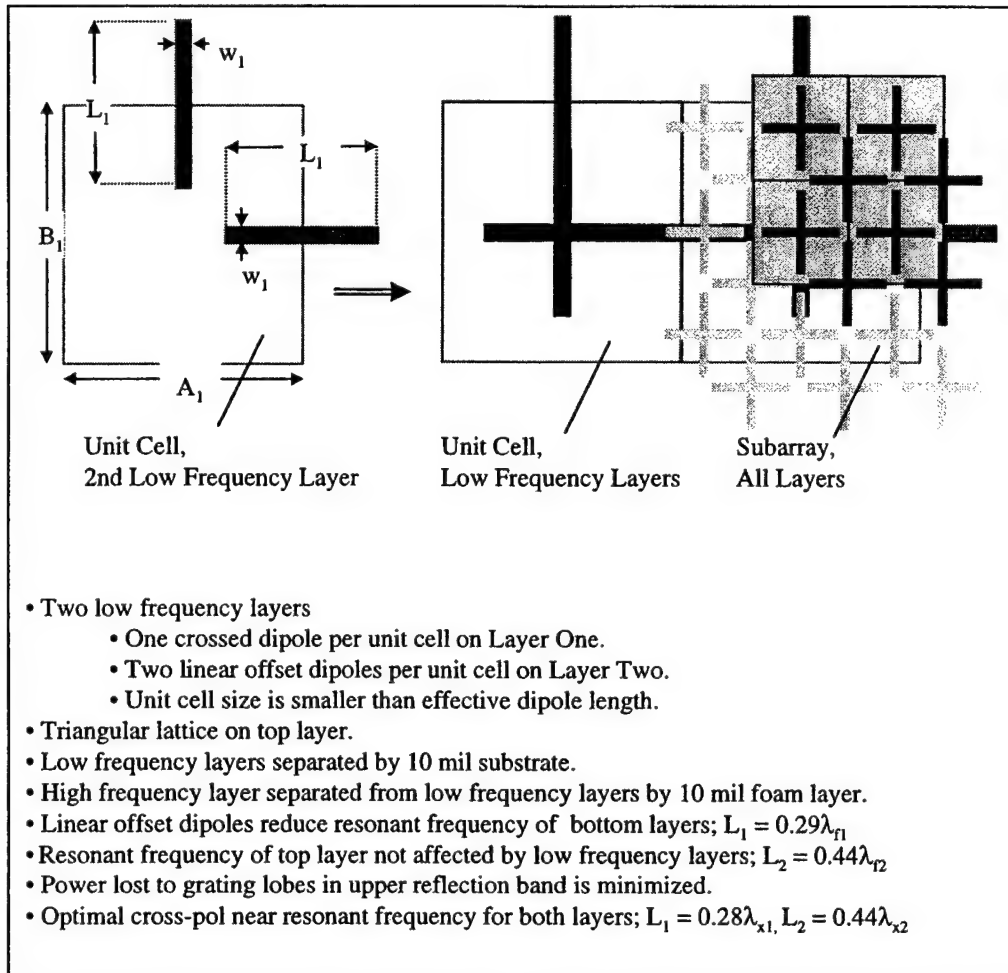
Finally, the behavior of the low-frequency transmission band has not changed significantly. At 13 GHz the transmitted power decreases and the cross-polarization increases as the resonant frequency of layer one decreases. The worst-case cross-polarization at 13 GHz is -20.6 dB.

#### ***Tightly Coupled Crossed and Linear Dipoles for Cross-Polarization Improvement***

The results above illustrate that a new, independent degree of freedom is required to simultaneously optimize co- and cross-polarization. Prior studies of single-polarized FSS showed that a pair of linear dipoles printed on opposite sides of a thin substrate and overlapping can be used to maintain the effective length of the elements while decreasing their physical length. A similar technique is applied here to the dual-polarized FSS. It is shown that this tightly coupled structure provides good co- and cross-polarized performance at 33 GHz and the 95-GHz performance is still very good. Figure 14a shows a side view of the three-layer structure. The low-frequency array layers, printed on opposite sides of a 10 mil substrate, are separated from the high frequency array layer by a 10-mil foam layer. As shown in Figure 14b, the crossed dipole on one side of the low-frequency substrate is centered in the unit cell, and there is one x- and one y-oriented linear dipole on the opposite side, offset by half of the unit cell size along the length of the dipole. In the plots that follow,  $a_1 = b_1 = 3.0$  mm,  $L_1 = 2.5$  mm,  $w_1 = 0.25$  mm,  $a_2 = 1.5$  mm,  $L_2 = 1.4$  mm, and  $w_2 = 0.08$  mm, and the elements of the high-frequency layer are arranged in a triangular lattice.



(a)



(b)

Figure 14. (a) Side view of triple layer FSS. (b) Top view of layer two unit cell and MLFSS subarray. Summary of results.

Figure 15 shows the reflected and transmitted power in the E-, H-, and D-planes for an incident field parallel to the dipoles along the x axis ( $\phi = 0^\circ$ ) and for  $\theta = 15^\circ$ ,  $30^\circ$ , and  $45^\circ$ . Figure 16 shows the phase of the reflected and transmitted wave for the same incident fields. Figure 17 shows the reflected and transmitted cross-polarization in the D-plane for  $\theta = 15^\circ$ ,  $30^\circ$ , and  $45^\circ$ , as well as the power lost to grating lobes in the E-plane for  $\theta = 15^\circ$ ,  $30^\circ$ , and  $45^\circ$ .

A reflection band is centered at 34.5 GHz with a common bandwidth of 1.5 GHz for all incident angles examined. The phase of the reflected field at 33 GHz varies between  $146.1^\circ$  and  $122.1^\circ$  over all incident angles, which satisfies the  $\Delta\Gamma \leq 45^\circ$  bandwidth requirement. Finally, the null in the cross-polarization ranges from 32 to 34 GHz for incident angles between  $15^\circ$  and  $45^\circ$  in the D-plane, and the worst case cross-polarization at 33 GHz is  $-29.5$  dB.

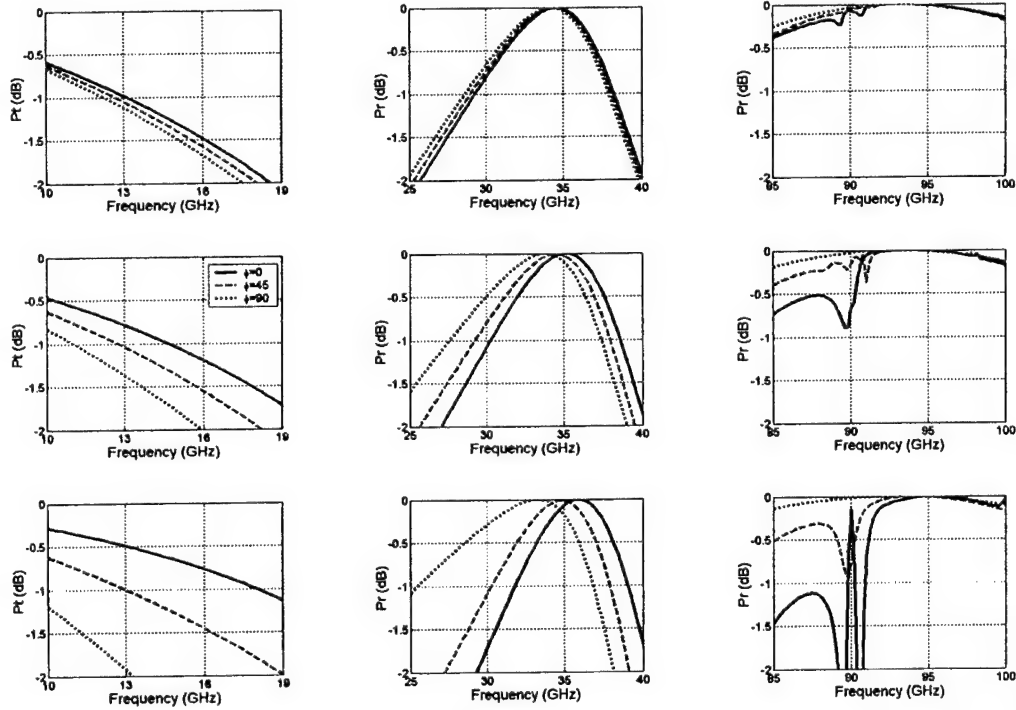


Figure 15. Triple layer crossed dipole FSS. Reflected/transmitted power in the E-, D-, and H-planes for  $\theta = 15^\circ$  (top),  $\theta = 30^\circ$  (center), and  $\theta = 45^\circ$  (bottom). X-polarized incident field.  $a_1 = b_1 = 3.0$  mm,  $a_2 = b_2 = 1.50$  mm,  $L_1 = 2.5$  mm,  $w_1 = 0.25$  mm,  $L_2 = 1.4$  mm,  $w_2 = 0.10$  mm,  $\epsilon_{r1} = 2.2$ ,  $\epsilon_{r2} = 1.04$ ,  $t = 10$  mil.

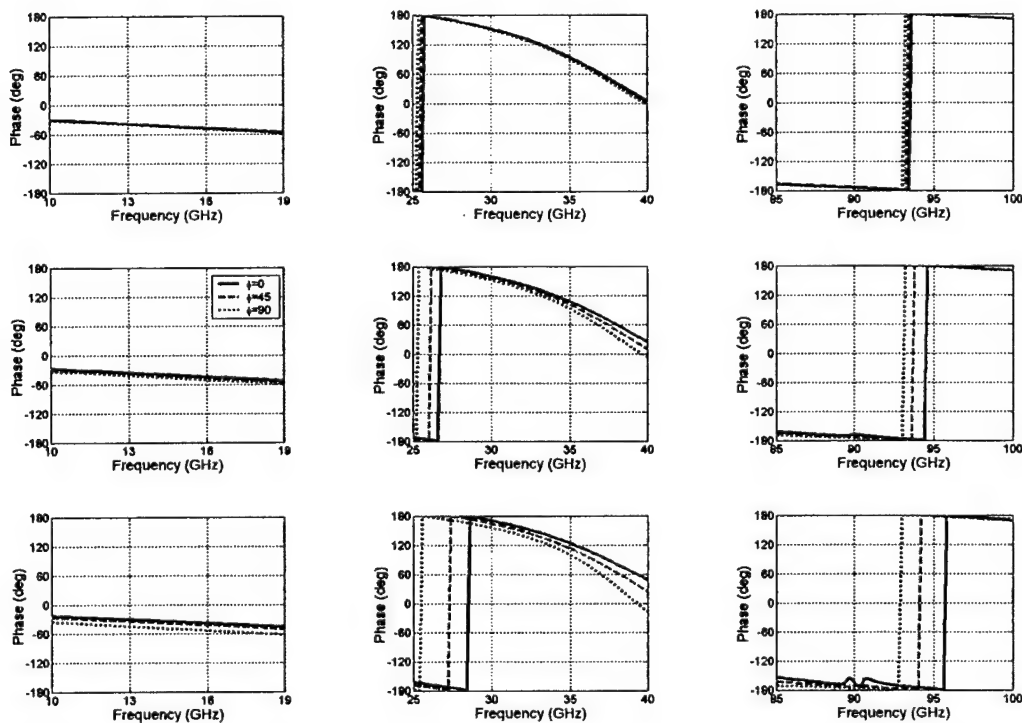


Figure 16. Triple layer crossed dipole FSS. Phase of reflected/transmitted field in the E-, D-, and H-planes for  $\theta = 15^\circ$  (top),  $\theta = 30^\circ$  (center), and  $\theta = 45^\circ$  (bottom). X-polarized incident field.  $a_1 = b_1 = 3.0$  mm,  $a_2 = b_2 = 1.50$  mm,  $L_1 = 2.5$  mm,  $w_1 = 0.25$  mm,  $L_2 = 1.4$  mm,  $w_2 = 0.10$  mm,  $\epsilon_{r1} = 2.2$ ,  $\epsilon_{r2} = 1.04$ ,  $t = 10$  mil.

The high-frequency reflection band at 95 GHz has more than 10 GHz bandwidth. As the incident angle increases a null occurs in the reflected power at about 90 GHz in the E- and D-planes. The power in the higher order grating lobes near this frequency is as high as  $-4$  dB in the E-plane for  $\theta = 45^\circ$ , but it is suppressed 30 dB at 95 GHz. The null in the cross-polarization of the upper reflection band varies between 92 and 94 GHz as the incident angle increases from  $15^\circ$  to  $45^\circ$ , and the worst-case cross-polarization at 95 GHz is  $-37.4$  dB. Finally, as expected, the phase of the reflected wave at 95 GHz is  $180^\circ$ . This is a consequence of the separation of the dipole layers for 33 and 95 GHz, and it could result in some defocusing of the antenna system, but is probably acceptable.

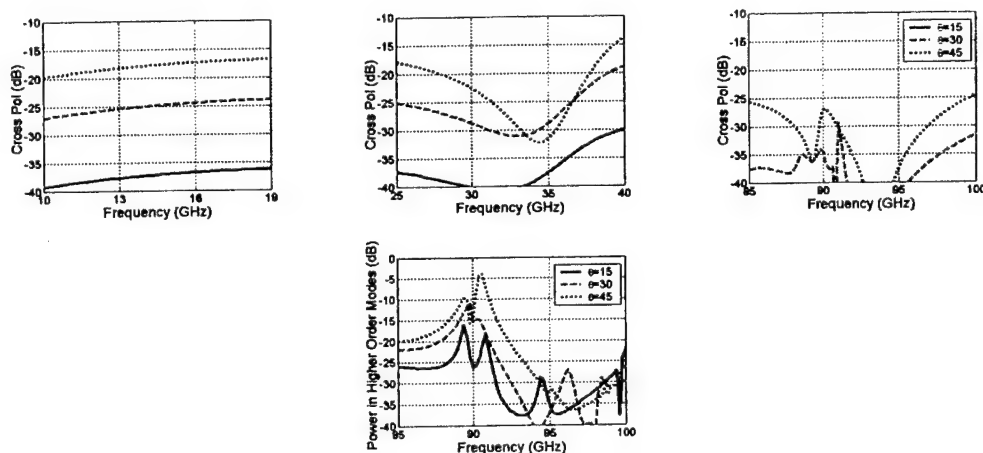


Figure 17. Triple layer crossed dipole FSS. (Top) Cross-polarization in the D-plane for  $\theta = 15, 30^\circ$ , and  $45^\circ$ . (Bottom) Power lost to grating lobes in the E-plane for  $\theta = 15, 30$ , and  $45^\circ$ . X-polarized incident field.  $a_1 = b_1 = 3.0$  mm,  $a_2 = b_2 = 1.50$  mm,  $L_1 = 15, 30$ , and  $45^\circ$ .  $w_1 = 0.25$  mm,  $L_2 = 1.4$  mm,  $w_2 = 0.10$  mm,  $\epsilon_{r1} = 2.2$ ,  $\epsilon_{r2} = 1.04$ ,  $t = 10$  mil.

While the two reflection bands are operating very close to the requirements set forth, the transmit band remains problematic. Due to the increase in the reflection bandwidth with incident angle, the scattering loss of the transmitted signal could be as high as 2.0 dB in the H-plane. The cross-polarization at 13 GHz is -38 dB for  $\theta = 15^\circ$  but increases to -26 dB for  $\theta = 30^\circ$  and further to -18.5 dB for  $\theta = 45^\circ$ .

The performance in the transmit band may be improved by reducing element widths and increasing the unit cell size on 33-GHz layers, in both cases decreasing the density of metallized elements. However, it is unlikely that these factors alone will achieve the desired transmit band performance. The effective dielectric constants of the foam layer and FSS substrates are also degrees of freedom that were not examined and are a potential means of improving overall performance. It is known that dielectric layers stabilize FSS performance over a range of scan angles, so this could lead to satisfactory performance at all three frequencies. Finally, it may be possible to add another 33-GHz layer spaced approximately  $\lambda/8$  below the existing layer. This "traditional" multi-layer FSS has a rapid transition between the lower transmission band and the first reflection band. None of the techniques described in this paragraph have been explored for the three-frequency design.

## Summary

The design of a multi-layer FSS for use as a subreflector in a dual-linear polarized radar system operating at 13, 33 and 95 GHz presented four major challenges. Due to concern about the availability of dielectric materials having the properties needed to optimize the FSS design, methods utilizing dielectric matching were not treated here. Rather, the design was constrained to use readily available substrates known to perform well at millimeter wave frequencies. Rogers Duroid 5880 was selected for the design studies.

Two of the remaining three challenges were successfully overcome by using a dual-resonant FSS comprised of tightly coupled linear and crossed dipoles for the 33 GHz reflecting layer. First, meeting the cross-polarization requirement of  $-30$  dB in for reflection was problematic. In the reflection band resulting from resonance of the crossed-dipole FSS, there is a distinct null where the cross-polarization level falls below  $-30$  dB over a narrow range of frequencies. The location of this null is highly dependent on the dipole length, as is the resonant frequency at which maximum reflection occurs with  $180^\circ$  phase shift. By adding a second layer of (linear) dipoles offset along the axis of the crossed dipole arms and separated by only the thin dielectric substrate, the resonant frequency for reflection can be matched to the cross-polarization null and the  $-30$  dB requirement was met.

Second, grating lobes were eliminated from the 95-GHz operating band. Because of the wide separation of the two reflection bands,  $95/33 = 2.88$ , grating lobes will contaminate any 95-GHz signal that scatters from the 33-GHz layer. Furthermore, the requirement to equalize the reflection coefficient phase of the 33 and 95 GHz signals dictates that the layers should be close together, which increases coupling between them and excitation of 95-GHz grating lobes. The addition of a thin foam spacer (10-mil) was sufficient to reduce grating lobe excitation below  $-30$  dB. It was not necessary to add tightly coupled linear dipoles to the 95-GHz crossed dipole reflector to meet the cross-polarization requirements.

The final challenge to be overcome was transmission loss and cross-polarization in the 13-GHz band. The desired performance was not achieved in this study. Further optimization may have yielded a subreflector meeting all requirements, but this was not pursued due to a change in radar system requirements that necessitated a completely different feed system.

## **CDMA CAPACITY INCREASES MEASURED USING TWO-ANTENNA-RECEIVER HANDSETS**

Michael J. Wengler, Gregory A. Breit, Hussein Hachem,  
Yi-Cheng Lin, Randy Standke, and Ernest Ozaki  
QUALCOMM, Inc.  
5775 Morehouse Drive  
San Diego, California, 92121  
[mwengler@qualcomm.com](mailto:mwengler@qualcomm.com)

**Abstract:** We report on the design, realization, lab testing, field testing, analysis and performance of two-antenna-receiver handsets in CDMA systems. These handsets can receive more than twice the data rate as single-antenna handsets for a given load on the CDMA system. Alternatively, more than twice the number of voice channels can be supported if two-antenna phones replace all single-antenna phones. This excess capacity can be used in conjunction with 4-antenna-receivers at the base-station to nearly double the capacity of CDMA systems. Alternatively, the extra capacity can be used to provide data services without reducing voice capacity of the system. We present two different two-antenna handsets, one for Cellular (~800 MHz) and the other for PCS (~1900 MHz). We present antenna range tests as well as field tests from which capacity increases are derived. We present performance improvement for various receiver architectures, considering the combining of from 4 to 8 fingers in a RAKE receiver, and considering 4 different combining algorithms. We discuss the effect of differences in the Mean Effective Gain (MEG) of the handset antennas. The field tests have been done using two commercial CDMA networks in San Diego as signal sources, one for Cellular frequencies and the other for PCS frequencies.

## 1. Introduction and Summary

---

The Capacity of a CDMA forward-link sector can be doubled if all the handsets in that sector use dual-antenna receivers. Capacity increase comes about because the average signal sensitivity of the phone receiver is effectively doubled through adaptively combining the two antenna-receiver chains. With twice the sensitivity, average base station transmit power per phone can be cut in half. Thus twice as many forward-link calls can be served.

The forward-link capacity is increased incrementally in proportion to the penetration of dual-antenna phones into the system. These phones could be pushed only into areas where forward-link capacity is tight, allowing the deferral of expensive system-wide upgrades. These phones could be selectively subsidized to customers who are identified as high-volume users in crowded sectors in the network.

The capacity increase can be used in three ways. First, where capacity is limited by the forward link, dual-antenna phones will raise total network capacity. Second, dual-antenna phones free up capacity for new forward-link intensive data services. Finally, The forward link capacity increase can be matched by a reverse link capacity increase [1,2].

The primary mechanisms by which the sensitivity is improved are *Aperture Gain*, *Interference Rejection*, and *Diversity Gain*. *Aperture Gain* results from the fact that two antennas absorb more signal power than one. *Interference Rejection* results from combining the antennas with weights chosen so that interfering signals picked up on both antennas tend to cancel each other. *Diversity Gain* arises from the fact that when one antenna is in a fade, the other is probably not.

Qualcomm may soon have available MSM chips in which two antennas can be combined using the Maximal Ratio Combining (MRC) algorithm in a 4-finger RAKE receiver. This configuration should produce forward-link capacity increases of about 50% over a single-antenna handset.

Future Mobile Station Modem (MSM) chips for dual-antenna receivers should 1) implement an Optimum Combining (OC) algorithm and 2) provide a 6-finger RAKE receiver. This configuration will increase forward-link system capacity by more than 100%.

Dual-antenna handsets have a primary antenna that is used for both transmit and receive. A secondary antenna, used for receive only, occupies much less volume than the primary antenna. The secondary antenna's small volume allows it to be put inside the plastics of even very small phones.

The secondary antenna will typically have a lower Mean Effective Gain (MEG) than the primary antenna, because the internal antenna suffers more blockage by



the head and the hand of the user. The lower MEG of the secondary antenna does not have a serious impact on capacity increase from antenna combining.

Fading correlation between the two antennas does not degrade the performance of any of the handsets we have tested. The highest correlations we have measured for all handsets considered is about 40%, even when we put the two antennas as close together as we could physically manage. This is well below the 70% correlation required to degrade performance [4].

## 2. Dual-antenna Phone Design

We have tested a few different dual-antenna designs, at both PCS (1900 MHz) and Cellular (800 MHz) frequencies. All of the test designs had a whip as primary antenna. We tested a few different secondary antennas. But all of the secondary antennas were some form of small-volume antenna that was mounted inside the plastic casing of the phone. The performances of all of the dual-antenna phones that we tested were similar.

In this paper we will describe two phones and the results we achieved with them. One of these phones is designed for PCS frequencies, and the other is designed for Cellular frequencies.

### 2.1 Secondary Antenna for PCS (1900 MHz)

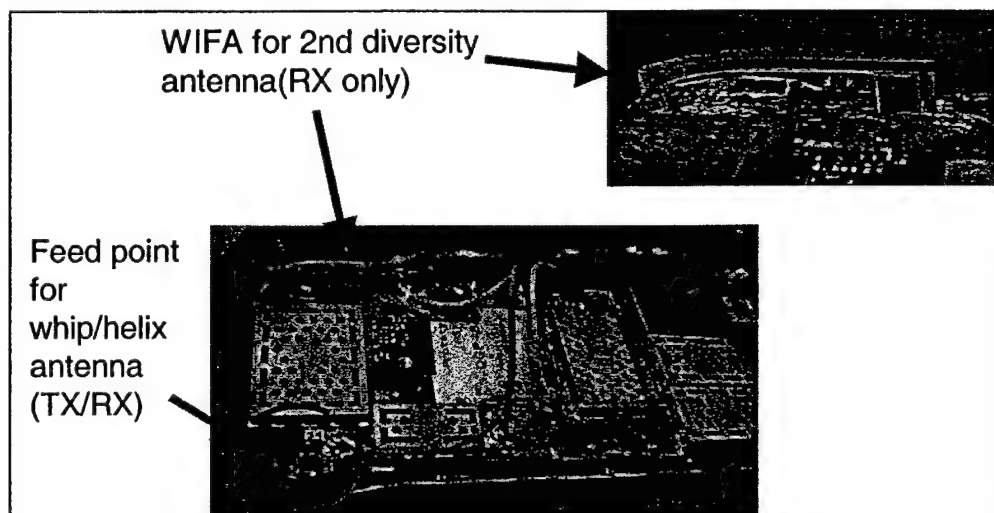


Figure 1 - Secondary WIFA antenna installed in one of the PCS phones.

A view of the secondary antenna for one of the PCS band test phones is shown in Figure 1. The photo is taken of the back of the phone, with the back plastic cover

removed. The secondary antenna is a Wire Inverted-F Antenna (WIFA). Because it is used for receive only, it covers less than half the bandwidth of the primary whip antenna (not shown).

## 2.2 Secondary Antenna for Cellular (800 MHz)

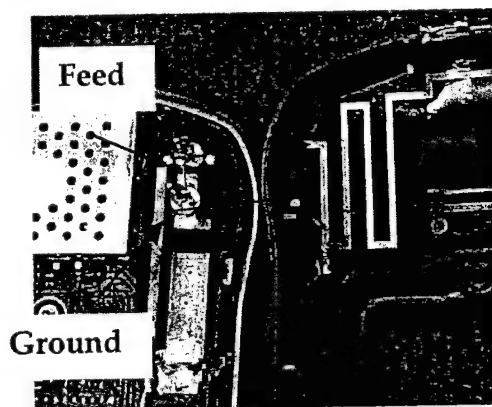


Figure 2 – Secondary MLA antenna for Cellular band phone.

A cellular-band antenna must be about twice the length of a PCS-band antenna. We use a Meander Line Antenna (MLA), shown in Figure 2, to fold a long antenna into the small phone body. The MLA is printed on flexible film so that it conforms to the inside of the back plastic cover of the phone. Spring-loaded pins make a simple, low-inductance connection to the antenna. The MLA can be routed to avoid high points on the phone circuit board like the perforated metal shield seen in the left of the figure. The MLA is also routed to avoid places where the user would be likely to place his hand or a finger.

## 3. Testing Methodology

We tested RF mock-ups of dual-antenna phones. These start out as commercial phones, but with the following changes made for testing. First, the secondary antenna is added internal to the phone. Second, the primary and secondary antennas are cabled to miniature co-axial connectors on the side of the phone body.

For testing, the antennas are cabled to the inputs of the "RF Channel Tool." This is a device that can record the signal received by up to 4 antennas at a time. The RF Channel Tool amplifies the received signals, downconverts them to an Intermediate Frequency, filters them, and then records digital samples of the baseband voltage. The recorded baseband voltages are post-processed after the drive test is finished.

The tests were carried out on a variety of drive routes in a test van. A real person held the phone being tested as though he were talking on it. The person was seated sometimes in the passenger seat of the van, sometimes in the back seat of the van. Different hand-positions were tested. In some runs, the tester deliberately avoided covering the internal antenna by keeping his whole hand low on the phone. In other runs, the tester deliberately covered the internal antenna with his index finger while holding the phone.

#### **4. PCS-band Results**

---

Our PCS-band results are described in some more detail in [3]. We outline the analysis and the results here.

The PCS-band testing was done using a test network operated by Qualcomm in San Diego. The network is comprised of seven sectors deployed on three base stations. The area covered by this network includes a mix of tall buildings, light industrial (2-4 story office buildings with medium density), and a few open areas. For these tests, the network was set to transmit pilot-only at 100% of its transmit power. The 100% transmit power condition emulates a fully loaded network. The pilot-only radiation is chosen to simplify the post-processing analysis of the received signals.

The forward link in a phone call is “good” when the phone receives the traffic power with sufficient average SINR (Signal to Interference+Noise Ratio) to be decoded with a specified low frame error rate. For the results shown here, we use a 3.9 dB Eb/Nt (Energy-per-bit over total Noise+Interference) threshold. This corresponds to an SINR threshold before processing gain of -17.2 dB. Choosing a higher or lower Eb/Nt would change the capacities we calculate for the forward link, but it would have only a minimal effect on the ratios of capacities calculated for different combining schemes, which is the main thrust of this work.

We calculate the traffic power required to achieve -17.2 dB SINR for each record in the drive test. The amount of traffic power required is different depending on the combining scheme employed. Thus for each record from our drive test, we can compare the required traffic power for each combining scheme tested.

We calculate the required traffic power relative to the total transmit power available from sectors in the system. We limit the maximum forward traffic power for each call in each sector to -9 dB (13%) of the total transmit power available from that sector. Any record that requires more than -9 dB transmit power is deemed to be “out-of-coverage.” To compare the different combining schemes, we limit the records looked at to those that are “in-coverage” for all combining schemes considered.

We correctly account for handoff in calculating the required transmit power. We follow IS-95 conventions for determining the handoff state of each record taken in the drive test. The traffic power for each record is calculated as the sum of the traffic powers from each sector currently in soft handoff. For example, a phone in 2-way handoff that requires  $-13$  dB power from each sector is calculated to need  $-10$  dB traffic power.

#### 4.1 Required TX Power

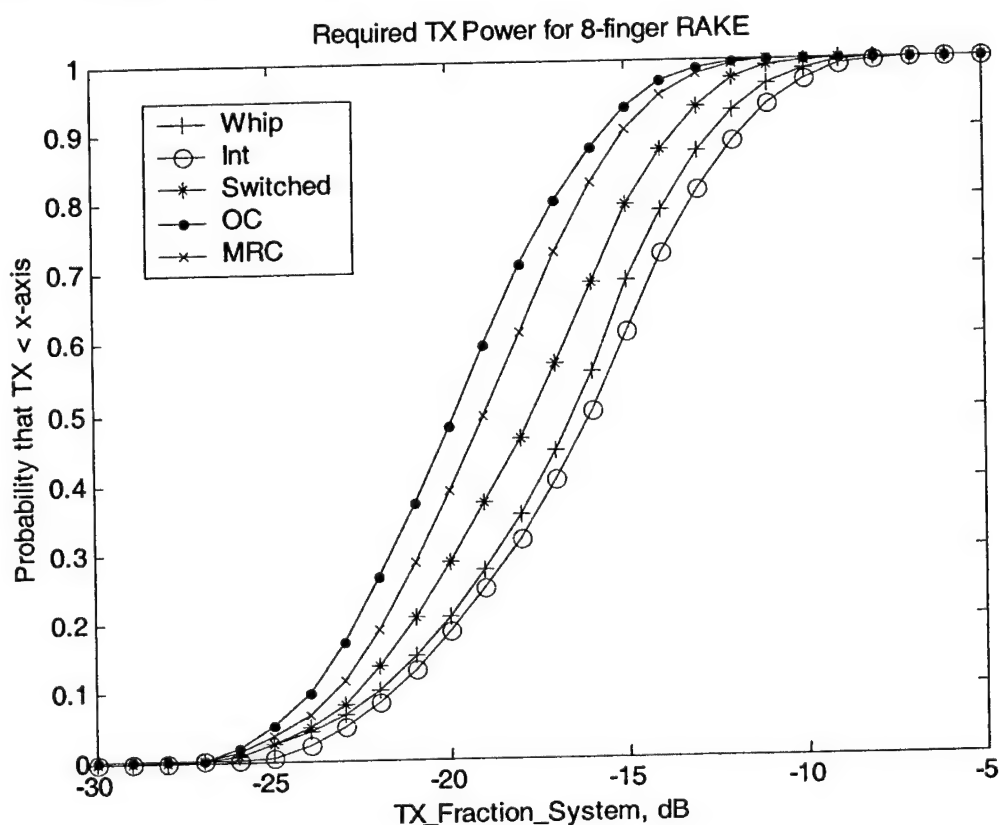


Figure 3 - Fractional TX Power required for 8-finger RAKE

To illustrate, we present the results from testing a modified Qualcomm QCP-1960 phone at PCS frequencies in Qualcomm's seven sector Over The Air test system. The phone tested is described above in Section 2.1. Figure 3 shows a Cumulative Distribution Function for required transmit powers using different antennas and combining schemes. Table 1 shows the forward link capacity improvement with respect to a whip antenna feeding a 4-finger RAKE receiver.

TABLE 1 Capacity Increases at PCS Band

RX Fingers	Whip	Int	OC	MRC	Switched
		Capacity relative to Whip, dB			
4	Reference	-0.6	2.5	1.8	1.0
6	0.3	-0.3	3.2	2.4	1.3
8	0.4	-0.3	3.5	2.7	1.3

#### 4.1.1 Internal Antenna

The rightmost line shows the single-antenna performance of the phone if only the internal antenna was used. The amount of forward traffic power required is between -25 dB and -9 dB of the total power a single sector can radiate. The higher transmit powers are required when either the phone is at a cell boundary, or it is seeing interference from adjacent sectors, or when the RF channel has a lot of multipath-induced self-interference. Conversely, when the phone is in a lower multipath environment and is primarily seeing only its serving sector, the required transmit power is much reduced.

#### 4.1.2 Whip Antenna

The second line from the right shows the performance of a single antenna phone using just the whip antenna. The whip performs a little better than the internal antenna due to its superior mean effective gain. Although the whip receives, on average, about 3 dB more power than the internal antenna, the improvement in required transmit power using the whip is only about 0.6 dB. This reflects the fact that the internal antenna sees 3 dB less signal, but also 3 dB less interference from multipath and interfering sectors.

#### 4.1.3 Switched

The third line from the right shows "Switched" performance that is, on average, 1.3 dB better than the whip used alone. This represents an absolute upper limit to what a switched-antenna receiver could accomplish using these two antennas. This limit is found by assuming that the better of the two antennas is always and immediately chosen. In a realistic algorithm, there would be a reduction from this gain due to the real overhead of the switching system.

#### 4.1.4 Maximal Ratio Combining (MRC)

The fourth line from the right, the second-best scheme shown in the figure, is "Maximal Ratio Combining" (MRC). In this scheme, the antennas are combined

to maximize sensitivity under the not-very-good assumption that the noise and interference the two antennas are receiving is uncorrelated. With this combining scheme, the mean required transmit power is reduced by 2.7 dB from what a single whip would require, assuming an 8-finger RAKE receiver. If there are only 4 fingers in the RAKE receiver, then the MRC performance advantage is reduced to 1.8 dB.

#### **4.1.5 Optimum Combining (OC)**

Finally, the best combining scheme investigated is called "Optimum Combining" (OC). Here, the antennas are combined with full knowledge of the interference correlation between the two antennas. Combining weights are found using Wiener-Hopf type calculations resulting in a Minimum Mean-Squared Error (MMSE) result. This has the effect of allowing the combiner to trade off gain on the signal against gain on the interference. OC requires 3.1 dB less transmit power than the whip for an 8-finger RAKE, or 2.5 dB better than the Whip if only a 4-finger RAKE receiver is used. No matter how many RAKE fingers are used, OC outperforms MRC by 0.7–0.8 dB.

#### **4.2 Dual-Antennas and RAKE Receiver Size**

The RAKE receiver combines multiple copies (fingers) of the received signal to synthesize a single, higher SINR copy. The multi-finger RAKE receiver is integral to efficient detection of CDMA signals. The RAKE is necessary to see forward capacity increases, and to implement features such as soft handoff in the phone.

One source of multiple fingers for the RAKE is multipath. Large buildings, hills, and "urban canyons" all cause reflections of RF that can result in an indirect signal path between a mobile and its serving sector. The RAKE allows most of the power from these different paths to be combined in the receiver to enhance SINR.

Soft-handoff requires a multi-finger RAKE receiver in the phone. In soft-handoff, the signal to the phone is being sent from two different sectors in the network. If at least one finger is assigned to signals arriving from each serving sector, then the phone receiver can combine the signal energies from both sectors simultaneously.

Existing CDMA phones use 4-finger RAKEs. This is a good size RAKE to use for a single-antenna phone, allowing up to 2 fingers to be assigned to each of two serving sectors in soft-handoff, for example. In Table 1 above, only 0.4 dB improvement is indicated when the number of fingers in the RAKE is doubled from 4 to 8 for a single Whip antenna phone.

For dual-antenna phones, the RAKE receiver must assign two fingers for each path arriving at the phone, in order that the gains from combining that path as seen on two separate antennas will be achieved. The 4-finger RAKE is limited to combining only two paths if each path is combined on two antennas.

From Table 1, we see significant improvement in the OC and MRC results when the number of fingers in the RAKE is increased. Going from 4 to 6 fingers, OC and MRC are improved by 0.6-0.7 dB. Going from 6 to 8 fingers provides only an additional 0.3 dB.

In conclusion: a 6-finger RAKE with OC is 2.9 dB better than a 6-finger RAKE with a single whip antenna. But it is 3.2 dB better than existing 4-finger single-antennas, and it is 0.7 dB better than a 4-finger OC.

## **5. Cellular-band Results**

---

The cellular-band tests were made on a commercial CDMA network in San Diego. Drive testing was done in the densest urban part of San Diego (downtown), along the freeways, and in the light-industrial neighborhoods close to Qualcomm headquarters.

Testing in a live, commercial network has certain advantages and certain challenges. Among the advantages is the fact that the network is indisputably "realistic," whereas test networks of limited scale such as the one we used for the PCS-band tests may not completely emulate real network features. Another advantage is that with wide coverage, a live network offers a greater variety of terrains under which to do testing.

Among the challenges of logging in a live network is the data analysis. Whereas a test network can be set to 100% pilot transmissions, simplifying data analysis and effectively emulating a fully loaded network, a live network will radiate an ever-changing mix of pilot, overhead, and traffic channels at an ever-changing total power level.

The data analysis on the live network must be done somewhat more indirectly than the PCS analysis on the Qualcomm test network. For the PCS data, we were able to estimate the interference and noise we were receiving directly from our measurements. For the cellular data, we cannot easily make such an estimate because we cannot distinguish between noise+interference on the one hand, and paging, synch, and traffic channels on the other.

Although the total signal radiated from live-network sectors is variable in traffic channel content, the pilot power from each sector is constant at a level of about 20% of the maximum sector transmit power. We can then use pilot measurements to characterize all of the paths over which radio energy makes it from the sectors

in the network to the mobile. From this a model of the noise+interference covariance matrix for a fully loaded network can be made.

With the network thus characterized, and the noise+interference for a fully loaded network thus modeled, the analysis of capacity in a fully loaded network proceeds much as it did for the PCS-band measurements [3].

### 5.1 Effect of Hand Position on Antenna Performance

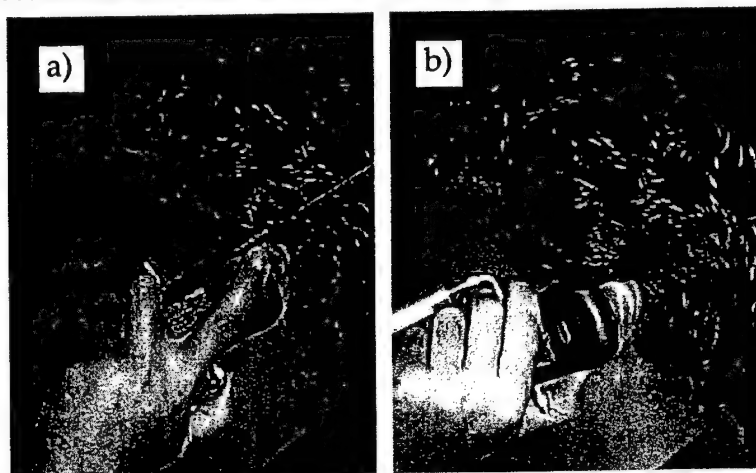


Figure 4 - Cellular Band Test Phone held a) With Finger and b) No Finger.

The tests were done with two different styles of holding the phone, illustrated in Figure 2. In runs labeled "Finger," the phone is held as in Figure 2 a). The index finger of the holding hand is covering the part of the phone that contains the secondary antenna. In the runs labeled "No Finger," the phone is held as in Figure 2 b), with no blockage of the secondary antenna by the index finger.

Figure 5 shows the spatially-averaged antenna gain for the primary (whip) and secondary (MLA) antennas as measured in an anechoic chamber in free space and including the effects of user head and hand losses. In this paper we assume this spatially averaged gain is equivalent to mean effective gain (MEG) [5], a quantity many researchers use to characterize the quality of antennas in land mobile environments. We believe this to be a good assumption for the multipath environments that are typical of cellular networks.

Figure 5 is based on tests in an antenna range. "Free Space" refers to testing the phone with nobody holding it, so there is no blockage from head, hand, or body. In this condition, the secondary antenna is nearly as good as the primary antenna. "Phantom Head" refers to tests in which the phone is attached to a plastic head model, but no blockage due to a hand is included. Head blockage is about 4 dB worse for the secondary antenna than for the whip. This indicates why whips are



so popular on cell phones, they are much less affected by head blockage than any other antennas that are acceptable. "Finger" and "No Finger" refer to hand holds as in Figure 2. The data for "No Finger" and "Phantom Head" are similar, suggesting that the "Phantom Head" is a good approximation to a phone held with no finger covering the secondary antenna. The "Finger" data indicates 3.5 dB of *additional* blockage of the secondary antenna. It is reasonable to attribute 3.5 dB blockage to the index finger covering the antenna. Although not shown in the figure, finger position had very little effect on the MEG of the whip antenna.

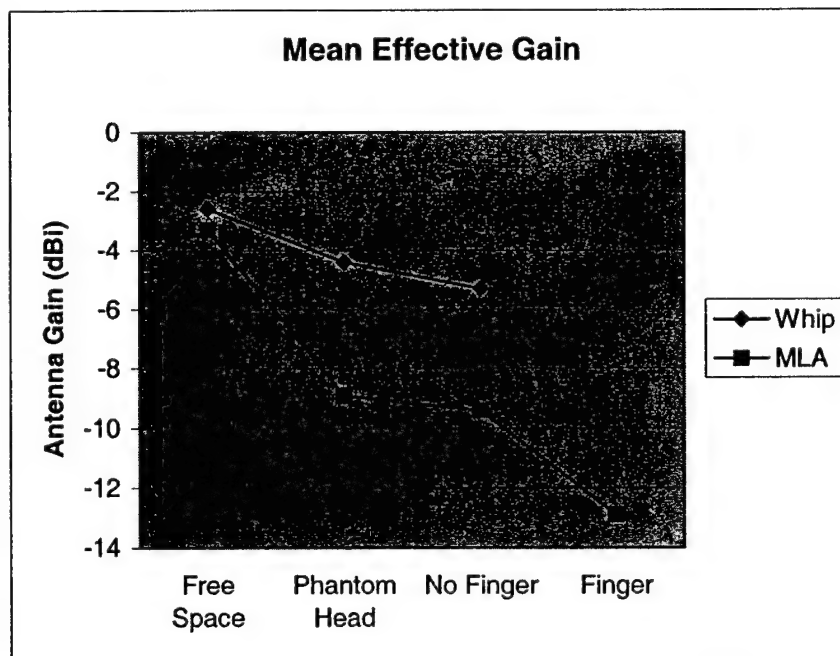


Figure 5 - Cellular Phone Antenna Gain.

## 5.2 Capacity in Cellular Band

Results for forward capacity increase in the cellular band are summarized in Tables 2 and 3. Each shows the capacity increase averaged over drive runs "Downtown," "Open," and "Light Industrial."

Tables 2 and 3 show similar trends to those seen in the PCS band in Table 1. The secondary antenna shows a somewhat lower system capacity used alone than does the whip antenna. Dual-antenna schemes increase capacity with OC most effective, Switched least effective, and MRC in the middle. Increasing from 4 to 6 fingers in the RAKE receiver gives a great boost to OC and MRC performance, but almost no improvement in single antenna performance.

TABLE 2 – Capacity in Cellular Band, No Finger Over Secondary Antenna

Relative Capacity, dB, No Finger Over MLA					
RX fingers	Whip	MLA	OC	MRC	Switched
4	Reference	-0.7	3.5	2.1	1.3
6	0.1	-0.6	4.1	2.6	1.4
8	0.1	-0.6	4.4	2.8	1.4

TABLE 3 – Capacity in Cellular Band, Finger Over Secondary Antenna

Relative Capacity, dB, Finger Over MLA					
RX fingers	Whip	MLA	OC	MRC	Switched
4	Reference	-1.7	2.9	1.7	0.9
6	0.1	-1.6	3.6	2.3	0.9
8	0.1	-1.6	3.8	2.4	1.0

The overall combining gains are fairly similar in the cellular and PCS bands tested.

### 5.3 Effect of Antenna MEG on Capacity

TABLE 4 – Relative Capacity vs MEG

	MEG (dB)	Relative Capacity, (dB)			
		Single	OC	MRC	Switched
Whip	-5.3	0.1			
MLA NoFinger	-9.4	-0.6	4.1	2.6	1.4
MLA Finger	-12.9	-1.6	3.6	2.4	0.9

The effect of antenna MEG on phone sensitivity can be seen by comparing the Whip and MLA columns in Tables 2 and 3 against the MEG values shown in Figure 5. This comparison, for 6-finger RAKE, is presented in Table 4.

The “Single” column shows the capacity of a single antenna phone when the MEG of the single antenna varies. The top row is for a single antenna whip phone. The next two rows are for a single antenna phone based on MLA, with no finger covering, and with finger covering respectively. While the MEG drops by a total of 7.6 dB across this comparison, the system capacity drops by only 1.7 dB.

The OC, MRC, and “Switched” columns allow an estimate of the effectiveness of the secondary antenna in a dual-antenna system as the MEG of the secondary antenna is decreased. The MLA performance as a single antenna declines by 1.0 dB when its MEG declines by 3.5 dB. The MLA’s ability to augment system capacity in dual-antenna schemes declines by 0.2-0.6 dB. From this, we conclude that we can tolerate a secondary antenna with MEG significantly inferior to that of the primary antenna without paying much of a cost in performance.

### 5.3.1 Capacity Gain vs. Difference in Received Powers

Another look at how combining gain works is seen in Figure 6. Here, the PCS band results summarized in Figure 3 and Table 1 above are re-analyzed. These records are sorted by the received power difference between the Whip and Internal antennas. With a 1-dB window size in power difference, the mean required transmit power is calculated. A 6-finger RAKE receiver is assumed. The results are expressed relative to the mean required transmit power for the phone with just a single Whip antenna.

The relative capacity of the Internal antenna is seen to decline from about 8 dB better than the Whip to about 8 dB worse than the Whip as its received power declines from about 10 dB better than the Whip (at the left end of the graph) to about 15 dB worse than the Whip (at the right end of the graph). When the relative powers of the two antennas are about equal, their relative capacities are also about equal.

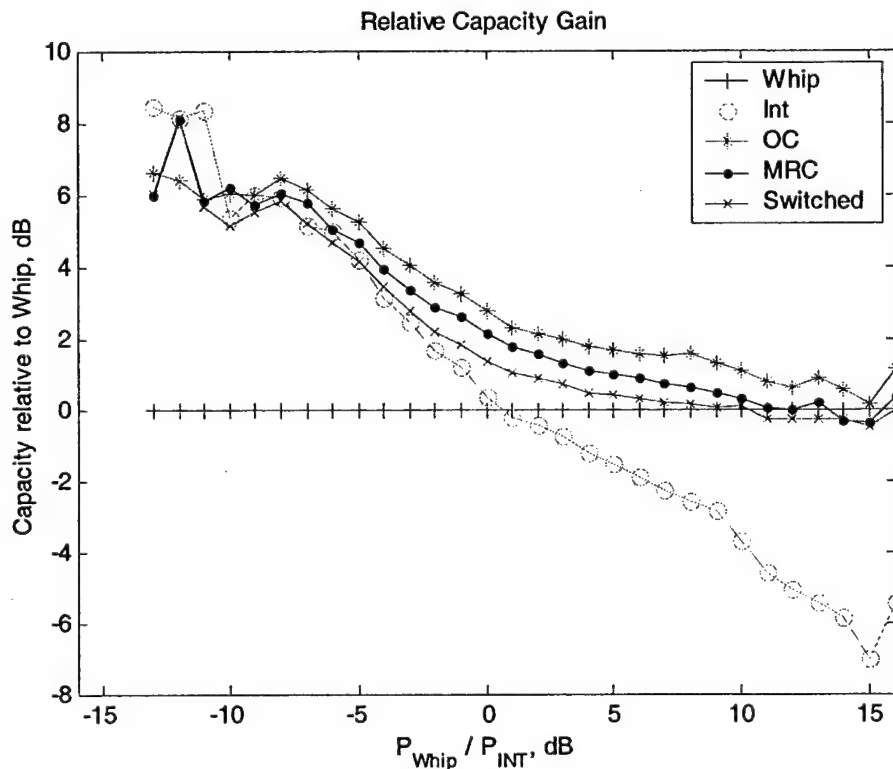


Figure 6 - Relative Capacity vs. RX Power Difference between Whip and Internal for PCS Points.

The 3 dual-antenna gains for OC, MRC, and Switched, are seen to exceed the single antenna (Whip and Int) gains when the Whip and Internal antennas receive

similar amounts of power. When the Whip is not receiving much power, the dual-antenna gains are not much above the Internal antenna gain, as seen on the left edge of the figure. Similarly, at the right end of the figure, the dual-antenna gains are not much better than the Whip alone when the Internal antenna is receiving reduced power levels.

We have been comparing dual-antenna gains to the Whip alone as reference. We make this choice of reference because it reflects the status quo. But what we see in this figure is that some of the advantage of the dual-antenna schemes is that there are times, due to random fading, when the internal antenna works better than the Whip, and *vice versa*, and that this accounts for much of advantage of a dual-antenna phone over a single antenna phone. But what we also see is that for those records where received power is about equal between the two antennas, OC and MRC are able to give additional gain beyond this.

### 5.3.2 Why MEG Hardly Matters: Receive vs. Transmit

The first reason that MEG matters so little is because we are considering the effect on the phone receiver. The effect of MEG on phone transmit power is much stronger, with about 1 dB more average phone transmit power required for every 1 dB reduction in MEG. But only the primary antenna is used for transmit. So we conclude that the MEG of the primary antenna is much more important than the MEG of the secondary antenna, because the MEG of the primary antenna has a large impact on the average power the phone must transmit.

### 5.3.3 Why MEG Hardly Matters: Noise vs. Interference Limited Receivers

The sensitivity of a phone receiver is limited by both the interfering RF power that the antenna picks up, and by the noise added by the receiver chain. With a reasonable antenna, the interfering RF power will vary from about -100 dBm up to about -30 dBm as the phone moves around the cell. The noise floor will stay fixed at about -100 dBm referred to the antenna connector. For the relatively small part of the cell where the receiver noise is equal to or greater than the interference, the receiver is said to be *noise limited*. In most of the cell, where the various interference powers are much larger than -100 dBm, the receiver is said to be *interference limited*.

Where the receiver is interference limited, the SINR is determined by the ratio of the signal to the interference powers. Decreasing MEG will simultaneously decrease both signal and interference so that the SINR is unaffected by MEG in the interference limited part of the cell.

The receiver is noise limited in only a small part of the cell, at the edge of coverage where received powers are about -100 dBm up to -95 dBm. Here the

SINR is mostly due to the ratio of the signal power to the noise floor. This ratio is proportional to the MEG.

Combining these effects, in most of the cell the phone is interference limited, and changes in MEG do not effect the sensitivity of the phone. In the small part of the cell on the edge of coverage, changes in MEG do effect the sensitivity of the phone. In determining the influence of MEG on the system capacity, it is the average effect of MEG on sensitivity which is important. Averaging the smaller noise-limited part of the cell with the larger interference-limited part of the cell, a relatively weak impact of MEG on average receiver sensitivity is seen.

## 6. Impact of Handoff State on Diversity Performance

TABLE 5 – Handoff statistics for drive tests.

Active Sectors	Percent of Records	
	PCS	Cellular
1	44.1%	54.5%
2	48.4%	41.2%
3	7.4%	4.3%
4	0.1%	0.0%

The handoff state is an important feature of this analysis. Mean handoff state was 1.6 and 1.5 sectors for PCS and cellular bands, respectively. Table 5 presents the distribution of handoff states for all the tests presented here. In general, handoff behavior was comparable between the two networks tested.

As described in Section 4, the handoff state, *i.e.* whether the phone is being served by only 1 sector (no handoff) or is in 2-way or 3-way handoff, has an effect on the load the phone presents to the system. Furthermore, higher handoff states require a larger number of RAKE receiver fingers, which are especially constrained in the dual-receive-chain diversity architecture (OC, MRC), where two fingers are devoted to each time-resolvable path being tracked by the receiver. Conceivably, diversity performance is compromised during high handoff states with smaller RAKE sizes (*i.e.* 4- or 6-finger). To investigate this effect, we repeated the analysis summarized in Tables 1, 2, and 3, but calculated separate mean TX powers for records corresponding to each handoff state. Tables 6 and 7 summarize these results for PCS and cellular bands, respectively.

In general, performance trends were comparable between the PCS and cellular bands. When single-receiver-chain phones (Whip, Internal, and Switched), are not in soft handoff (*i.e.* "1-way"), we observe negligible capacity increase as more fingers are introduced to the RAKE. In handoff, capacity improvements with

added fingers are more apparent; even more so with dual-receive-chain phones (OC, MRC).

TABLE 6 Capacity Increases by Handoff State, PCS Band

Handoff State	RX Fingers	Whip	Internal	OC	MRC	Switched
			Capacity relative to Whip, dB			
1-way (No Handoff)	4	Reference	-0.7	3.2	2.4	1.6
	6	0.1	-0.7	3.5	2.7	1.7
	8	0.1	-0.7	3.6	2.8	1.7
2-way	4	Reference	-0.5	2.4	1.7	1.0
	6	0.3	-0.2	3.2	2.4	1.2
	8	0.4	-0.1	3.6	2.7	1.3
3-way	4	Reference	-0.5	2.0	1.3	0.6
	6	0.4	-0.1	2.7	2.0	1.0
	8	0.6	0.0	3.3	2.6	1.1

TABLE 7 Capacity Increases by Handoff State, Cellular

Handoff State	RX Fingers	Whip	Internal	OC	MRC	Switched
			Capacity relative to Whip, dB			
1-way (No Handoff)	4	Reference	-1.1	4.0	2.4	1.5
	6	0.0	-1.1	4.4	2.7	1.5
	8	0.0	-1.1	4.5	2.8	1.5
2-way	4	Reference	-1.2	3.0	1.7	0.9
	6	0.1	-1.1	3.7	2.3	1.0
	8	0.1	-1.1	4.0	2.5	1.0
3-way	4	Reference	-1.3	2.5	1.7	0.9
	6	0.2	-1.2	3.3	2.4	1.1
	8	0.2	-1.2	3.6	2.8	1.1

The poorest diversity performance is observed when the receiver's ability to implement soft handoff is constrained by number of RAKE fingers, namely 3-way handoff with a 4-finger RAKE. In this scenario, although the active set contains three sectors, only two may be temporally combined at any time since the spatial

combining architecture requires two fingers for each path tracked. Despite this constraint, significant diversity gains are still observed (2.0 and 2.5 dB, PCS and cellular respectively) relative to the single-whip architecture, where each of the four RAKE fingers is allowed to track a separate time-resolvable path. Furthermore, our results suggest that the overall impact of this diminished performance is small, since the amount of time spent in 3-way handoff is less than 10%. This is apparent in the overall averages shown in Tables 1, 2, and 3.

## **7. Diversity Gain, Aperture Gain, and Interference Rejection**

The kinds of gains expected from a two-antenna system are Diversity Gain, Aperture gain, and Interference Rejection. From comparing the results of the different combining algorithms above, a certain amount can be said about the relative importance of these terms.

### **7.1 Diversity Gain**

The signals received at mobile phones nearly always suffer from fading. In the worst fading environments, the signal can fall by 99% below its mean level about 1% of the time.

Diversity Gain refers to the improvement in received signal level if the better of two receive antennas is used. As long as the fading is not completely synchronized between the two antennas, it is possible to improve the average signal level in this way.

The Switching algorithm investigated above assumes instantaneously and perfectly picking the better of two antennas in each record. All of the improvement of the Switching algorithm over the Whip antenna used alone is Diversity Gain. From Table 1, this puts Diversity Gain at about 1.1 dB.

### **7.2 Aperture Gain**

Aperture refers to the collecting-area of an antenna, the space around the antenna from which it can absorb signal power. Intuitively, the aperture of M antennas should be about M times as large as the aperture of one antenna. This simple situation can be complicated by the following considerations. First, if the antennas are too close together, then their apertures will overlap, and the total aperture will be less than the sum of the individual apertures. Second, if the secondary antenna is less efficient than the primary antenna, then the total aperture would be expected to be less than the twice the aperture of the primary antenna.

Both of these complications arise in the handsets investigated. First, the antennas on the handset are quite close together. Second, the secondary antenna does see less radiation than the primary antenna due to head and hand blockage. Thus we do expect an aperture gain of significantly less than 3 dB.

We can estimate the Aperture Gain from results in Table 1. We assume that the MRC gain of 2.4 dB is comprised of Diversity Gain and Aperture Gain. Since 1.1 dB is the amount of Diversity Gain in the Switched system, which maximizes it, we conclude there is between 0 and 1.1 dB of Diversity Gain in the MRC case. That means there is between 1.3 and 2.4 dB of Aperture Gain in the MRC case.

### **7.3 Interference Rejection**

When a signal arrives at two antennas, it arrives with some RF phase difference between the two antennas. When an interferer arrives, it also has some RF phase difference between the two antennas. If the interferer and the signal have different RF phase differences, then the voltages from the two antennas can be combined with weights that tend to make the interfering signal smaller, while preserving or even enhancing the arriving signal voltage.

In simple cases with a strong signal and a single strong interferer, Optimum Combining will nearly completely cancel the interference out, resulting in a high Signal to Interference Ratio. In more complicated cases, with multiple interferers and receiver noise to consider, OC will make the best possible trade-off between signal enhancement and interference rejection.

OC gain should be composed of Aperture, Diversity, and Interference Rejection gains. Again using Table 1, and building on the results of sections 7.1 and 7.2, we conclude there is at least 0.7 dB of Interference Rejection gain in the OC case, along with between 0 and 1.1 dB of Diversity Gain and between 0 and 2.4 dB of Aperture Gain.

### **7.4 Summary of Gain Components**

We attempt to break out the Diversity Gain, Aperture Gain, and Interference Rejection components of the total dual-antenna combining gain in a quantitative way. But we do not have exact definitions of these gain components. Then it is probably best to conclude that Diversity Gain, Aperture Gain, and Interference Rejection are all in the neighborhood of 1 dB, and are all playing approximately equal roles in the total combining gain that we see.



## **8. Usefulness of Forward Capacity Increase**

---

The capacity increase can be used in three ways. First, in parts of systems where capacity is limited by the forward link, dual-antenna phones will raise forward capacity so that the higher reverse capacity becomes the limit. Second, new data services demand more resources on the forward link than the reverse link. By introducing dual-antenna phones, forward link capacity is freed-up for use in data services. Finally, The forward link capacity increase can be matched by a reverse link capacity increase. A method to nearly double reverse link capacity by upgrading to dual-polarized antennas at the base stations is described elsewhere [1,2].

## **9. Antenna Performance**

---

There are two antenna-performance issues unique to dual-antenna phones that should be considered and compared with phone performance. The first is Mean Effective Gain (MEG), and its possible imbalance between the primary and secondary antennas. The second is the question of antenna independence, measured typically by the Fast Fading Correlation.

### **9.1 Mean Effective Gain**

Mean Effective Gain (MEG) is a good way to characterize the effectiveness of an antenna at coupling to signals it is likely to receive. The MEG comes from averaging the antenna gain for signals coming in from a mix of directions consistent with what the phone would see in use.

#### **9.1.1 MEG of the Primary Antenna (Whip)**

The MEG of a whip on a handset held vertically with no head or hand near it is likely to be 0 dB or even higher. However, in use the following factors will reduce the MEG, even for a whip:

- The antenna-handset will be held with about 60° of tilt away from vertical
- The head will block some directions and absorb some radiation
- The hand will provide additional blockage and absorption

The biggest effect of holding the handset is reduction in gain especially in the direction of the head. The effect of this on MEG is to reduce it typically by a few dB at the frequencies in the PCS band but can be as large as -5 to -8 dB for the cellular band.

### 9.1.2 MEG of the Secondary Antenna, and Imbalanced MEG

The secondary antennas we consider are placed inside the phone plastics. In this location, these antennas are much more susceptible to blockage by the phone itself, and by the hand or fingers of the user. Efforts are made to put them as high on the back of the phone as possible to minimize that blockage. Even so, the secondary antenna MEGs are anywhere from 4 to 15 dB less than that of the Primary antenna.

## 9.2 Fast-Fading Power Correlation

For a dual-antenna receiver to work, it is necessary that the two antennas not see exactly the same signals. It may be thought that if two antennas are too close together, the signals they see will be too similar to be exploited for combining-gain in a dual-antenna system. In fact what we have seen is that every phone we have tested has had combining gain. It appears that any reasonable dual-antenna design will work.

The most common metric to describe the similarity between signals from two antennas is the Fast-Fading Power Correlation. We will refer to this simply as "correlation." Fast-fading refers to variation in received power as an antenna moves over a distance scale of  $\sim 1$  m or less. Correlation can range theoretically from  $-1$  where the fading is exactly opposite on each antenna, to  $1$  where the two antennas fade simultaneously. Low or zero correlation means that whether or not one antenna is in a deep fade makes no difference to the probability that the second antenna will also be in a deep fade.

We find no measurable degradation due to fast-fading correlation between the primary and secondary antennas. First, we have found it is difficult to design two antennas that are more than 40% correlated, even when the antennas are quite close together. Second, we expect MRC to work without degradation up to about 70% correlation, with OC working well to even higher levels of correlation.

## 10. References

- 
- [1] R. Padovani, "Further Capacity Improvements in CDMA Cellular systems," *Proc. IEEE*, in press.
  - [2] L. Aydin, E. Esteves, R. Padovani, "Reverse Link Capacity and Coverage Improvement for CDMA Cellular Systems Using Polarization and Spatial Diversity," *Proceedings of the IEEE International Conference on Communications 2002*, Vol. 3, pp. 1887–1892, 2002.

- [3] "CDMA Forward-Link Capacity Improvements With Dual-Antenna Handsets," *Qualcomm Document # 80-H0567-1*.
- [4] W.C. Jakes, ed., **Microwave Mobile Communications**, IEEE Press: New York, 1994.
- [5] T. Taga, "Analysis of Mean Effective Gain of Mobile Antennas in Land Mobile Radio Environments", *IEEE Trans. Veh. Technol.* Vol. 39, pp. 117-131, May 1990.

# MEASUREMENT AND ANALYSIS OF A CONFORMAL WING ARRAY

David Curtis, Boris Tomasic, Ryan Thomas, Scott Santarelli, Hans Steyskal

Air Force Research Laboratory  
Sensors Directorate  
Antenna Technology Branch, AFRL/SNHA  
80 Scott Drive, Hanscom AFB  
01731-2909

## Abstract

An experimental conformal array of microstrip patch elements was built on the surface of a scaled aircraft wing. The array wraps completely around the wing in a belt-like fashion, oriented in a plane perpendicular to the wing's leading edge. The goals of this effort were to characterize the electromagnetic performance of the array using analysis, simulation and measurement, and to develop methods of pattern control for this unusually shaped array. While considerable research on conformal arrays has been reported in the literature, this work addresses the more generalized case of a conformal array with variable curvature on a non-canonical surface. Because of this, the array far-field pattern can not be obtained through a modal expansion, as may be done for circular and even elliptical conformal arrays. A first-order electromagnetic analysis is presented which accounts for the variable curvature of this wing array, and its elements, including mutual coupling effects. Element patterns simulated using this analysis are presented and compared against measured element patterns. The use of an array pattern synthesis technique is described which provides a robust and practical approach to conformal array pattern control. Examples of this method are given for several cases, and comparisons are made between array patterns that were synthesized using simulated versus measured element patterns.

## 1.0 Introduction

Airborne phased array antennas are typically planar in shape and often reside within a box-like radome that has fairings to blend the radome into the smooth curvature of the aircraft. While this may not be a major problem at higher frequencies, planar arrays at lower frequencies are often too large to fly, or have limited gain due to the lack of sufficient planar real estate aboard the aircraft. Conformal arrays which are wrapped around the fuselage or reside upon sections of the wings offer the prospect of utilizing far more surface area of the aircraft, and thus, can increase array gain performance without increasing aerodynamic drag. The curvature of conformal arrays also can potentially improve scanning performance in many cases because the active region of the array may be commutated around the aircraft's curvature, enabling beam scanning well beyond the typical  $\pm 60^\circ$  scan limits of most planar electronically scanned arrays. The penalties for these improvements include the need to understand the significantly more

complicated electromagnetic behavior of these arrays, develop conformal array design and simulation tools, and develop an adequate means of conformal array control.

The conformal wing array studied in this effort is shown in Fig. 1. It is comprised of 116 cylindrically curved, rectangular microstrip patch antenna elements arranged in a conformal ring oriented perpendicular to the wing's leading edge. The array elements were designed as linearly polarized E-plane patches, and have an arbitrarily chosen center frequency of 5.45 GHz. They were fabricated from Rogers Duroid on a numerically controlled micro-router machine. The average measured bandwidth of these elements was about 1%. Despite design efforts to control variations in center frequency, some elements exhibited resonance between 5.35 GHz and 5.45 GHz. The radius of curvature of this wing section varies from as small as  $\lambda/2$  up to  $>1000\lambda$  at the center frequency. Despite the narrow bandwidth of these elements, they are ideally suited for this investigation which seeks to characterize the electromagnetic behavior and control of a conformal array with highly variable curvature. Details of the element and array designs were provided in a previous paper [1].

## 2.0 Electromagnetic Analysis of Conformal Arrays With Variable Curvature

### 2.1 Conformal Wing Array Geometry

As illustrated in Fig. 2, the element numbering scheme begins with Element 1, located just above the centerline of the leading edge of the wing. Element index,  $n = \{1, 2, 3, \dots, 116\}$ , increases from the leading edge to the trailing edge above the wing, and from the trailing edge to the leading edge below the wing, with Element 116 located just below Element 1. Fig. 2 also illustrates the system of global coordinates, which are used to describe the geometry of the wing, and a generalized system of local coordinates, which are used to describe the local geometry and orientation of any given element in the array. The global coordinate system  $(x, y, z)$  in spherical coordinates  $(r, \theta, \phi)$  is centered at the center of mass of the wing section. The local coordinate system and local geometry are different for every element in the array. Relative to the center of mass, the  $n^{\text{th}}$  element location in the global coordinate system is described by vector  $\mathbf{r}'_n$ . The observation point in the far-field region ( $r \gg \lambda$ ) is defined by vector  $\mathbf{r} = \hat{\mathbf{r}}r$ , where  $r = |\mathbf{r}|$ , and unit vector  $\hat{\mathbf{r}} = \mathbf{r} / r$  is defined in global coordinates along a ray from the origin to the far-field observation point.

### 2.2 Element Far-Field Pattern

For a plane wave incident upon the array at an angle which illuminates the  $n^{\text{th}}$  element, the incident voltage at the  $n^{\text{th}}$  element port is described by a complex-valued coefficient,  $a_n$ ,

$$a_n = |a_n| e^{j\alpha_n}, \quad (1)$$

and the resulting power incident on the  $n^{\text{th}}$  element,  $P_n^{\text{inc}}$ , is given as follows, where  $Z_C$  is the characteristic impedance of the element feed port transmission line.

$$P_n^{inc} = \frac{|a_n|^2}{Z_c} \quad (2)$$

For the case of a singly excited element in a conformal, match-terminated array environment, the electric field pattern observed in the far-field can be written as follows,

$$\mathbf{E}_n(\mathbf{r}, \theta, \phi) = \sqrt{\frac{\zeta_o P_n^{inc}}{4\pi}} \frac{e^{jk r_n}}{r_n} \mathbf{e}_n(\theta, \phi), \quad (3)$$

where vector,  $\mathbf{e}_n(\theta, \phi)$ , is the complex-valued electric field pattern of the  $n^{th}$  array element, and  $\zeta_o = \sqrt{\mu_o \epsilon_o} = 367.7$  ohms, is the characteristic impedance of free-space. Substituting Eq. 2 into Eq. 3, and using the scalar  $r_n = |\mathbf{r} - \mathbf{r}'_n|$ , defined as the distance from the  $n^{th}$  element to the far-field observation point, we can write the following.

$$\mathbf{E}_n(\mathbf{r}, \theta, \phi) = \frac{1}{\sqrt{4\pi}} \sqrt{\frac{\zeta_o}{Z_c}} \frac{e^{jk r_n}}{r_n} a_n \mathbf{e}_n(\theta, \phi) \quad (4)$$

The  $n^{th}$  element far-field pattern,  $\mathbf{e}_n(\theta, \phi)$ , can be decomposed into components in the  $\hat{\theta}$  and  $\hat{\phi}$  directions, as follows,

$$\mathbf{e}_n(\theta, \phi) = \hat{\theta} e_{n\theta}(\theta, \phi) + \hat{\phi} e_{n\phi}(\theta, \phi) \quad (5)$$

where

$$e_{n\theta}(\theta, \phi) = |e_{n\theta}(\theta, \phi)| e^{j\psi_{n\theta}(\theta, \phi)} \quad (6a)$$

$$e_{n\phi}(\theta, \phi) = |e_{n\phi}(\theta, \phi)| e^{j\psi_{n\phi}(\theta, \phi)}. \quad (6b)$$

The gain of the  $n^{th}$  element may be written as,

$$g_n(\theta, \phi) = \frac{\mathbf{E}_n(\mathbf{r}) \cdot \mathbf{E}_n^*(\mathbf{r})}{\zeta_o S_{on}}, \quad (7)$$

where

$$S_{on} = \frac{P_n^{inc}}{4\pi r_n^2}. \quad (8)$$

Substituting Eq. 8 into Eq. 7, the element gain can be written in terms of  $\hat{\theta}$  and  $\hat{\phi}$  components, as follows.

$$g_n(\theta, \phi) = |e_{n\theta}(\theta, \phi)|^2 + |e_{n\phi}(\theta, \phi)|^2 \quad (9)$$

### 2.3 Array Far-Field Pattern

In the following development of the far-field conformal array gain, it is assumed that a plane wave is incident within the field of view of an active aperture of  $N$  consecutive elements. Using the equation for  $E_n(r)$ , the electric field of the  $n^{\text{th}}$  element, as given in Eq. 4, the far-field pattern of an array of  $N$  elements is obtained by superposition of the fields from each element as,

$$E(r) = \sum_{n=1}^N E_n(r), \quad (10)$$

where

$$E(r) = \frac{1}{\sqrt{4\pi}} \sqrt{\frac{\zeta_o}{Z_c}} \frac{e^{-jkr}}{r} \sum_{n=1}^N a_n e_n(\theta, \phi) e^{jkr'_n \cdot \hat{r}} \quad (11)$$

In this expression, we have used the far-field approximation,  $r_n \approx r$ , in the amplitude factor  $1/r_n$ , since  $r \gg D/\lambda$ . Consequently, the array gain may be written as,

$$G(\theta, \phi) = \frac{E_n(r) \cdot E_n^*(r)}{\zeta_o P_{on}} \quad (12)$$

where,

$$P_o = \sum_{n=1}^N P_{on} \quad (13)$$

and upon substitution of Eq. 13 into Eq. 12, the final form of the  $N$ -element conformal array gain may be written as,

$$G(\theta, \phi) = \frac{\left| \sum_{n=1}^N a_n e_n(\theta, \phi) e^{jkr'_n \cdot \hat{r}} \right|^2}{\sum_n |a_n|^2} \quad (14)$$

As in all arrays, the gain of the conformal wing array is a function of the magnitudes,  $|a_n|$ , of each element excitation coefficient,  $a_n$ . To produce a beam in the  $(\theta_o, \phi_o)$  direction, the phase of each  $a_n$  must be,

$$\alpha_n = -kr'_n \cdot \hat{r} - \psi(\theta_o, \phi_o) \quad (15)$$

The magnitudes of the excitation coefficients can vary depending on the array pattern requirements. Specific cases can be studied which yield low sidelobes, produce nulls in the pattern, or even produce multiple main beams. In addition, a particular set of coefficients can be chosen to achieve maximum gain at a particular scan angle [2].

As seen from Eq. 14, the element patterns,  $e_n(\theta, \phi)$ , must be known in order to evaluate the gain patterns of a conformal array with variable curvature, however, this is not a simple task. For large radii of curvature, it is common practice to approximate the variably curved conformal array element patterns by the element patterns of a large planar array. In this technique, the planar element patterns are oriented parallel to the local radius of curvature of the variably curved conformal array. This technique is the so-called zeroth-order solution because the elements are modeled as tilted, flat elements on a variably curved surface. This technique works rather poorly when the array's radius of curvature approaches the physical size of the element.

In this paper, we extend the realism of the analysis of a variably curved conformal array one step farther by approximating its 2-D local curvature using a circular array, whose radius approximately matches the local curvature of the variably curved array. This approach takes into account array curvature, conformal element curvature, and mutual coupling effects, to first order. To facilitate the electromagnetic computations in this analysis, a commercial code was used known as "Cylindrical Microstrip Patch Analysis", or CyMPA, [3]. This code uses the Method of Moments with a cylindrical modal expansion to compute the element patterns, element impedances, and mutual coupling for circularly cylindrical arrays. In our case, the cylinder width is only one element, which reduces the cylinder to a circular ring.

## 2.4 First-Order Approximation of Mutual Coupling

To this point, we have described the gain of an  $N$ -element active aperture region of the conformal wing array without specifically addressing mutual coupling. However, as with linear and planar arrays, mutual coupling can have a significant effect on the radiation pattern of the conformal wing array. In this case, mutual coupling varies not only as a function of interelement separation distance, but also as a function of local array curvature. At elements 1 and 116, which reside on the leading edge of the wing, the rate of change in array curvature is so fast that these elements essentially experience edge effects similar to that of the endmost elements in linear or planar arrays when no "dummy" elements are used. Along the leading edge of the conformal wing, it is impossible to extend the ground plane and provide "dummy" elements to soften the abrupt end of the mutual coupling environment, because the ground plane is the wing itself.

A scattering matrix formulation is used to examine the mutual coupling in the variably curved conformal wing array. Referring to Fig. 3, electromagnetic coupling between elements  $n$  and  $n'$ , can be characterized by a scattering coefficient  $S_{nn'}$ , which is defined as the geometric mean of the scattering coefficients  $S_{ii'}$  and  $S_{jj'}$ , given as,

$$S_{nn'} = \sqrt{S_{ii'} S_{jj'}} \quad (16)$$

$S_{ii'}$  is defined as the coupling coefficient between elements  $i$  and  $i'$  on a circle corresponding to the local geometry at element  $n$ , and similarly,  $S_{jj'}$  is the coupling coefficient between elements  $j$



and  $j'$  on a different circle corresponding to the local geometry at element  $n'$ . With this approach, the scattering matrix of the variably curved conformal array satisfies the symmetry condition, such that,  $S_{nn'} = S_{n'n}$ . For large, smoothly varying curvature, this approximation gives adequate accuracy assuming that elements  $n$  and  $n'$  are not too far apart. For elements with  $|n - n'| > 3$  or 4, we set  $S_{nn'} = 0$ , because mutual coupling falls off exponentially and its effects are assumed minimal at this separation distance. Thus, the scattering matrix of the variably curved conformal array is symmetric and has non-zero elements along and near its diagonal.

Using the CyMPA code to compute a scattering coefficient,  $S_{in}$ , between the  $i^{th}$  and  $n^{th}$  elements, the scan-dependent active reflection coefficient at the  $n^{th}$  element is given by,

$$\Gamma_n(\theta, \phi) = \sum_{i=1}^N \frac{a_i(\theta_o, \phi_o)}{a_n(\theta_o, \phi_o)} S_{in} = |\Gamma_n(\theta_o, \phi_o)| e^{j\gamma_n(\theta_o, \phi_o)} \quad (17)$$

In Eq. 17,  $a_i$  and  $a_n$  are the incident voltages at elements  $i$  and  $n$ , respectively, and  $(\theta_o, \phi_o)$  is the desired scan direction of the main beam. For the case of our conformal wing array,  $\phi_o = 0$ . Since conformal element impedance varies as a function of curvature, ideally, each element should have a different design to accommodate the variable curvature around the wing, and as a result, each element should also have a different impedance. If this were the case, each element would require a different impedance matching network, such that  $|\Gamma_n| = 0$ , for all  $n$ . However, for practical reasons, all elements were based on only one element design which exhibited fairly good VSWR for all radii, and these are matched at broadside, at the center frequency [1].

The total voltage at the  $n^{th}$  element port can be written in terms of the incident voltage,  $a_n$ , and the reflected voltage,  $b_n$ , as follows,

$$c_n = a_n + b_n = |c_n| e^{j\delta_n} \quad (18)$$

After calculating the active reflection coefficient of the  $n^{th}$  element using Eq. 17, the total voltage at the  $n^{th}$  element port now be written in terms of the  $n^{th}$  active reflection coefficient  $\Gamma_n(\theta_o, \phi_o)$  as

$$c_n(\theta_o, \phi_o) = a_n(\theta_o, \phi_o) (1 + \Gamma_n(\theta_o, \phi_o)) \quad (19)$$

Eqs. 17-19 were used in a Matlab code that used the scattering parameter output from CyMPA, to compute the theoretical array patterns, including the case of the maximum gain pattern, which were reported earlier [1].

### 3.0 Element Pattern Measurements

#### 3.1 Experimental Configuration

The antenna element patterns were measured in a 70' x 35' x 40' anechoic chamber. Fig. 4, shows the location of the measurement equipment in the anechoic chamber and the general experimental setup. The wing section is mounted end-on to an antenna mount that rotates in the

$\phi$ -plane with respect to the global coordinate system in Fig. 2. Thus, the wing is oriented so its leading edge is vertical. As the antenna mount is rotated, elevation-plane element patterns are measured by rotating the antenna mount azimuthally with respect to the ground. The antenna mount positioner and the analog-to-digital converter (ADC) that records the measured element patterns are controlled using a GPIB instrument bus connected to a Windows NT workstation. The ADC is connected to a single Element-Under-Test (EUT) through a triple stage receiver. The receiver-ADC pair is manually moved to each element in the array, one at a time, in order to measure and digitally record the 116 different element patterns. The ADC samples the received EUT signal at a rate of 10 MS/s. Since it takes several minutes for the antenna mount to rotate through 360°, the amount of data that would be acquired for each element would be too large to permit continuous-sweep measurements.

Instead, the mount is rotated in short discrete angular sweeps and data is recorded at fixed angular positions when the mount comes to rest in between movements. The antenna mount positioner provides the absolute angle data necessary to achieve precise angular synchronization between the antenna mount rotation angle and the sampled data. However, since Windows NT is an event-driven operating system, not a real-time operating system, the action of starting and stopping the data acquisition for each discrete sweep causes the measurement phase reference to be lost. To maintain phase reference, the output of the RF source is split into two paths. A large portion is radiated at the EUT from a C-band standard gain horn, while a much smaller portion is transmitted over a coax cable to a second receiver-ADC pair, where it is demodulated, sampled, and used as a phase-reference for element pattern measurements. The output phase of the EUT is compared to the reference phase, and their difference is recorded as the measured phase of the EUT. Fig. 5 shows a block diagram of the RF source and reference signal configuration.

Measurement linearity is paramount to achieving accurate, repeatable measurements. To determine the linearity of each receiver, the RF power at the receiver input port is compared to the power measured at the receiver output port. Output power readings above the 1 dB compression point are considered to be in the non-linear region of the receiver, and are avoided by reducing the input power. The RF source output power is then set to fall midway within the linear range of the receivers, illustrated in Fig. 6. With the equipment used in this experiment, the receivers exhibit linearity up to a maximum input power level of -17 dBm, corresponding to the 1 dB compression point of the receivers. Using the definition of dynamic range that is based on the 1 dB compression point, the receivers and ADCs used in these measurements exhibited a dynamic range of 55 dB.

A block diagram of the measurement configuration is shown in Fig. 7. The absolute gain of a single element is measured using a standard gain horn mounted directly below and in front of the wing EUT. The difference between the power received at the output of the standard gain horn and the absolute gain listed in the standard gain horn's "certified gain table" is added to the received power measured at the output port of the EUT. The resulting value is the measured absolute gain of the EUT at broadside. Element 39, exhibited a measured absolute gain of +3.4 dBi. This value is fairly low compared to typical microstrip patch elements, which have absolute gains of about +7 dB. As discussed in Section 4, however, this was the case for more than 75 % of the elements in the array.

### 3.2 Platform-Induced Multipath

In order to take accurate element pattern measurements, it is critical to excite the wing array elements with a plane wave and eliminate multipath due to the plane wave bouncing off the walls, floors, and ceiling of the anechoic chamber, and from the equipment within the chamber. However, our wing section also has some inherent "multipath" such as scattering from the edges of the wing, which is an important feature of the measured element patterns. The anechoic chamber is equipped with 24" anechoic absorber designed to have a return loss of -70 dB for X-band radiation at broadside. However, some of the radiation is incident on the absorber at shallow oblique angles, where the absorber performance is considerably derated. Scattering and reflections of the plane wave from these portions of the chamber induce undesired multipath in the pattern measurements. In order to determine the presence of this multipath, and measure its extent, the phase and amplitude of the incident plane wave was measured in the anechoic chamber's quiet zone using a standard gain horn mounted to a horizontal sled. The sled was located perpendicular to the angle of plane wave incidence, and positioned just below the wing array. A standard gain horn was used as a probe, and was positioned in front of the array at the same height as the array elements. The probe was moved linearly across the sled in front of the array while the received amplitude and phase were recorded using a receiver-ADC pair. This effectively measured a horizontal slice of the quiet zone immediately in front of the array.

As seen in Fig. 8, the results of this scan indicate a relatively flat amplitude profile of the incident wavefront, with a ripple of just  $\pm 0.15$  dBm. The standard gain horn used as the probe in this measurement has a gain response that is flat to within  $\pm 0.3$  dB, which is greater than the observed ripple. Fig. 8 also shows the phase profile of the incident wavefront, which exhibits 70 degrees of curvature from edge to center, measured over a distance of 6 feet. This phase difference is due to the nearly quarter wavelength difference in path length between the transmit paths when the probe is at the end limits of the sled track, compared to the transmit path when the probe is at the center of the sled track. These results indicate that the wave incident on the wing array is relatively free of chamber-induced multipath, to within the tolerances of the equipment and measurement techniques. Therefore, it is concluded that any ripple observed in the measured element pattern data, greater than  $\pm 0.3$  dB, is likely a direct result of multipath from the wing itself. Examples of this ripple, which was observed in only some of the wing array's element patterns, can clearly be seen in Figs. 14-16.

To model the ripple found in the half power beamwidth of the element patterns, the wing can be analyzed in the far field. A length  $L$  separates the EUT and the scattering point, e.g. wing trailing edge. The distance difference changes as the wing rotates. For a given angle,  $\alpha$ , that changes by a small increment,  $\Delta\alpha$ , the distance the two elements travel with the respect to one another ( $\Delta s$ ) is

$$\Delta s = L \cos(\alpha) \Delta\alpha \quad (20)$$

This is a fraction of a wavelength and therefore a fraction of a ripple for some small angle rotated  $\Delta\alpha$ . Every wavelength of distance difference causes a full period of ripple as the phase vectors of the sources constructively and destructively interfere. Thus, the ripples per radian that the pattern sees for this angle  $\alpha$  is

$$\omega_R = \frac{\text{ripples}}{\text{radian}} = \frac{L \cos(\alpha)}{\lambda} \quad (21)$$

Converting the units from ripple per degree to ripples per radian, and using a wavelength of 2.2 inches, which corresponds to the operating frequency of 5.45 GHz, allows the distance from the EUT to the interference point to be calculated.

To investigate the angular spatial frequency of the ripple in an element pattern in more detail, we worked only with the HPBW portion of the pattern. This region of the pattern is then approximated by a function obtained using a fourth-order polynomial. By subtracting this polynomial from the measured data, the shape of the element pattern is removed, leaving only the platform-induced ripple. Taking the Fast Fourier Transform (FFT) of the resulting ripple data provides a power spectrum of the ripple, enabling the dominant spatial frequencies of the ripple to be identified. Fig. 9 is a plot of the FFTs from each element for which this technique was applied. With this data it is possible to correlate dominant ripple to the physical features of the wing that produce scattering. As seen along the ridge inside the white box in Fig. 10, element 72 is about 18" from the interference point and element 110 is nearly 4.5' from the interference point. These are the approximate distances of the elements from the trailing edge of the wing.

### 3.3 Measured Patterns

Absolute gain patterns were measured for the array elements when illuminated by the far-field standard gain horn oriented in both E and H polarizations, producing co-pol and cross-pol relative linear polarizations. This was achieved by rotating the far-field standard gain horn by 90°. Fig. 10 shows the absolute gain patterns of element 39, for the co-pol and cross-pol states, respectively. The peak for the cross-polarization pattern is about 27 dB down from the peak of the co-polarization pattern.

## 4.0 Comparison of Theoretical vs. Measured Element Patterns

This section compares the measured element patterns versus the simulated element patterns that were computed to first-order using CyMPA. While our theoretical electromagnetic model accounts for the local curvature of the wing at the center of each element, any variation in curvature across the surface of a particular element is not accounted for, nor are the multipath effects induced by the global geometry and edges of the wing surface. Comparisons are made for sectors of the variably curved wing surface that have radically different rates curvature, in order to demonstrate the conditions under which our model most accurately predicts and fails to predict the measured element pattern behavior.

### 4.1 Absolute Gain

Our experimental results indicated that element 39 has an absolute gain of 3.4 dBi. By converting the remaining element gains to an absolute scale, the mean gain of all elements was found to be about 1.9 dBi. However, there are a few elements whose absolute gains fall well below this average. These outliers most likely occur due to poor electrical connections, or peeling of the microstrip's copper cladding from the extremely thin dielectric layer in the narrow

regions of the element feed microstrip transmission lines, as well as element impedance mismatches which may result from slight frequency shifts in the element resonant frequency. In order to mitigate the effects of the outliers on the calculation of the mean, the median gain was computed across all elements and found to be 2.8 dBi. In previous work [1], our theoretical model predicted the mean absolute gain across all elements to be about 6.5 dBi. Although there is almost a 4 dB discrepancy between the predicted and measured gains, there seems to be no observable element gain dependence as a function of element location for either the simulated or measured data.

## 4.2 Normalized Pattern Characteristics

The simulated element patterns were computed with respect to each element's local angular coordinate system, in which  $\gamma_n = \beta_n - \phi$  is the angle between the  $n^{\text{th}}$  element normal vector and the far-field observation point, as shown in Fig. 2. Thus,  $\gamma_n = 0^\circ$  represents element broadside in local coordinates. In order to make a direct comparison between the predicted and measured pattern characteristics, each measured pattern was translated from global to local coordinates by aligning the direction of the element normal with local  $0^\circ$ . The element normals were readily available, since they had been previously computed as part of the conformal wing design process [1].

Figs. 11-16 are plots of normalized element patterns as a function of local angle, where the simulated element pattern is shown as a dashed curve and the measured pattern is shown as a solid curve. The dotted curve is a "smoothed" version of the measured data. Each point along this curve represents the mean value of the measured data within a  $\pm 7.5^\circ$  kernel, that is, within a symmetric window. This function allows us to view the envelopes of the measured patterns more clearly and compute the beam centers with greater precision. The location of the beam center in each plot is denoted by a vertical line and was determined by computing the midpoint between the 3-dB points of the smoothed, measured element pattern.

Following the theoretical development in Section 2, the simulated element patterns are computed for the EUT on a conducting circular cylinder of radius equal to the radius of curvature of the conformal wing surface at the location of the element center. An equal number of neighboring elements are placed on each side of the EUT around the virtual cylinder in an attempt to capture the effects of mutual coupling. Since the elements along the conformal wing surface experience radically different radii of curvature at their element centers, as well as different rates of curvature within the local environment of the EUT, we may expect the angular region of validity for our model predictions to be a function of element location. For example, consider an element positioned along a relatively linear section of the wing, such as element 108, Fig. 14. Our approach models this element and its nearest neighbors rather accurately when computing the radiation pattern because the radius of curvature along this entire section of the wing is large and constant. Therefore, we would expect the angular region of validity for element 108 to be roughly the same as for an element in a linear array, from  $-90^\circ$  to  $+90^\circ$ . On the other hand, an element located along the leading edge of the wing, such as element 1, experiences a much smaller radius of curvature at the element center. In addition, the radius of curvature changes along the element itself, as well as within the local environment of the element. The difference between the theoretical circular cylindrical surface and the actual



conformal wing surface grows quickly as one moves away from the element center. In this case, we expect the angular region of validity to be much smaller than that for a linear array, and possibly skewed in angle space, as illustrated in Fig. 11, for element 1.

A direct comparison of the simulated patterns with the measured data reveals several trends. First, notice the large pattern ripples that occur towards the left of beam center for measured elements located near the bottom of the leading edge, that is, elements 108, 115, 116, and 1. As discussed in Section 3, these ripples can be attributed to multi-path from the trailing edge of the wing. Since our model does not incorporate such methods as the geometric theory of diffraction (GTD) or the uniform theory of diffraction (UTD) to account for scattering from the complex wing geometry, these ripples do not appear in the predicted patterns.

Secondly, as is evident from Figs. 11-16, the measured HPBW's are slightly narrower than those predicted by the model for all elements. This can be attributed to the fact that the theoretical model only accounts for four elements on each side of the EUT when determining the effects of mutual coupling, whereas the experimental elements have several neighboring elements, regardless of the location of the EUT along the conformal wing surface. These additional elements absorb energy, contributing to the narrowing of the element pattern HPBW.

Third, there is a subtler trend for elements along the top leading edge in which the measured element patterns become increasingly asymmetric as one moves towards the leading edge of the wing. Elements 2 and 16 represent the two extremes of this phenomenon. The same trend is evident for elements along the bottom leading edge of the wing, although it is much less pronounced. Our model does not predict this behavior. This is most likely due to the fact that our simulation symmetrically places the same number of elements around both sides of the EUT virtual cylinder when computing the element pattern, subjecting the EUT to an electromagnetic environment in which the mutual coupling is symmetrical. Thus, the simulated patterns exhibit perfect symmetry regardless of the element location along the wing surface. In the case of the conformal wing, elements near the leading edge do not follow the same symmetric distribution as the modeled elements on the virtual cylinder. On the wing, the measured element patterns are asymmetric with respect to the beam center. In contrast, as one moves away from the leading edge, elements are much more likely to have a symmetrical distribution of surrounding elements, and hence, these elements exhibit more symmetrical measured element patterns.

Finally, for several elements, the measured beam centers are shifted from element broadside, as is evident in Figs. 11-16. Furthermore, the magnitude of this shift depends on the location of the element along the conformal surface, as is shown in Fig. 17. In this figure, the angular offset of the beam center is plotted as a function of element location, for leading edge elements, where a positive offset corresponds to a rightward shift with respect to broadside, as in Fig. 11, and a negative offset corresponds to a leftward shift. Notice that the labeling of the  $x$ -axis starts with element 16, proceeds counter-clockwise around the leading edge of the wing, and ends with element 108. The top leading edge elements (2 – 16) show a small positive bias, indicating that the beam center is shifted towards the leading edge for these elements. The bottom leading edge elements (108 – 115) show smaller offsets with no bias, indicating that, in general, the beam center coincides with broadside for these elements. Elements 1 and 116 show a strong tendency for the main beam to shift in the positive global angle direction. These

phenomena most likely result from complex mutual coupling interactions described previously and the geometry of the wing surface, neither of which is incorporated into our model.

## 5.0 Conformal Array Pattern Control

The far-field pattern characteristics of the conformal wing array differ significantly as a function of the global scan angle,  $\theta_o$ , and whether all, or just a portion of the array is chosen as the active aperture. It is possible to optimize radiation pattern behavior in specific directions by selecting  $N$  consecutive elements to be active, while match-terminating all remaining elements. Typically,  $N$  will be less than half the total number of elements since it is not possible for both the top and bottom surfaces of the wing to face in the same direction, although we later show that some benefit can be derived by using all the array elements, even if they are on the other side of the wing. One approach is to choose an appropriate number of elements to achieve a desired projected aperture which faces into a particular scan region, described by  $\beta_i^- \leq \phi \leq \beta_i^+$ , where  $\beta_i^-$  and  $\beta_i^+$  are the local scan limits associated with the  $i^{th}$   $N$ -element active aperture. As the array's main beam is scanned toward either  $\beta_i^-$  or  $\beta_i^+$ , the array gain will decrease as a function of the  $N$  active element patterns, the overall curvature of the active aperture, and the extent of the projected aperture relative to scan direction. When gain roll-off exceeds some criteria, the  $N$ -element active aperture can be commutated around the curvature of the wing, a few elements at a time, thus establishing a new active aperture and a new scan region. As with linear and planar arrays, control of a conformal array pattern is achieved by determining an appropriate vector of complex-valued coefficients,  $a_n$ , as defined in Eq. 1. The approach described in this section iteratively computes these coefficients.

### 5.1 Conformal Array Pattern Synthesis Using Alternating Projections

In order to explore what patterns are achievable we use a pattern synthesis method based on alternating projections [5]. This is an iterative numerical approach which offers great flexibility and handles both shaped beam and pencil beam synthesis and arbitrary sidelobe envelopes. We apply this method to synthesize power patterns, that is, without constraints on the far field phase. The method is illustrated in Fig. 18, which shows a set of desirable patterns  $F_d$  and a set of realizable patterns  $F_r$ , and where we alternately find the closest point (projection) on the two sets until a common point (or the particular point of the realizable set which is closest to the desirable set) is found. Denoting by  $g_n(\phi)$  the field pattern of array element  $n$  in its array environment, the set of realizable patterns is represented by

$$F_r(\phi) = \sum_1^N a_n g_n(\phi), \quad (22)$$

where  $a_n$  are arbitrary complex excitation coefficients of the  $N$  elements. The set of desirable patterns may be represented by upper and lower bounds on the pattern,  $M_u(\phi)$  and  $M_l(\phi)$ , as shown in Fig. 19, and a desirable pattern  $F_d(\phi)$  may be represented by the discrete set of samples  $F_d(\phi_m)$ ,  $m=1 \dots M$ , ( $M \gg N$ ). The iterations now proceed as follows:

Projecting  $F_r(\phi) \rightarrow F_d(\phi)$

From  $F_r$ , the desirable pattern  $F_d$  is obtained by the rule, for  $m=1, \dots, M$

$$\text{if } M_l(\varphi_m) < |F_r(\varphi_m)| < M_u(\varphi_m), \text{ then } F_d(\varphi_m) = F_r(\varphi_m), \quad (23)$$

$$\text{if } |F_r(\varphi_m)| < M_l(\varphi_m), \text{ then } F_d(\varphi_m) = M_l(\varphi_m) * F_r(\varphi_m) / |F_r(\varphi_m)|, \quad (24)$$

$$\text{if } |F_r(\varphi_m)| > M_u(\varphi_m), \text{ then } F_d(\varphi_m) = M_u(\varphi_m) * F_r(\varphi_m) / |F_r(\varphi_m)|. \quad (25)$$

### Projecting $F_d(\varphi) \rightarrow F_r(\varphi)$

From  $F_d$  the realizable pattern  $F_r$  is obtained by solving the following overdetermined system of equations in the least-mean-square sense, which leads to a new set of  $\{a_n\}$  and thus to a new  $F_r(\varphi)$ .

$$F_r(\varphi_m) \equiv \sum a_n g_n(\varphi_m) = F_d(\varphi_m) \quad m=1, \dots, M \quad (26)$$

A weakness of the method of alternating projections is that it may get hung in a local minimum, as represented by the parts on the far right of the sets in Fig. 18, if an unsuitable starting point is chosen. As a precaution, therefore, we occasionally try different starting values for the element excitations, such as random values or values which are uniform in amplitude and focused in the desired main beam direction. So far, our results indicate that local minima do not pose a serious problem. Convergence of the method is fast, usually a few hundred iterations were adequate, which only took seconds on a 1.5 GHz PC.

## 5.2 Results Using Measured Element Patterns

Fig. 20 shows an example of a synthesized pattern for a  $135^\circ$  look direction, assuming elements 1-10 are active. These elements all have a local normal within  $\pm 22^\circ$  from the desired look direction. Imposing the desired upper and lower pattern bounds,  $M_u(\varphi)$  and  $M_l(\varphi)$ , as shown by the dotted lines, we obtain the best realizable pattern via alternating projections, shown by the solid line. The null-to-null beamwidth was set to 35 degrees, and in this case the desired sidelobe level of  $-30$  dB is practically realizable. The synthesized array distribution has a reasonable taper for a low-sidelobe pattern, as shown in Fig. 21, with the exception of the large amplitude of element 8. The reason is that this element pattern has a much lower amplitude than its neighbor elements, and therefore, it requires a correspondingly higher excitation to contribute equally to the array pattern. After a careful investigation of performance of individual elements, it appears that the microstrip feed on element 8 peeled away from the dielectric, creating considerable signal loss.

For the chosen active aperture of 10 array elements, the minimum sidelobe level of about  $-27$  dB cannot be suppressed further by lowering the desired sidelobe level or broadening the desired main beam. Thus, this level represents a sidelobe floor. Increasing the active array to include elements 1-15 only reduces this level by 3dB to  $-30$  dB, but allows a reduction in beamwidth from 35 to 23 degrees, as seen in Fig. 22. This beamwidth reduction fully corresponds to the increase in array size.

We next consider the case where all 116 elements are active. In this case the sidelobe floor lies at about  $-40$  dB and for the  $135$  degree scan direction the null-to-null beamwidth is about 7 degrees, as shown in Fig. 23. The corresponding array excitation is shown in Fig. 24. A few exceptional high values again indicate the presence of some bad elements, as described in Section 4. However, more interesting is that most elements on the bottom of the wing have



small, but non-zero excitations and thus contribute to the total pattern. Apparently the elements looking in the wrong direction help by canceling the sidelobes of elements looking in the desired direction, which is a kind of domino effect.

Finally, we attempt to synthesize a beam in the forward direction ( $\phi_0 \approx 180$  degrees), which is difficult since the projected area of the array is small, and very few elements radiate efficiently in that direction. Employing the eight elements (No. 1-7 and 116), whose normals are within 60 degrees of the desired look direction, we find that the projected area is  $13.5 \text{ cm} \approx 2.5$  wavelengths, which corresponds to an expected null-to-null beam width of about 48 degrees. Setting the desired beamwidth equal to this estimate and gradually reducing the desired sidelobe level we find that we can realize patterns with a uniform sidelobe level of about -20 dB, as shown in Fig. 25 full line. At this look direction, it appears difficult to suppress the sidelobe floor below about -27 dB, although more elements allow for considerably narrower main beams, as seen in Fig. 26.

### 5.3 Comparison of Results Using Theoretical vs. Measured Element Patterns

In an earlier stage of this project, we used theoretical element patterns for the synthesis of the total array pattern [1], [6]. It is of interest to compare those patterns with the present array patterns, which are based on measured element patterns. The theoretical array elements were designed with the code CyMPA, which models microstrip patches on dielectric covered, circular cylinders. Array element patterns  $g_n(\phi)$ , which include mutual coupling effects, were computed with this code by approximating each element and its neighbors with the corresponding, locally osculating circular array. A further approximation was incurred for cases where the radius of curvature was  $> 20\lambda$  or negative, in which the radius was to  $20\lambda$ . The reason is that CyMPA is based on an eigenfunction expansion which is limited to moderately large radii of curvature. A comparison of computed and measured element patterns is given in Section 4. The case of a desired beam in the  $135^\circ$  direction with null-to-null beamwidth  $29^\circ$  and sidelobe level of -40 dB is shown in Figs. 27 and 28, using computed and measured patterns, respectively, for elements 1-15. In other cases studied, overall structure of array patterns synthesized using computed and measured element patterns agreed fairly well, although the presence of high frequency ripple lead to a slightly higher sidelobe floors.

## 6.0 Conclusions

This investigation sought to characterize the electromagnetic behavior of a wing-shaped conformal array which has a highly variable rate of curvature, and further, to demonstrate an effective beamforming technique used for controlling the wing array's far-field array pattern. This paper brings to a close the work reported last year [1], with a strong emphasis on analyzing individual measured element pattern performance, and comparing measured element patterns against theoretical element patterns computed using CyMPA. The measured and theoretical patterns were then used to synthesize conformal array patterns.

The comparison analysis presented here suggests that our theoretical model generally makes accurate predictions of measured patterns for elements located on flat sections of the conformal wing surface. In contrast, the model does not completely capture the pattern behavior

of elements located on sharply curved sections of the wing. This result, is not surprising, since our model only approximates the local curvature of the patch elements themselves and does not account for scattering and multipath due to the overall geometry of the wing. The infinite cylinder model used in CyMPA ignores any scattering from the ends of a finite wing. However, a 3-D wing array would have several of these 2-D line arrays in parallel, which would increase the gain in the scan direction and reduce the illumination of the ends.

We have also explored pattern synthesis for a conformal wing array. Our computer model is based on a representative wing profile and on measured array element patterns which include the effects of mutual coupling and the local radius of curvature, to first-order. Therefore, the synthesized patterns should be highly realistic in a plane that is oriented transverse to the wing. The pattern synthesis method based on alternating projections appears to be highly efficient for this non-conventional array shape, and no convergence problems due to local minima were observed. Comparing the measured and computed element patterns we observe a high frequency ripple in the measured patterns but not in the computed patterns. This is presumably due to diffraction at the sharp trailing edge of the wing, and thus should be included in any realistic computer model. Its effect on the total array pattern is to raise the sidelobe floor, since these noise-like contributions can not be made to cancel over extended angular sectors. Alternatively, and preferably, this diffraction could be suppressed by some lossy surface coating on the wing. High quality patterns with uniform low sidelobes are achievable for most beam directions. An interesting finding is that, apparently, elements looking in the wrong direction help by canceling the sidelobes of elements looking in the desired direction, which is a kind of domino effect. This effect was stronger with computed than with measured element patterns. Possible future research in this area may include a more detailed analysis of pattern behavior for elements on sharply curved sections of the wing, as well as an attempt to reconcile the 4-dB absolute gain discrepancy between computed and measured patterns, seen across the elements.

## References

- [1] D. Curtis et al.: "Conformal Array Control using Digital Beamforming," Antenna Application Symposium, Allerton Park, Monticello, IL, Oct. 2001
- [2] J.C. Sureau and A. Hessel, "On the Realized Gain of Arrays", IEEE Trans. on Antennas and Prop., Jan. 1971.
- [3] Z. Sipus, *CyMPA – Program for Analyzing Microstrip Patch Array on Circular-Cylindrical Structures*, AFRL/EOARD Contract F61775-99-WE040 Final Technical Report, Apr. 2000.
- [4] R. Thomas, D. Curtis, E. Wisniewski, "Measurement of Element Patterns In A Conformal Wing Array", in 2002 Antenna Measurements and Techniques Symposium, Nov. 2002.
- [5] O. Bucci, D'Elia, G. Mazzarella, G. Panariello: *Antenna Pattern Synthesis: A New General Approach*. Proc. IEEE, March 1994.
- [6] H. Steyskal, "Pattern Synthesis For A Conformal Wing Array", in Proceedings of the 2002 IEEE Aerospace Conference, March 2002.

## Figures



Fig 1: Conformal wing array in anechoic chamber, set for element pattern measurements.

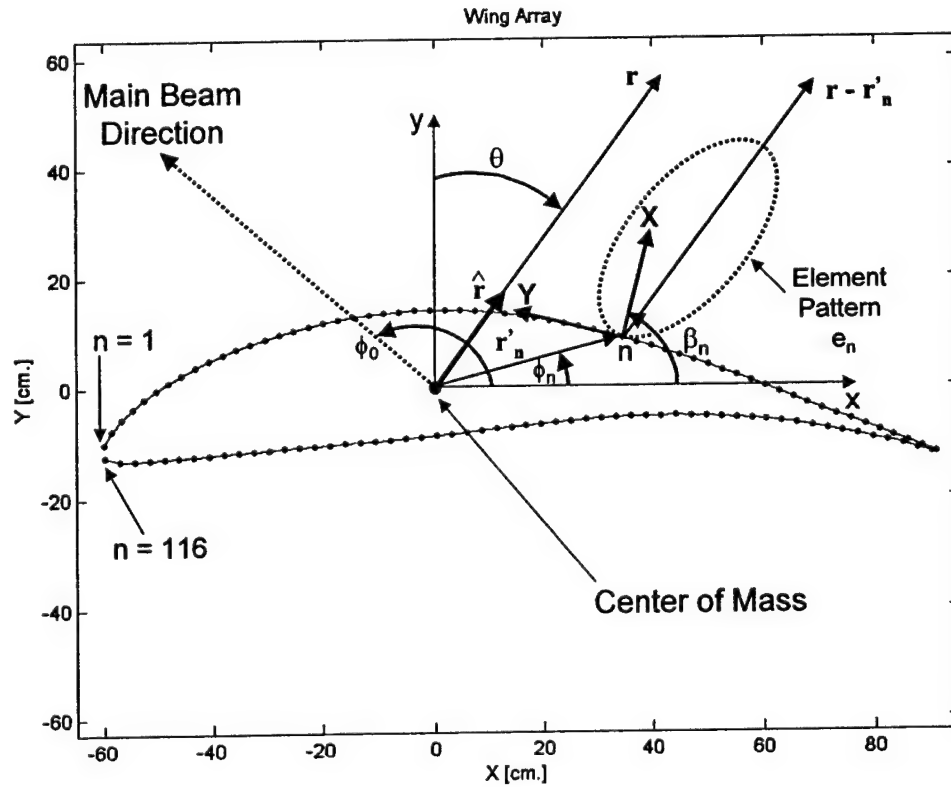


Fig. 2: Element indexing scheme, and variables used in the global and local coordinate systems.

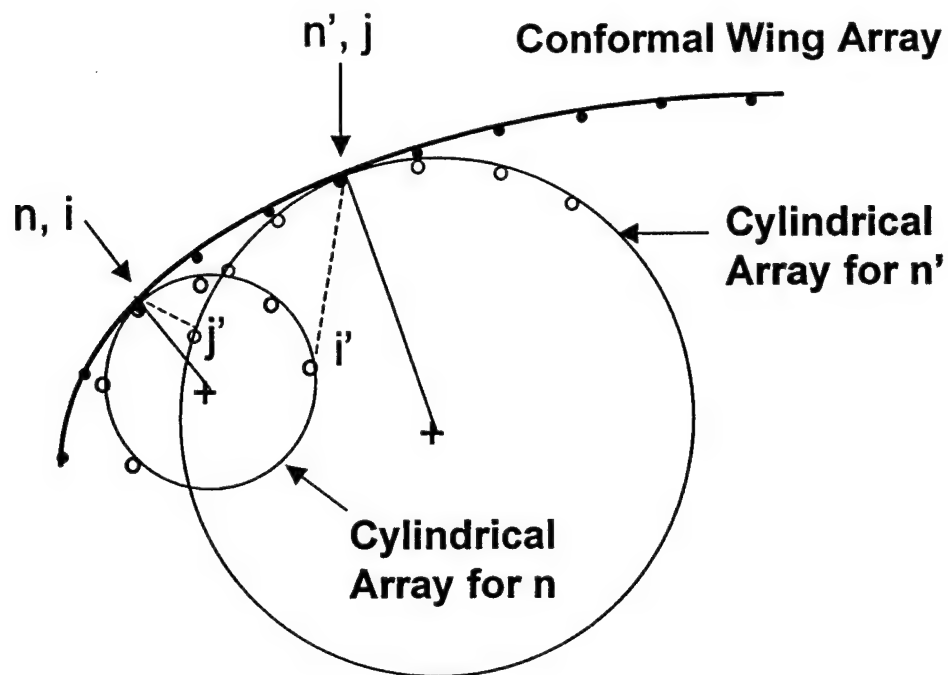


Fig. 3: Local geometry used in first-order approximation of mutual coupling

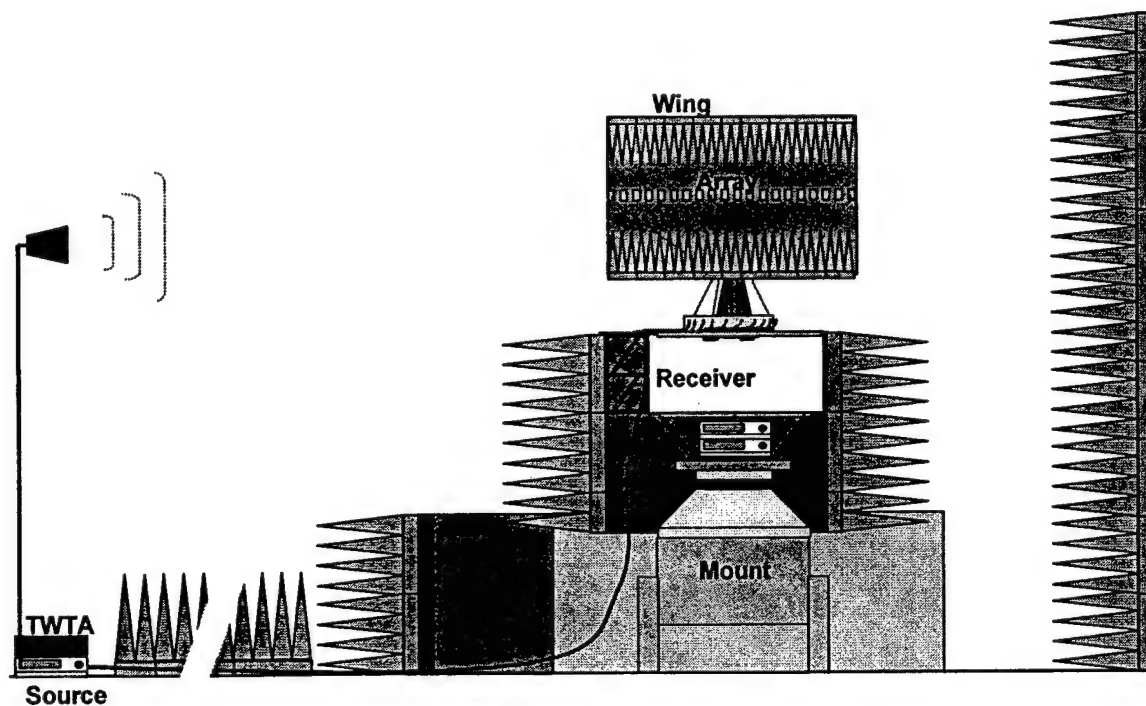


Fig. 4: Conformal array element pattern measurement configuration in anechoic chamber.

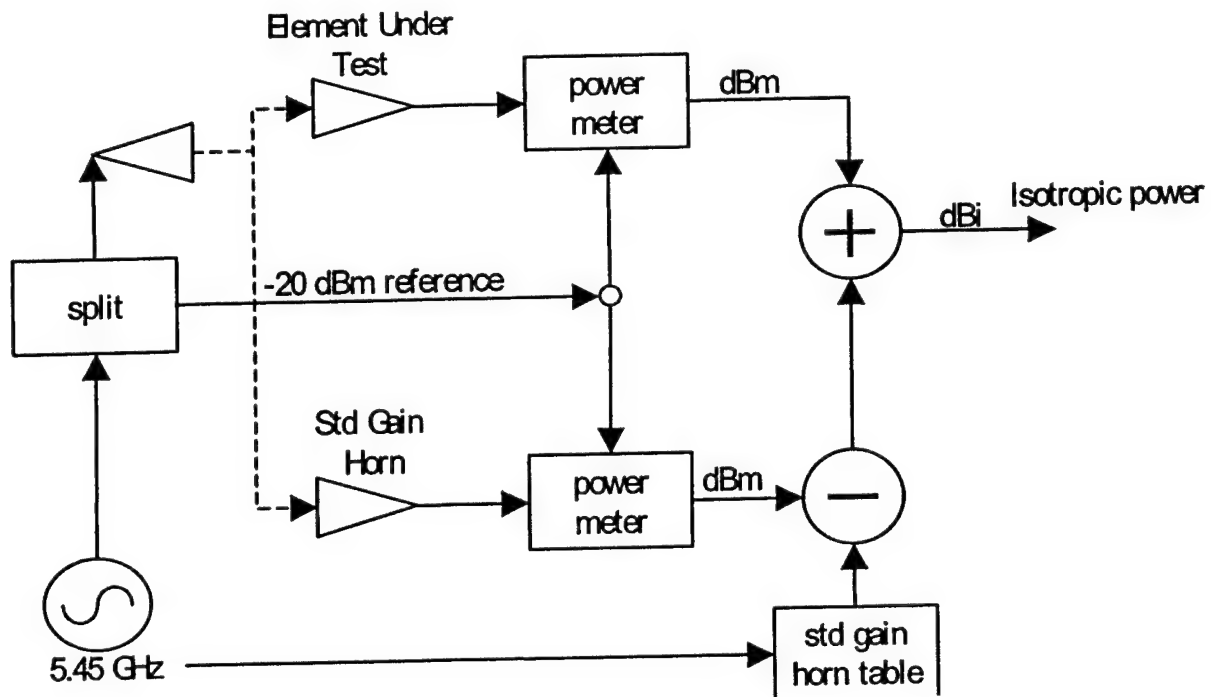


Fig. 5: Block diagram of the RF source and reference signal configuration

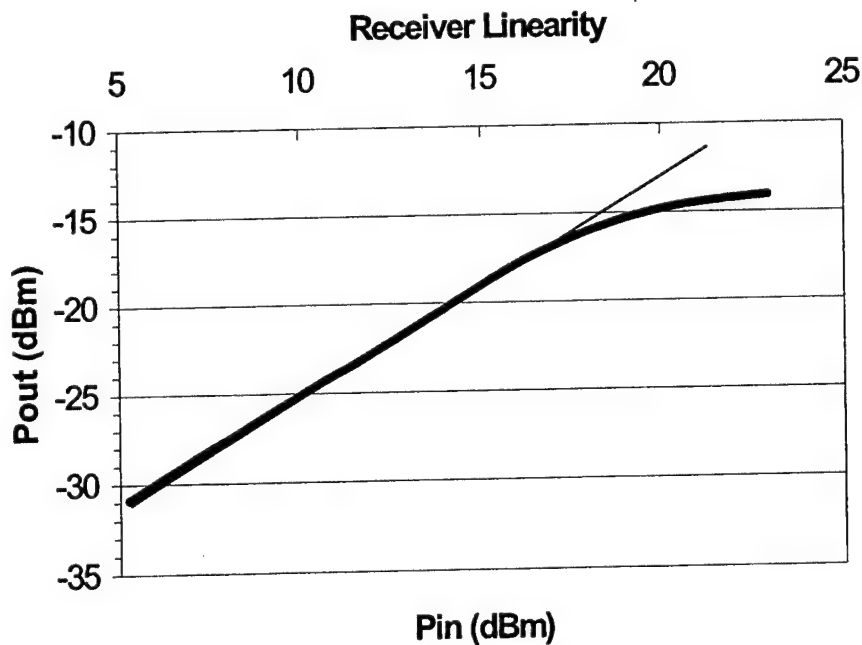


Fig. 6: Illustrating the linear range of RF receiver operation lies along the straight line projection, below the 1 dB compression point.

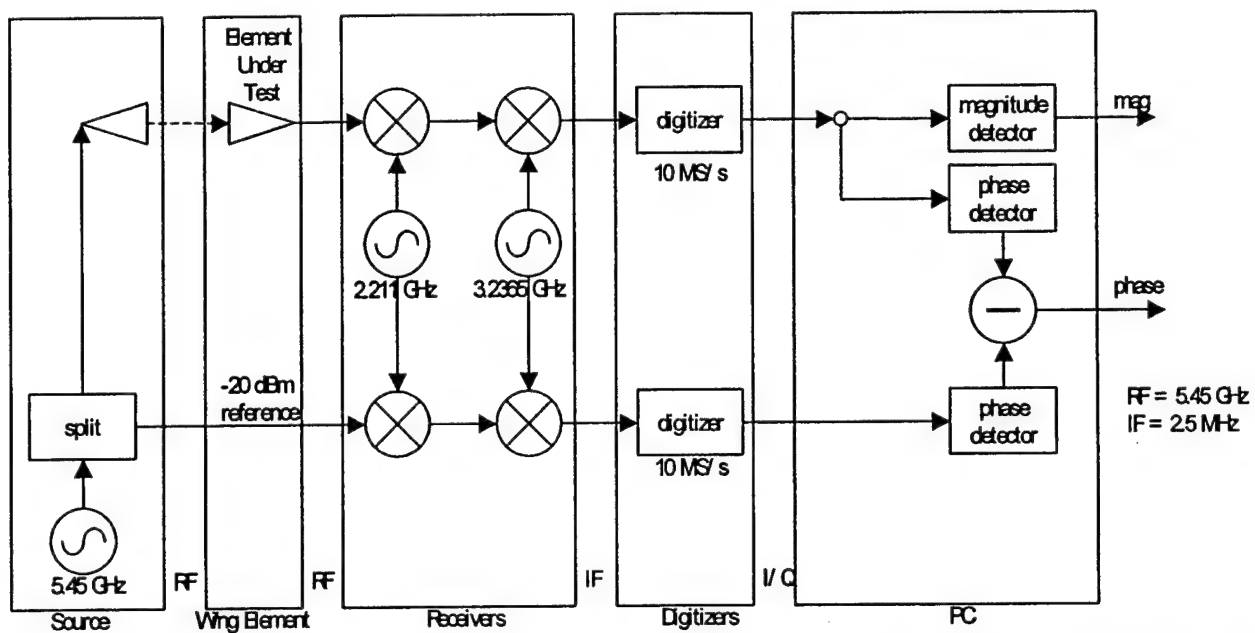


Fig. 7: Block diagram of the configuration used in conformal array measure patterns measurements.

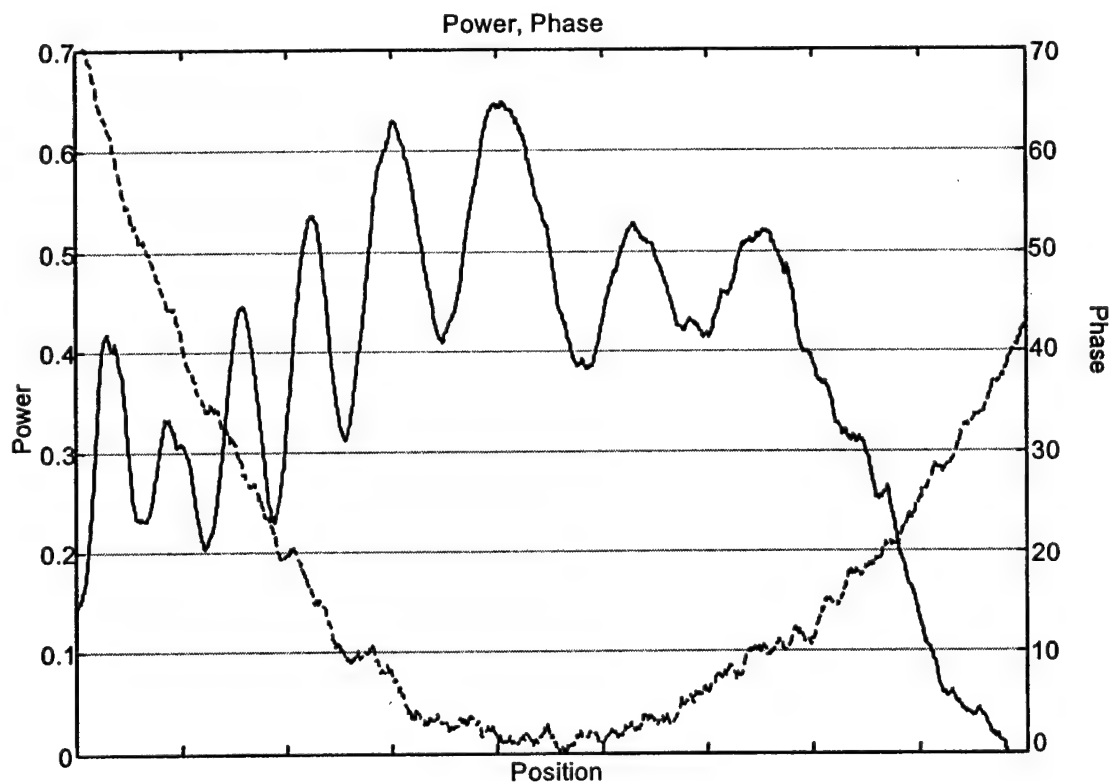


Fig. 8: Combined plots of the measured amplitude and phase variation along a horizontal slice of the quiet zone, measured along a 6' long sled oriented perpendicular to the incident wavefront.

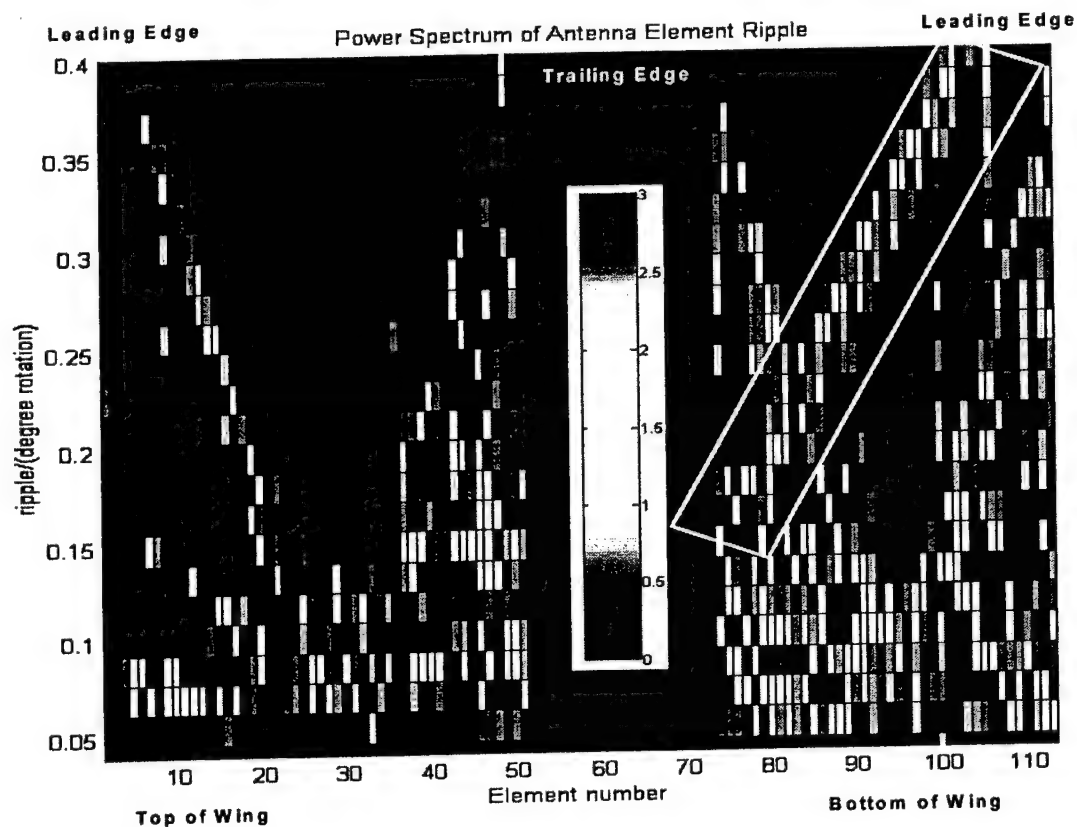


Fig. 9: FFT power spectra of spatial ripple as a function of element number in the array.

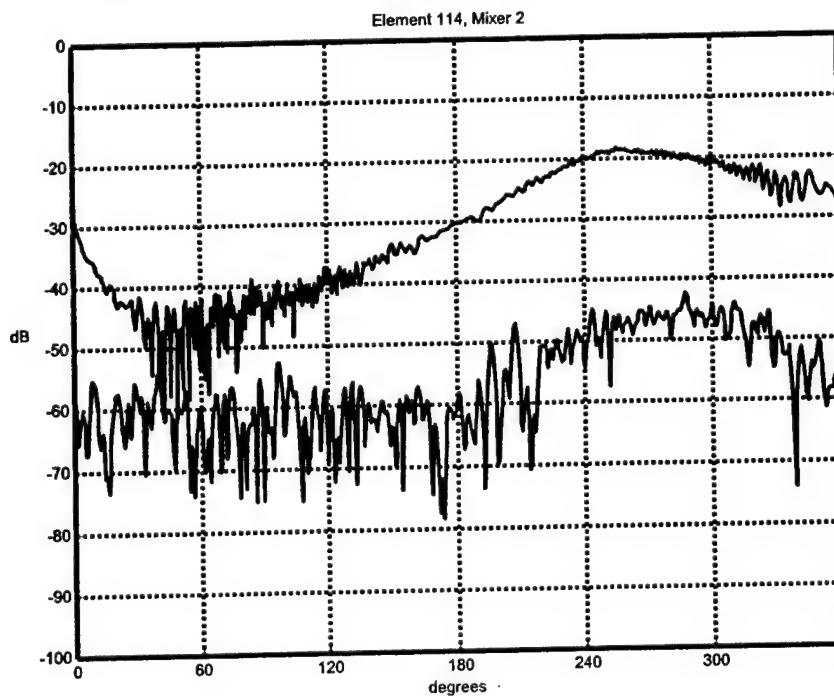


Fig. 10: Plots of co-pol and cross-pol absolute gain, measured for element 39.

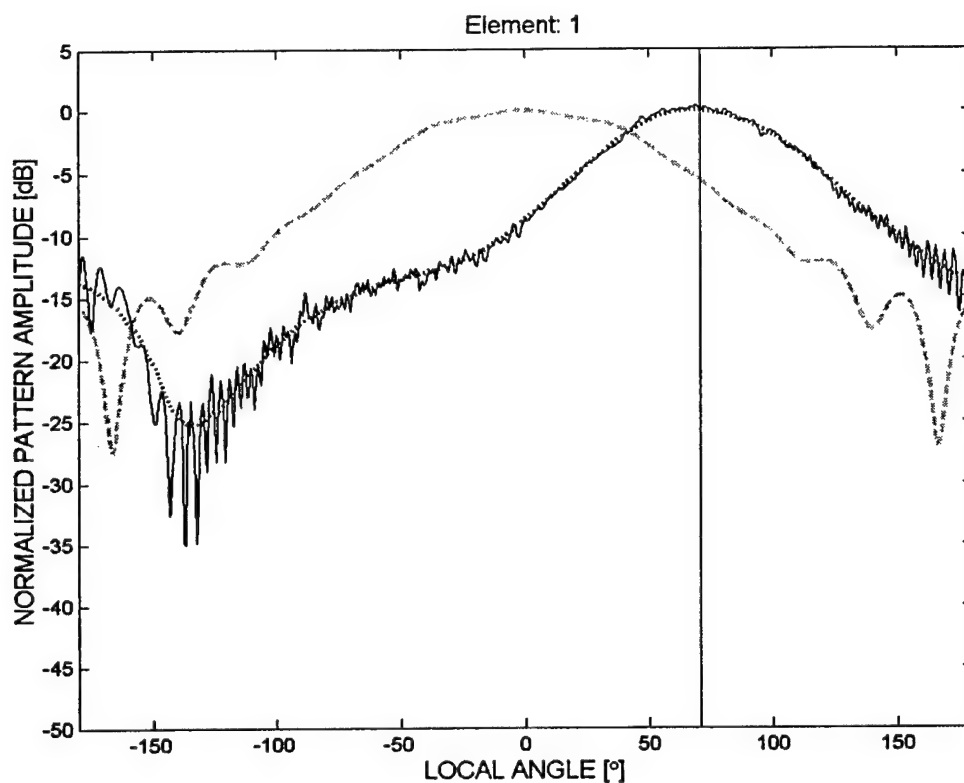


Fig. 11: Power patterns of Element #1, measured data (solid), smoothed version of measured data (dotted), theoretical (dashed)

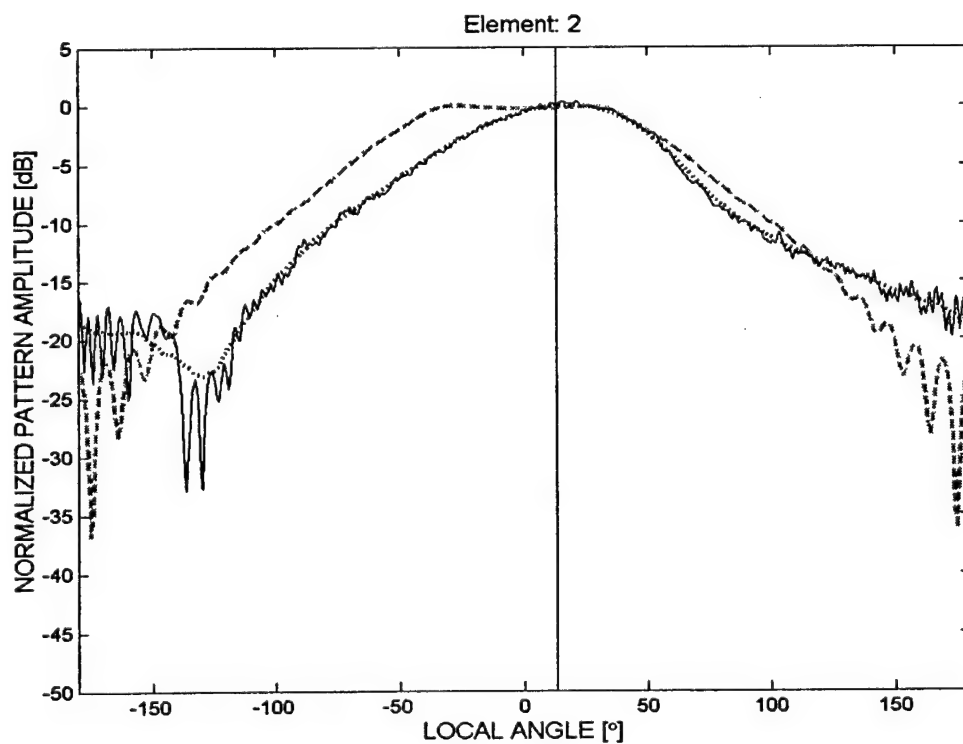


Fig. 12: Power patterns of Element #2, measured data (solid), smoothed version of measured



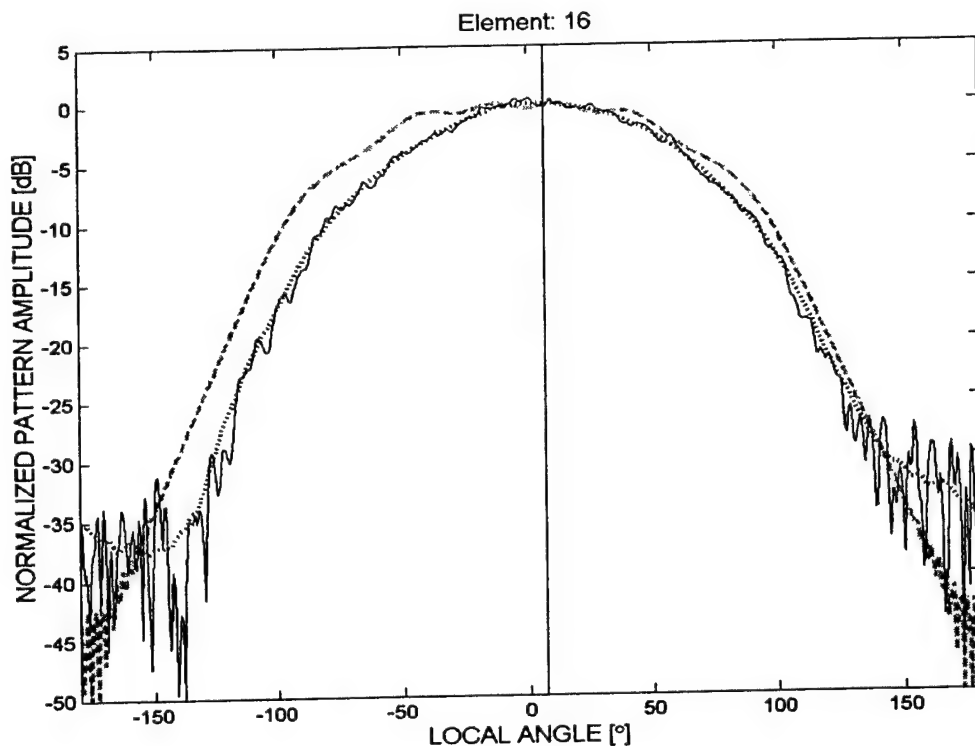


Fig. 13: Power patterns of Element #16, measured data (solid), smoothed version of measured data (dotted), theoretical (dashed)

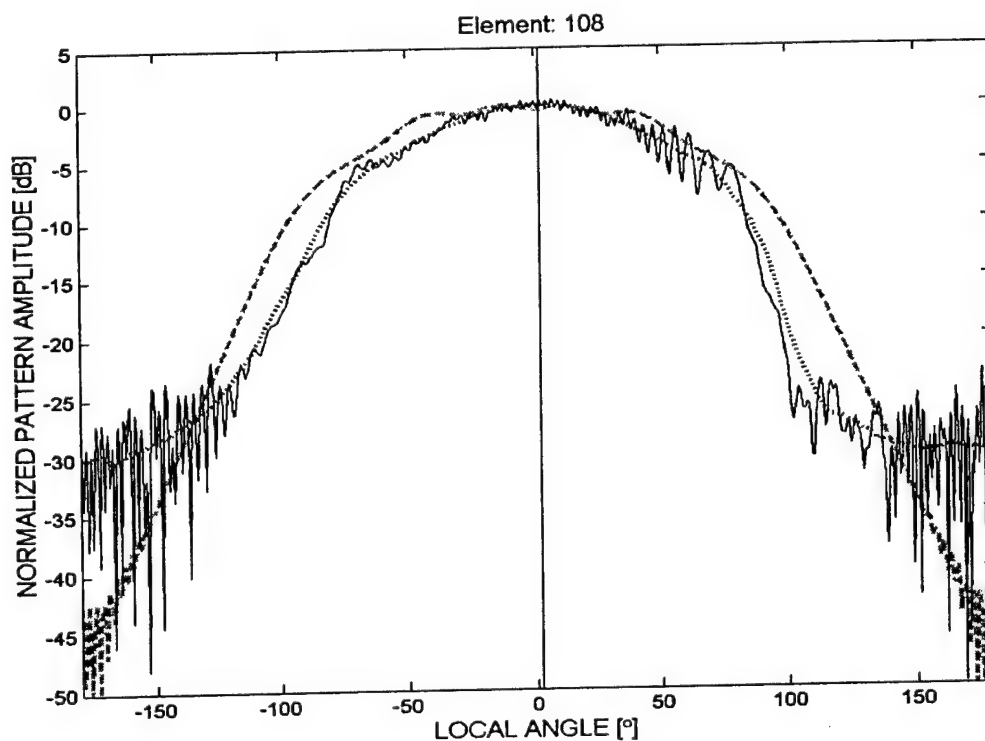


Fig. 14: Power patterns of Element #108, measured data (solid), smoothed version of measured

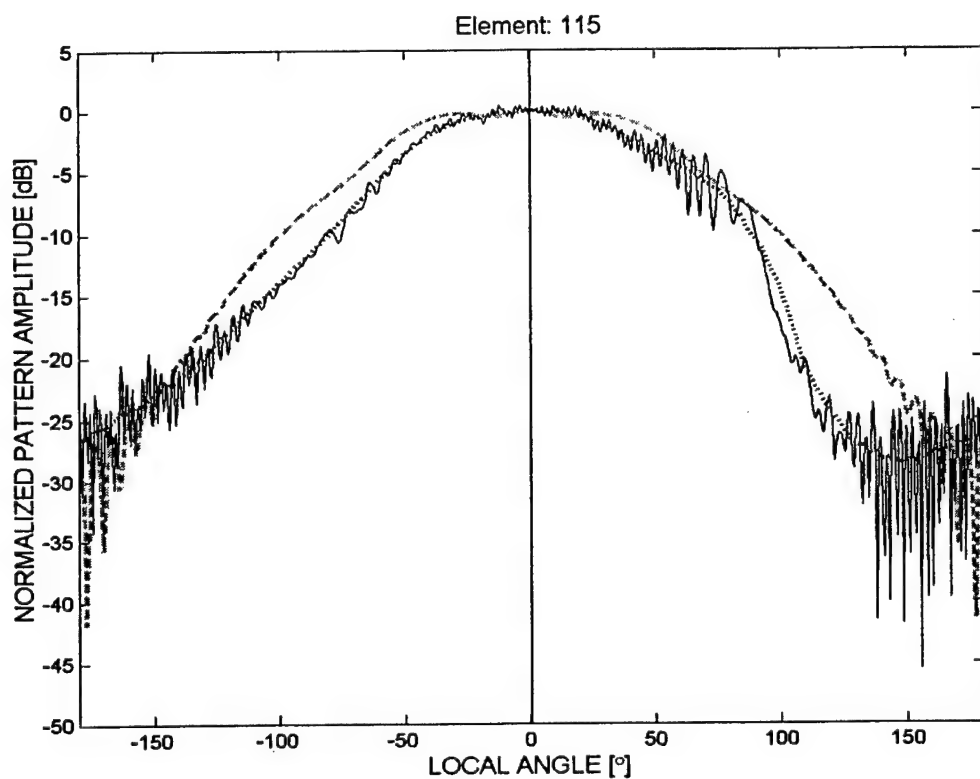


Fig. 15: Power patterns of Element #115, measured data (solid), smoothed version of measured data (dotted), theoretical (dashed)

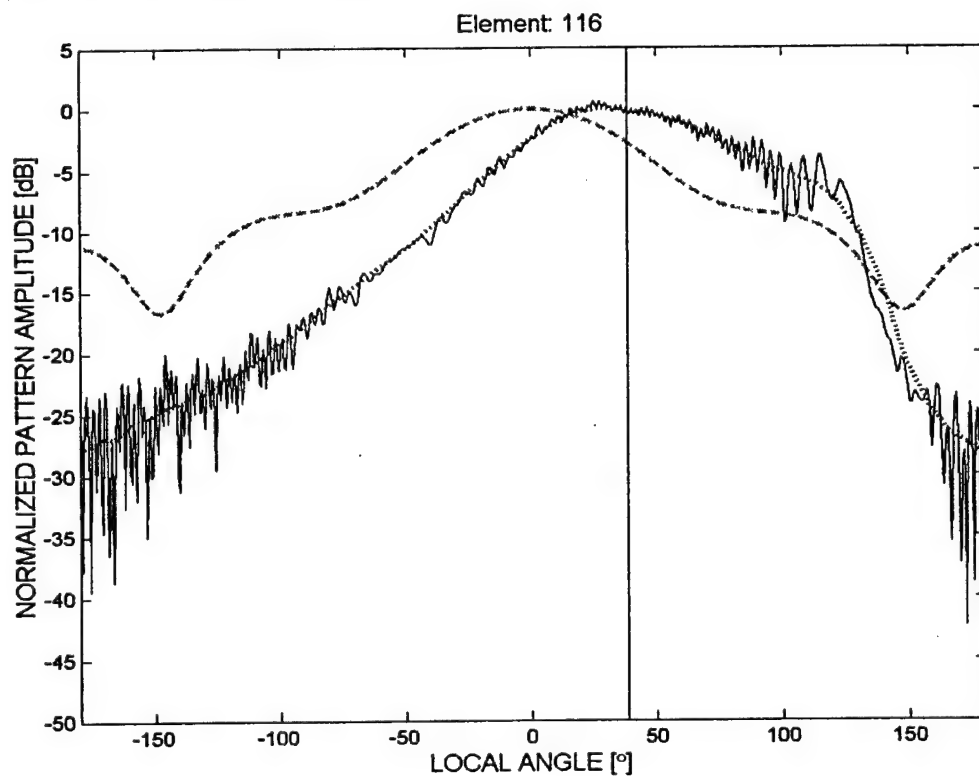


Fig. 16: Power patterns of Element #116, measured data (solid), smoothed version of measured

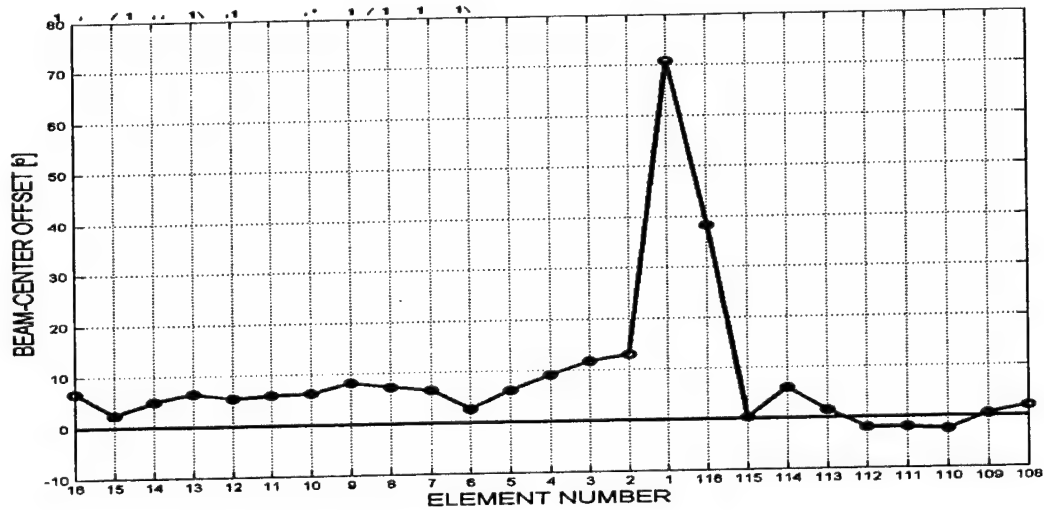


Fig. 17: Plot of element "beam center" offset, in degrees, relative to each element's local broadside.

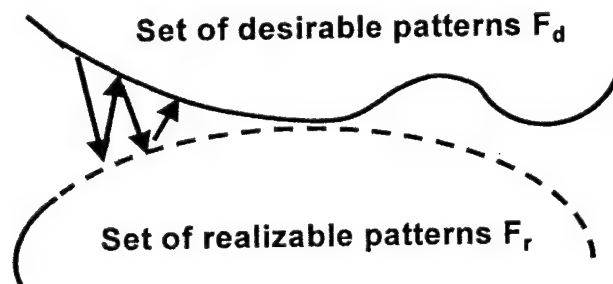


Fig. 18: Illustrating array pattern synthesis using the method of alternating projections.

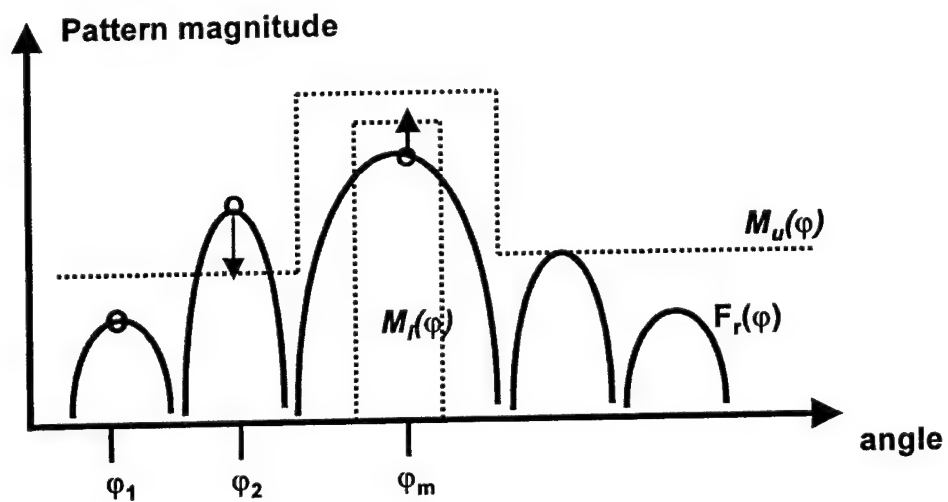


Fig. 19: The upper and lower bounds  $M_u(j)$  and  $M_l(j)$  define desirable patterns,  $F_r(j)$  represents a

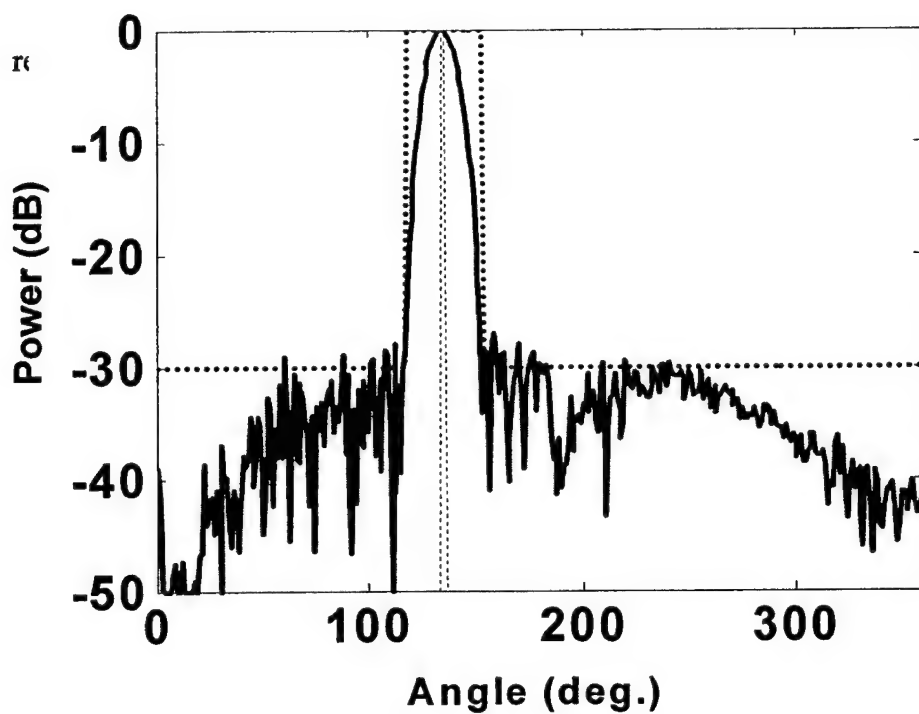


Fig. 20: Synthesized pattern for a 135-degree look direction (45 degree forward upward) with elements 1-10 active. Sidelobe floor is about -27 dB with 10 elements. Null-to-null beamwidth is 35 deg.

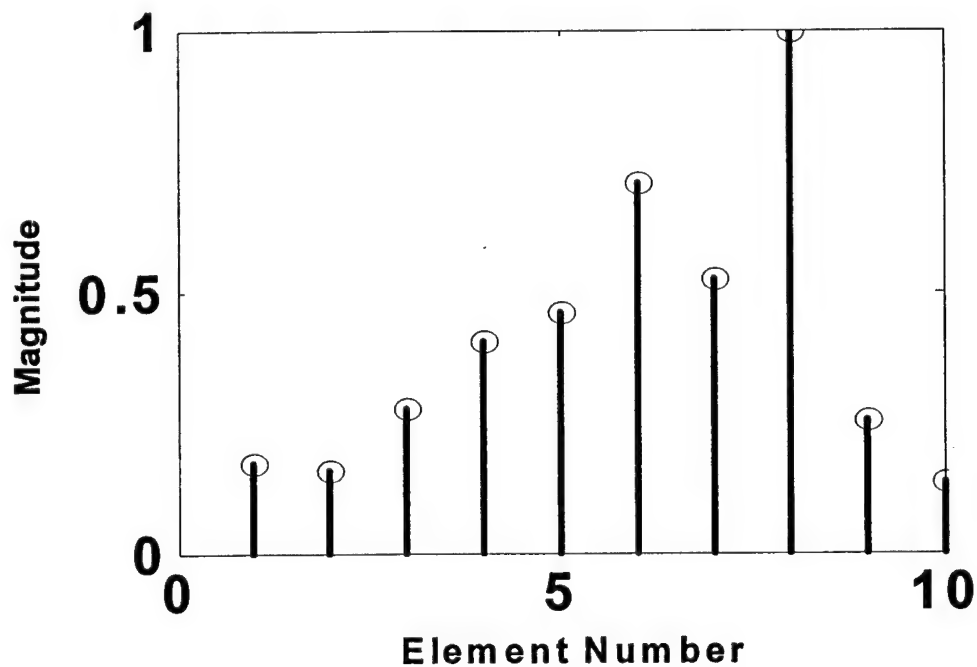


Fig. 21: Element excitations corresponding to the synthesized pattern in Fig. 20.

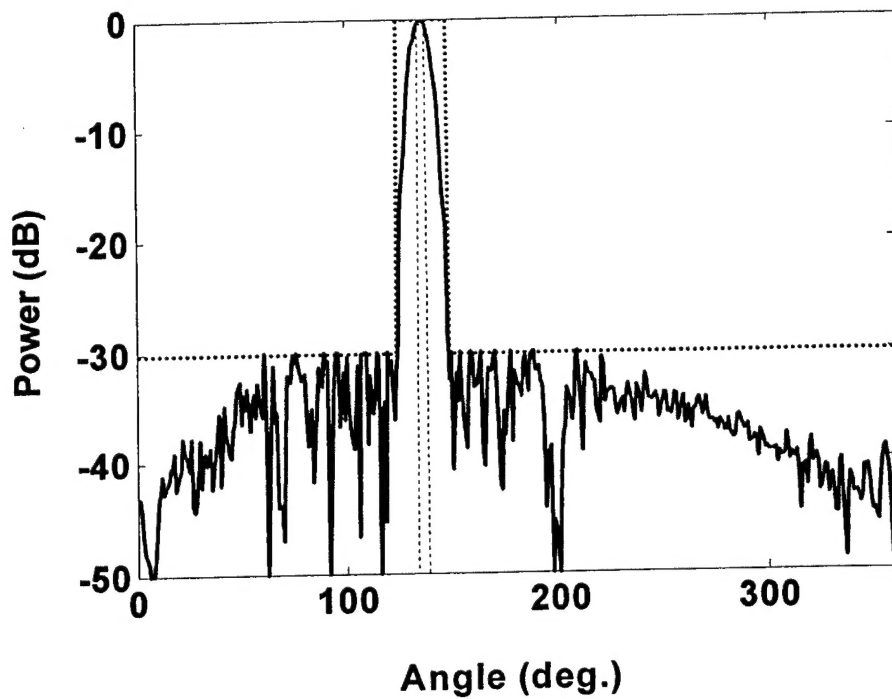


Fig 22: Activating elements 1-15 reduces the sidelobe floor to about  $-30$  dB and a yields a significant reduction in beamwidth. Null-to-null beamwidth is 23 degrees

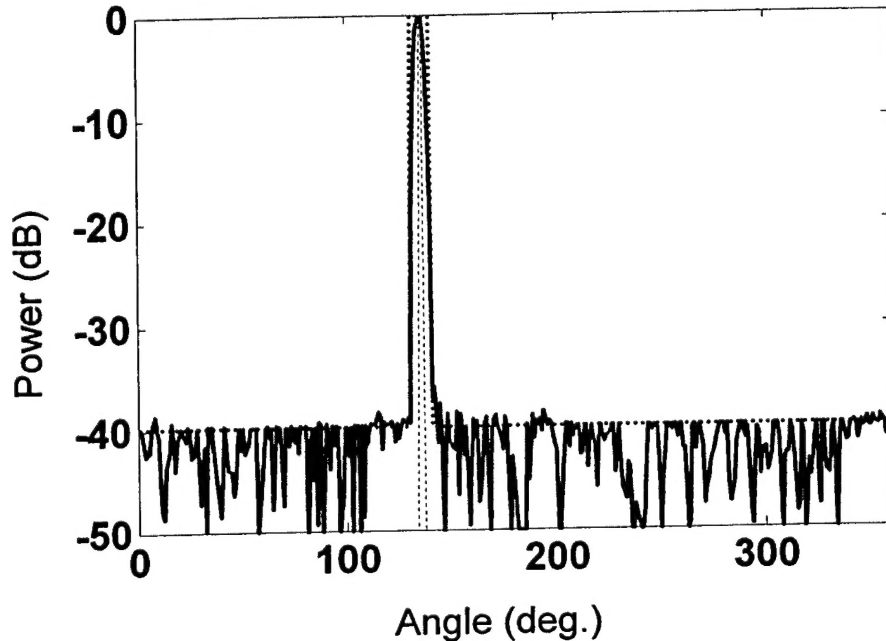


Fig 23: Synthesized 135 – degree beam whit all 116 elements active and corresponding array excitation. Note that all even elements on the bottom side of the wing are slightly excited. Large spikes in element excitation indicate bad element connections. Null-to-null beamwidth is 9 deg.

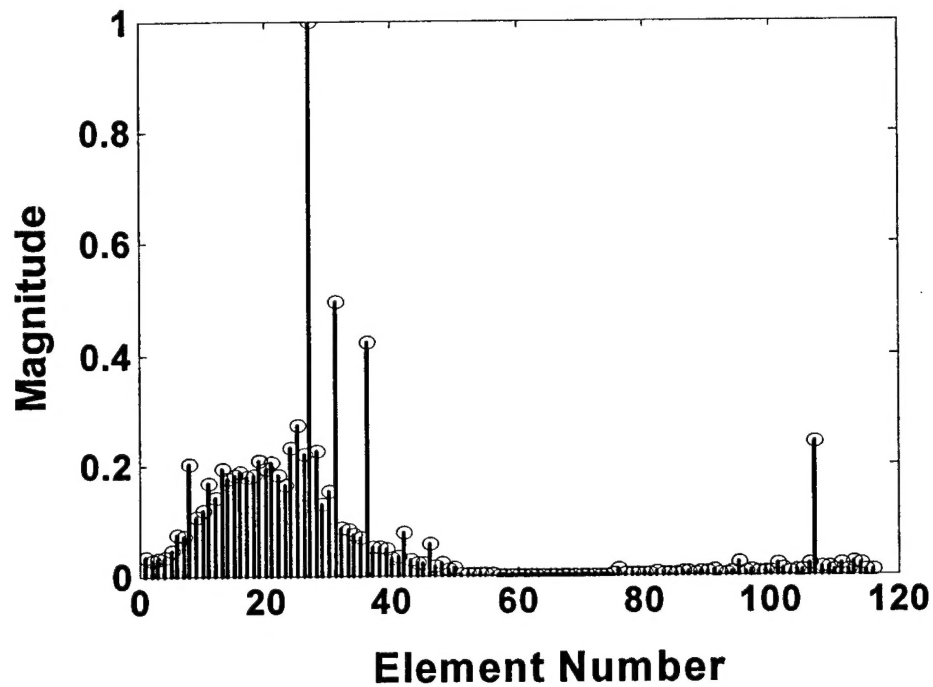


Fig. 24: Excitation coefficients for synthesized array pattern shown in Fig. 23.

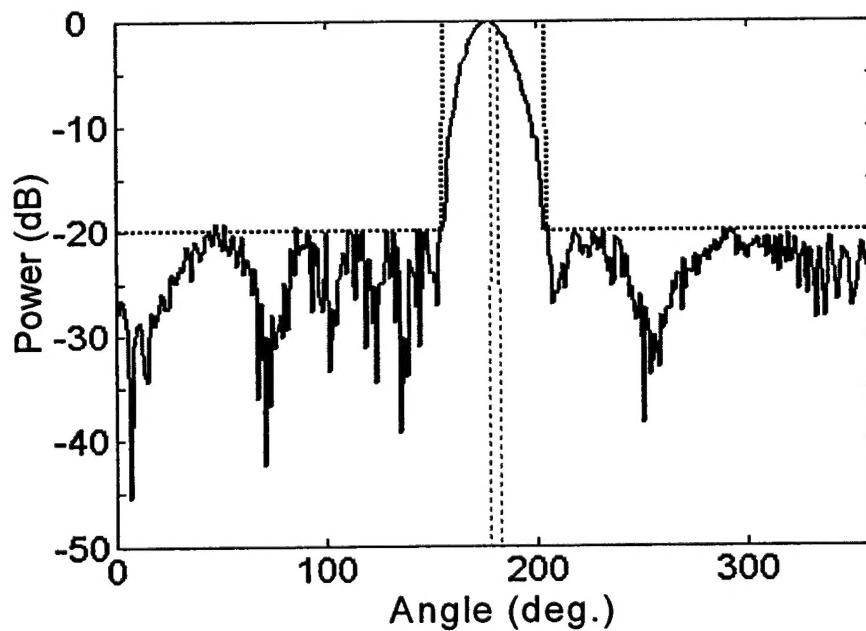


Fig. 25: With the main beam in the forward direction, where the projected aperture is minimum, the sidelobe floor lies at roughly  $-20$  dB, with 8 elements active (No. 1-7, 116). Null-to-null beamwidth is 48 deg.

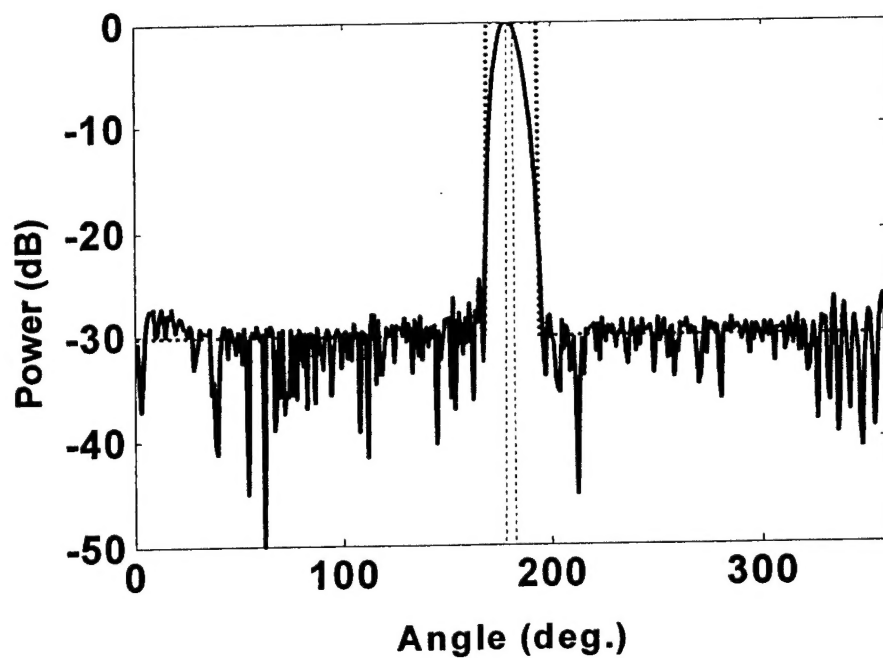


Fig. 26: With the main beam in the forward direction, activating more elements leads to a significant beamwidth reductions but only slight sidelobe reductions. Shown here is the case where all 116 elements are active, resulting in a beamwidth of 24 deg.

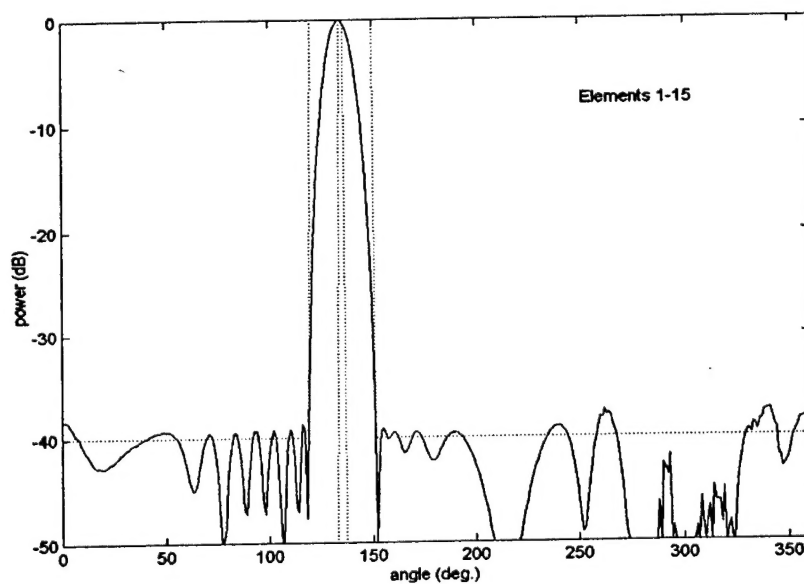


Fig. 27: From our earlier work [1], computed element patterns were used to synthesize an array pattern with close to  $-40$  dB sidelobes with only 15 elements active.

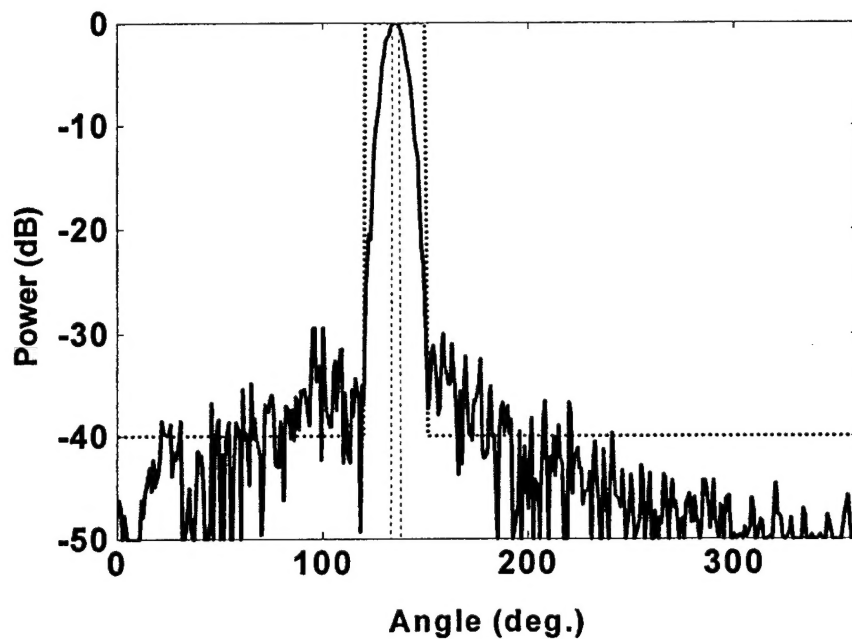


Fig. 28: Measured element patterns were used to synthesis the same array pattern shown in Fig. 26, however, in this case, the high-frequency ripple in the measured element patterns limits the sidelobe level increases to roughly  $-30$  dB.